Title
Advances in Zero-Field Nuclear Magnetic Resonance Spectroscopy

Author
Theis, Thomas

Publication Date
2012

Peer reviewed|Thesis/dissertation

Advances in Zero-Field Nuclear Magnetic Resonance Spectroscopy

By

Thomas Theis

A dissertation submitted in partial satisfaction of the

requirements of the degree of Doctor of Philosophy

in

Chemistry

in the

Graduate Division

of the

University of California, Berkeley

Committee in charge:

Professor Alexander Pines
Professor Dmitry Budker
Professor David Wemmer

Spring 2012

Abstract

Advances in Zero-Field Nuclear Magnetic Resonance Spectroscopy

by

Thomas Theis

Doctor of Philosophy in Chemistry

University of California, Berkeley

Professor Alexander Pines, Chair

In the course of the last century, Nuclear magnetic resonance (NMR) has become a powerful and ubiquitous analytical tool for the determination of molecular identity, structure, and function. Traditionally, the great analytical power of NMR comes at the cost of mobility and large expenses for cryogenic cooling. This thesis presents how zero-field NMR detected with an atomic magnetometer is emerging as a new, potentially portable and cost-effective modality of NMR with the ability of providing information-rich and high-resolution spectra. A detailed description of the zero-field NMR spectrometer and its operation is provided. The thesis details how the acquired zero-field NMR spectra result from the electron mediated scalar interaction (*J*-coupling) of nuclear spins in an analyte. Simple rules of addition of angular momenta are introduced for the prediction of the observed spectral lines overcoming the need for numerical simulations and enabling unambiguous assignment of peaks to different molecules. Additional information can be obtained in the near zero field regime, where the Zeeman interaction can be treated as a perturbation to the *J*-coupling. The presence of small magnetic fields results in splitting of the zero-field NMR lines, imparting additional information to the pure zero-field spectra. In addition to the utilization of the atomic magnetometers for enhanced sensitivity, hyperpolarization schemes can be implemented. This thesis shows that chemically specific zero-field NMR spectra can be recorded using hydrogenative and non-hydrogenative parahydrogen induced polarization (PHIP, NH-PHIP), enabling high-resolution NMR. The increased sensitivity enables detection of compounds with ^{13}C or ^{15}N in natural abundance. Since PHIP and NH-PHIP operate *in situ*, and eliminate the need for a prepolarizing magnet, they broaden the analytical capabilities of zero-field NMR. Lastly, this thesis gives insight into the PHIP and NH-PHIP mechanism by developing an appropriate theoretical framework.

Dedication

To my wife & to my son.

Acknowledgments

I am incredibly grateful for the fabulous opportunity to conduct all my graduate work in a great work environment and I want to thank each and everyone who has contributed, not only to the work, but also to the experience of grad school overall. It was a pleasure to interact with so many inspiring individuals. Any attempt of creating an exhaustive list of all the people that have contributed to the experience at Berkeley is prone fail. At the same time, I do want to express my gratitude to absolutely everybody that has made my experience into what it was and has thereby enabled this thesis.

Foremost, I want to thank my adviser Alex Pines and my committee members Dima Budker and Dave Wemmer, who guided me through the Ph.D. program.

My special thanks go to the people that were directly involved with my work and helped with all aspects of the work presented in this thesis: Micah Ledbetter, Gwendal Kervern, Mark Butler, Paul Ganssle, John Blanchard, Hattie Ring, Doug Shin, Pete Mustonen and Vik Bajaj. I also want to give special thanks to all those that have originally introduced me to the lab and taught me all the ins and outs of basic NMR when I first joined the lab: Louis Bouchard, Scott Burt and Leif Schroeder.

Furthermore, I want to thank Alyse Jacobson who always was incredibly helpful and takes wonderful care of the lab's administration.

I am particularly grateful for all the fabulous conversations and interactions centered around science and outside of science, which helped me along through the entirety of the grad school program. I that sense, in no particular order I thank all fellow students and postdocs that have shared time with me in the pines lab: Franz Schilling, Sean Osterday, David Trease, Marcus Donaldson, Jeff Paulsen, Claudia Avalos, Elad Harel, Emilee Sena, Dan Kennedy, Tom Teisseyre, Aleks Kijac, Dan Baum, Misha Berger, Monica Smith, Chang Shin, Lindsay Sperling, Phuong Dao, Scott Seltzer, Jinny Sun, Haijing Wang, Anna Parker, Nick Halpern-Manners, Matt Ramirez, David Michalak, Chip Crawford, Tyler Meldrum, John Franck, Dominic Graziani and Ngoc Do.

Finally I have to express my gratitude to our family friends Daniel, Annie and Makaio Pak, who have become a second family to me, to my wife and our son. At any stage we could ALWAYS be sure of their help and support, and that is truly invaluable.

Table of Contents

1. Introduction

Nuclear magnetic resonance experiments are typically performed in high magnetic fields, often in excess of 10 T, in order to maximize chemical shifts, in order to achieve high nuclear spin polarization and efficient detection via inductive pickup.[1,2] The advent of alternative methods of detection based on superconducting quantum interference devices (SQUIDs)[3] or atomic magnetometers [4,5] has enabled NMR experiments in low (Earth's field) and even zero magnetic field, generating significant experimental [6–21] and theoretical [16,22] interest. Atomic magnetometers [4,23] and SQUIDs [3] are sensitive to low-frequency signals, offering dramatically improved signal-to-noise ratio (compared to inductive pickup coils) in low-field NMR[6,11,17,24] and magnetic resonance imaging[12,25,26]. This is leading to the development of portable sensors for chemical analysis and imaging by elimination of cryogenically cooled superconducting magnets. This new type of spectrometers has enabled chemical analysis via ^{129}Xe chemical shifts [10] and spin-spin or *J*-couplings between ^{1}H-^{13}C, ^{1}H-^{29}Si, and ^{1}H-^{19}F in low- or zero-magnetic field [6,13,19]. In regard to portability and cost effectiveness, atomic magnetometers are an ideal tool because, in contrast to SQUIDs, they do not require cryogenic cooling. The work presented in this uses atomic magnetometers to detect NMR at zero field. The primary advantage of zero-field NMR detection is that the NMR spectra become simpler than at small fields (~Earth's field) where the *J*-coupling and Zeeman contributions are comparable in strength. In addition, at zero magnetic field the resonance frequencies of the nuclear spins and the magnetometer's alkali spins are matched, thereby operating in the regime where atomic magnetometers are most sensitive.[19,21]

Much effort has been devoted to the interpretation of NMR spectra acquired in the low-field regime.[13,16,20,22,27,28] At low fields the effect of a magnetic field does not fully truncate the transverse components of the *J*-coupling and the emerging patterns quickly become complex (e.g. Earth's field NMR spectra). One way to reduce complexity (other than increasing the magnetic field) is to eliminate the magnetic field entirely[19]. Pure *J*-coupling spectra result that are more amenable to straightforward interpretation.

This thesis, first, provides theoretical background and describes the experimental details of the zero-field NMR spectrometer in Chapters 2 and 3 respectively. Then, in Chapter 4, a formalism is provided to readily interpret and assign spectral features arising in zero-field NMR. Simple rules governing the addition of angular momenta can be used to predict the number of lines and their positions for given spin systems. This work overcomes the need for numerical simulations for chemical identification and makes the assignment of peaks more intuitive, thereby moving beyond just-fingerprinting applications. Furthermore, it has been pointed out in the literature, that pure zero-field NMR leaves some ambiguity in determination of chemical groups, and that this ambiguity can be removed by application of small magnetic fields[22]. In Chapter 5 this thesis shows that by application of a small magnetic field, where the Zeeman interaction is only a perturbation to the *J*-coupling a significant amount of additional information can be obtained and ambiguities can be removed concerning the nuclear species in a spin system.

To further increase the sensitivity of zero-field NMR it the atomic magnetometer may be combined with hyperpolarization schemes[29–32]. A variety of available hyperpolarization techniques such as dynamic nuclear polarization (DNP),[32,33] chemically induced DNP (CIDNP)[34], spin-exchange optical pumping (SEOP)[35–37] of noble gases and parahydrogen induced polarization (PHIP)[31,38–41]suggests that sensitivity limitations given by the Boltzmann thermal polarization can be overcome for a large range of analytes. Most of these hyperpolarization techniques, DNP[9,42–44], CIDNP[45–47], SEOP[48] and PHIP[21,49], have been shown to greatly enhance sensitivity of low-field NMR experiments where thermal polarization is even lower. Chapter 6 of this thesis shows that through the combination of an atomic magnetometer with parahydrogen induced polarization (PHIP)[31,38,39] the sensitivity of zero-field NMR can be greatly enhanced. High-resolution, high signal-to-noise ratio, zero-field NMR spectra result. The acquired spectra are information rich and chemically specific. The sensitivity is sufficient to easily observe complex spectra exhibiting ^{1}H-^{13}C *J*-couplings in compounds with ^{13}C in natural abundance in just a few transients, a task that would require considerable signal averaging using thermal prepolarization. Similarly, in Chapter 7, it is shown that non-hydrogenative parahydrogen-induced polarization[50–52] (NH-PHIP) can also dramatically enhance the sensitivity of zero-field NMR. The thesis demonstrates the detection of pyridine, at concentrations as low as 6 mM in a sample volume of 250 μL, with sufficient sensitivity to resolve all identifying spectral features because the NH-PHIP mechanism is non-reactive, operates *in situ*, and eliminates the need for a prepolarizing magnet, its

combination with optical atomic magnetometry could greatly broaden the analytical capabilities of zero-field and low-field NMR. Lastly in Chapter 8 a theoretical formalism is developed that explains in detail how parahydrogen derived scalar order is imposed on analytes and converted into detectable magnetization. This formalism is relevant for both, the hydrogenative and the non-hydrogenative modalities of PHIP at zero magnetic field.

2. Theoretical Background

In this Section the essential background will be provided to enable understanding of the later more advanced Chapters. A basic quantum mechanical description of a standard high-field NMR experiment will be provided, forming a starting point for understanding zero-field NMR and parahydrogen induced polarization. The notion of a density matrix and the role of commutators will be introduced in this first Section.

In high-field NMR the primary spreading parameter giving spectral information is the chemical shift. Chemical shift is the resonant frequency of a nucleus relative to a standard. The physical effect results from diamagnetic shielding of the nucleus by the surrounding electrons, such that chemical shift is an indirect measure of the electron density at a given position in a molecule. In high-field NMR this effect is typically much larger than the so called *J*-coupling interaction and is the primary indicator for chemical identity in the context of standard high-field NMR experiments. *J*-coupling is the scalar interaction between nuclei mediated by bonding electrons in a molecule. At zero-magnetic field in an isotropic liquid the *J*-coupling interaction is the only observable interaction on the timescales of zero-field NMR and is, hence, responsible for the appearance of the zero-field NMR spectra presented throughout this thesis. In this Chapter, the treatment of the evolution of a density matrix under a *J*-coupling Hamiltonian and/or chemical shift will be introduced, in the context of high-field Fourier-Transform NMR (FT-NMR) experiments. In the subsequent Chapters the evolution under *J*-couplings alone will be in the center of the discussions.

Furthermore, the addition of quantum mechanical angular momenta will be reviewed in this Chapter. This concept is typically of secondary importance in high-field NMR experiments but, as will be shown in Chapter 4, it forms the basis for understanding zero-field NMR spectra. The reason is that in high-field experiments the strong magnetic field and the chemical shifts truncates parts of the *J*-coupling Hamiltonian, however at zero-magnetic field the full spherical symmetry of the *J*-coupling Hamiltonian has to be taken into account. Lastly, in the present Chapter, the concept of para-hydrogen induced polarization will be introduced and the classical high-field NMR description of PHIP experiments will be reviewed and spectra acquired from hydrogenations of symmetric substrates will be described.

2.1 Quantum mechanical description of a FT-NMR experiment

This review is intended to provide the necessary tools for understanding the basic quantum mechanical description of the simplest pulsed NMR experiment i.e. ninety, pulse, acquire on a two-level system formed by a single spin one-half. At the end of this Section an introduction to the treatment of *J*-coupled spin one-half systems at high magnetic fields is given. Other appropriate sources for the basics of NMR as presented here are Levitt's book "Spin Dynamics"[53] or Cavanagh's book "Protein NMR Spectroscopy"[54]. Some of the quantum mechanical basics presented in this first Section can also be found in Sakurai's book "Modern Quantum Mechanics"[55] for example.

2.1.1 Basis states

In a two level system we represent each of the two states of the system, α and β as a vector:

$$|\alpha\rangle = \begin{pmatrix} 1 \\ 0 \end{pmatrix} \text{ and } |\beta\rangle = \begin{pmatrix} 0 \\ 1 \end{pmatrix}. \tag{2.1}$$

These are referred to as the ket vectors, the corresponding bra vectors are

$$\langle\alpha| = (1 \quad 0) \text{ and } \langle\beta| = (0 \quad 1). \tag{2.2}$$

Together they form the basis of the "bra-ket" notation. (A more formal introduction of basis states is provided in Section 2.2.1.)

In this two level system we can describe any state or superposition state $|\psi\rangle$ as a linear combination of the two vectors:

$$|\psi\rangle = c_1|\alpha\rangle + c_2|\beta\rangle . \tag{2.3}$$

In this equation the coefficients c_1 and c_2 can be imaginary such that they can carry phase information. The bra-ket notation in the spin one-half case can now be simplified and $|\psi\rangle$ can be expressed as

$$|\psi\rangle = \begin{pmatrix} c_1 \\ c_2 \end{pmatrix} \text{ and } \langle\psi| = (c^*_1 \; c^*_2) = \left(|\psi\rangle\right)^\dagger \;, \tag{2.4}$$

where, the coefficients c_n are the individual components of the vector $|\psi>$. One important property of the basis states, in this case $|\alpha\rangle$ and $|\beta\rangle$ is that they be orthonormal. This means that they should have the following properties: The inner product of two basis states gives the Kronecker delta:

$$\langle n|m\rangle = \delta_{nm} \begin{cases} 1 \text{ if } n = m \\ 0 \text{ if } n \neq m \end{cases}, \tag{2.5}$$

where $|n>$ and $|m>$ are general basis states of systems with more than just two energy levels. The stated property of orthonormality also implies that the sum over all outer products of basis states gives the identity matrix

$$\sum_n |n\rangle\langle n| = \hat{\mathbf{1}}, \tag{2.6}$$

where n sums over all basis states of the system under consideration. This is the useful "resolution of the identity" as will be shown and used in Eq. (2.10)

2.1.2 Expectation values and the density matrix

The expectation value of a measurable quantity is defined as follows:

$$\langle A\rangle = \langle\psi|A|\psi\rangle = \int_{-\infty}^{+\infty} \psi^* A \psi \, d\tau \;. \tag{2.7}$$

Here A represents an operator with some associated physical measurable quantity (examples follow). In the spin one-half case operators are two by two matrices that act on the wave functions represented by vectors with two components. When evaluating the above equation with unspecified variables we obtain the following.

$$\begin{aligned}\langle A\rangle = \langle\psi|A|\psi\rangle &= (c^*_1\ c^*_2)\begin{pmatrix} A_{11} & A_{12} \\ A_{21} & A_{22}\end{pmatrix}\begin{pmatrix} c_1 \\ c_2\end{pmatrix} \\ &= c^*_1c_1A_{11} + c^*_1c_2A_{12} + c^*_2c_1A_{21} + c^*_2c_2A_{22}\end{aligned} \tag{2.8}$$

As is apparent from Eq. (2.8) there are quadratic terms (like $c_1^*c_1$) of the coefficients, which determine the expectation value. Therefore, it seems reasonable to concern ourselves with an object that carries these quadratic terms, in addition this object should be independent of a specific observable. This object is the density matrix ρ, defined as

$$\rho = |\psi\rangle\langle\psi| = \begin{pmatrix} c^*_1c_1 & c^*_1c_2 \\ c^*_2c_1 & c^*_2c_2\end{pmatrix}. \tag{2.9}$$

In NMR the density matrix the diagonal terms are called populations and the off-diagonal elements are called coherences.

In order to calculate an expectation value of some observable using the density matrix we need to evaluate Eq. (2.7)

$$\langle A\rangle = \langle\psi|A|\psi\rangle. \tag{2.7}$$

We make use of Eq (2.6), the resolution of the identity, and can derive Eq. (2.10) which serves as the basis of understanding the origin of NMR signals and will find ample use in the remainder of this thesis.

$$\begin{aligned}&= \sum_n \langle\psi|A|n\rangle\langle n|\psi\rangle \\ &= \sum_n \langle n|\psi\rangle\langle\psi|A|n\rangle \\ &= \mathrm{Tr}(|\psi\rangle\langle\psi|A) = \mathrm{Tr}(\rho A).\end{aligned} \tag{2.10}$$

2.1.3 Time evolution of the density matrix

The initial density matrix in a simplified case representing 100% polarization is the density matrix in which only state $|\alpha\rangle$ is populated, we call this matrix I^α

$$I^{\alpha} = |\alpha\rangle\langle\alpha| = \begin{pmatrix} 1 & 0 \\ 0 & 0 \end{pmatrix}. \tag{2.11}$$

It is useful to express all our matrices in the form of the Pauli spin matrices because they obey cyclic commutation relationships which have useful properties for the prediction of time-evolution as we will see in Eq. (2.23) through Eq. (2.25) (Note: The notation used in this thesis suppresses $\hbar$) For a two level system (one spin) the fundamental Pauli-matrices are:

$$I_z = \frac{1}{2}\begin{pmatrix} 1 & 0 \\ 0 & -1 \end{pmatrix}, \; I_x = \frac{1}{2}\begin{pmatrix} 0 & 1 \\ 1 & 0 \end{pmatrix} \text{ and } \; I_y = \frac{1}{2}\begin{pmatrix} 0 & -i \\ i & 0 \end{pmatrix}. \tag{2.12}$$

Using these we can write I^{α} as

$$I^{\alpha} = \frac{1}{2}\hat{1} + I_z. \tag{2.13}$$

In order to examine how this density matrix evolves under some Hamiltonian H it is reasonable to start by examining the time dependent Schrödinger equation:

$$\frac{d}{dt}|\psi\rangle = -iH|\psi\rangle, \tag{2.14}$$

which can be solved to give

$$|\psi(t)\rangle = \exp(-iHt)|\psi(0)\rangle \; . \tag{2.15}$$

Similarly, for the bra we obtain

$$\langle\psi(t)| = \langle\psi(0)|\exp(iHt) \; . \tag{2.16}$$

Thus for the density matrix as a function of time we derive

$$|\psi(t)\rangle\langle\psi(t)| = \exp(-iHt)|\psi(0)\rangle\langle\psi(0)|\exp(iHt) \tag{2.17}$$

or

$$\rho(t)=\exp(-iHt)\rho(t=0)\exp(iHt). \tag{2.18}$$

The expression exp(-iHt) is often referred to as the propagator and replaced by U(t), such that

$$\rho(t) = U(t)\rho(t=0)U(-t) \; . \tag{2.19}$$

In the specific case of pulses exp(-iHt) is sometimes replaced by $R_\phi(\theta)$ which represents a rotation by angle θ and phase ϕ, as will be shown below. On the basis of the presented equations all evolution of density matrices can be addressed.

2.1.4 Commutators and the sandwich formula

Before jumping into how to easily evaluate this equation we will make a sideline discussing commutators and their use in the context. It will become apparent instantaneously why this is useful.

The commutator of two operators is defined as

$$[A,B] = AB - BA. \tag{2.20}$$

If [A,B]=0 then A and B are said to commute. Furthermore, if [A,B]=0 then

$$[\exp(A),\exp(B)] = 0 \ , \ [A,\exp(B)] = 0 \ , \ [B,\exp(A)] = 0. \tag{2.21}$$

For the density matrix in Eq. (2.18) this has the following implications;

$$\text{if } [H,\rho] = 0 \text{ then } \rho(t) = \rho(t=0). \tag{2.22}$$

This means there is no time evolution, however if the commutator of the density matrix and the Hamiltonian is nonzero then time evolution is to be expected.

In the special case of cyclic commutation relationships the time evolution is easy to evaluate. Luckily cyclic commutation relationships apply for the Pauli spin matrices.

$$[I_x,I_y]=iI_z \quad [I_z,I_x]=iI_y \quad [I_y,I_z]=iI_x. \tag{2.23}$$

In this case the sandwich relationships apply. If [A,B] = i C and circular permutations thereof,

$$\text{then} \quad \exp(-i\theta A)B\exp(i\theta A) = B\cos\theta + C\sin\theta. \tag{2.24}$$

If the order in inverted such that [B,A]=-iC and its cyclic permutations

$$\text{then} \quad \exp(-i\theta B)A\exp(i\theta B) = A\cos\theta - C\sin\theta. \tag{2.25}$$

2.1.5 Hamiltonians during the NMR experiments and their action

The Hamiltonians acting during an NMR experiment, in the simplest case, is $H=-\gamma B\mathbf{I}$. Here γ is the gyromagnetic ratio of the examined spin. B represents the strength of an applied magnetic field acting on the spin and **I** is the spin operator. During the sequence of a basic NMR experiment consisting of a pulse and subsequent acquisition only two different Hamiltonians need to be considered. The Hamiltonian during the pulse is typically represented as

$$H=-\gamma B_1 I_x \text{ or } H=-\gamma B_1 I_y, \tag{2.26}$$

if a RF pulse with phase x or phase y of strength $B_1$is applied.

The Hamiltonian during the period of free evolution which is

$$H=-\gamma B_0 I_z . \tag{2.27}$$

The frequency $\omega=-\gamma B$ defines the precession frequency which is the so called Larmor frequency, i.e. $-\gamma B_0 = \omega_0$ is the precession frequency during free evolution and $\gamma B_1 = \Omega_1$ is the precession frequency when the pulse is applied.

At this point we have all the tools to evaluate what happens to the density matrix I^{α} when applying a 90 degree pulse. (Here the concept of rotating frames will not be introduced and RF pulses are treated as magnetic fields in the x or y direction without z component, the interested reader is referred to the literature[53,54])

We are now in a position to evaluate Eq.(2.18) under the specific action of these Hamiltonians. For a pulse along y, Eq.(2.18) can now be expressed as:

$$\begin{aligned}\rho(t)&=\exp(-i\Omega_1 t I_y)\rho(t=0)\exp(i\Omega_1 t I_y)\\ &=\frac{1}{2}\hat{\mathbf{1}}+I_z\cos(\Omega_1 t)+I_x\sin(\Omega_1 t) .\end{aligned} \tag{2.28}$$

If we choose $\omega_1 t$ to be exactly 90° (i.e. a 90° pulse) then only $\frac{1}{2}\hat{1}+I_x$ remains after the pulse. At this point the Hamiltonian changes because the pulse is stopped and the free evolution under $H=\omega_0 I_z$ begins. We can propagate the density matrix after the pulse under this Hamiltonian:

$$\begin{aligned}\rho(t) &= \exp(-i\omega_0 t I_z)\left(\frac{1}{2}\hat{1} + I_x\right)\exp(i\omega_0 t I_z) \\ &= \frac{1}{2}\hat{1} + I_x\cos(\omega_0 t) + I_y\sin(\omega_0 t) \\ &= \frac{1}{2}\begin{pmatrix} 1 & \cos(\omega_0 t) - i\sin(\omega_0 t) \\ \cos(\omega_0 t) + i\sin(\omega_0 t) & 1 \end{pmatrix}.\end{aligned} \tag{2.29}$$

In the NMR experiment I^-, representing a coherence between the two available states, is the observable hence we obtain the signal using Eq. (2.10) as:

$$s(t) = \mathrm{Tr}(\rho I^-) = \cos(\omega_0 t) + i\sin(\omega_0 t) = \exp(-i\omega_0 t), \tag{2.30}$$

which after Fourier transform gives a delta function i.e. one peak at frequency ω_0, as shown in Figure 2.1

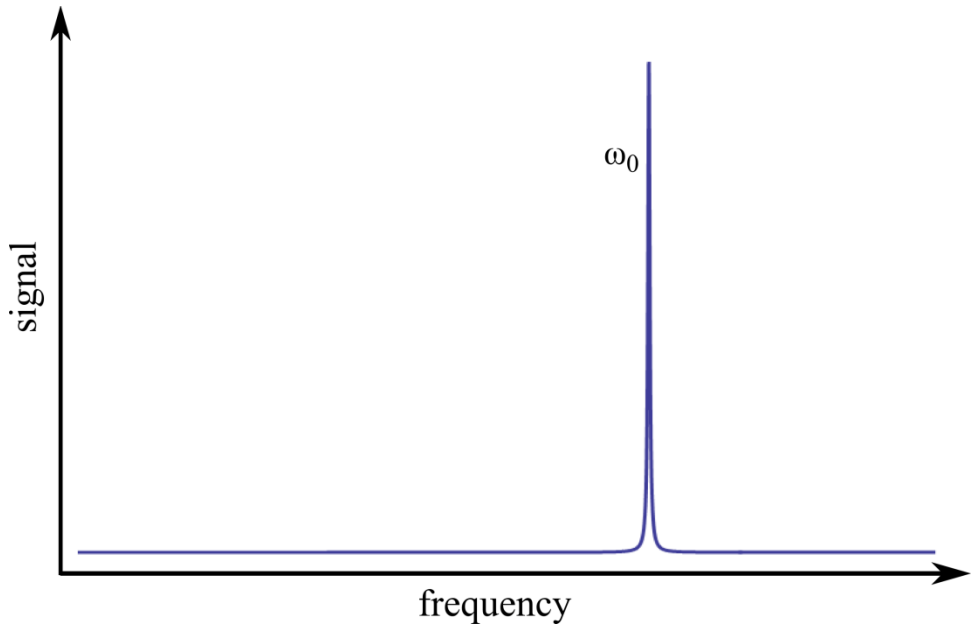

Figure 2.1 NMR signal from an uncoupled spin one-half system. Only one frequency ω_0 is observed. Instead of the delta function expected from Eq. (2.30). A Lorentzian line-shape is shown assuming some exponential relaxation of the signal which after FT-transform gives the Lorentzian line shape convoluted with the original δ-function.

2.1.6 High-field NMR experiments on two coupled spins

Before addressing how the Hamiltonian in a two-spin system looks and how the evolution in the two-spin system proceeds, some basic characteristics of the two-spin system will be described: What are the basis states? How does a density matrix for two coupled spins look? How do we construct a complete set of spin operators?

The basis states can be constructed such that they obey the orthonormality condition given in Eq. (2.5) (a more formal introduction of basis states follows in Section 2.2.2):

$$|\alpha\alpha\rangle = \begin{pmatrix} 1 \\ 0 \\ 0 \\ 0 \end{pmatrix} \quad |\alpha\beta\rangle = \begin{pmatrix} 0 \\ 1 \\ 0 \\ 0 \end{pmatrix} \quad |\beta\alpha\rangle = \begin{pmatrix} 0 \\ 0 \\ 1 \\ 0 \end{pmatrix} \quad |\beta\beta\rangle = \begin{pmatrix} 0 \\ 0 \\ 0 \\ 1 \end{pmatrix} . \tag{2.31}$$

All states and superposition states are now represented by vectors with four components such that the density matrix becomes:

$$\begin{pmatrix} c_{11} \\ c_{12} \\ c_{21} \\ c_{22} \end{pmatrix} \begin{pmatrix} c^*_{11} & c^*_{12} & c^*_{21} & c^*_{22} \end{pmatrix} = \begin{pmatrix} c_{11}c^*_{11} & c_{11}c^*_{12} & c_{11}c^*_{21} & c_{11}c^*_{22} \\ c_{12}c^*_{11} & c_{12}c^*_{12} & c_{12}c^*_{21} & c_{12}c^*_{22} \\ c_{21}c^*_{11} & c_{21}c^*_{12} & c_{21}c^*_{21} & c_{21}c^*_{22} \\ c_{22}c^*_{11} & c_{22}c^*_{12} & c_{22}c^*_{21} & c_{22}c^*_{22} \end{pmatrix} . \tag{2.32}$$

In this density matrix, similarly to the case of only one spin one-half, the diagonal elements are referred to as populations and the off-diagonal elements are coherences.

As described above for the spin one-half case there are only four pertinent operators: ½**1**, I_x, I_y and I_z, which are represented by two-by-two matrices. For two coupled spins there will be 16 spin operators represented by four-by-four matrices.

If we name the two coupled spins **I** and **S** we can construct sixteen spin operators by combining the four spin one-half operators using the Kronecker product ($\otimes$) in the 16 possible combinations as shown in Eq.(2.33)

$$\begin{aligned}
&\frac{1}{2}\hat{1} = 2\frac{1}{2}\hat{1}\otimes\frac{1}{2}\hat{1} \\
&I_x = 2\sigma_x\otimes\frac{1}{2}\hat{1} \qquad I_y = 2\sigma_y\otimes\frac{1}{2}\hat{1} \qquad I_z = 2\sigma_z\otimes\frac{1}{2}\hat{1} \\
&S_x = 2\frac{1}{2}\hat{1}\otimes\sigma_x \qquad S_y = 2\frac{1}{2}\hat{1}\otimes\sigma_y \qquad S_z = 2\frac{1}{2}\hat{1}\otimes\sigma_z \\
&2I_xS_x = 2\sigma_x\otimes\sigma_x \quad 2I_xS_y = 2\sigma_x\otimes\sigma_y \quad 2I_xS_z = 2\sigma_x\otimes\sigma_z \\
&2I_yS_y = 2\sigma_y\otimes\sigma_y \quad 2I_yS_z = 2\sigma_y\otimes\sigma_z \quad 2I_yS_x = 2\sigma_y\otimes\sigma_z \\
&2I_zS_z = 2\sigma_x\otimes\sigma_z \quad 2I_zS_x = 2\sigma_z\otimes\sigma_z \quad 2I_zS_y = 2\sigma_z\otimes\sigma_y .
\end{aligned} \tag{2.33}$$

In so doing we obtain the operators that can be used to represent density matrices and Hamiltonians acting on them with their elements in the order

$$\{|\alpha\alpha\rangle, |\alpha\beta\rangle, |\beta\alpha\rangle \ |\beta\beta\rangle\}.$$

For example the new two spin operator I_y is formed as:

$$I_y = 2\sigma_y\otimes\frac{1}{2}\hat{1} = 2\begin{pmatrix} 0 & -i/2 \\ i/2 & 0 \end{pmatrix}\otimes\frac{1}{2}\begin{pmatrix} 1 & 0 \\ 0 & 1 \end{pmatrix} = \frac{1}{2}\begin{pmatrix} 0 & 0 & -i & 0 \\ 0 & 0 & 0 & -i \\ i & 0 & 0 & 0 \\ 0 & i & 0 & 0 \end{pmatrix} \tag{2.34}$$

In isotropic liquids the Hamiltonian for two spins has to take into account two primary effects. These are the different chemical shift of the two spins (ω_1 vs ω_2) and the *J*-coupling, *J*. The Hamiltonian under chemical shift only is

$$H_{CS} = \omega_1 I_z + \omega_2 S_z . \tag{2.35}$$

The Hamiltonian under *J*-coupling only is

$$H_J = 2\pi J\ \mathbf{I}\cdot\mathbf{S} = 2\pi J\ (I_zS_z + I_xS_x + I_yS_y). \tag{2.36}$$

However, in a typical situation, where $\Delta\omega=(\omega_1 - \omega_2) >> 2\pi J$, the chemical shift difference truncates the off-diagonal elements of the full scalar **I·S** term and the Hamiltonian is

$$H = \omega_1 I_z + \omega_2 S_z + 2\pi J\, I_z S_z\,. \tag{2.37}$$

It is important to note that

$$[I_z, S_z] = [I_z, I_z S_z] = [S_z, I_z S_z] = 0\,, \tag{2.38}$$

and therefore the different parts of the Hamiltonian acting on the density matrix can be evaluated independently and sequentially.

The only part that has not been addressed thus far, is how to evaluate the *J*-coupling term $I_z S_z$ acting on the density matrix. For that purpose it is useful to be aware of the following cyclic commutation relations:

$$\begin{aligned} [2I_z S_z,\, I_x] &= i\, 2I_y S_z \\ [2I_z S_z,\, S_x] &= i\, 2I_z S_y \\ [2I_x S_z,\, I_y] &= i\, 2I_z S_z \\ [2I_z S_x,\, S_y] &= i\, 2I_z S_z\,, \end{aligned} \tag{2.39}$$

and

$$\begin{aligned} [2I_z S_z,\, I_z] = [2I_z S_z,\, S_z] &= 0 \\ [2I_z S_z,\, \mathbf{1}] &= 0 \\ [2I_z S_z,\, 2S_x I_x] = [2I_z S_z,\, 2I_x S_y] &= 0 \\ [2I_z S_z,\, 2I_y I_x] = [2I_y S_z,\, 2I_x S_y] &= 0. \end{aligned} \tag{2.40}$$

With the knowledge of the commutation relations we can track the evolution of a coupled two-spin system in a standard FT-NMR experiment.

An idealized, initial, fully polarized state is given as

$$\rho_0 = \frac{1}{4}\hat{\mathbf{1}} + \frac{1}{4} I_z + \frac{1}{4} S_z\ . \tag{2.41}$$

Under a 90_y-pulse the Hamiltonian $H_1 = (I_y + S_y)\Omega_1$ with $\Omega_1 t = \pi/2$ acts on ρ_0 and transforms the density matrix into

$$\rho_1 = \frac{1}{4}\hat{\mathbf{1}} + \frac{1}{4} I_x + \frac{1}{4} S_x\,. \tag{2.42}$$

The period of free evolution can now be examined in two steps. First, evolution under the chemical shift is considered and second, evolution under

the *J*-coupling. The chemical-shift Hamiltonian is $H_2 = \omega_1 I_z + \omega_2 S_z$ and it transforms ρ_1 into

$$\rho_2 = \frac{1}{4}\hat{\mathbf{1}} + \frac{1}{4}[I_x \cos(\omega_1 t) + I_y \sin(\omega_1 t) + S_x \cos(\omega_2 t) + S_y \sin(\omega_1 t)]\,. \tag{2.43}$$

Lastly, the *J*-coupling Hamiltonian $H_3 = 2\pi J\, I_z S_z$ acts on ρ_2 resulting in

$$\begin{aligned}\rho_3 = \frac{1}{4}\hat{\mathbf{1}} + \frac{1}{4}(&I_x \cos(\omega_1 t)\cos(\pi J t) + I_y \sin(\omega_1 t)\cos(\pi J t) \\ &+ 2I_y S_z \cos(\omega_1 t)\sin(\pi J t) - 2I_x S_z \sin(\omega_1 t)\sin(\pi J t) \\ &+ S_x \cos(\omega_2 t)\cos(\pi J t) + S_y \sin(\omega_2 t))\cos(\pi J t) \\ &+ 2I_z S_y \cos(\omega_2 t)\sin(\pi J t) - 2I_z S_x \sin(\omega_2 t)\sin(\pi J t)\,.\end{aligned} \tag{2.44}$$

Evaluation of these expressions in matrix form leads to

$$\rho_3 = 1/2 \begin{pmatrix} 0 & e^{-i(\omega_2+\pi J)t} & e^{-i(\omega_1+\pi J)t} & 0 \\ e^{i(\omega_2+\pi J)t} & 0 & 0 & e^{-i(\omega_1-\pi J)t} \\ e^{i(\omega_1+\pi J)t} & 0 & 0 & e^{-i(\omega_2-\pi J)t} \\ 0 & e^{i(\omega_1-\pi J)t} & e^{i(\omega_2-\pi J)t} & 0 \end{pmatrix}. \tag{2.45}$$

Now we can apply Eq. (2.10) to calculate the expected signal as

$$s(t) = Tr(\rho(I^- + S^-)) = \frac{1}{2\sqrt{2}}(e^{i(\omega_1+\pi J)t} + e^{i(\omega_1-\pi J)t} + e^{i(\omega_2+\pi J)t} + e^{i(\omega_2-\pi J)t}), \tag{2.46}$$

where I^- and S^- are given as

$$I^- = \frac{1}{\sqrt{2}}\begin{pmatrix} 0 & 0 & 0 & 0 \\ 0 & 0 & 0 & 0 \\ 1 & 0 & 0 & 0 \\ 0 & 1 & 0 & 0 \end{pmatrix} \qquad S^- = \frac{1}{\sqrt{2}}\begin{pmatrix} 0 & 0 & 0 & 0 \\ 1 & 0 & 0 & 0 \\ 0 & 0 & 0 & 0 \\ 0 & 0 & 1 & 0 \end{pmatrix}. \tag{2.47}$$

Equation (2.46) can be Fourier transformed and it is becomes apparent that we obtain a spectrum with two doublets centered on ω_1 and ω_2 respectively as depicted in Figure 2.2.

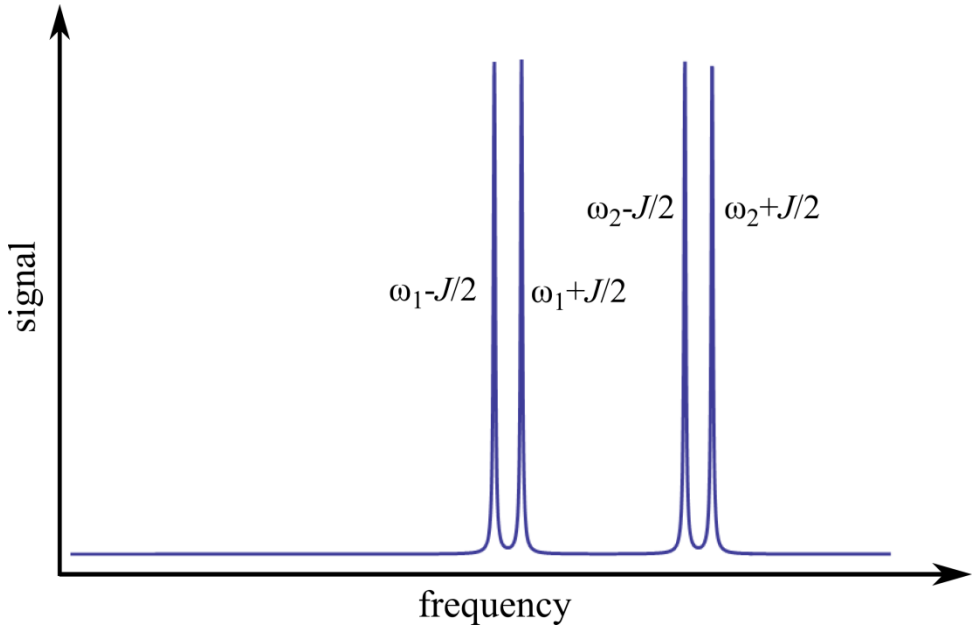

Figure 2.2 NMR signal from a two spin system with two distinct chemical shifts ω_1 and ω_2, and a scalar coupling constant *J*. Instead of delta functions that would be obtained from Eq (2.46) Lorentzian line shapes are drawn assuming some relaxation rate associate with the signal.

2.2 Spin operators and the addition of angular momenta

This Section will provide the basis for understanding the essential differences between zero-field NMR and standard high-field NMR as presented in the preceding Chapter. These differences are the result of the lack of a magnetic field in the Hamiltonian in zero-field NMR. In Eq. (2.37) we have seen that at high magnetic field the Hamiltonian is well described as a combination of local magnetic fields inducing frequency differences and the truncated action of the *J*-coupling. The frequency differences at high magnetic field are a result of differing chemical shifts or differing gyromagnetic ratio. At zero field these frequency differences vanish, and the full *J*-coupling Hamiltonian remains as presented in Eq. (2.36) The zero-field Hamiltonian and the high-field Hamiltonian have different symmetry. The high-field Hamiltonian is dictated by the magnetic field in a given invariant direction, whereas the *J*-coupling Hamiltonian is spherically symmetric. This change in symmetry has profound effects on the spectra and their interpretation. A reasonable approach to interpret zero-field NMR spectra is based on the description of spin and angular momentum as used in optical spectroscopy. The fundamental connection between zero-field NMR and the optical atomic spectroscopy of electron spins is primarily the same spherical symmetry in these two, at first glance, separate fields. Properties of spin one-half particles and the addition of angular momenta are described in many quantum mechanics textbooks. Here only some of the most essential features important to the interpretation of zero-field NMR spectroscopy shall be shown and later applied in every subsequent Chapter. Here, first, basic properties of spin one-half operators will be discussed, followed by a description of the addition of angular momentum for two spin one-half particles, which will lead into the description of the addition of angular momentum in general. Similar introductions to the addition of angular momenta presented here can also be found for example in the Cohen-Tannoudji's book "Quantum Mechanics"[56], Shankar's book "Principles of quantum mechanics"[57] or "Optically Polarized Atoms: Understanding Light-Atom Interactions "[58] by Auzinsh et al..

2.2.1 Basic properties of spin one-half operators

It is useful to start by introducing a general angular momentum **I** that consists of three observables $\{I_x, I_y, I_z\}$ such that the scalar square $\mathbf{I}^2$ is given as

$$\mathbf{I}^2 = I_x^2 + I_y^2 + I_z^2 \,. \tag{2.48}$$

Also, in the case of a general angular momentum the circular commutation relationships, given in Eq. (2.23), hold.

$$[I_i,I_j]=\varepsilon_{ijk} i I_k \,, \tag{2.49}$$

where ε_{ijk} is the Levi-Civita Symbol, which is equal to 1 if the elements i,j,k are in alphabetical order and -1 if they are out of alphabetical order.

An additional important property is that $\mathbf{I}^2$ commutes with each of the three components of **I**

$$[\mathbf{I}^2, I_x]= [\mathbf{I}^2, I_y]= [\mathbf{I}^2, I_z]=0. \tag{2.50}$$

Furthermore, $\mathbf{I}^2$ and I_z form a complete set of commuting observables (C.S.C.O.) in the spin state space. This space is spanned by the eigenstates of $\mathbf{I}^2$ and I_z such that

$$\begin{aligned} \mathbf{I}^2 \left|i,m_i\right\rangle &= i(i+1)\left|i,m_i\right\rangle \\ I_z \left|i,m_i\right\rangle &= m_i \left|i,m_i\right\rangle. \end{aligned} \tag{2.51}$$

In Eq. (2.51) i is half-integer and m_i ranges from i to $-i$. The value of i is the spin of the particle under consideration. The state space spanned by the vectors $|i,m_i>$ has a dimension of $(2i+1)$.

In addition, it is also useful to be aware of the raising and lowering operators, that are defined and act on the basis states as follows:

$$\begin{aligned} I_\pm &= I_x \pm i I_y \\ I_\pm \left|i,m_i\right\rangle &= \sqrt{i(i+1) - m_i(m_i \pm 1)}\left|i,m_i \pm 1\right\rangle. \end{aligned} \tag{2.52}$$

The most widely examined nuclei in NMR such as ^{1}H, ^{13}C, ^{15}N, ^{31}P, ^{19}F are all spin 1/2 particles. Also in this thesis only systems containing spin 1/2 nuclei are examined. It is hence worthwhile to consider some of the special

properties of angular momentum 1/2. The state space in this case is two dimensional and the basis states can be denoted as {|+>,|–>}. "+" referring to m_i=+1/2 and "–" referring to m_i =-1/2.The value of i is omitted since there is only one option i =1/2 In the basis of I_z these states are represented as the vectors used in Eq.(2.1). In that same basis the Pauli matrices introduced in Eq. (2.12) form the three components of the angular momentum **I**. Beside their cyclic commutation relations they have a few more important properties.

The Pauli matrices are traceless:

$$\mathrm{Tr}[I_x]= \mathrm{Tr}[I_y]= \mathrm{Tr}[I_z]=0. \tag{2.53}$$

The square of any Pauli matrix is 1/4 identity

$$I_x^2 = I_y^2 = I_z^2 = 1/4\ \mathbf{1}. \tag{2.54}$$

As a consequence $\mathbf{I}^2$ is also proportional to identity

$$\mathbf{I}^2 = I_x^2 + I_y^2 + I_z^2 = 3/4\ \mathbf{1}. \tag{2.55}$$

With these properties at hand we are in a place to consider the addition of two spin one-half particles in the next Section.

2.2.2 Addition of two spin one-half angular momenta

In networks of more than one spin, coupled by some interaction, it is important to have the ability to describe the system on the basis of its overall properties rather than on the basis of the characteristics of the individual spins. This is especially true in a case, such as zero-field NMR, where the spin-spin interaction is the only interaction determining the Hamiltonian. Hence it is worthwhile to find the operators and states resulting from the addition of the individual angular momenta.

Let us denote, similarly as in the preceding Chapter **I** and **S** to be the spin operators of two spin-one half particles to be added. The state space will now be spanned by four vectors formed using the tensor product of the spin one-half basis states:

$$\left|i,m_i\right\rangle \otimes \left|s,m_s\right\rangle := \left|i,m_i,s,m_s\right\rangle . \tag{2.56}$$

In the specific case of two spin one-half particles, where i and s are always equal to 1/2 and m_i and m_s can only be ±1/2. Thus the following notation for the four spin states is appropriate:

$$\{|++\rangle,|+-\rangle,|-+\rangle,|--\rangle\}, \tag{2.57}$$

where i and s are omitted and "+" indicates m=+1/2 and "–" indicates m=–1/2.

These are eigenvectors of the four observables $\mathbf{I}^2$, $\mathbf{S}^2$, I_z, and S_z, which form a complete set of commuting observables (C.S.C.O.). The following eigenvalues result when applying these operators to the basis states.

$$\begin{aligned}
&\mathbf{I}^2|m_i,\ m_s\rangle=\mathbf{S}^2|m_i,\ m_s\rangle=\frac{3}{4}|m_i,\ m_s\rangle \\
&I_z|m_i,\ m_s\rangle=m_i|m_i,\ m_s\rangle \\
&S_z|m_i,\ m_s\rangle=m_s|m_i,\ m_s\rangle.
\end{aligned} \tag{2.58}$$

Let us consider the total angular momentum operator

$$\mathbf{F} = \mathbf{I} + \mathbf{S}, \tag{2.59}$$

which characterizes the two-spin system rather than the two spins as separate entities.

This total angular momentum **F** now consists of the set

$\{F_x=I_x+S_x,\ F_y=I_y+S_y,\ F_z = I_z+S_z\}$.

In this new space we should now find the eigenvalues of $\mathbf{F}^2$ and F_z.

$\mathbf{F}^2$ is calculated as

$$\begin{aligned}
&\mathbf{F}^2=(\mathbf{I}+\mathbf{S})\cdot(\mathbf{I}+\mathbf{S})=\mathbf{I}^2+\mathbf{S}^2+2\mathbf{I}\cdot\mathbf{S} \\
&=\mathbf{I}^2+\mathbf{S}^2+2I_z\cdot S_z+(I_+S_-+I_-S_+)\ ,
\end{aligned} \tag{2.60}$$

where I_+,I_-,S_+ and S_- are the raising and lowering operators.

Using the properties of Eq. (2.58) above we obtain for F_z:

$$\begin{aligned} F_z|++\rangle &= 1|++\rangle \\ F_z|+-\rangle &= 0|+-\rangle \\ F_z|-+\rangle &= 0|-+\rangle \\ F_z|--\rangle &= -1|++\rangle \end{aligned} . \tag{2.61}$$

Similarly, for $\mathbf{F}^2$ using Eq (2.58) we obtain

$$\begin{aligned} \mathbf{F}^2|++\rangle &= 2|++\rangle \\ \mathbf{F}^2|+-\rangle &= |+-\rangle + |-+\rangle \\ \mathbf{F}^2|-+\rangle &= |-+\rangle + |+-\rangle \\ \mathbf{F}^2|--\rangle &= 2|--\rangle \end{aligned} . \tag{2.62}$$

In the product basis we thus obtain F_z and $\mathbf{F}^2$ represented as

$$F_z = \begin{pmatrix} 1 & 0 & 0 & 0 \\ 0 & 0 & 0 & 0 \\ 0 & 0 & 0 & 0 \\ 0 & 0 & 0 & -1 \end{pmatrix} \qquad \mathbf{F}^2 = \begin{pmatrix} 2 & 0 & 0 & 0 \\ 0 & 1 & 1 & 0 \\ 0 & 1 & 1 & 0 \\ 0 & 0 & 0 & 2 \end{pmatrix}. \tag{2.63}$$

As can be observed $\mathbf{F}^2$ is not diagonal in the product basis. This is because $\mathbf{F}^2$ does not commute with I_z nor S_z, which is a result of the terms I_x, S_x, I_y and S_y contained in $\mathbf{F}^2$.

To solve the problem of adding the angular momenta we need to diagonalize $\mathbf{F}^2$. This way we find the new eigenvectors

$$\begin{aligned} &|++\rangle \\ &\frac{1}{\sqrt{2}}\left(|+-\rangle + |-+\rangle\right) \\ &\frac{1}{\sqrt{2}}\left(|+-\rangle - |-+\rangle\right) \\ &|--\rangle. \end{aligned} \tag{2.64}$$

Finally, we should associate a total spin f and a magnetic component m_f with each of these states, which are found by applying $\mathbf{F}^2$ and F_z to these states.

The eigenvalues in the order of the states in Eq. (2.64) are {2 , 2, 0, 2} and {1, 0, 0, -1} respectively. If we know choose f and m_f such that they obey

$$\begin{aligned} \mathbf{F}^2 \left| f, m_f \right\rangle &= f(f+1) \left| f, m_f \right\rangle \\ \mathrm{F_z} \left| f, m_f \right\rangle &= m_f \left| f, m_f \right\rangle . \end{aligned} \tag{2.65}$$

similar to Eq.(2.58). We obtain f to have the values 1 and 0 while the allowed values for m_f are -1 0 and 1. In this new basis we now can characterize the states as $|f, m_f>$ such that:

$$\begin{aligned} \left|1,1\right\rangle &= \left|++\right\rangle \\ \left|1,0\right\rangle &= \frac{1}{\sqrt{2}}\left(\left|+-\right\rangle + \left|-+\right\rangle\right) \\ \left|0,0\right\rangle &= \frac{1}{\sqrt{2}}\left(\left|+-\right\rangle - \left|-+\right\rangle\right) \\ \left|1,-1\right\rangle &= \left|--\right\rangle . \end{aligned} \tag{2.66}$$

The states with f =1 form a triplet and the f =0 state is a singlet state. Note the differing symmetry of triplet and singlet states. The triplet states are symmetric under the exchange of two particles whereas the singlet state is antisymmetric under the exchange of two particles. This property is of fundamental importance for the following discussions and throughout the remainder of the thesis.

2.2.3 Addition of two arbitrary angular momenta

Let us consider the addition of two arbitrary angular momenta **I** and **S**, for both of which a standard basis is spanned by {$|i, m_i>$} and {$|s, m_s>$} which are eigenvectors of $\mathbf{I}^2$, $\mathrm{I_z}$ and $\mathbf{S}^2$, $\mathrm{S_z}$ respectively. Being angular momentum operators the following equations hold:

$$\begin{aligned} \mathbf{I}^2 \left| i, m_i \right\rangle &= i(i+1) \left| i, m_i \right\rangle \\ \mathrm{I_z} \left| i, m_i \right\rangle &= m_i \left| i, m_i \right\rangle \\ \mathrm{I_\pm} \left| i, m_i \right\rangle &= \sqrt{i(i+1) - m_i(m_i \pm 1)} \left| i, m_i \pm 1 \right\rangle . \end{aligned} \tag{2.67}$$

And similarly

$$\begin{aligned}
\mathbf{S}^2 \left| s, m_s \right\rangle &= s(s+1) \left| s, m_s \right\rangle \\
\mathrm{S_z} \left| s, m_s \right\rangle &= m_s \left| s, m_s \right\rangle \\
\mathrm{S_{\pm}} \left| s, m_s \right\rangle &= \sqrt{s(s+1) - m_s(m_s \pm 1)} \left| s, m_s \pm 1 \right\rangle .
\end{aligned} \tag{2.68}$$

Just as in the two spin one-half case we define the total angular momentum as

$$\mathbf{F}=\mathbf{I}+\mathbf{S} \tag{2.59}$$

We obtain a basis that diagonalizes $\mathbf{I}^2$, $\mathbf{S}^2$, $\mathrm{I_z}$, $\mathrm{S_z}$ easily by forming the tensor product.

$$\left| i, m_i \right\rangle \otimes \left| s, m_s \right\rangle := \left| i, m_i, s, m_s \right\rangle . \tag{2.69}$$

The problem to be solved is exactly the same as for the addition of two spin-one-half angular momenta: We need to find a orthonormal basis that diagonalizes $\mathbf{I}^2$, $\mathbf{S}^2$, $\mathbf{F}^2$ and $\mathrm{F_z}$ that will then be characterized by the total spin f and its z-component m_f with states denoted as $|f,m_f>$.

The questions to be addressed are:

(1) what are the possible values for m_f?

(2) what are the possible values for f?

(3) what are the degeneracies associated with the new states?

(4) how do we perform the basis change from the basis $\{|i,m_i, s,m_s>\}$ to the basis $\{|f, m_f>\}$?

In the following the answers for these questions will be provided and important properties of the obtained states will be discussed with the purpose of providing the tools necessary to understand zero-field NMR spectra. However, no rigorous derivations will be provided and the interested reader is referred to quantum mechanics text books[55–57] for complete deductions.

(1) The vectors $\left| i, m_i, s, m_s \right\rangle$ are already eigenvectors of $\mathrm{F_z}$ with eigenvalues

$$m_f = m_i + m_s , \tag{2.70}$$

consequently m_f takes on the values

$$m_f = i+s,\ i+s-1,\ldots\ldots,-(i+s). \tag{2.71}$$

(2) The values of f are obtained by calculating the eigenvalues of $\mathbf{F}^2$ resulting as $f(f+1)$, such that f takes on the values

$$f = i+s,\ i+s-1,\ldots\ldots,|i-s|. \tag{2.72}$$

(3) For one given value of f the z-component, m_f, takes on the values $m_f = f,\ f-1,\ldots,-f$ Hence for a group of vectors with one specific f there are $2f+1$ vectors $|f,m_f\rangle$ that form a degenerate manifold. The overall dimension of the eigenvector space is identical in the product basis $\{|f,m_f\rangle\}$ or the total angular momentum basis $\{|i,m_i,\ s,m_s\rangle\}$ and given as $(2i+1)(2s+1)$.

(4) The requested basis change can be performed using the so called Clebsch-Gordan (CG) coefficients. These coefficients connect the two bases. The resolution of the identity given in Eq. (2.6) allows us to express the states $|f,m_f\rangle$ as:

$$\left| f,m_f \right\rangle = \sum_{m_i}\sum_{m_s} |i,\ m_i,s,m_s\rangle\langle i,\ m_i,s,m_s \left| f,m_f \right\rangle . \tag{2.73}$$

The coefficients $\langle i,\ m_i,s,m_s \left| f,m_f \right\rangle$ are referred to as Clebsch-Gordan coefficients. These coefficients are tabulated in standard tables in textbooks[56] and it shall suffice to say that they can be calculated using the following properties: a) For the vector with maximum $m_f = i+s$ the CG coefficient is one. b) Repeated application of the lowering operator F_- to gives additional CG coefficients for states with $f=i+s$. c) The next CG-coefficient with $f=i+s-1$ and $m_f=i+s-1$ is obtained by requiring real CG-coefficients (by convention) and orthonormality to the preceding total-f states. d) The additional states in the $f=i+s-1$ group are obtained by applying the lowering operator again. Proceeding iteratively, all CG-coefficients are obtained.

It is useful to be aware of the fact that CG-coefficients are only non-zero whenever

$$m_f = m_i + m_s \text{ and } |i-s| \le f \le i+s. \tag{2.74}$$

This is also referred to as the triangle selection rule for CG-coefficients, which states in words: The CG-coefficient is only non-zero if it is possible to form a triangle with sides of length i, s and f.

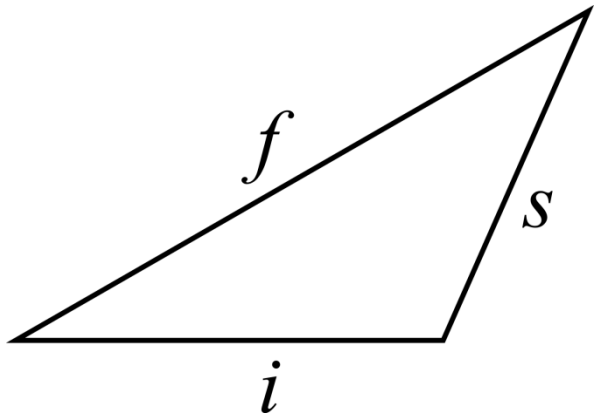

Figure 2.3 Illustration of the triangle rule for the addition of angular momenta. The value for the total spin *f* is restricted such that only values for *f* are allowed such that is possible to form a triangle with sides of length *i, s* and *f*. This requirement limits *f* to be smaller or equal to *i+s* and larger or equal to the absolute value of *i-s*.

2.2.4 The Wigner-Eckart Theorem

As introduced in Eq. (2.8) the expectation value for a given observable is defined as $\langle\psi|A|\psi\rangle$ in the context of the present discussion it will be our goal to obtain these expectation values for given angular momentum states.

$$\left\langle f',\, m_f' \middle| \mathrm{A} \middle| f,\, m_f \right\rangle. \tag{2.75}$$

As a first step it is possible to determine whether the expectation value is zero or non-zero for a given pair of angular momentum states. This is usually done invoking the Wigner-Eckart Theorem. Let us first describe how the Wigner-Eckart theorem works for expectation values associated with scalar and vectorial observables and then the general form will be given for expectation values associated with spherical tensor operators of arbitrary rank. Scalar and vectorial operators are given as rank zero and rank one operators respectively.

For, example if A is a scalar "a", then it immediately follows from the orthonormality of the basis states that

$$\left\langle f',\, m_f' \middle| a \middle| f,\, m_f \right\rangle = a\left\langle f',\, m_f' \middle| f,\, m_f \right\rangle = a\,\delta_{\mathrm{f',f}}\delta_{\mathrm{m_f',m_f}} = \begin{cases} 1 \text{if } f = f' \text{ and } m_f' = m_f \\ 0 \text{ otherwise} \end{cases} \tag{2.76}$$

If the observable is a component of a first rank tensor such as for example $\mathbf{F}=\{F_x, F_y, F_z\}$ then we can also evaluate the expectation value associated with each of these components. For example

$$\begin{aligned}\left\langle f',\, m_f' \middle| \mathrm{F_x} \middle| f,\, m_f \right\rangle &= \left\langle f',\, m_f' \middle| \frac{\mathrm{F^- - F^+}}{\sqrt{2}} \middle| f,\, m_f \right\rangle = \delta_{f',f,f\pm1}\delta_{m_f',m_f\pm1} \\ &= \begin{cases} 1 \text{if } f+1 \geq f' \geq |f-1| \text{ and } m_f' = m_f \pm 1 \\ 0 \text{ otherwise} \end{cases}.\end{aligned} \tag{2.77}$$

And similarly

$$\begin{aligned}\left\langle f',\, m_f' \middle| \mathrm{F_z} \middle| f,\, m_f \right\rangle &= \delta_{f',f,f\pm1}\delta_{m_f',m_f} \\ &= \begin{cases} 1 \text{if } f+1 \geq f' \geq |f-1| \text{ and } m_f' = m_f \\ 0 \text{ otherwise} \end{cases}\end{aligned} \tag{2.78}$$

These results can be confirmed by invoking the general form of the Wigner-Eckart Theorem, which separates the matrix elements, such as e.g. the shown expectation values, into parts dependent on spatial orientation and the rest.

$$\left\langle f',\, m_f' \middle| \mathrm{T}_k^q \middle| f,\, m_f \right\rangle = \left\langle f' \middle\| \mathrm{T}_k \middle\| f \right\rangle \left\langle f',\, m_f';\, k,\, q \middle|\, f,\, m_f \right\rangle. \tag{2.79}$$

The parts dependent on spatial orientation, (i.e. on m, and q) are given entirely as CG-coefficients.

In order to link this to the previous examples it is important to understand that T_k^q are the components of a spherical tensor operator of rank k with (2k+1) components *q* that take on the values *q=k, k-1,……,-k.* In the example of the scalar operator $a=T_0^0$ which is the only component of a rank zero operator. In the case of the vector **F** the spherical tensor operator of rank one has the three components $F_z = T_1^0$, $F^+= T_1^1$ and $F^-= T_1^{-1}$. And in general for matrix elements of T_k^q between angular momentum manifolds:

$$\left\langle f',\, m_f' \middle| \mathrm{T}_k^q \middle| f,\, m_f \right\rangle = 0 \quad \text{unless } k+f \geq f' \geq |k-f| \text{ and } m_f' = m_f + q. \tag{2.80}$$

This directly leads us to the results of Eq. (2.77) and Eq. (2.78). In physical terms it is reasonable to assert that T_k^q imparts angular momentum (*k,q*) to the states it acts on as exemplified by Eq. (2.52), (2.72) and (2.73).

2.2.5 Eigenvalues of a scalar-coupling Hamiltonian

The Hamiltonian for two coupled spins of arbitrary size (integer or half integer) is given as

$$\mathrm{H} = J(\mathbf{I}\cdot\mathbf{S}), \tag{2.81}$$

where J is the coupling strength and **I** and **S** are the spin operators as introduced above. In order to find the energy values of the system the expectation values of H are to be calculated

$$E_{f,m_f} = \langle f,\ m_f \left| J(\mathbf{I}\cdot\mathbf{S}) \right| f,\ m_f \rangle. \tag{2.82}$$

I·**S** can be replaced by operators, of which we know how they act on the $|f,m_f\rangle$basis. Since,

$$\mathbf{F}^2 = (\mathbf{S}+\mathbf{I})^2 = \mathbf{S}^2 + \mathbf{I}^2 + 2\mathbf{S}\cdot\mathbf{I}, \tag{2.83}$$

we can rearrange to obtain

$$\mathbf{S}\cdot\mathbf{I} = \frac{1}{2}(\mathbf{F}^2 - \mathbf{S}^2 - \mathbf{I}^2). \tag{2.84}$$

Since, $\mathbf{F}^2$, $\mathbf{S}^2$ and $\mathbf{I}^2$ act as

$$\begin{aligned} \mathbf{F}^2 \left| f,m_f \right\rangle &= f(f+1)\left| f,m_f \right\rangle \\ \mathbf{S}^2 \left| f,m_f \right\rangle &= s(s+1)\left| f,m_f \right\rangle \\ \mathbf{I}^2 \left| f,m_f \right\rangle &= i(i+1)\left| f,m_f \right\rangle, \end{aligned} \tag{2.85}$$

we obtain the eigenvalues given in terms of the quantum numbers as

$$E_{f,m_f} = \frac{J}{2}[\,f(f+1) - s(s+1) - i(i+1)]. \tag{2.86}$$

This is an important result for zero-field NMR spectroscopy as will become apparent in the later discussions.

2.3 Parahydrogen induced polarization in high-field NMR

In 1986 Weitekamp and Bowers discovered parahydrogen induced polarization (PHIP) and introduced the acronym PASADENA for (Parahydrogen and Synthesis Allow Dramatically Enhanced Nuclear Alignment)[30]. In this effect the parahydrogen spin order is transferred to a substrate using a hydrogenation reaction. After hydrogenation the symmetry of the para-state is broken and can then be transformed into detectable magnetization. In this Section the underlying physics will be explained followed by a discussion of hydrogenations with parahydrogen of symmetric substrates, giving an interesting perspective on the PASADENA effect leading into PHIP applied at zero magnetic field.

2.3.1 The hydrogen molecule and its spin states

In order to understand the PHIP effect it is useful to start with an examination of the hydrogen molecule, its states and possible wave functions. In general under the Born-Oppenheimer approximation the total wave function of a molecule can be separated into an electronic, a vibrational, a rotational and a nuclear wave function such that

$$\Psi_{total} = \Psi_e \Psi_\upsilon \Psi_r \Psi_n \tag{2.87}$$

The Pauli principle states, for half-integer nuclei (fermions), that Ψ_{total} has to be antisymmetric under exchange of two identical particles. In order to make a statement about the symmetry of the total wave function we shall examine the individual factors. The temperature regime that we are interested in is ~100 °C and below. In this regime only the electronic and vibrational ground states are populated. The electronic ground state is the symmetric $^1\Sigma_g^+$ state. The vibrational ground state is well represented by symmetric ground state of a harmonic oscillator with $\nu=0$. At the same time, a wide range of rotational and nuclear states are populated at a given temperature determined by the Boltzmann distribution. As a result of the stated Pauli principle, the symmetries of the nuclear and vibrational states must be correlated.

The nuclear states are given by the wave functions presented in Eq. (2.64) resulting from the addition of two spin one-half nuclei. Where the symmetric triplet states are referred to as the ortho states and the antisymmetric singlet state is referred to as the para state.

$$\left.\begin{aligned} |1,1\rangle &= |++\rangle \\ |1,0\rangle &= \frac{1}{\sqrt{2}}\left(|+-\rangle + |-+\rangle\right) \\ |1,-1\rangle &= |--\rangle \end{aligned}\right\}\text{ortho}$$
$$\left.\begin{aligned} |0,0\rangle &= \frac{1}{\sqrt{2}}\left(|+-\rangle - |-+\rangle\right) \end{aligned}\right\}\text{para}. \qquad (2.88)$$

The rotational states of parahydrogen can be described by the spherical harmonics

$$\Psi_{l,m_l}(\vartheta,\varphi) = Y_{l,m_l}(\vartheta,\varphi) = P_l^{m_l}(\cos\vartheta)\, e^{im_l\varphi}, \qquad (2.89)$$

where l is the rotational quantum number. The spherical harmonics depend on the Legendre-polynomials, $P_l^{m_l}$, which alternate from symmetric to antisymmetric depending on l. The spherical harmonics under point inversion obey

$$Y_{l,m_l}(\vartheta,\varphi) \rightarrow Y_{l,m_l}(\pi-\vartheta,\pi+\varphi) = (-1)^l Y_{l,m_l}(\vartheta,\varphi)\,. \qquad (2.90)$$

As a result of the Pauli principle in combination with the stated symmetry properties the para state "lives" in even rotational states and the ortho state "lives in" odd rotational states. This property is crucial to the enrichment of parahydrogen.

2.3.2 Enrichment of parahydrogen

In order to produce parahydrogen in essence all we need to do is to populate the rotational ground state with $l = m_l = 0$. This is a symmetric rotational state, which therefore must contain the antisymmetric nuclear spin state, the para state. A reasonable path to populate the ground state is by cooling the hydrogen and establishing thermal equilibrium at the lower temperature. The equilibrium ortho-para mixture can be predicted by calculating the rigid-rotor partition function using the characteristic

temperature of rotation for hydrogen Θ_R. Each manifold of states given by l is $(2l+1)$ times degenerate, since m_l ranges from $-l$ to $+l$ in steps of 1. The rotational energy is given as

$$E_1 = \Theta_R \; l(l+1)\, k_b \,, \tag{2.91}$$

where k_b is the Boltzmann constant and Θ_R is given as

$$\Theta_R = \hbar^2 / 2 k_b M \; = 85.3 \text{ K} \,, \tag{2.92}$$

with $M = \mu r_{12}^2$ the moment of inertia for the inter-nuclear distance r_{12} and μ the reduced mass of molecular hydrogen. This results in an ortho to para ratio given as

$$\frac{N_{ortho}}{N_{para}} = \frac{3 \sum_{\text{odd } l} (2l+1)\, e^{-\Theta_R\, l(l+1)/T}}{\sum_{\text{even } l} (2l+1)\, e^{-\Theta_R\, l(l+1)/T}} \,. \tag{2.93}$$

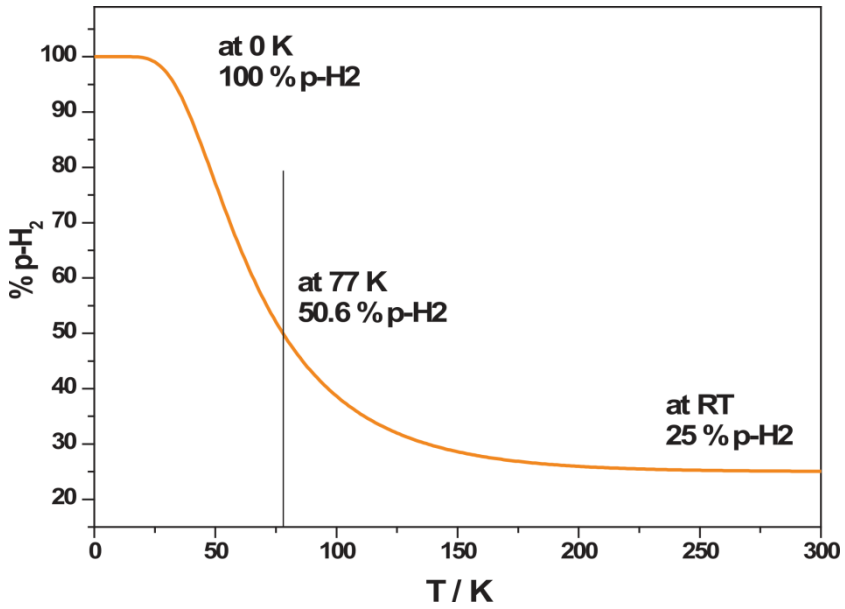

Figure 2.4 Plot of the thermally equilibrated percentage of parahydrogen in a mixture of ortho- and parahydrogen as a function of temperature. At room temperature (RT) a statistical 3:1 ratio is the thermodynamic equilibrium. At liquid nitrogen temperatures of 77 K the thermal equilibrium is a 1:1 mixture and at temperatures below 30 K almost all hydrogen is parahydrogen when thermally equilibrated.

In Figure 2.4 resulting from this ratio the percentage of parahydrogen is plotted as a function of temperature. As can be seen, at room temperature (RT) the thermal equilibrium is given as a statistical 3:1 mixture. At liquid nitrogen temperatures of 77 K, ~50.6% parahydrogen is obtained, and starting at ~30K close to 100 % parahydrogen can be produced.

The last difficulty to overcome lays in establishing thermal equilibrium at a given temperature. The interconversion between the ortho and the para form of hydrogen is associated with a half-time of approximately three weeks. In order to establish thermal equilibrium faster it is possible to bring the hydrogen in contact with a paramagnetic surface, which has strong magnetic gradients that can intermittently mix the singlet and the triplet states thereby inducing transitions. Presently a parahydrogen production station is in place operated at temperatures between 20 and 35 K that will be described in detail in Section 3.2.6 .

As depicted in Figure 2.5 normal hydrogen flows into copper tubing that is filled with iron oxide, where it comes into contact with the paramagnetic surface and thermal equilibrium is quickly established. The copper tubing is contained in a vacuum shroud for insulation and brought in touch with a cold finger, typically operated at 30 K producing close to 100% parahydrogen. The cold finger is cooled by expansion of compressed Helium. More detailed information is given in the experimental Section 3.2.6.

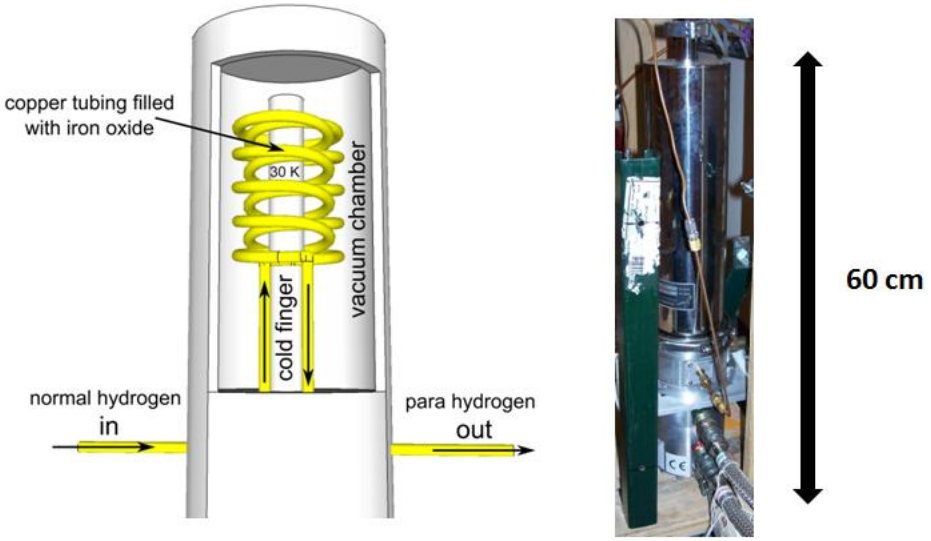

Figure 2.5 Schematic of the parahydrogen-production setup on the left and a photograph of the containing vacuum chamber to the right. Normal hydrogen flows in a tube filled with iron-oxide powder cooled to ~30 K. The iron-oxide catalyzes the para- to orthohydrogen conversion thereby establishing thermal equilibrium at the desired temperature.

2.3.3 Parhydrogen induced polarization (PHIP)

The underlying principle of the PHIP effect is the conversion of the parahydrogen singlet state into a state with observable magnetization. In the hydrogen molecule itself it is difficult to break the symmetry of the wave functions, hence the first step in PHIP experiments is a chemical manipulation. In most cases a hydrogenation reaction is performed. As shown in Figure 2.6 parahydrogen can be added onto a double (or triple) bond via some transition-metal catalyst. In the specific case of Figure 2.6 Wilkinson's catalyst is chosen for the catalysis of an alkene. After hydrogenation the parahydrogen derived protons are typically in location of differing chemical shift. This change in symmetry then allows for manipulations of the spin states.

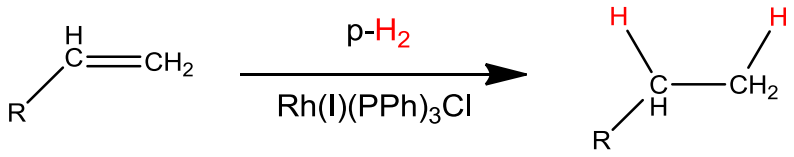

Figure 2.6 Schematic of a typical hydrogenation reaction. Rhodium(I)tris[triphenylphosphine chloride] also known as Wilkinson's catalyst catalyzes the hydrogenation of an alkene to form a alkane. The alkane contains two additional hydrogen atoms derived from the same original hydrogen molecule.

Before hydrogenation the density matrix describing the para spin state in the Zeeman basis is given as the outer product [introduced in Eq (2.9)] of the singlet states given in Eq. (2.88):

$$\rho = |S_0\rangle\langle S_0| = \begin{pmatrix} 0 & 0 & 0 & 0 \\ 0 & \frac{1}{2} & -\frac{1}{2} & 0 \\ 0 & -\frac{1}{2} & \frac{1}{2} & 0 \\ 0 & 0 & 0 & 0 \end{pmatrix} = \frac{1}{4}\mathbf{1} - \mathbf{I}\cdot\mathbf{S}\,, \tag{2.94}$$

where

$$\mathbf{I}\cdot\mathbf{S} = I_x S_x + I_y S_y + I_z S_z\,. \tag{2.95}$$

Upon hydrogenation this density matrix is projected onto a new spin system given in the substrate and represents a highly ordered density matrix far away from thermal equilibrium, thus carrying a high degree of polarization that can be exploited.

In an idealized case, which will serve best for an introductory discussion, the only difference in the adduct consists of a differing chemical shift ω_1 and ω_2 for the two parahydrogen derived protons. Additional *J*-couplings that may be present in the substrate will be ignored for the purpose of this introduction to PHIP because they typically represent a weaker interaction than the chemical shift difference and also the effect of *J*-coupling will be discussed in great detail in later Chapters since in zero-field NMR chemical shifts are absent. On this basis the next two Sections will discuss how to extract and use this polarization to obtain detectable signal.

2.3.4 The PASADENA effect

The classic PASADENA (Parahydrogen and Synthesis Allows Dramatically Enhanced Nuclear Alignment) experiment consists of a hydrogenation reaction conducted with parahydrogen at a high magnetic field under which the chemical-shift differences dominate any *J*-coupling interactions. Under these conditions it is appropriate to use a sudden approximation in which the parahydrogen singlet state is projected onto the new Hamiltonian given as introduced in Eq. (2.35)

$$H=\omega_1 I_z+\omega_2 S_z=\begin{pmatrix} \frac{\omega_1+\omega_2}{2} & 0 & 0 & 0 \\ 0 & \frac{\omega_1-\omega_2}{2} & 0 & 0 \\ 0 & 0 & \frac{-\omega_1+\omega_2}{2} & 0 \\ 0 & 0 & 0 & \frac{-\omega_1-\omega_2}{2} \end{pmatrix}. \qquad (2.96)$$

This Hamiltonian is diagonal in the Zeeman basis. After the hydrogenation of a single molecule, the off-diagonal elements of the initial density matrix will begin to evolve at some frequency given by the difference in chemical shifts. Over the course of many hydrogenation reactions of individual molecules additional off-diagonal terms experience the same evolution but with random phase thereby averaging the off-diagonal terms to zero. This process is referred to as incoherent averaging. After this process, only elements of the original density matrix on the diagonal remain. In the discussed case **I·S** is converted into I_zS_z:

$$\frac{1}{4}\mathbf{1}-\mathbf{I}\cdot\mathbf{S}=\begin{pmatrix} 0 & 0 & 0 & 0 \\ 0 & \frac{1}{2} & -\frac{1}{2} & 0 \\ 0 & -\frac{1}{2} & \frac{1}{2} & 0 \\ 0 & 0 & 0 & 0 \end{pmatrix} \xrightarrow[\text{averaging}]{\text{incoherent}} \begin{pmatrix} 0 & 0 & 0 & 0 \\ 0 & \frac{1}{2} & 0 & 0 \\ 0 & 0 & \frac{1}{2} & 0 \\ 0 & 0 & 0 & 0 \end{pmatrix} = \frac{1}{4}\mathbf{1}-I_zS_z. \qquad (2.97)$$

In other words, the singlet state $1/\sqrt{2}\left(|+-\rangle - |-+\rangle\right)$ is split into its components in the Zeeman basis $\frac{1}{2}|-+\rangle$ and $\frac{1}{2}|+-\rangle$.

In order to examine the type of NMR signal obtained after hydrogenation of many individual molecules we can examine the effect of a RF pulse on $-I_zS_z$ and calculate the ensuing evolution. Following the concepts introduced in Section 2.1.6 $-I_zS_z$ is transformed as by a pulse of angle θ as follows:

$$-I_zS_z \xrightarrow[\substack{\text{angle } \theta \\ \text{y-pulse}}]{} -I_zS_z\cos^2(\theta) - I_xS_x\sin^2(\theta) - \sin(\theta)\cos(\theta)(I_zS_x + I_xS_z). \quad (2.98)$$

Both I_zS_z and I_xS_x are not directly observed in simple NMR experiments, which can be verified using the trace formula of Eq. (2.10). The only term we should concern ourselves with hence is $-(I_zS_x+I_xS_z)$. To choose the pulse angle that gives maximum signal the expression $\sin(\theta)\cos(\theta)$ has to be maximized and we thus find the first maximum with application of a 45° pulse.

Evaluation of Eq. (2.18) gives the evolution of $I_zS_x+I_xS_z$ under the Hamiltonian $H = \omega_1 I_z + \omega_2 S_z + 2\pi J\, I_zS_z$ as

$$\rho(t) = e^{-iHt}(-I_zS_x - I_xS_z)e^{-iHt} = \frac{1}{4}\begin{pmatrix} 0 & -e^{-it(\omega_2+\pi J)} & -e^{-it(\omega_1+\pi J)} & 0 \\ -e^{it(\omega_2+\pi J)} & 0 & 0 & +e^{-it(\omega_1-\pi J)} \\ -e^{it(\omega_1+\pi J)} & 0 & 0 & +e^{-it(\omega_2-\pi J)} \\ 0 & +e^{it(\omega_1-\pi J)} & +e^{it(\omega_2-\pi J)} & 0 \end{pmatrix}. \quad (2.99)$$

Using the trace formula introduced in Eq (2.10) we obtain:

$$s(t) = Tr(\rho(t)(I^- + S^-)) = \frac{1}{4\sqrt{2}}(-e^{i(\omega_1+\pi J)t} + e^{i(\omega_1-\pi J)t} - e^{i(\omega_2+\pi J)t} + e^{i(\omega_2-\pi J)t}), \quad (2.100)$$

which clearly indicates the expected peaks and their relative amplitudes in a PASADENA experiment as shown in Figure 2.7. It is worthwhile to recall that the signal is maximized with a 45° pulse and that a 90° pulse would not result in any signal in the discussed scenario.

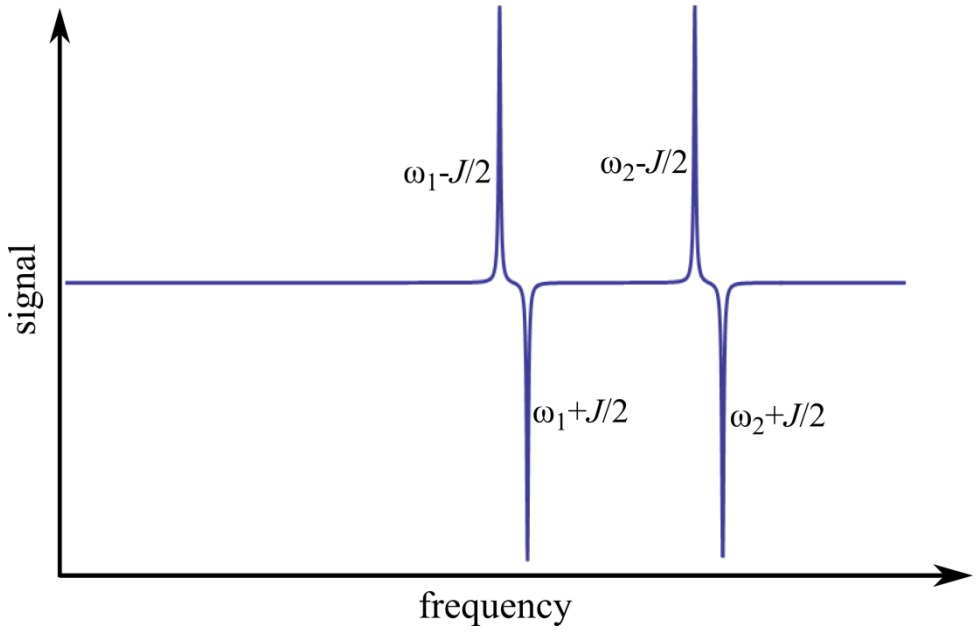

Figure 2.7 Simulated PASADENA spectrum for a typical two-spin system with frequencies ω_1 and ω_2 and a *J*-coupling constant *J*. In the specific case (ω_1-ω_2)/*J*=7. The peaks of individual doublets appear 180° out of phase. These individual peaks are said to be antiphase.

2.3.5 The ALTADENA effect

In ALTADENA (Adiabatic Longitudinal Transport After Dissociation Engenders Net Alignment) experiments, also, hydrogenation reactions are conducted with parahydrogen and signals are observed in high-field-NMR spectrometers. What distinguishes ALTADENA experiments from PASADENA experiments is that the hydrogenation is conducted at a low magnetic field where the chemical shift differences are small as compared to the *J*-coupling. Subsequently, the sample is transferred into the magnet such that the density matrix can adiabatically follow the change from low-field to high-field where the signal is acquired.

Under idealized circumstances, that is, in the absence of additional *J*-couplings to nuclei not derived from parahydrogen, the density matrix before and after hydrogenation in ALTADENA experiments is identical because the symmetry of the Hamiltonian after hydrogenation is the same as before

hydrogenation. We can hence describe the density matrix after hydrogenation by Eq.(2.94), where only the singlet is populated. The population in the singlet state is then adiabatically transferred into its corresponding states at high field. Since the states $|++\rangle$ and $|--\rangle$ are identical at high and low field these do not change upon the transfer and will not be populated. The assignment of the $|+-\rangle$ and $|-+\rangle$ states to the singlet S_0 or the triplet T_0 is less obvious. During the adiabatic transfer there are avoided crossings, hence the energetically lower singlet will transfer to the energetically lower state at high field. In the case that the second spin, S, has the lower frequency then $|-+\rangle$ is the state with lower energy at high field and it is this state that will be populated. The density matrix is hence transformed as follows during adiabatic transfer:

$$\frac{1}{4}\mathbf{1}\text{-}\mathbf{I}\cdot\mathbf{S}=\begin{pmatrix}0&0&0&0\\0&\frac{1}{2}&-\frac{1}{2}&0\\0&-\frac{1}{2}&\frac{1}{2}&0\\0&0&0&0\end{pmatrix}\xrightarrow[\text{transfer}]{\text{adiabatic}}\begin{pmatrix}0&0&0&0\\0&0&0&0\\0&0&1&0\\0&0&0&0\end{pmatrix}=\frac{1}{4}\mathbf{1}\text{-}(I_zS_z+\frac{1}{2}(I_z\text{-}S_z)). \qquad (2.101)$$

As discussed above the signal obtained from I_zS_z is maximized with a 45° pulse but ALTADENA experiments produce the additional term I_z-S_Z, which produces signals maximized with a 90° pulse.

$$\text{-}(I_z\text{-}S_z)\xrightarrow[\text{y-pulse}]{\text{angle }\theta}\text{-}I_z\cos(\theta)\text{-}I_x\sin(\theta)+S_z\cos(\theta)+S_x\sin(\theta). \qquad (2.102)$$

The $-I_x+S_x$ term evolves under the magnetic field Hamiltonian. We employ Eq. (2.18) and obtain the density matrix as a function of time.

$$\rho(t)=e^{-iHt}(-I_x+S_x)e^{-iHt}=\frac{1}{2}\begin{pmatrix}0&+e^{-it(\omega_2+\pi J)}&-e^{-it(\omega_1+\pi J)}&0\\+e^{it(\omega_2+\pi J)}&0&0&-e^{-it(\omega_1-\pi J)}\\-e^{it(\omega_1+\pi J)}&0&0&+e^{-it(\omega_2-\pi J)}\\0&-e^{it(\omega_1-\pi J)}&+e^{it(\omega_2-\pi J)}&0\end{pmatrix}. \qquad (2.103)$$

Once again using the trace formula of Eq. (2.10), then, gives the signal as a function of time:

$$s(t)=Tr(\rho(t)(\mathrm{I}^-+\mathrm{S}^-))=\frac{1}{2\sqrt{2}}(-e^{i(\omega_1+\pi J)t}-e^{i(\omega_1-\pi J)t}+e^{i(\omega_2+\pi J)t}+e^{i(\omega_2-\pi J)t}). \qquad (2.104)$$

This signal is multiplied by an exponentially decaying function and Fourier-transformed to give the spectrum depicted in Figure 2.8.

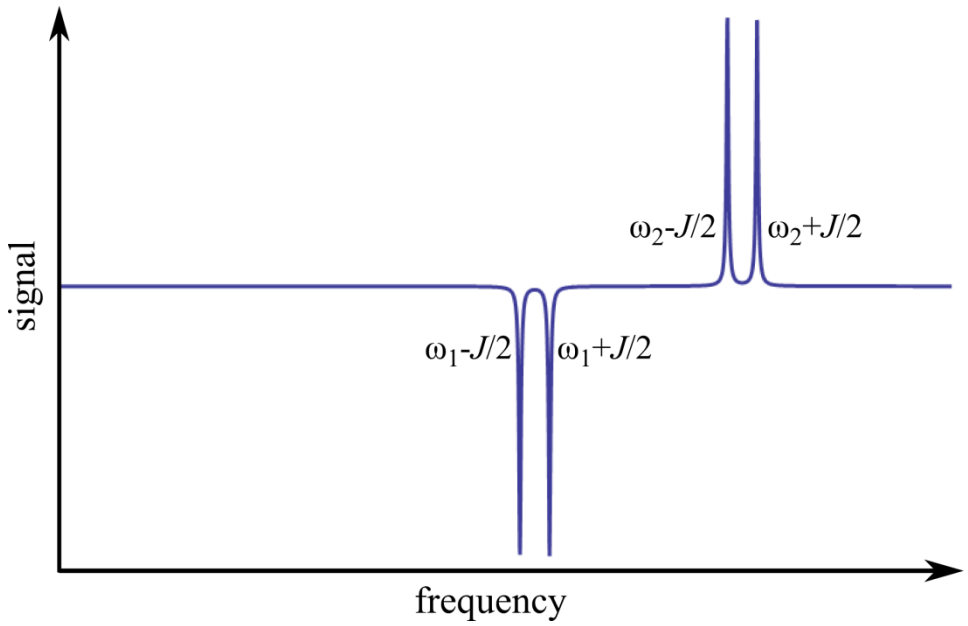

Figure 2.8 Simulated ALTADENA spectrum for a typical two-spin system with frequencies ω_1 and ω_2 and a *J*-coupling constant *J*. In the specific case $(\omega_1-\omega_2)/J=7$. The doublets as entities appear 180° out of phase. The doublets are said to be antiphase.

2.3.6 PHIP experiments on symmetric molecules

Before undertaking PHIP experiments at zero magnetic field where there are no chemical shifts it seems worthwhile to perform classical PHIP experiments (ALTADENA and PASADENA) on a symmetric substrate to examine whether signals can be obtained even if the two parahydrogen derived protons are in chemically equivalent positions with identical chemical shifts. To that end, hydrogenations of butyne shown in Figure 2.9 were conducted in both the ALTADENA and PASADENA mode. After the hydrogenation reaction hyperpolarized butane is formed. (These experiments were conducted at the initial stages for preparation of this thesis)

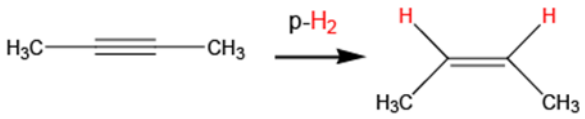

Figure 2.9 Schematic showing the hydrogenation reaction of butyne. The product butene contains two parahydrogen derived hydrogen atoms.

When the hydrogenation was conducted at high magnetic field (PASADENA) and a 45° pulse was applied the spectrum shown in Figure 2.10 was obtained. Despite the chemical equivalence of the hydrogenated sites a strong PASADENA signal is observed after a small amount of hydrogenation (~1% of the substrate). Primarily signals at 5.3 ppm are expected corresponding to the parahydrogen derived protons in the vinyl positions of butene. As is typical for the PASADENA experiments, the signals are antiphase and separated by distances determined by the *J*-coupling constants in the molecule. At 1.55 ppm also strong signals are observed, however, the majority of the observed signal is associated with thermal signal from butyne that has not been hydrogenated yet representing ~99% of the sample. At the same time, at somewhat lower chemical shift an antiphase signal can be observed to overlap with the thermal butyne signal. This antiphase PASADENA signal is associated with the methyl groups of the hyperpolarized butene.

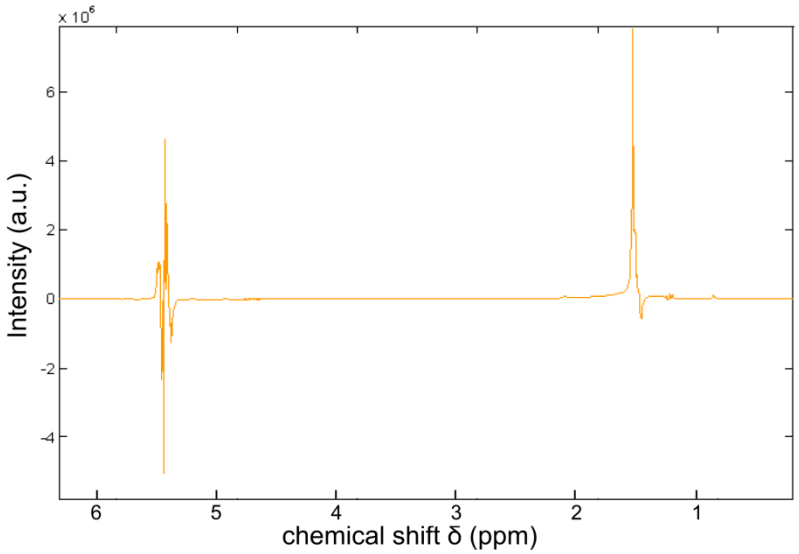

Figure 2.10 PASADENA spectrum acquired from the hydrogenation of butyne to form butene. The antiphase quartet at 5.3 ppm can be assigned to the parahydrogen derived vinyl protons in butene. The antiphase doublet expected for the methyl groups in butene appearing at 1.55 ppm overlaps with the thermal signal of the remaining butyne that has not reacted yet.

Similarly, hydrogenation reactions were carried out at low magnetic fields (~0.5 G) and the sample was subsequently transferred into the magnet and a 90° pulse was applied (ALTADENA). The resulting spectrum is shown in Figure 2.11. Strong antiphase signals at 5.3 and 1.55 ppm separated by the chemical shift are observed as predicted for ALTADENA experiments. The component at 1.55 ppm that is in phase with the signal at 5.3 ppm is signal from thermally polarized butyne which is partially canceled out by the hyperpolarized butene signal.

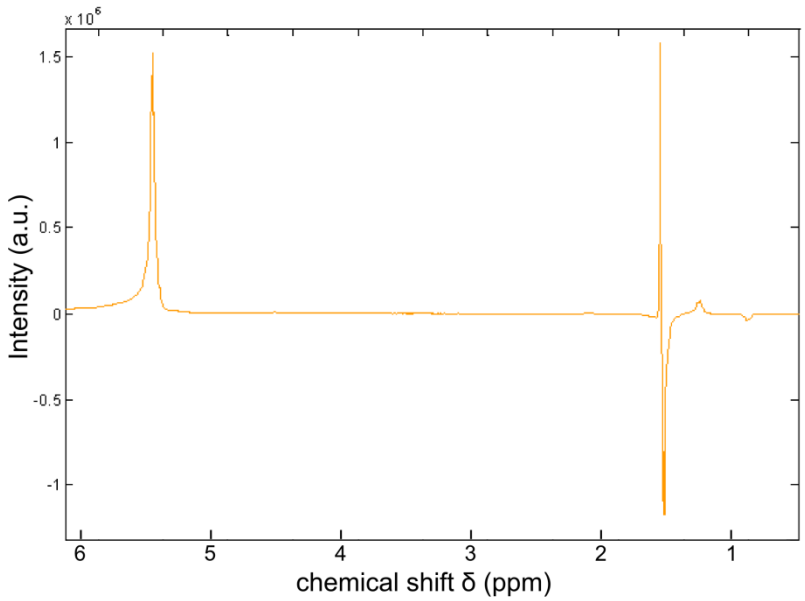

Figure 2.11 ALTADENA spectrum acquired from the hydrogenation of butyne to form butene. The inphase quartet at 5.3 ppm can be assigned to the parahydrogen derived vinyl protons in butene. The in phase doublet expected for the methyl groups in butene at 1.55 ppm is antiphase with respect to the quartet but partially canceled by the thermal signal of the remaining butyne that has not reacted yet.

The take home message from this Section is that the chemical equivalence of the hydrogenated sites does not preclude the PHIP from becoming observable. However, the magnetic equivalence in this butyne/butene model system is broken by the methyl groups which do not have the same coupling constants to the individual parahydrogen derived protons in butene. In order to further convince ourselves that breaking the magnetic equivalence by means of *J*-couplings in a hydrogenated product is sufficient, simulations have been undertaken for a simpler model spin system. This model consists of two parahydrogen derived nuclei coupled to two additional spin one-half nuclei. This model spin system is depicted in Figure 2.12 along with a simulated PASADENA spectrum for that spin system. The parameters were chosen randomly as follows: The nutation frequency of spins I and S are set to 50 Hz, the nutation frequency of both spins R is set to 200 Hz. The *J*-coupling constant between spins I and S is chosen to equal 10 Hz and the additional couplings that break the magnetic equivalence are set to 7 Hz all other possible

coupling constants are set to zero. The magnetic equivalence is broken because the coupling constant of I to R_1 (7 Hz) is different from the coupling constant of I and R_2 (0 Hz) and similarly (J_{SR_1}= 0Hz ≠ J_{SR_2}= 7 Hz).

The simulations are carried out following the procedures described in the previous Sections. A brief outline of the important steps in these simulations seems most appropriate to wrap up this introductory Chapter.

The initial density matrix in the parahydrogen molecule is 1/4 **1-I·S**. The state space is 16-dimensional. And all involved matrices are 16-by-16 matrices

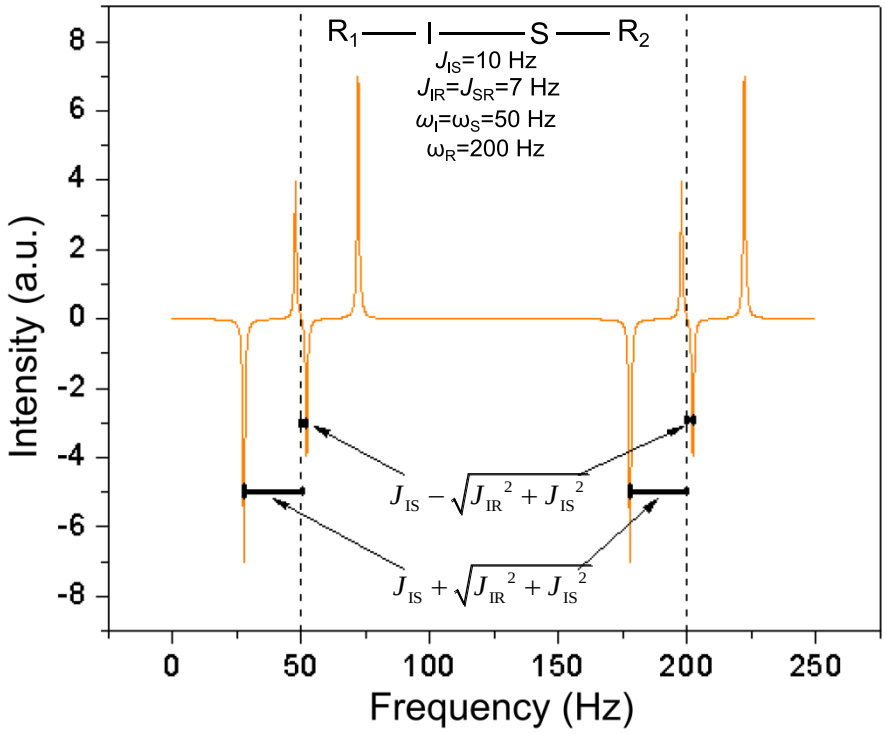

Figure 2.12 Simulated PASADENA spectrum for a four-spin model system. The symmetry of the singlet state of parahydrogen is broken solely on the basis of *J*-coupling constants. The coupling constant of I to R_1 (7 Hz) differs from the coupling constant of S and R_1 (0 Hz). Similarly, the coupling constant of S to R_2 (7 Hz) differs from the coupling constant of I to R_2 (0 Hz). This difference suffices to obtain observable PHIP.

that are formed by using the Kronecker product much in the same way as going from one to two spins as performed in Eq. (2.33).

In this 16-dimensional state space the initial density matrix, ρ_0, for an individual parahydrogenated molecule is:

$$\rho_0 = 1/16\ \mathbf{1}\text{-}\mathbf{I}\cdot\mathbf{S}. \tag{2.105}$$

In order to take into account all hydrogenation reactions occurring at random points in time, incoherent averaging is performed. This averaging process is accounted for by expressing ρ_0 in the eigenbasis of the Hamiltonian of the spin system:

$$H = \omega_I (I_z + S_z) + \omega_R (R_{1z} + R_{2z}) + 2\pi J_{IS} (\mathbf{I}\cdot\mathbf{S}) + 2\pi J_{IR} (I_z R_{1z} + S_z R_{2z}), \tag{2.106}$$

and eliminating all off-diagonal elements. This results in the averaged density matrix over all hydrogenation reactions ρ_{av}. Next a 45° pulse is simulated by applying the adequate propagator $U(\pi/4)$ to the density matrix.

$$\rho_1 = U(\pi/4)\ \rho_{av}\ U^{-1}(\pi/4), \tag{2.107}$$

where

$$U(\pi/4) = \exp(-i\ H_{pulse}\ t) = \exp(-i\ (I_y+S_y+R_{1y}+R_{2y})\ \pi/4). \tag{2.108}$$

This density matrix is then propagated under the Hamiltonian given in Eq. (2.106), giving the time dependent density matrix after the pulse $\rho(t)$

$$\rho(t) = \exp(-i\ H\ t)\ \rho_1\ \exp(i\ H\ t), \tag{2.109}$$

and the signal can then be calculated using the trace formula of Eq. (2.10) as:

$$s(t)=Tr(\rho(t)\ (I^-+S^-+ R_1^-+ R_2^-). \tag{2.110}$$

This signal is then Fourier-transformed and plotted as given in Figure 2.12. This simulation confirms that the magnetic equivalence of I and S can be broken with the effect of *J*-couplings alone and PHIP can be converted into observable signal also under the condition of identical chemical shift, which was encouraging for the future experiments using PHIP at zero-magnetic field where chemical shift differences are entirely absent.

3. The zero-field-NMR spectrometer: operation and setup

The detection of the zero-field NMR signal is performed with an atomic magnetometer.[4,23,59–61] In the last decade atomic magnetometers have become one of the most sensitive magnetic sensors with demonstrated sensitivities below $1\text{fT}/\sqrt{\text{Hz}}$.[23] Thereby beating SQUIDS (super conducting quantum interference devices),[62–65] which have previously held the record as the most sensitive magnetometers. Atomic magnetometers are particularly appealing in the context of NMR measurements. They are small in size (mm scale) with large potential for further miniaturization and unlike SQUIDS, they do not require cryogenic temperatures for operation. These characteristics of atomic magnetometers give zero-field NMR great potential of becoming a low cost and portable NMR platform, giving NMR access to spaces inaccessible by traditional NMR spectrometers. In this Chapter the operation and the experimental setup of ^{87}Rb vapor magnetometer will be discussed in the context of zero-field NMR measurements.

3.1 Rubidium magnetometer: basics of operation

In the present work a rubidium-87-vapor magnetometer is employed. The central component is a glass cell filled with rubidium-87 and nitrogen buffer gas. The magnetometer is operated with a pump laser, for polarizing the rubidium atoms, and a probe laser, orthogonal to the pump beam, detecting a perpendicular component of the magnetization, thereby measuring the magnetic field experienced by the ^{87}Rb atoms. The details of the measurement will be expanded on in the following Sections. An overview of the essential components, of the experimental setup, is provided in Figure 3.1. As shown in a), four layers of μ-metal and one innermost layer of a ferrite shield is used to shield out the Earth's magnetic field and the surrounding noise. Any remaining fields are reduced to the μG level with a set of three orthogonal shimming coils (not shown but discussed in more detail in Section 3.2). Part b) of Figure 3.1 shows the arrangement of magnetometer cell, sample, pump beam and probe

beam. The cell is arranged at a 45° angle with respect to the pump and the probe beam traveling in the horizontal plane such that both beams intersect inside the Rb-vapor cell at a 90° angle. The sample is arranged vertically immediately above the magnetometer cell. In this configuration the magnetometer is arranged to detect magnetic fields in the vertical direction produced by the sample. The direction of propagation of the pump beam is defined as z-direction, the direction of propagation of the probe beam is defined as x-direction and the vertical direction of the detected magnetic field is defined as y-direction. In part c) the mode of operation is illustrated. In brief, the pump beam is circularly polarized, pumping the rubidium atoms into a stretched state aligned with the pump beam in the z-direction. The action of a magnetic field in the vertical y-direction is to rotate the polarized spins in the horizontal plane. The combined action of continued pumping and a small magnetic field causes a steady state polarization aligned, at a given angle between the z- and the x-direction. With the probe beam the component of polarization in the x-direction is detected. This is then a direct measure of the magnetic field we strive to observe. The ensuing Sections 3.1.1-3.1.3 provide a more detailed explanation of these effects.

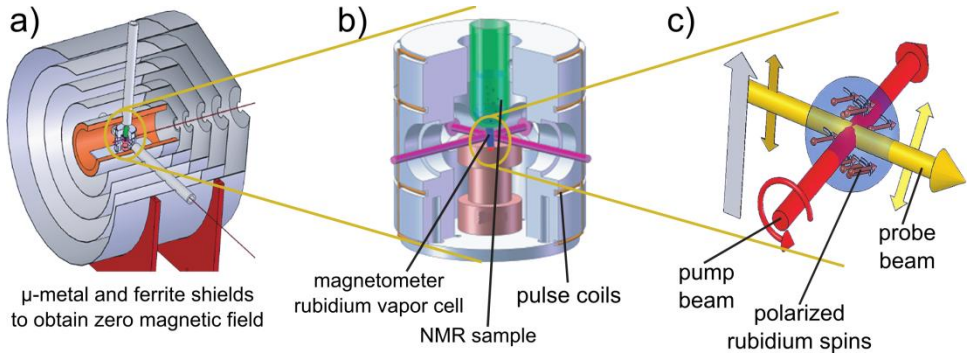

Figure 3.1 Overview of a typical zero-field NMR spectrometer. Part a) shows the magnetic shielding containing the sample and the detector. Part b) zooms inside the shields, showing the arrangement of rubidium cell, heater, NMR sample, pulse coils, pump and probe laser beams. Part c) indicates the mode of operation. The circularly polarized pump beam aligns the rubidium spins, which slightly rotate under the influence of magnetic field. The linearly polarized probe beam detects the effect of the magnetic field by experiencing rotation/birefringence caused by the slightly rotated rubidium spins.

3.1.1 Optical pumping

The characteristics of ^{87}Rb exploited in magnetometry applications are primarily dictated by the lone electron in the valence shell. This electron is in the $^2S_{1/2}$ state as its ground state. The pump beam is tuned to the D1 line, inducing transitions between the $^2S_{1/2}$ ground state and the $^2P_{1/2}$ state. Figure 3.2 shows the states and the relevant energy differences for the D1 transition in ^{87}Rb. The hyperfine states with f=1 or f=2 are a result of the combination of the angular momentum, **J**=**L**+**S**, with the nuclear spin **I** in ^{87}Rb as **F**=**J**+**I**.(l=0, j=1/2, s =1/2, i=1/2)

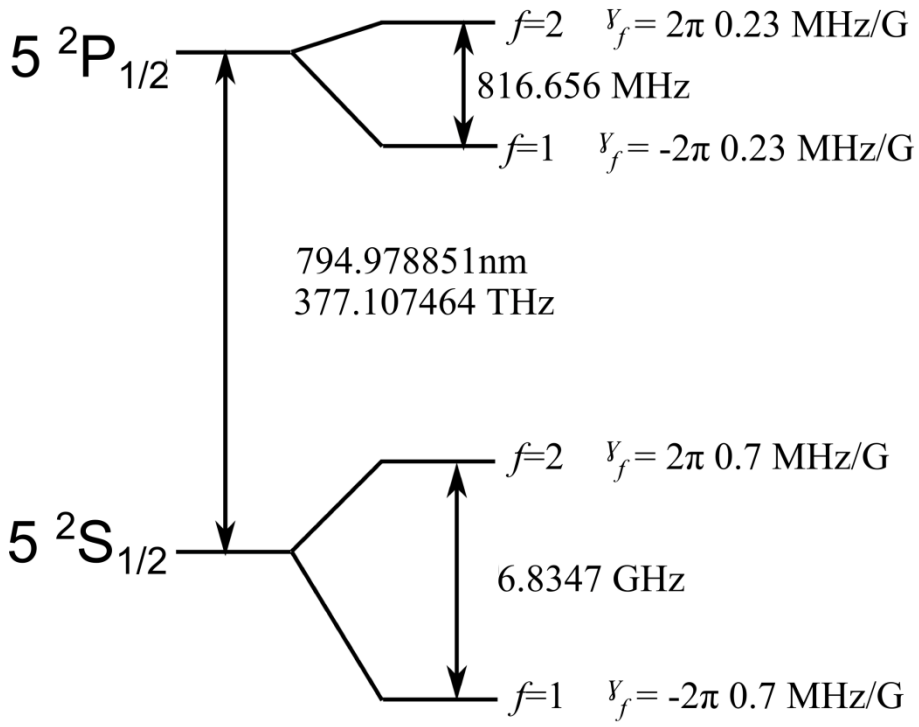

Figure 3.2 Energy level diagram of ^{87}Rb for the D1 transition. The excited-state values are taken from the literature[66,67]. The approximate gyromagnetic ratios for each level are given, for the corresponding Zeeman splittings between degenerate magnetic sublevels.

Optical pumping of alkali vapors has been extensively studied in the literature[35,58,61,68] and here only an introductory overview shall be provided.

For the purposes of optical pumping σ+ circularly polarized light tuned to the D1 line is employed. All photons in the beam have the same spin projection along the direction of propagation of the pump beam. This direction is conventionally defined as the z-direction. Along this axis all photons have angular momentum +1. This angular momentum can be transferred to a rubidium atom upon absorption of a photon. Large degrees of polarization, on the order of unity, can be obtained by this form of optical pumping[69]. In the described magnetometer a polarization on the order of 50% is ideal. As indicated in Figure 3.3 levels with lower m_f are depopulated and excited states with $m_f' = m_f+1$ are populated. Simultaneously, the Rb-cell contains a large amount of N_2 buffer gas causing large amounts of collisional quenching.

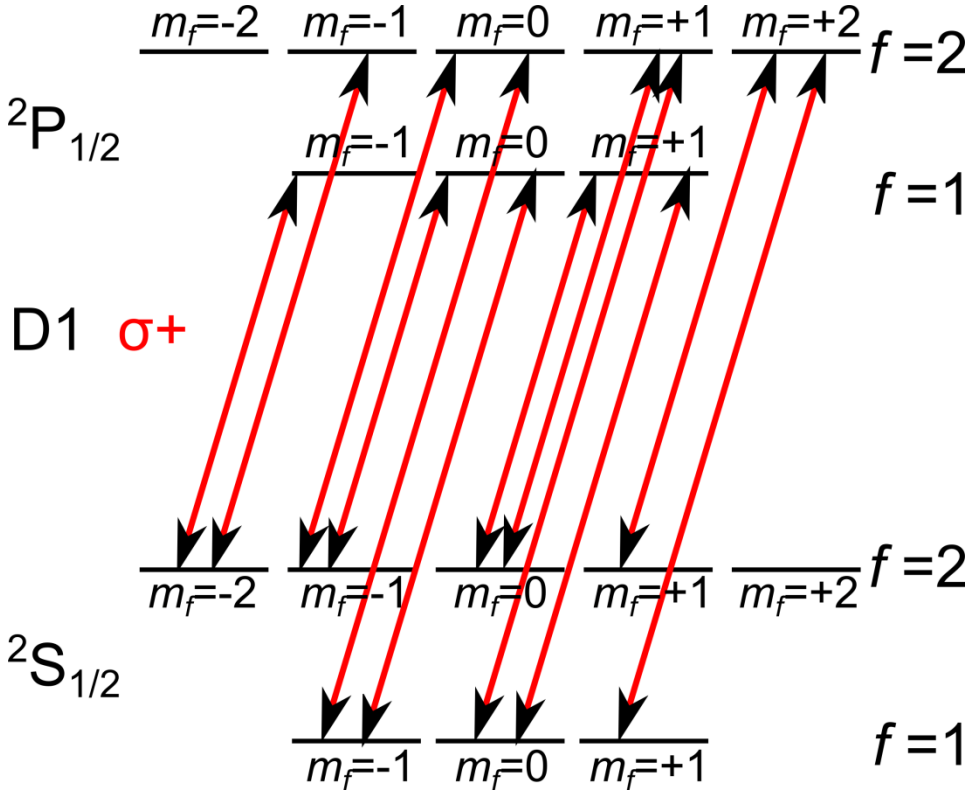

Figure 3.3 Energy level diagram for the D1 transition in ^{87}Rb illustrating the effect of σ+ circularly polarized light tuned to the D1 transition optically pumping the Rb-vapor resulting in polarization as depicted in Figure 3.4.

Also, given a large rubidium density, Rb-Rb collisions cause collisional mixing. These relaxation mechanisms are non-radiative processes with equal probability of inducing decay into any of the Zeeman ground-state levels thereby partially counteracting the effect of the pumping. The relative rates of relaxation and pumping determine the steady state polarization. The relaxation processes are random in nature, such that eventually the m_f =+2 becomes primarily populated. This m_f=+2 state is transparent to the incident pump beam. To achieve 50% polarization the relaxation rate has to equal the pumping rate. The power level of the pump laser is adjusted accordingly. In the next Section the different types of collisions and their consequences for the operation of the magnetometer are discussed in more detail.

3.1.2 Relaxation mechanisms and the SERF regime

There are different types of collisions and respective relaxation mechanisms for a ^{87}Rb atom in the glass cell. These collisions can be categorized as spin-destruction collisions, spin-exchange collisions and collisions with the wall. In cells, such as used here, with a large alkali density spin exchange collisions are most frequent. In spin-exchange collisions, the direction of the electron spin is reversed while the nuclear spin and the total spin, $\sum m_f$,are conserved. These collisions are alkali-alkali collisions and can be represented as:

$$\mathrm{A}(\uparrow) + \mathrm{B}(\downarrow) \rightarrow \mathrm{A}(\downarrow) + \mathrm{B}(\uparrow). \tag{3.1}$$

As result, the spin-exchange collisions change the value of m_f by ±1, ±2 and can also change the hyperfine state in a given electronic state, such as within the $^2S_{1/2}$ state. The overall effect is to redistribute the population among all Zeeman sublevels in a given electronic state. If the spin exchange collision rate is much faster than the optical pumping rate, then a spin population described by a Boltzmann distribution is obtained. For example at a polarization level P of 0.5 the distribution depicted in Figure 3.4 is obtained. The population in each level is given by a Boltzmann distribution as

$$\rho = e^{\beta m_f}, \tag{3.2}$$

with

$$\beta = \ln\left(\frac{1+P}{1-P}\right). \tag{3.3}$$

The polarization level P itself is primarily dependent on the ratio of the optical pumping rate to the rate of depolarization. As implied above, there is a different type of collisions, so called spin destruction-collisions responsible for depolarization. These can be either collisions with the buffer gas, or with other alkali atoms. They can be represented as:

$$A(\uparrow) + B(\downarrow) \rightarrow A(\downarrow) + B(\downarrow). \tag{3.4}$$

Unlike in the case of spin-exchange collisions, these spin-destruction collisions do not conserve total angular momentum and hence depolarize the alkali vapor. The Rb-Rb spin-destruction collisions typically have cross sections that are two to four orders of magnitude smaller than the cross sections of spin-exchange collisions and are hence much less frequent.

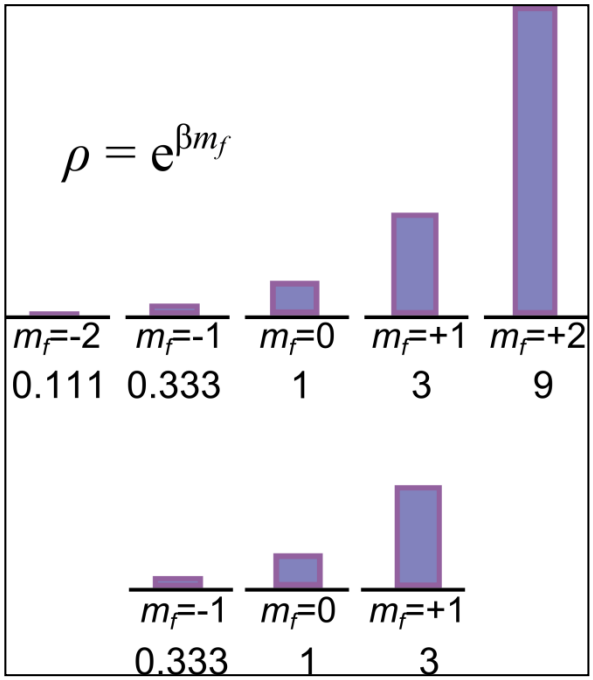

Figure 3.4 Energy level diagram for the D1 transition in ^{87}Rb, illustrating the distribution of populations at a polarization level of P=0.5. Under each Zeeman level labeled by its magnetic component m_f the numerical value for the population ρ is given.

In addition to spin-destruction collisions between gas molecules and atoms also collisions with the wall can cause large amounts of depolarization. Especially in small cells as used here, (5 mm × 2 mm × 1 mm) collisions with the wall can be a major source of relaxation. In order to suppress collisions with the wall the cell contains buffer gas, which reduces diffusion of the ^{87}Rb atoms towards the walls. Here the 1200 Torr of N_2 are chosen as a good intermediate value for minimizing the total amount of depolarizing collisions, by balancing wall collisions and spin-destruction collisions. The buffer gas is also important to broaden the detection bandwidth such that signals up to 400 Hz can easily be detected.

The regime described here is the so called spin-exchange relaxation free (SERF) regime. Two important conditions have to be met in order to be in this regime. First, as described, the spin relaxation rate has to be much faster than the optical pumping rate and any other relaxation rate. Second, magnetic fields experienced by the rubidium vapor have to be small such that spin-rotations induced by the magnetic field also occur at a much slower rate than the spin-exchange-relaxation rate. In order to understand this effect let's consider the effect of a magnetic field on the Zeeman levels.

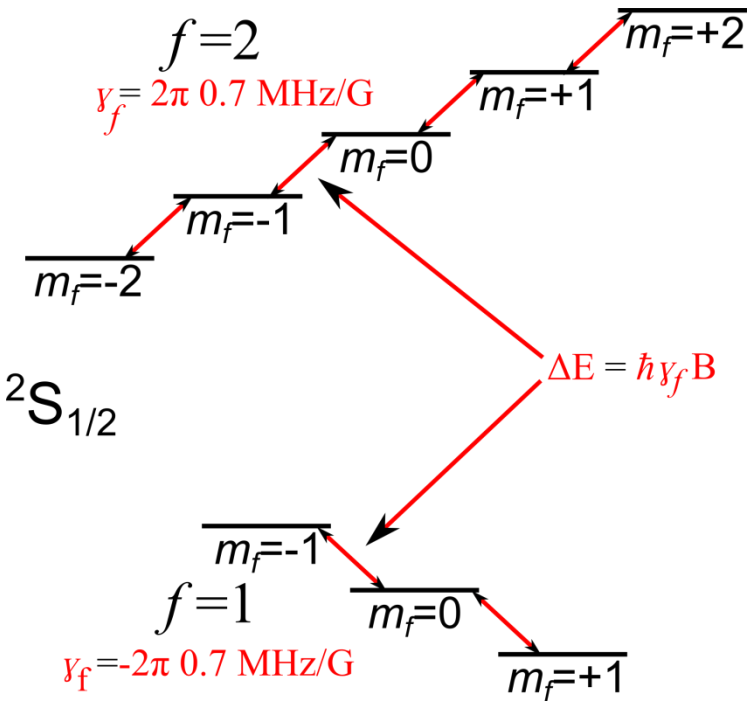

Figure 3.5 Illustration of the effect of magnetic field on the energy level diagram of the hyperfine levels of the $^2S_{1/2}$ manifold in ^{87}Rb.

For small magnetic fields non-linear Zeeman effects can be ignored and we can write the energy of the Zeeman levels as:

$$E_{f,m_f} = \hbar\, \gamma_f\, m_f\, |B|, \tag{3.5}$$

where B is the magnetic field and γ_f is the gyromagnetic ratio γ_f, which is equal to 2π 0.7 MHz/G for the f =2 manifold and -2π 0.7MHz/G for the f =1 manifold as indicated in Figure 3.2. Figure 3.5 shows the spreading of the Zeeman sublevels under the influence of a magnetic field. The precession frequency of the spins at 100% polarization is.

$$\omega_0 = \frac{\Delta E}{\hbar} = 2\gamma_f\, |B|. \tag{3.6}$$

Under SERF conditions, all Zeeman levels of both hyperfine states (f =1 and f =2) are populated according to the Boltzmann distribution described in Eq.(3.2) and depicted in Figure 3.4. Since these hyperfine states have opposite γ_f the average spin precession frequency depends on the level of polarization. In the present case this average precession frequency is given as function of polarization as, [61]

$$\omega_q = \omega_0 \left(2 - \frac{4}{3 + P^2}\right), \tag{3.7}$$

such that for P=1, $\omega_q = \omega_0$ and for P=0 , $\omega_q = 2/3\ \omega_0$. As described above the magnetometer is typically operated at P≈0.5. In that case we obtain an effective Larmor frequency of $\omega_q = 10/13\ \omega_0$.[61]

It should now be obvious that this type of averaging is only possible if the spin-exchange relaxation rate is fast as compared to the optical pumping and the precession frequency, such that the distribution of populations remains in a steady state. If these conditions are met the measurement is spin-exchange relaxation free (SERF), because the overall frequency is shifted and remains narrow. This should be contrasted to the alternative approach of observing a precession at ω_0, which would be quickly dephased by the spin-exchange-collisions that are difficult to suppress given their relatively large cross section. Details of the employed detection modality follow in the next Section.

3.1.3 Magnetic field detection with the probe beam

In the previous Section it has been established how polarization is created and alligned with the pump beam. Next, the effect of the magnetic field on the polarized rubidium spins will be described, followed by explanations of the detection modality. (Note: As we have seen in the previous Section spin-exchange collisions fully mix the populations of the hyperfine states. Here, we will use this effect to simplify the description of the probing process and ignore the individual hyperfine states but rather focus on the electron alone and describe the $^2S_{1/2}$ ground state and the $^2P_{1/2}$excited state as composed of only two respective states with m_S= +1/2 and m_S= -1/2. A complete analysis including all details of the hyperfine states follows from there in a straightforward way.)

The polarized steady state in the z-direction given by a Boltzmann distribution can be described by a density matrix.

$$\rho_P \propto S_z, \tag{3.8}$$

where the proportionality constant is dependent on the polarization. As described in Eq. (2.24) a magnetic field in the vertical direction, defined here as the y-direction, induces a rotation of the polarization along S_z into S_x.

$$e^{(-iS_y t)} S_z e^{(+iS_y t)} = S_z \cos(\omega_q t) + S_x \sin(\omega_q t). \tag{3.9}$$

Counteracting this rotation is the continued action of the pump beam and the relaxation, resulting in a steady state polarization with components along S_z and S_x. Figure 3.6 illustrates this effect. The steady state angle θ, between the z and the x component, is dependent on the magnetic field B_y, the optical pumping rate R_{OP} and the relaxation rate R_{rel}. The components of the polarization under the influence of these different effects can be calculated by finding the steady state solutions to the Bloch equation as described in the literature[61,70]. Here, only the results are presented. In the presence of a pure B_y field the angle θ is found as:

$$\tan\theta = \frac{S_x}{S_z} = \frac{\gamma_e B_y}{R_{OP} + R_{rel}}, \tag{3.10}$$

where γ_e is the gyromagnetic ratio of a bare electron. The signal detected by the probe is proportional to S_x and we obtain:

$$signal \propto S_x = \frac{S_0 \gamma_e B_y (R_{OP} + R_{rel})}{(R_{OP} + R_{rel})^2 + (\gamma_e B_y)^2} . \tag{3.11}$$

S_0 represents the steady state S_z (=1/2 P_z) polarization in the absence of a magnetic field.

For sake of completeness it is worth mentioning that in the presented setup the magnetometer is actually also sensitive to the two remaining components of a magnetic field B_x and B_z as follows

$$S_x = S_0 \frac{\kappa_y + \kappa_x \kappa_z}{1 + \kappa_x^2 + \kappa_y^2 + \kappa_z^2} , \text{ with } \boldsymbol{\kappa} = \frac{\gamma_e}{(R_{OP} + R_{rel})} \mathbf{B} . \tag{3.12}$$

In the case of a pure B_y field Eq. (3.11) results. In Section 3.2.8 below details of Eq. (3.12) are elaborated upon in the context of initially reducing the magnetic field as far as possible.

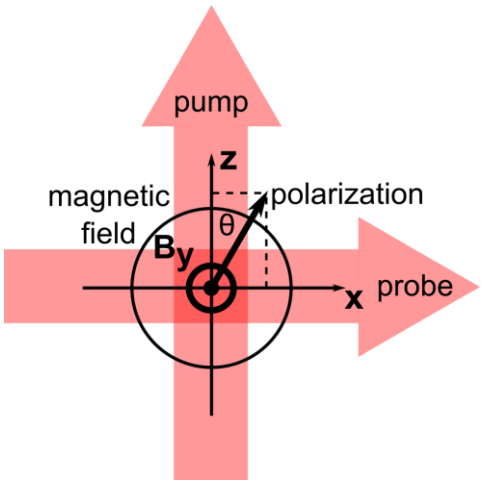

Figure 3.6 Illustration of the simultaneous effect of the pump beam and a small magnetic field, B_y. The pump beam aligns the polarization along z while, B_y, coming out of the plane, induces rotation of the polarized state such that a steady state polarization results at angle θ in the x-z plane. The probe beam detects the x-component of the polarization.

Finally, to measure the S_x component we assert that the probe beam travels in an orthogonal direction to the pump beam and we define this direction as the x-direction. The probe beam consists of linear polarized light with a ~ 2 times lower power level than the pump beam and is tuned ~200 GHz off resonance from the D1 line. (ca. 2 to 4 times the optical line width) The reason for low power and off-resonance tuning is to avoid optical pumping by the probe beam, as much as possible. The linearly polarized probe beam can be understood as being composed of equal amounts of σ+ and σ- circularly polarized light. When interacting with Rb vapor polarized in the x-direction the σ+ component can be absorbed by Rb atoms in the m_s=-1/2 state. Where as the σ- component is absorbed by Rb atoms in the m_s=+1/2 state. If a S_x polarization is present then the populations of the m_s=+1/2 and the m_s= -1/2 state differ such that the rubidium vapor becomes birefringent for the probe beam and the linearly polarized light is rotated. This rotation is detected and gives a direct measure of the magnetic field experienced by the cell. The experimental implementation is detailed in the next Section.

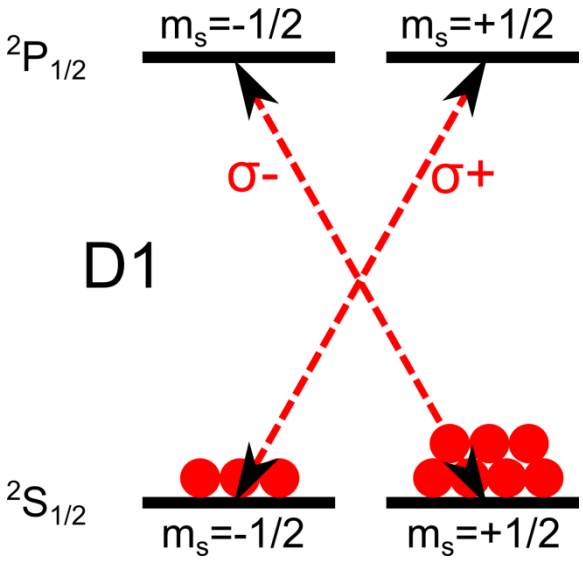

Figure 3.7 Illustration of the effect of the probe beam, explaining the birefringent property of the vapor cell. The σ- and the σ+ components of linearly polarized light experience different extents of virtual absorption, depending on the polarization of the rubidium atoms in the direction of propagation of the probe beam.

The fundamental sensitivity limit of the described alkali vapor magnetometers is due to shot-noise and given as[4,60]:

$$\delta B = \frac{1}{\gamma_e \sqrt{n T_2 V t}}, \tag{3.13}$$

where γ_e is the gyromagnetic ratio, n is the number density of alkali atoms T_2 is the relaxation time, V is the volume of the cell and t is the measurement time. For SERF magnetometers the relaxation time T_2 is determined by the spin destruction collisions limiting the fundamental sensitivity for cells smaller than one cm^3 to about 1 $fT/\sqrt{Hz}$. [60] In Section 3.2.8 the experimental sensitivity measurement is detailed.

3.2 Experimental configuration

In this Section a general overview of the experimental setup including all experimental components will be provided and a detailed description of their function is given. In the subsequent Sections the individual components are presented individually and further details are provided. In Figure 3.8 all individual components are shown and their connections are indicated schematically. In Figure 3.9 a photograph of the inside of the magnetometer is shown providing a look at the central components.

At the center of the experiment is the NMR tube. Typically, standard 5mm NMR tubes are employed, 7" to 9" long. The NMR tube is filled with 50 to 300 µL of a liquid sample. In experiments employing thermal prepolarization the sample is pneumatically shuttled from the prepolarizing magnet outside the magnetic shields to just above the magnetometer cell filled with rubidium vapor in the center of the magnetic shields. The distance between the Rb-cell and the bottom of the NMR tube is ~1 mm. For maximum

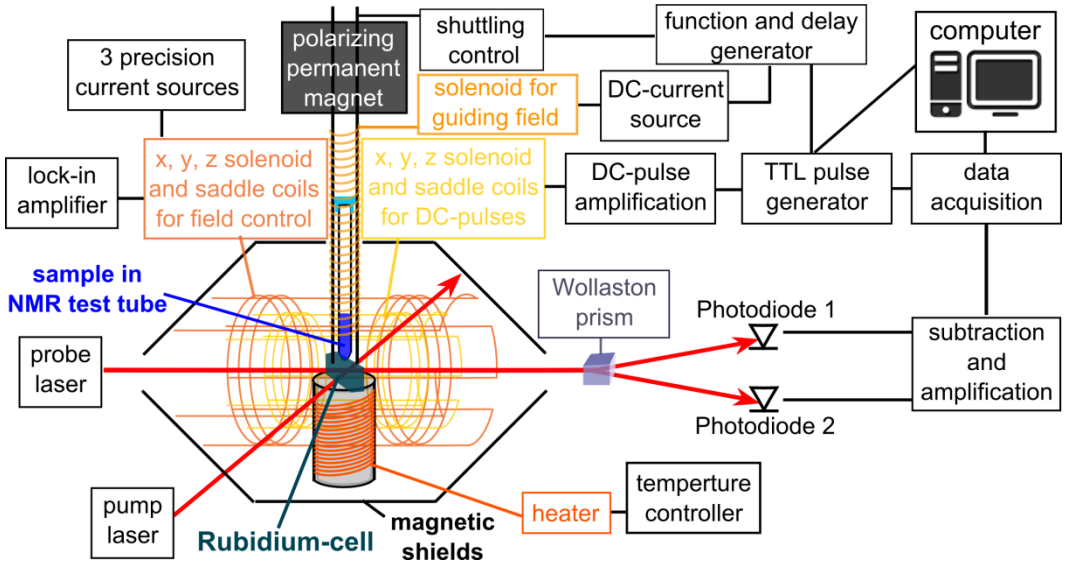

Figure 3.8 Schematic overview of the important components of a zero-field NMR spectrometer.

signal the smallest possible distance is desirable. Simultaneously, thermal insulation between Rb-cell and NMR sample is required; also the Rb-cell must be protected from impact by the shuttling NMR tube in order to ensure stable operation of the magnetometer and to avoid damage to the Rb-cell.

During the shuttling process a "guiding field" is provided inside the "shuttling tube" the sample travels in. This field is provided by a solenoid wrapped around the shuttling tube creating a field aligned with the direction of shuttling of the sample. This field ensures adiabatic transport of the sample's magnetization into the detection region, thereby avoiding scrambling of the magnetization during the shuttling process. The pneumatic shuttling setup will be detailed in Section 3.2.5.

The rubidium cell is mounted on an aluminum nitride spool around which, a twisted pair of wire is wrapped and used to provide resistive heating. The cell is typically operated between 180 °C and 210 °C. Details about the heater are provided in Section 3.2.3.

Zero-magnetic field is established by multiple layers of magnetic shielding. Depending on configuration, 4 to 6 layers of magnetic shielding are used as can best be seen in Fig 3.1a). The outer shields are μ-metal shields and in some cases a ferrite shield is used as the innermost shield to reduce Johnson-noise from that shield. In order to cancel any remaining magnetic fields, down to the μG level a set of three solenoid and saddle coils are employed. The fields are controlled with Krohn-Hite® model 523 low noise precision current sources. Additionally, a SRS® DSP lock in amplifier model SR830 is connected to these "field coils" in order to apply oscillating magnetic fields (test signals) for purposes of calibration and for determining the sensitivity of the magnetometer as a function of frequency. Details of the calibration procedure are provided in Section 3.2.8.

Outside the magnetic shielding, typically above the shields, a permanent magnet is installed for purposes of prepolarization. Depending on the setup permanent magnets with magnetic field strengths between 0.6 T and 2 T have been used.

In order to excite coherences in the NMR sample, after prepolarization and shuttling down to the detection region, three "pulse coils" are installed. Similarly to the field coils, the pulse coils consist of two saddle coils and a Helmholtz coil for the x, y and z directions. They are used to apply DC pulses of magnetic field. The desired pulse sequences are programmed on the

computer. The pulse sequence is then loaded onto the TTL pulse generator, PulseBlaster from Spin Core Technologies® model JP303. The PulseBlaster sends TTL pulses to a home built amplification circuit which provides the pulses to the pulse coils. Details of the pulse amplification circuit are provided in Section 3.2.4.

Once the NMR sample is excited, the produced NMR signal is detected by the rubidium vapor. This magnetometer cell has dimensions of 5 x 2 x 1 mm and was microfabricated using the techniques described in Ref. [71]. The cell is operated in pump-probe mode as described in the previous Section 3.1. The setup of the employed optics will be described in Section 3.2.1. For purposes of this overview it shall suffice to say that the rotation experienced by the linear polarized pump beam is read out using a Wollaston prism and two photodiodes which detect the intensity of the two counter-rotating components of the linearly polarized pump beam. The intensity difference detected by the two photodiodes is the measure of the magnetic field emitted by the NMR sample. The voltages produced by the photodiodes are connected to a home built subtraction and amplification circuit, details of which are provided in Section 3.2.2. Alternatively a SRS model SR560 low-noise preamplifier has been used in alternative configurations.

After amplification of the signal it is sent to a data acquisition (DAQ) card. Here the National Instruments® NI USB-6229 DAQ card was employed, which eventually sends the acquired and digitized signal to the computer for further processing. For purposes of triggering and synchronization a function and delay generator is connected to the PulseBlaster, the shuttling control circuit and the guiding-field solenoid. Here the SRS® model DS345 function generator was used.

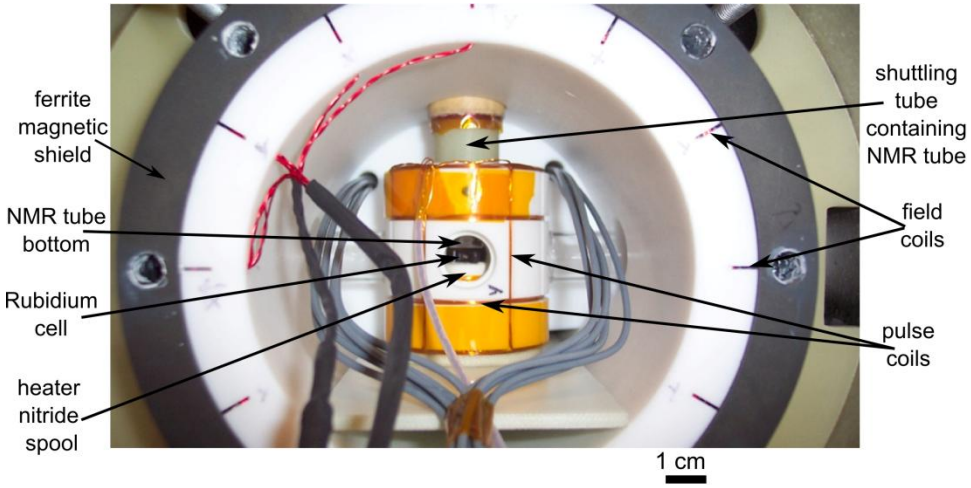

Figure 3.9 Photograph of the inside of the zero-field NMR spectrometer.

3.2.1 Optics

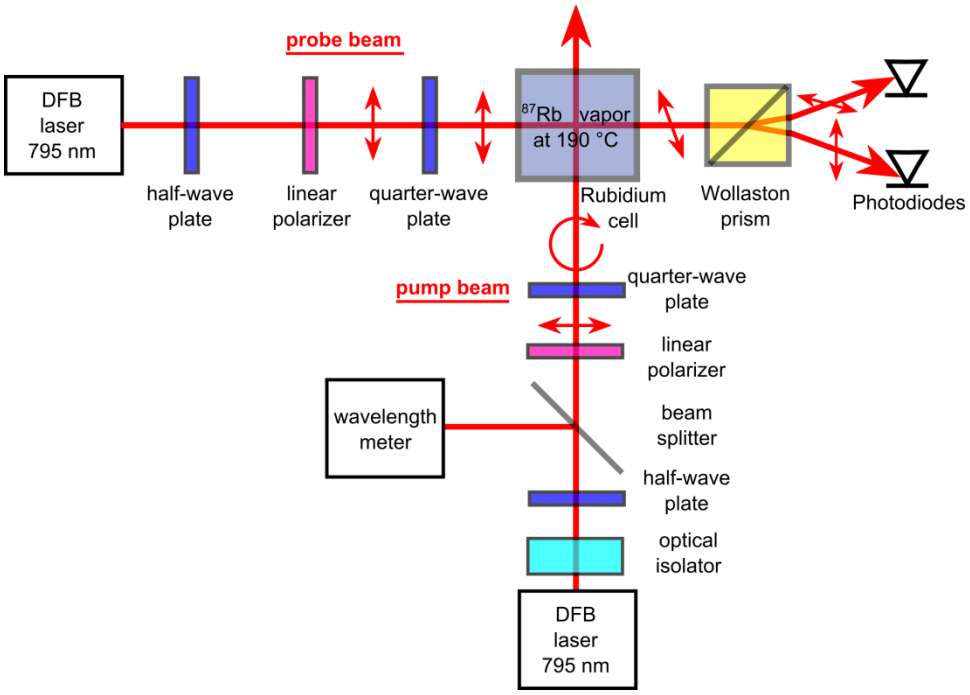

Figure 3.10 Configuration of the pump and the probe beam, displaying the optical elements used to achieve the desired characteristics of the pump and probe beams.

A typical configuaration of the optical components is shown in Figure 3.10. For the pump laser a DFB laser is employed and tuned on resonance of the D1 line at 794.798 nm. A Thorlabs® ITC502 laser diode combi controller is used to adjust fequency and amplitude of the laser. The pump laser is typically operated such that ~15mW arrive at the Rb-cell. In order to avoid reflections into the laser an OFR® optical isolator follows immediately after the laser. Next the pump beam travels through a half-wave plate used to rotate the light with respect to the following linear polarizer as desired to adjust the power level. However, before the pump reaches the linear polarizer a small fraction of the photons are diverted with a beam splitter to a wavelength meter to initially tune the laser. The majority of the pump beam reaches the linear polarizer where the linear polarization of the incident beam is increased by ~5 orders of magnitude, creating close to100% linearly polarized light. In order to convert the linear polarization into circular polarization a quarter wave plate is used.

The transmission axis of the linear polarizer is alligned at a 45° angle between the fast and the slow axis of the quarter wave plate such that circular polarization results. This circularly polarized pump beam then reaches the Rb-cell and pumps the Rb into a stretched state alligned with the direction of the pump beam as described in Section 3.1.1.

The probe beam is also controlled with a Thorlabs® ITC502 laser diode combi controller controller and is tuned ~100-200 GHz off resonance. The intensity of the probe beam is further reduced by the half wave plate and the linear polarizer. By turning the polarization with respect to the transmission axis of the linear polarizer the intensity is reduced such that the probe beam induces a minimal amount of pumping in the Rb cell, yet suffices for sensitive detection. The typical power level of the probe reaching the Rb cell is ~5 mW. Before reaching the Rb-vapor cell a quarter wave plate is inserted and its optical axis is alligned close to parallel with the liner polarization of the beam such that it barely affects the polarization. This quarter wave plate is used to correct for birefringence of the glass cell walls of the Rb-cell by turning it slightly off-axis. Finally, after the Rb-vapor imparts rotation, in dependence of the magnetic field, on the probe beam the beam is split by a Wollaston prism into its two circular components and their relative intensity is detected on the photodiodes. At zero magnetic field and in the absence of a sample the magnetometer signal is "zeroed" (balanced) by adjusting the Wollaston prism such that the intensities detected on both photodiodes is equal.

3.2.2 Subtraction and amplification circuit

Once the two components of the probe beam hit the photodiodes the induced voltages are amplified and subtracted by the circuit displayed in Figure 3.11. The circuit consists of two op-amps connected to the respective photodiodes in the inverting amplifier configuration. This is then followed by the subtraction stage.

The photodiodes are reversed biased for fast response times, i.e. the n-type region is connected to the positive terminal such that in the absence of photons the resistance of the photodiode is large and no current flows. The gain of the op-amp in the inverting configuration is given as $-R_f/R_{Ph}$ such that[72]

$$V_{out} = -V_{in} \frac{R_f}{R_{Ph}} . \tag{3.14}$$

When the photodiode is irradiated with light the resistance of the photodiode drops, and current flows. The voltage is then amplified by the inverting amplifier.

Both photodiodes are connected in an identical manner; since we are interested in measuring the difference in signal from both photodiodes the outputs of the inverting amplifiers V_a and V_b are connected to a differential amplifier.

For the differential amplifier the output voltage is given as[72]

$$V_{out} = \frac{R_2}{R_1}(V_b - V_a). \tag{3.15}$$

The circuit is configured such that the gain can be switched between (R2/R1)=100 and (R2/R1)=1000 and is chosen depending on application. During most NMR measurements a gain of 1000 is chosen but during initial adjustments and setup where large test signals are applied a gain of 100 is preferred to avoid saturation of the signal.

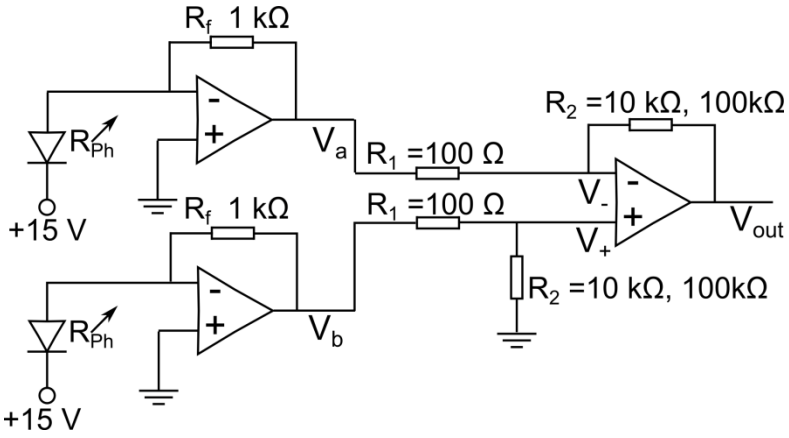

Figure 3.11 Circuit diagram of the subtraction and amplification circuit built to detect the intensity difference on the photodiodes. The photodiodes are connected to op-amps in the inverting configuration followed by an op-amp configured as differential amplifier.

3.2.3 Heater

The Rb-cell is heated to between 180°C and 210° C. These elevated temperatures are chosen to achieve a large Rb density in the gas phase. The temperatures are chosen for maximized sensitivity. The temperature is reached by resistive heating. A 19 gauge thick and ~30 ft long copper wire with high temperature coating is wrapped around a nitride spool as indicated in Figure 3.12, Figure 3.8 or Figure 3.9. Before wrapping the wire around the nitride spool the wire is folded over once and extensively twisted (forming a twisted pair) to minimize magnetic fields that could be produced by the heater. Despite these efforts to reduce magnetic fields produced by the heating process the heater is a major source of noise if a DC-current flows through the heater during acquisition. Therefore two different heating modes have been implemented. In the DC configuration shown in Figure 3.12 the heater is simply turned off during acquisition, whereas in the AC configuration resistive heating is performed at a high frequency of ~10 kHz far away from the signals of interest and outside the bandwidth (~400 Hz) of the magnetometer.

Figure 3.12 a) shows the heater in the DC configuration. An Omega® model CNI3243 PDI temperature controller measures the temperature with a thermocouple placed on the aluminum nitride spool. This temperature controller regulates the temperature via an SRS model DS345 function generator. The function generator is used to turn the heater off during the acquisition period. Typically acquisition periods have the same length as the prepolarization periods during which the heater is on. Depending on the measurements the acquisition and prepolarizing periods are set between 5 and 60 s. The function generator connects to Darlington pair, which has a large enough current gain such that sufficient current is drawn from the Kepco® bipolar operational power supply/amplifier.

Figure 3.12 b) shows the heater configuration in AC mode. The same temperature controller, function generator and power supply/amplifier are used. However, now the function generator is set to put out a high frequency signal 5 kHz or above and is connected directly to the power amplifier. The temperature controller modulates the amplitude of the high frequency signal and in this configuration the heating is constantly on, also during acquisition.

The advantage of the DC-mode is that potential noise from the heater is entirely eliminated, however the disadvantage is that the dropping temperature of the cell during acquisition causes large drifts of the signal, which are avoided in the AC-configuration.

The temperature range of 180-210° C is chosen to maximize the signal. It may, however, be advisable to choose even higher temperatures associated with higher rubidium densities. In the present configuration the heaters tend to fail if run at even higher temperatures but experimental adjustments could be made to prevent failure.

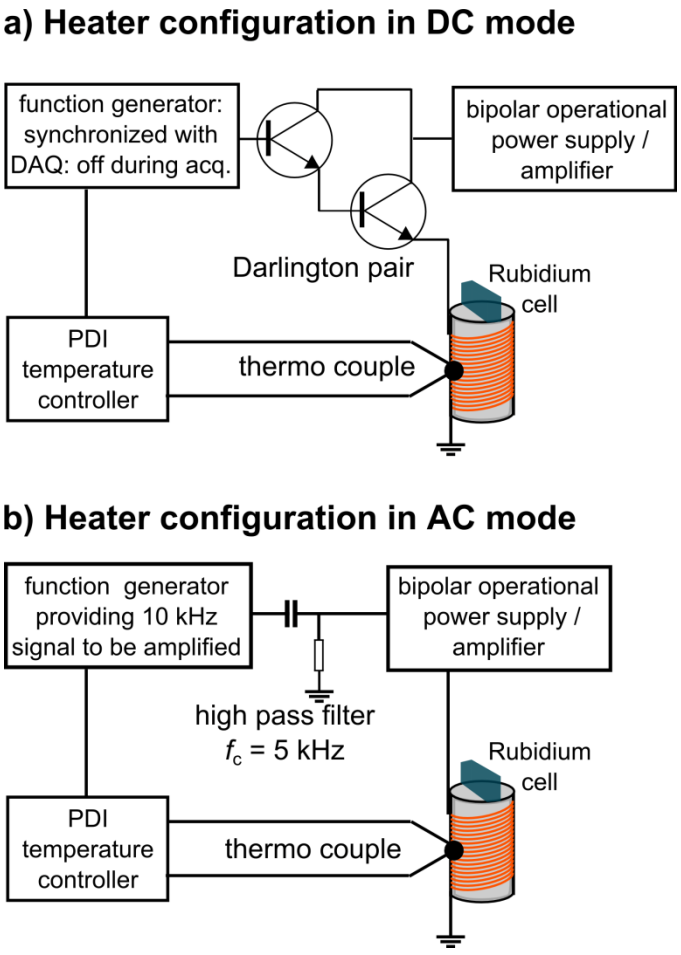

Figure 3.12 Configuration of the electrical components used for heating the rubidium vapor cell in DC or AC mode.

3.2.4 DC pulses

Pulses of DC-magnetic field are applied to the NMR sample to excite coherences. The pulse sequences are first encoded on the computer then loaded onto the Spin Core Technologies® PulseBlaster which puts out TTL signals that are amplified in a amplification stage. In Figure 3.13, the employed pulsing circuit is shown. Besides amplification we also desire to apply pulses for two directions from single sided TTL signals. As shown in the figure, TTL_1 is connected to an op-amp in the non-inverting configuration[72]

$$V_{out} = V_{in}\left(1+\frac{R_2}{R_1}\right) = V_{in}\left(1+\frac{1000\,\Omega}{100\,\Omega}\right) = 11\,V_{in}\,. \tag{3.16}$$

After this first small amplification step the signal is fed into an NPN transistor, which gets saturated, such that +15V are applied to the coil for the time the TTL_1 signal is high.

TTL_2 is connected to an op-amp in the inverting configuration such that

$$V_{out} = -V_{in}\left(\frac{R_2}{R_1}\right) = -V_{in}\left(\frac{1000\,\Omega}{100\,\Omega}\right) = -10\,V_{in}\,. \tag{3.17}$$

Similarly this signal is then fed into a PNP transistor, that gets saturated, such that -15V are applied to the coil for as long as TTL_2 is high.

This configuration allows for application of pulses in two opposite directions with single sided TTL signals. However, since the components for either direction are not identical pulses have to be separately calibrated for both directions.

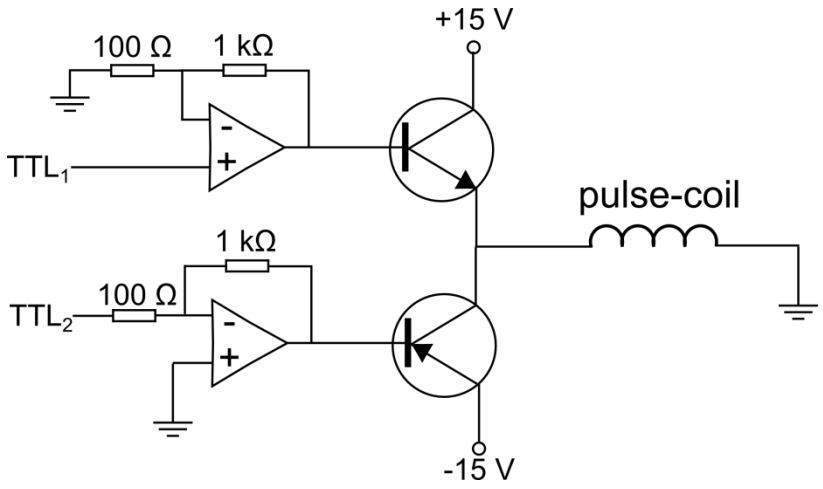

Figure 3.13 Circuit diagram of the pulsing circuit used to apply pulses of DC magnetic field onto the NMR sample. Two TTL lines are followed by op-amps in the inverting and in the non-inverting configuration, which control transistors such that pulses in two opposite directions can be applied using single sided TTL signals.

3.2.5 Prepolarization and shuttling

The prepolarizing and sample transfer step from the prepolarizing magnet to the detection region are critical for high SNR experiments. The prepolarization time should typically be at least three times T_1 or longer. The sample-transfer or shuttling time should be fast compared to T_1, yet slow enough to allow for adiabatic transfer of the polarized spin state into the detection region preserving the polarization. Figure 3.14 shows the experimental configuration of the shuttling setup which enables effective polarization and sample transfer.

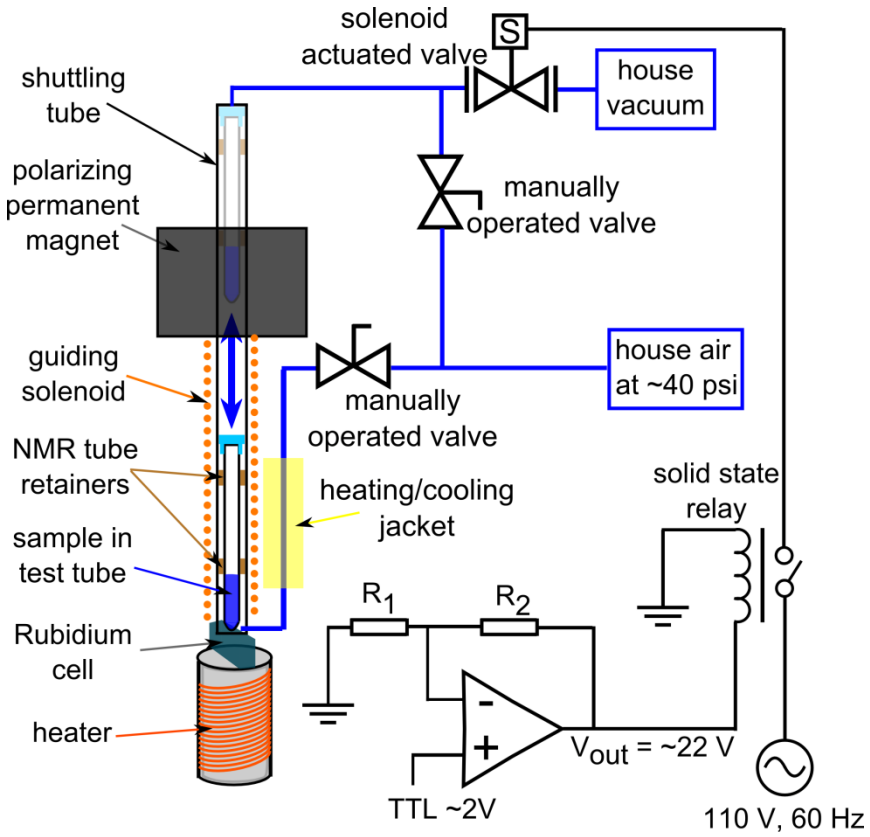

Figure 3.14 Schematic of the pneumatic shuttling setup built for efficient sample transfer from prepolarization region to the detection region and vice versa. Also heating and cooling is implemented to control the temperature of the NMR sample.

The sample is filled in a standard 5mm NMR tube. Onto the NMR tube two retainers are mounted which keep the NMR tube centered inside the shuttling tube and allow for efficient pneumatic control. The shuttling tube is connected, on the bottom to an inlet of air stream, whose temperature is controlled by the heating and cooling jacket. The heating and cooling jacket allows for controlling the sample temperature. Additionally this air stream from the bottom helps to lift the sample up into the magnetic field of the prepolarizing magnet. The top of the shuttling tube is connected such that either vacuum or slight pressure is applied. The solenoid actuated valve turns the vacuum on and off and is indirectly controlled by a function generator via the depicted circuit. The employed circuit consists of a op-amp in the non-inverting configuration with a gain of $(1+R_2/R_1) = 11$. After this amplification stage the TTL signal controls a solid state relay switching the solenoid actuated valve on or off, which is operated with 110V / 60Hz AC power.

The shuttling speed can be controlled with the displayed manually controlled valves, which control the pressure difference above and below the NMR tube. The shuttling time is typically adjusted between 0.1 s and 0.5 s. Faster shuttling speeds are associated with stronger impacts on the bottom of the shuttling tube, risking damage to the NMR tube, whereas slower speeds can involve more signal loss due to relaxation during the shuttling time.

During the shuttling process of the NMR tube from the prepolarizing region to the detection region the guiding solenoid is turned on to provide a guiding field of ~1G. This ensures that the Larmor-frequency even of low γ nuclei such as ^{15}N to always be above the rate of change of the Hamiltonian as discussed in the following.

We can undertake exemplary estimations to convince ourselves that adiabaticity of the transport is guaranteed even under conditions of relatively strong inhomogeneties. We make the following assumptions: The sample leaves a prepolarizing magnetic field in the horizontal direction of 10 kG at a velocity of 200 cm/s. The field drops exponentially such that after 0.5 cm the magnetic field has half its original value; i.e. with a half-time of (0.5cm/(200cm/s)) = 0.0025 s Under these assumptions the prepolarizing field drops as

$$B_P(t) = 10kG\ (1-\exp(-1/(0.0025s)\ t). \qquad (3.18)$$

We also assume a constant vertical field in the guiding solenoid of B_G =1 G. To remain in an adiabatic regime the rate of change of the angle θ between both

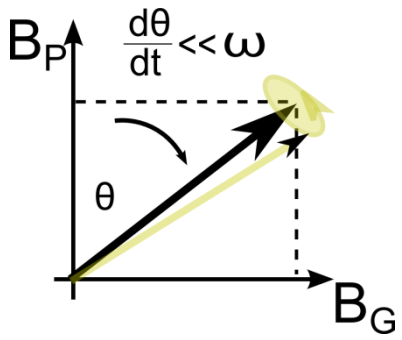

Figure 3.15 Illustration of polarization transfer from a prepolarizing field B_P into a perpendicular guiding field B_G. For adiabatic polarization transfer the rate of change of the angle dθ/dt has to be slower than the Larmor precession frequency ω.

fields (or both Hamiltonians) has to be much slower than the rate of precession of the spins about the Hamiltonian at any point in time. In Figure 3.15 the change of the Hamiltonian is shown as going from a prepolarizing field B_P to a perpendicular guiding field B_G. The Laromor precession frequncy around the field is indicated by a cone around the field containing both componets of B_P and B_G during the transfer.

Making use of the fact that the angle θ between B_P and B_G is given as $\theta(t) = \arctan(B_G / B_P)$, we can evaluate dθ/dt and compare the frequency of precession with the rate of change of the angle θ as a function of transfer time as plotted in Figure 3.16. The rate of change of the angle θ is largest when the two fields B_P and B_G are comparable in size. But as can be seen from the plot the dθ/dt remains smaller than the nutation frequency ω even under these unfavorable conditions of low γ, large magnetic field gradients and fast transfer speeds.

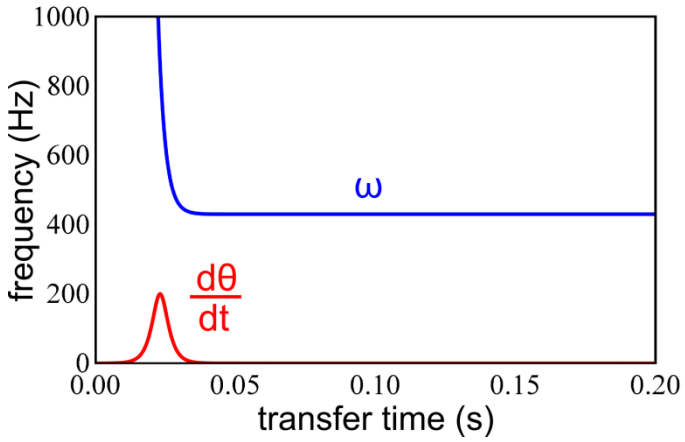

Figure 3.16 Comparative plot of the Larmor frequency ω and the rate of change for the angle θ as a function of polarization transfer time. The parameters used in this simulation are: prepolarizing field, B_P= 10kG, guiding field, B_G=1G, gyromagnetic ratio γ = 430 Hz/G, sample velocity, v=200cm/s, exponential magnetic field gradient EG = 2/cm.

3.2.6 Parahydrogen production equipment

As described in Section 2.3.2 for the production of close to 100% parahydrogen, normal hydrogen gas has to be brought in contact with a catalyst that induces the ortho to para conversion at temperatures of below 30K. In Figure 3.17 a schematic diagram of the experimental configuration of all components is provided. The presented setup was used to fill a 10L aluminum cylinder with 150 psi of parahydrogen, which was subsequently used for experiments during the following days (up to four).

Before filling the aluminum cylinder with parahydrogen all traces of oxygen need to be removed from the cylinder since oxygen significantly increases the rate of relaxation of the parahydrogen in the cylinder. To that end, the aluminum cylinder is evacuated with the membrane pump to ~ 1 mbar and subsequently filled with nitrogen up to 200 psi (~14 bar) and evacuated again. This flushing procedure is repeated four times essentially eliminating all oxygen. Once the aluminum cylinder has been evacuated the fifth time the actual parahydrogen fill begins. All tubing, from the pressure regulator of the compressed hydrogen cylinder up to the needle valve, is filled with 150 psi of hydrogen. This includes the copper coil inside of the Janis Research®, Model CCS-200/202 "Non-Optical, Sample in Vacuum 10 K Cryocooler with SHI Coldhead". The copper coil contains iron oxide as conversion catalyst. It is made with 3/8" OD 1/8''ID copper tubing and has a total length of ~4 ft. The needle valve is adjusted such that ca. 700 sccm are measured on the hydrogen flow meter. At the beginning of the filling process the out-streaming hydrogen is directed towards the exhaust. Then the Sumimoto (SHI)® model HC-2 helium compressor is turned on to start cooling the cold finger. The temperature is adjusted to 30K with the LakeShore Cryotronics®, Model 321 temperature controller, which is connected to the heating element in the cold finger. To provide sufficient insulation the cryostat is evacuated with a Pfeiffer® model TMH07IP turbo-molecular pump. As soon as the temperature in the cryostat has reached 30K the produced parahydrogen is directed toward the aluminum cylinder. The filling process then takes ~4h.

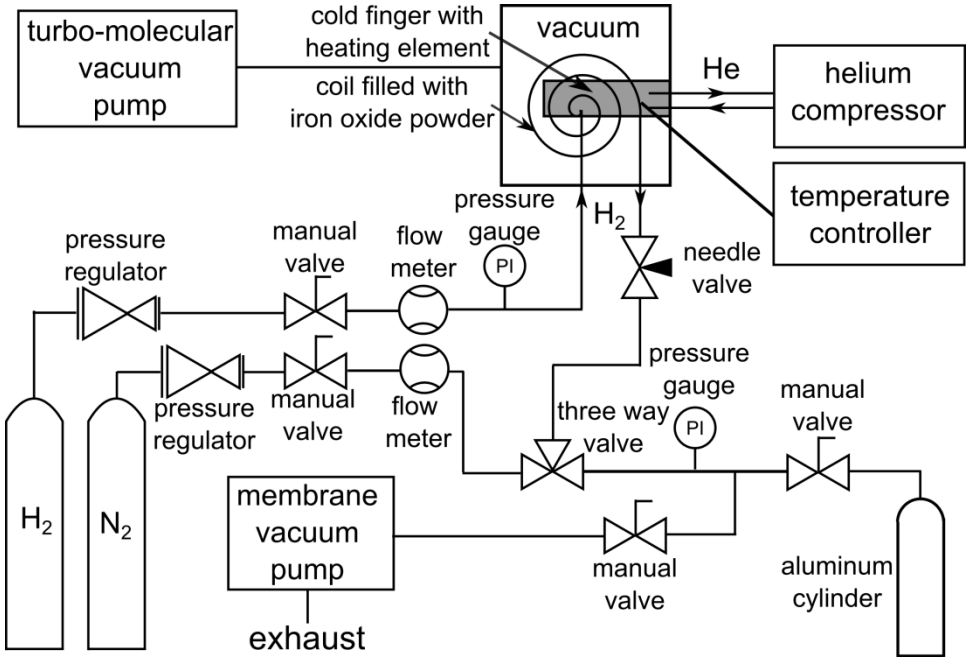

Figure 3.17 Flow chart for the production of parahydrogen. During the filling process, normal hydrogen flows from the compressed hydrogen cylinder into the iron oxide containing tubing, held at 30K. There it is converted into parahydrogen. From the cryostat on, the parahydrogen flows into the aluminum cylinder where it is stored.

3.2.7 Gas manifold for PHIP experiments

The gas manifold used to bubble parahydrogen through the NMR tube, next to the rubidium cell, is configured such that nitrogen and parahydrogen can be bubbled through the solution interchangeably. Figure 3.18 shows a schematic of the employed setup. At the beginning of an experiment the NMR tube is filled with a solution containing solvent, hydrogenation substrate and hydrogenation catalyst. Typically volumes between 50 and 400 μL are employed. Subsequently, the entire manifold is pressurized to ~70 psi.

One of the important features of the gas manifold is the ability of stopping the bubbling in a short time (< 200 μs) relative to the bubbling and the acquisition time, such that no bubbles occur during acquisition distorting the signal. This is achieved by means of the short valves connecting the inlet

and the outlet. As long as one of the short valves is open it is guaranteed that no bubbles occur and that the sample stays in the NMR tube.

During the pressurization stage the manual short is open such that the system can be pressurized quickly without necessitating flow through the NMR tube. Only once the system is at a stable pressure, the manual short is closed and the solenoid actuated valve is activated. When both short valves are closed the needle valve at the outlet is opened slowly and the bubbling in the NMR tube is monitored ensuring gentle bubbling which does not spew the sample out of the NMR tube. The flow rate typically used is ~300 sccm. The pressure difference before and after the NMR tube is typically kept below 1 psi, which is sufficient for gentle bubbling through the 1/32'' Teflon® tubing feeding into the NMR tube.

In Figure 3.18 b) a typical time sequence of bubbling and acquisition is shown. During the initial 5s bubbling time the short valves are closed and the exhaust valve is open. To stop the bubbling the exhaust is closed and the short is opened. (Closing the exhaust is not critical but it conserves parahydrogen.) Before pulse and acquisition a setting delay of 200 μs is interleaved that allows for the remaining bubbles to disappear such that the solution sits physically still during acquisition.

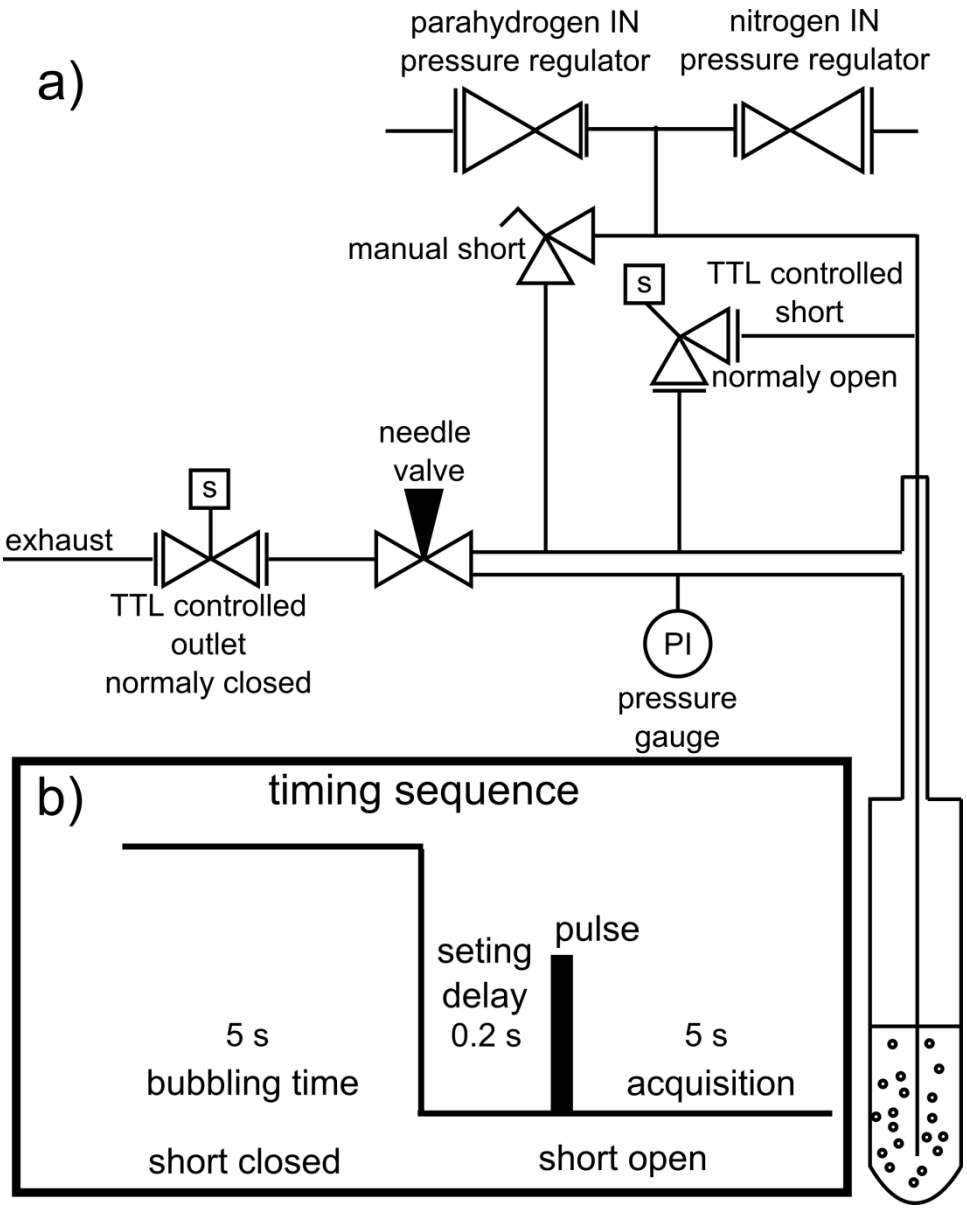

Figure 3.18 (a) Gas manifold used for controlling the bubbling during a zero-field PHIP experiment. (b) typical timing sequence for a zero-field PHIP experiment.

3.2.8 Calibration and sensitivity of the magnetometer

When initially setting up the magnetometer and before acquiring spectra a number of calibrations need to be performed. The magnetic fields needs to be reduced with the field coils as much as possible, the magnetometer signal as a function of frequency needs to be calibrated and the sensitivity of the magnetometer should be determined.

To reduce the magnetic fields first the pump beam is blocked and the Wollaston prism is turned until the intensity difference detected on the photodiodes is zero. Subsequently the pump beam is unblocked and signal is measured according to Eq. (3.12), which can be rewritten for purposes of illustration as

$$\text{Signal} \propto \frac{\Delta B\, B_y + B_x B_z}{\Delta B^2 + B_x{}^2 + B_y{}^2 + B_z{}^2}. \tag{3.19}$$

According to this proportionality, a dispersive Lorentzian, the signal is plotted as a function of B_y in Figure 3.19.

$\Delta B = \frac{(R_{OP} + R_{rel})}{\gamma_e}$ is the linewidth of this Lorentzian.

The magnetometer is most sensitive when operated in the central linear region close to zero magnetic field, where the slope is largest.

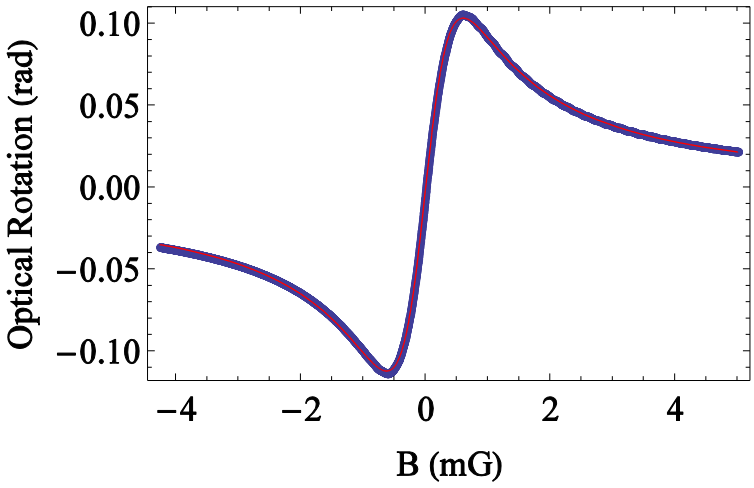

Figure 3.19 Typical appearance of the magnetometer response as a function of magnetic field as dispersive Lorentzian.

At the time the pump is unblocked and some magnetic field is detected the the DC level of the magnetometer signal changes accordingly. Since, primarily, the y-magnetic field in the vertical direction is measured, B_y is adjusted until the measured DC-level returns to zero. Of course, there are also contributions of the x and the z magnetic field. In order to reduce, e.g., the x field, an oscillating magnetic field in the z direction is applied at ~0.5 Hz. A dispersive Lorentzian as shown in Figure 3.19 is observed. Subsequently the x field is adjusted until the contribution from the oscillating z field is no longer detected. This is possible because the product of x and z fields are detected as shown in Eq. (3.19). To reduce the z field the same procedure is followed: An oscillating field is applied in the x direction and the z field is adjusted. The procedure of reducing B_y, B_x and B_z is performed iteratively until all fields are no longer detected. Unfortunately, there are additional effects that cause fictitious fields such as light shifts or improper alignment of the laser beams. (The pump and probe beam may not intersect at a perfect right angle.)

These effects are also compensated for when following the above "field-zeroing procedure" such that some actual magnetic fields may remain. At that point the fields have to be further adjusted by observing the NMR signals as a function of magnetic field. As will be described in great detail in Chapter 5 the zero-field NMR signals can be split by application of a magnetic field. The magnetic fields can be further reduced by minimizing the splitting of the zero-field-NMR lines.

Next, the detected signal as a function of frequency has to be calibrated. To that end, a lock-in amplifier is used to apply an oscillating magnetic field ranging from 2 to 402 Hz in steps of 10 Hz. The real and the imaginary part of the signal relative to the applied magnetic field are recorded with the lock-in amplifier.

The relative phase, Φ, is calculated as:

$$\Phi = \arctan\left(-\frac{\mathrm{Re(signal)}}{\mathrm{Im(signal)}}\right), \tag{3.20}$$

and the magnitude of the signal, A, is calculated as:

$$\mathrm{A} = \sqrt{\left(\mathrm{Re(signal)}\right)^2 + \left(\mathrm{Im(signal)}\right)^2}. \tag{3.21}$$

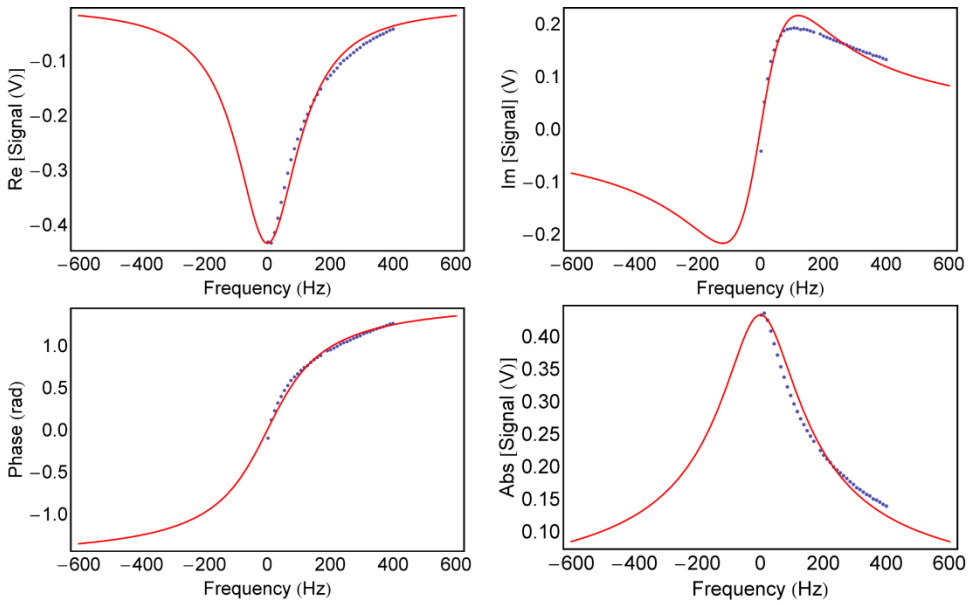

Figure 3.20 Calibration curves of the magnetometer response as a function of test frequency. The acquired calibration data is fit to a complex Lorentzian as given by Eq. (3.22). with the following parameters: a=52, dν=120, $\varphi = \pi$

The data can then be fit to a complex Lorentzian, which in return is used to correct the phase and the amplitude in the acquired NMR spectra. Figure 3.20 depicts exemplary calibration data fit to a complex Lorentzian of the form

$$\frac{\mathrm{a}}{\mathrm{d}\nu + i\,\nu} e^{i\varphi}, \tag{3.22}$$

with the a, dν and φ as fitting parameters. In this specific case the parameters are chosen as described in the caption of Figure 3.20.

As can be observed, this calibration is quite crucial since the phase changes from zero to almost 1.3 radians at 400Hz and the magnitude drops by close to 65% at 400 Hz.

Often times a better fit to the data is obtained using polynomial fits, not following a particular physical model as the Lorentzian does. Either way produces well phased spectra with the appropriate amplitudes.

Finally, the sensitivity of the magnetometer is determined. After the discussion of the calibration experiment one may expect a frequency dependent sensitivity. This is indeed the case if sensitivity is dependent solely on characteristics of the rubidium cell, however if the noise is dominated by noise sources outside the rubidium cell, such as for example Johnson noise from the shields then the noise is attenuated in the same way as the signal and the sensitivity does not change strongly as function of frequency. Often times low frequency noise from the building does indeed cause worse sensitivity below ~10 Hz and SNR is essentially flat out to 500 Hz. As a standard in these experiments the sensitivity was determined at 100 Hz. To that end, a 100 Hz signal of known amplitude, V, is applied to a coil generating a field, B_y, in the vertical direction. This coil has to be previously calibrated such that a magnetic field of known strength, B_y, is detected. This signal is then acquired for a time, t. The acquired signal is Fourier-transformed and the signal-to-noise ratio (SNR) is measured. In this context, the sensitivity, δB, is defined as the detectable field strength per square root of unit time with an SNR of one. In other words the sensitivity is simply equal to the calibrated rms-noise floor and is calculated from the measured quantities as:

$$\delta B = \frac{\mathrm{B_y}\sqrt{\mathrm{t}}}{\mathrm{SNR}}, \tag{3.23}$$

where B_y can be calculated after calibration of the coil as:

$$B_y = \alpha \frac{V}{R}, \tag{3.24}$$

where α is determined from previous calibration and R is a chosen resistance, connected to the coil in order to obtain the desired magnetic field. Typical values are α = 44 μT/A, V=0.1V and R=10^6 Ω giving a field of B_y = 4.4 pT. Application of this field and acquisition for t = 1 s typically results in an SNR of ~150 such that the sensitivity results as $\delta B \approx 30$ fT/$\sqrt{\text{Hz}}$. These are only representative values, which vary from magnetometer to magnetometer and depend on the exact configuration but illustrate how the sensitivity is determined.

4. Zero-field NMR using thermal polarization

The timing sequence of a typical zero field NMR experiment consists of prepolarization in a permanent magnet outside of the magnetic shields, sample transfer from prepolarization region into the detection region by shuttling, application of a pulse inducing observable coherences and acquisition. While the experimental aspects have been described in Chapter 3, here the zero-field NMR experiment will be described with the focus on the NMR sample.

Before going into any detail, it is important to be aware of a change in the definitions of the axes. While in Chapter 3 the z-direction is given as the direction of propagation of the pump beam in the horizontal plane, in the context of the NMR experiment itself, it is more appropriate to define z in the vertical direction along which the NMR sample is polarized initially. Accordingly, the x and y axes are defined to lay in the horizontal plane for the discussions of the NMR experiments. This does represent a source of potential confusion but it seems inappropriate in either context to deviate from defining the direction of polarization as z-axis. Unfortunately, they do not coincide for the NMR sample and the rubidium vapor.

4.1 Zero-field NMR experiment on two coupled spins

As introduction to the zero-field NMR experiment, first, a description will be provided, on the basis of a system composed of two nuclei, I and S, with differing gyromagnetic ratio that are coupled by a *J*-coupling interaction.

In the prepolarizing magnet the density matrix formed is much like in the case of the high-field experiment given in Eq. (2.41) however here, since we use two heteronuclear spins the individual z-terms, I_z and S_z are scaled by the individual gyromagnetic ratios γ_I and γ_S.

$$\rho_0 = \gamma_I I_z + \gamma_s S_z. \tag{4.1}$$

After prepolarization, the sample is adiabatically shuttled (see Section 3.2.5) into the detection region through the guiding solenoid, which maintains a field of ~1G during the shuttling process. The shuttling process is typically fast as compared to any relaxation such that the density matrix is practically unchanged; only, the magnetization of the sample is aligned with the guiding field in the vertical direction once the sample has arrived in the detection region.

Immediately after turning off the guiding field a pulse of magnetic field in the horizontal plane (x or y) can be applied. The pulse that maximizes the signal is strongly dependent on γ_I and γ_S. As will be described below the term that is detected is I_z-S_z and with the pulse we seek to maximize this contribution. The expression for the initial density matrix can be expressed as:

$$\rho_0 = \gamma_I I_z + \gamma_s S_z = \frac{\gamma_I + \gamma_s}{2}(I_z + S_z) + \frac{\gamma_I - \gamma_s}{2}(I_z - S_z). \tag{4.2}$$

From this expression it is immediately apparent that for all heteronuclear pairs the initial density matrix does already contain an I_z-S_z component and furthermore, if γ_I and γ_S have opposite sign it is best not to apply any pulse but much rather to start acquisition immediately after turning off the guiding solenoid. However, if γ_I and γ_S have the same sign the signal can be enhanced by the application of a pulse of DC-magnetic field in a direction perpendicular to the polarization, which can convert I_z+S_z into I_z–S_z and vice versa. The pulse Hamiltonian for a pulse in the y-direction is given as:

$$H_P = B_y(\gamma_I I_y + \gamma_s S_y), \tag{4.3}$$

which rotates the spins by angles $\alpha_I = B_y \gamma_I t$ and $\alpha_S = B_y \gamma_S t$ in dependence of the respective gyromagnetic ratios. Given these rotation angles it may take an arbitrarily long time to perfectly invert I_z+S_z, however typically a reasonably short pulse can be found that performs the desired inversion with a high enough accuracy keeping the amount of lost signal to a minimum. A particularly good example is the heteronuclear combination of ^{1}H and ^{13}C because in that case the gyromagnetic ratios are roughly related as $\gamma(^{13}C) \approx 1/4\ \gamma(^1H)$. As depicted in Figure 4.1, in that case, a 4π rotation of the protons corresponds, roughly, to a π rotation of the ^{13}C and when applying a pulse of the appropriate length, this can be used to invert the I_z+S_z and I_z–S_z contributions in the density matrix.

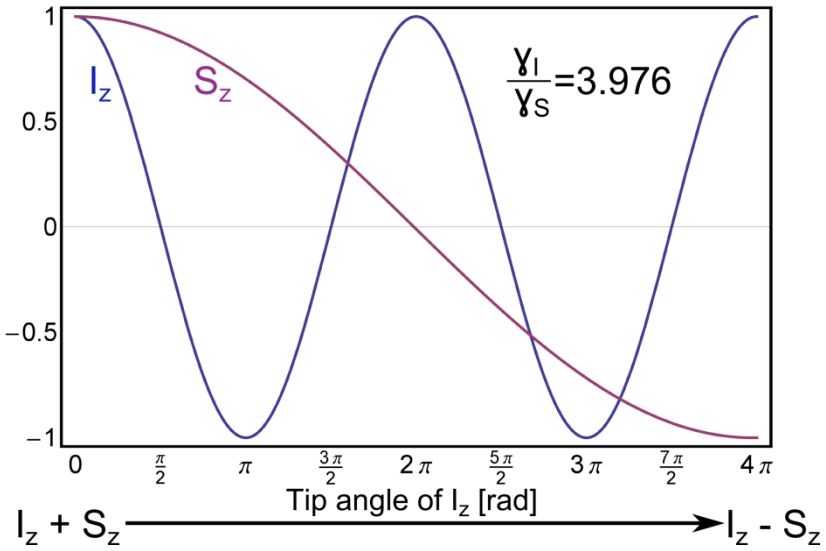

Figure 4.1 Effect of a DC-magnetic field pulse in y on the initial density matrix. Converting I_z+S_z into I_z-S_z after a 4π rotation of protons in the case where I spins are ^{1}H and S spins are ^{13}C

In the context of the present thesis only molecules containing ^{1}H and ^{15}N or ^{1}H and ^{13}C were analyzed. In the case of ^{1}H-^{15}N pairs no pulses were applied because of the opposing sign of the gyromagnetic ratios and in the case of ^{1}H-^{13}C pairs the described 4π proton pulse was used.

Finally, after shuttling, turning off the guiding field and the pulse, evolution and detection at zero magnetic field begins.

At zero magnetic field the Hamiltonian is given as

$$H_{ZF} = J\,\mathbf{I}\cdot\mathbf{S}, \tag{4.4}$$

The components of the initial density matrix are I_z+S_z and I_z-S_z. I_z+S_z commutes with $\mathbf{I}\cdot\mathbf{S}$, therefore only the I_z-S_z component produces observable oscillations. To illustrate these effects, remember that the eigenstates of the Hamiltonian $J\,\mathbf{I}\cdot\mathbf{S}$ are the singlet state S_0 and the triplet states T_{-1}, T_0 and T_1, as introduced in Section 2.2.2. In Figure 4.2 I_z+S_z and I_z-S_z are represented as populations and coherences between the available states. I_z+S_z can be represented as populations in the T_{-1} and T_{+1} state, which do not evolve and I_z-S_z is a coherence under the *J*-coupling Hamiltonian oscillating at the frequency *J*, which is equal to the energy separation between singlet and triplet states.

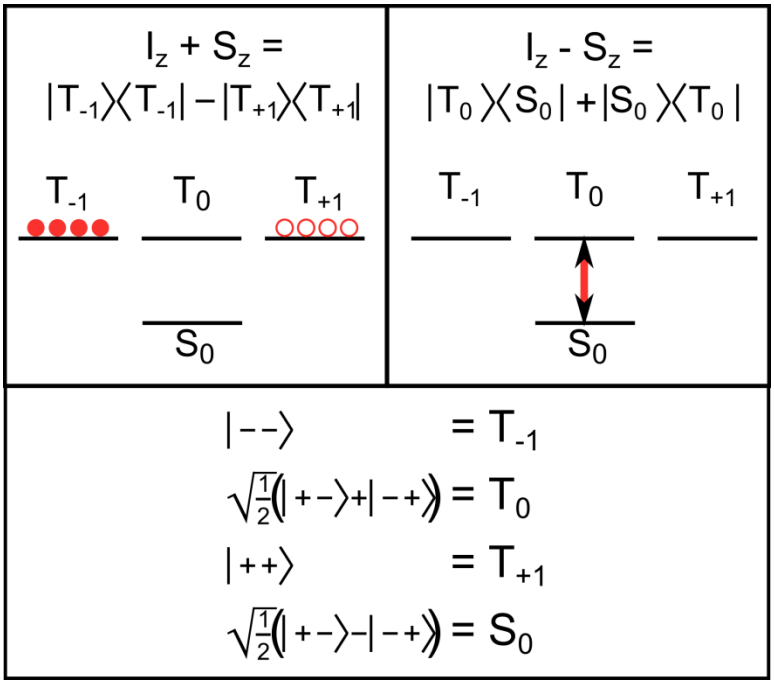

Figure 4.2 Energy level diagram of a simple *J*-coupling Hamiltonian and depiction of the I_z+S_z and I_z-S_z components of a density matrix as population and coherence respectively

As discussed in Section 3.1.3 the observable is magnetization in the z-direction (y-direction of the magnetometer). Since $\gamma_I \neq \gamma_S$, I_z-S_z bears magnetization. This magnetization is detected with the magnetometer.

The detected signal is described by a coherence between the singlet state S_0 and the central triplet state T_0. Given that this is a transition between two states, a formalism can be constructed, using matrices reminiscent of the Pauli matrices, in order to describe the observed transition: They are called zero-quantum operators describing transitions conserving m_f.

$$ZQ_x = I_xS_x + I_yS_y = \frac{1}{2}\begin{pmatrix} 0 & 0 & 0 & 0 \\ 0 & 0 & 1 & 0 \\ 0 & 1 & 0 & 0 \\ 0 & 0 & 0 & 0 \end{pmatrix}, \tag{4.5}$$

$$ZQ_y = I_yS_x + I_xS_y = \frac{1}{2}\begin{pmatrix} 0 & 0 & 0 & 0 \\ 0 & 0 & -i & 0 \\ 0 & i & 0 & 0 \\ 0 & 0 & 0 & 0 \end{pmatrix}, \tag{4.6}$$

$$ZQ_z = \frac{1}{2}(I_z - S_z) = \frac{1}{2}\begin{pmatrix} 0 & 0 & 0 & 0 \\ 0 & 1 & 0 & 0 \\ 0 & 0 & -1 & 0 \\ 0 & 0 & 0 & 0 \end{pmatrix}. \tag{4.7}$$

These operators are connected with the states represented in Figure 4.2 such that the following identities hold:

$$\begin{aligned} ZQ_x &= I_xS_x + I_yS_y = \frac{1}{2}\left(|T_0\rangle\langle T_0| + |S_0\rangle\langle S_0|\right), \\ ZQ_y &= I_yS_x - I_xS_y = \frac{1}{2}\left(i|T_0\rangle\langle S_0| - i|S_0\rangle\langle T_0|\right), \\ ZQ_z &= \frac{1}{2}(I_z - S_z) = \frac{1}{2}\left(|S_0\rangle\langle T_0| + |T_0\rangle\langle S_0|\right), \end{aligned} \tag{4.8}$$

Using these zero-quantum operators, the zero-field Hamiltonian introduced in Eq. (4.4) can be decomposed as:

$$H_{ZF} = J\,\mathbf{I}\cdot\mathbf{S} = I_xS_x + I_yS_y + I_zS_z = ZQ_x + I_zS_z. \tag{4.9}$$

The I_zS_z part of the Hamiltonian can be ignored because it commutes with $ZQ_z = I_z\text{-}S_z$, the initial density matrix. We can hence represent the Hamiltonian as ZQ_x. The initial density matrix, ZQ_z, is then in a perpendicular position to the Hamiltonian and the evolution of the density matrix can be described as rotation of the density matrix about the Hamiltonian as depicted in Figure 4.3. The evolution of the density matrix can then be calculated as:

$$\begin{aligned} \rho(t) &= \exp(-i\,J\,ZQ_x)\,ZQ_z\,\exp(i\,J\,ZQ_x) \\ &= ZQ_z\cos(J\,t) + ZQ_y\sin(J\,t). \end{aligned} \tag{4.10}$$

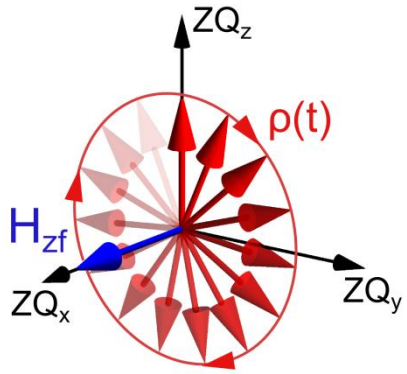

Figure 4.3 Illustration of the evolution of an initial density matrix along ZQ_z precessing about a zero-field Hamiltonian aligned with ZQ_x

The effect of the zero field Hamiltonian is hence described as inducing an oscillation between I_z-S_z magnetization and its opposite $-(I_z$-$S_z)$, via the ZQ_y term, which does not bear magnetization. The oscillation occurs at the frequency given by the *J*-coupling. For the simplest case of two spins I and S the zero-field NMR spectrum consists of one line at frequency *J*. The spectrum of ^{13}C-formic acid presents such a simple situation: One proton coupled to one carbon-13 nucleus. In Figure 4.4 the associated zero-field spectrum is shown. The observed line occurs at the frequency J = 221 Hz.

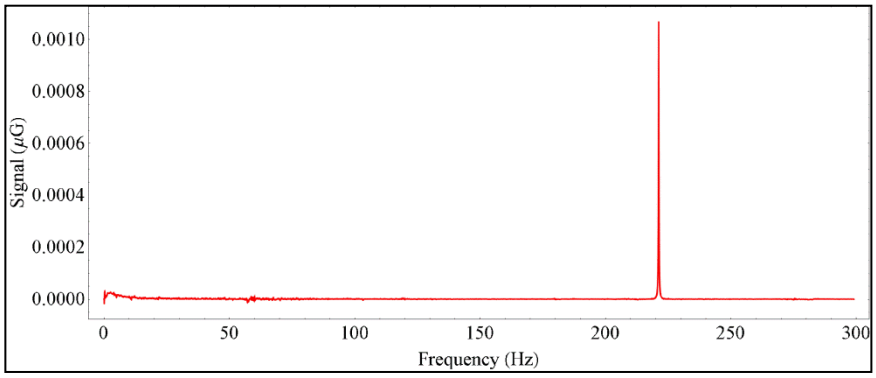

Figure 4.4 Zero-field-NMR spectrum of ^{13}C formic acid. One single peak at the frequency given by the *J*-coupling between the ^{13}C spin X and the ^{1}H spin A. J_{XA}=221 Hz.

4.2 Zero-field NMR formalism for a general spin system

For a general spin system involving an arbitrary number of coupled spins the Hamiltonian is given by:

$$\mathrm{H}_{\mathrm{ZF}} = \sum_{j,k>j} J_{j,k} \mathbf{I}_j \mathbf{I}_k . \tag{4.11}$$

The initial density matrix can be described as:

$$\rho_0 = \sum_j \gamma_j \mathrm{I}_{zj} . \tag{4.12}$$

Under the zero-field Hamiltonian this density matrix evolves according to Eq. (2.18) as

$$\rho(t) = \exp(-iH_{ZF}t)\rho(0)\exp(iH_{ZF}t), \tag{4.13}$$

and the signal is subsequently calculated as

$$s(t) = Tr\left(\rho(t) \sum_j \gamma_j \mathrm{I}_{zj} \right). \tag{4.14}$$

In cases with many spins in a molecule that constitute a complicated *J*-coupling network it is sometimes necessary to resort to numerical simulations but it will be the task of the following Sections to present an array of zero-field spectra of varying complexity and interpret in detail the observed spectral patterns without such full numerical simulations.

We present a straightforward path for the interpretation of zero-field spectra associated with spin systems commonly found in organic molecules. First, we review the interpretation of "zero-order spectra" which result when a system is determined by one single *J*-coupling constant, i.e. spin systems of one nucleus coupled, by the same *J*-coupling constant, to multiple nuclei with differing gyromagnetic ratio. We show experimental examples for such simple cases which are formic acid-[^{13}C], formaldehyde-[^{13}C] and methanol-[^{13}C]. Then we focus on the interpretation of spectra from molecules with more complex *J*-coupling networks. The experimental spectra are compared to simulated "first-order spectra" which result when the zero-order systems are perturbed by additional weaker *J*-couplings. We provide a perspective giving

insight into the underlying quantum mechanics of the problem, resulting in simple equations for the observed frequencies. Detailed discussions for five exemplary cases are given. These are methylformate-[^{13}C], formamide-[^{15}N], ethanol-[1-^{13}C], ethanol-[2-^{13}C] and glycerol-[2-^{13}C]. The first-order spectra typically agree well with the experimental data but in order to judge the accuracy of the first order description additional second order simulations are shown which are in excellent agreement with the experimental data. In previous publications the analysis of zero-field NMR spectra was restricted to the expected patterns produced by the "zero-order energy levels". This zero order approach does correctly predict the position of multiplets even for the more complex spin systems. However, within these multiplets the exact number of lines and their amplitudes was not predictable without computer based numerical calculations. The analysis presented here makes the assignment of peaks straightforward and more intuitive.

4.3 Notation of spin systems in zero-field NMR

Spin systems that can give a zero-field NMR signals consist of spins with differing gyromagnetic ratio coupled by scalar *J*-coupling. The simplest type of observed systems are XA_n groups where X is a spin with gyromagnetic ratio γ_X and A_n are equivalent spins with gyromagnetic ratio γ_A ($\neq \gamma_X$) which are coupled to X by a scalar *J*-coupling constant J_{XA}. Typically, X is either ^{15}N or ^{13}C and A_n are protons (^1H), they are however not restricted to those choices. If such a XA_n spin system is fully isolated then the "zero-order spectra" result. These spectra are simple and can be readily understood as will be reviewed in the next Section. However, in many organic molecules XA_n systems are perturbed by additional spins B_m forming $(XA_n)B_m$ spin systems, where the B_m spins also have the same gyromagnetic ratio as the A_n spins ($\gamma_B = \gamma_A$), i.e. B_m typically are additional protons. Distinguishing the spins A_n from the spins B_m is the relative strength of the *J*-coupling in these systems. The spins within the parentheses, X and A_n, are strongly coupled to one another and the spins outside the parentheses B_m weakly couple into the system acting as a perturbation. In typical organic molecules where X is either a ^{13}C or a ^{15}N nucleus and A_n and B_m are protons (^1H) the one bond coupling constants between X and A_n ranges from ~70 Hz to ~250 Hz whereas the coupling constants between X and B_m or A_n and B_m are an order of magnitude weaker and typically range between ~-20 to ~20 Hz..

This chosen nomenclature is not in agreement with the standard Pople nomenclature [73,74] used at high magnetic fields, which is based on differences in chemical shifts relative to *J*-couplings. Given that at zero magnetic field all chemical shifts vanish and even different nuclei have the same precession frequency the chosen notation seems more practical. Table 4.1 provides an overview of the nomenclature along with the letters chosen for the angular momentum of the individual groups in the spin system which become significant for the interpretation of the observed spectra discussed below.

Table 4.1. Notation for spin systems and the associated angular momenta in zero-field NMR .

Nuclear type in $(XA_n)B_m$	Spin	Angular momentum	Total angular momentum
Heteronucleus (typically ^{13}C or ^{15}N)	X	**S**(=1/2)	
n spin(s) strongly coupled to X $^1J_{XA}$>70 Hz (typically ^1H)	A_n	$\mathbf{I}_A$ = up to n×1/2	$\mathbf{S}+\mathbf{I}_A=\mathbf{F}_A$ $f_A=\lvert s-i_A\rvert...\lvert s+i_A\rvert$
m spin(s) weakly coupled to X and A ($^{\geq 2}J_{XB}$,$^{\geq 2}J_{AB}$) <20 Hz (typically ^1H)	B_m	$\mathbf{I}_B$ = up to m×1/2	$\mathbf{F}_A+\mathbf{I}_B=\mathbf{F}$ $f=\lvert f_A-i_B\rvert...\lvert f_A+i_B\rvert$

4.4 *J*-coupling spectra of XA_n systems

In this Section we provide a review of zero-field spectra resulting from pure XA_n systems on the basis of simple rules governing addition of angular momenta. This material has been covered briefly in Ref. [19]. The energy levels and frequencies arising from pure XA_n systems is what we refer to here as the "zero order" description because it does not take into consideration neighboring groups that may also couple to a XA_n system. Pure XA_n systems, consisting of one spin-1/2 nucleus, X, coupled by J_{XA} to n equivalent spin-1/2 nuclei, A_n give simple zero-field NMR spectra, provided that X and A have a differing gyromagnetic ratio.

As simple examples we show, in Figure 4.5, spectra of an XA group (^{13}C formic acid), an XA_2 group (^{13}C formaldehyde) and an XA_3 group (^{13}C methanol). Note, in most common organic molecules n rarely exceeds 3, and thus the number of lines in these systems is small. From Figure 4.5 it is apparent that the XA group produces one line at frequency J_{XA} = 221.1 Hz, the XA_2 group produces one line at 3/2 J_{XA} = 245.85 Hz and the XA_3 group produces two lines at J_{XA} = 141.0 Hz and 2 J_{XA} = 282.0 Hz respectively.

For odd n, an XA_n system produces (n+1)/2 lines at frequencies ranging from J_{XA} to (n+1)/2×J_{XA} in steps of J_{XA}. For even n, the number of lines is n/2 with frequencies ranging from 3/2 J_{XA} to (n+1)/2×J_{XA} in steps of J_{XA}.

In order to analyze the spectra let us denote the angular momentum of spin X as **S** and the angular momentum of the spins A_n as $\mathbf{I}_A$ Since X is a spin 1/2-paricle, the quantum number s equals 1/2 in all cases. Similarly, since the A_n are spin 1/2-particles, i_A ranges from 0 to n/2 in steps of 1 for even n, and from 1/2 to n/2 in steps of 1 for odd n. Lastly, let us introduce $\mathbf{F}_A$ as the sum of $\mathbf{I}_A$ and **S**, such that the associated quantum number f_A ranges from i_A+s to $|i_A$-$s|$ in integer steps. These three quantum numbers fully determine the XA_n systems. By evaluating the Hamiltonian (see Section 2.2.5) we obtain n+1 angular momentum manifolds whose energies are given by

$$E^0 = J_{XA}/2\ [f_A(f_A+1)-i_A(i_A+1)-(s(s+1)], \qquad (4.15)$$

which results in simple structure of the energy levels and their spacing. For all XA_n systems the energies range from -((J_{XA} × n/4)+1/2) to (J_{XA} × n/4) in steps

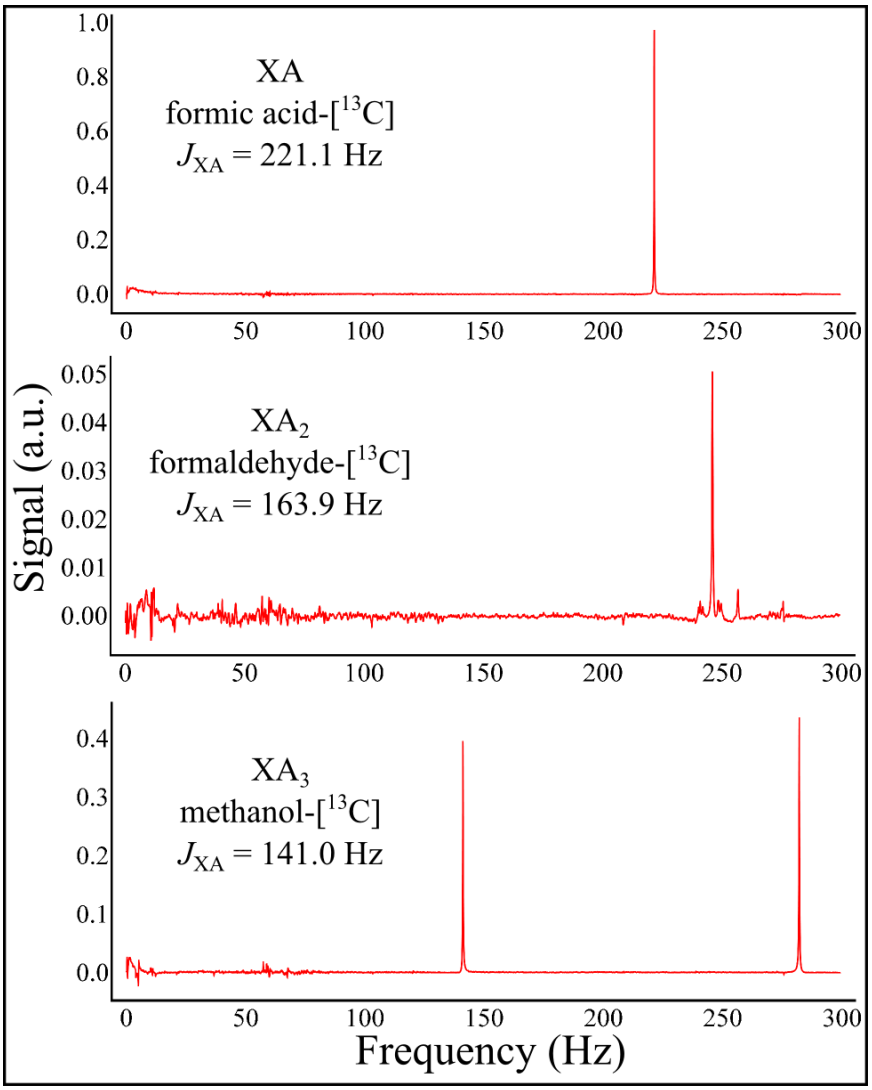

Figure 4.5 Zero-field NMR spectra of ^{13}C formic acid, ^{13}C formaldehyde and ^{13}C methanol as examples of pure XA_n systems for n=1, 2 and 3 respectively.

of $1/2J_{XA}$, however omitting -1/4 J_{XA} or -1/2 J_{XA} in the cases of odd and even n respectively.

Figure 4.6 shows the energy levels for the XA, XA_2 and XA_3 systems. The angular momentum manifolds are labeled according to their quantum numbers. Energy levels in each angular momentum manifold are labeled with their magnetic quantum number m_{fA}. n the case of XA_3 the manifolds with i_A =1/2 occurs twice because in a A_3 system consisting out of three spin one-half

particles it is possible to combine the individual spins in two different ways to obtain i_A=1/2

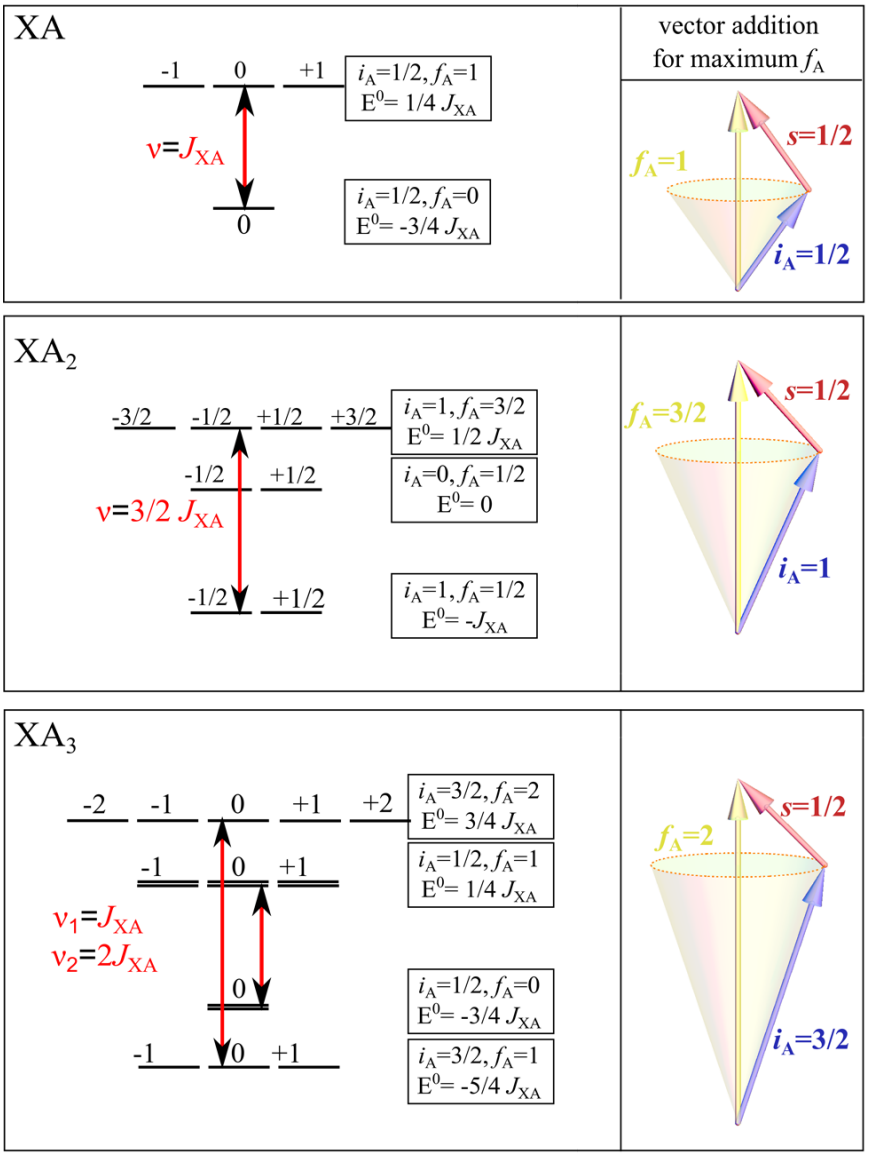

Figure 4.6 Energy level diagrams for XAn systems with n=1,2 and 3. The allowed transitions between different energy level manifolds are indicated by red arrows. Each manifold is labeled by its characteristic quantum numbers. The quantum number for *s* equa1s 1/2 in all systems under consideration and is thus omitted. Next to the energy level diagram a geometrical picture for addition of angular momentum is provided for the case of maximum f_A. The length of the depicted arrows is given as $\sqrt{(k(k+1))}$ where *k* refers to the respective quantum number.

Since the observable in these experiments is a vector operator we can derive the selection rules for transitions in these systems as:

$$\Delta i_A=0;\ \Delta s=0;\ \Delta f_A=0,\pm1 \text{ and } \Delta m_{fA} = 0. \qquad (4.16)$$

Employing these selection rules the allowed transitions are found to occur exactly at the frequencies described in the beginning of this Section (or given as $J_{XA}(f_A+1/2)$ for $f_A \geq 1/2$ where f_A ranges from 0 or 1/2 (odd vs. even n) to (n+1)/2). This analysis predicts the observations in Figure 4.5; for the XA system only one peak is expected at J_{XA}, and for the XA_2 system, only one peak is expected at 3/2 J_{XA}. For the XA_3 system, two peaks at J_{XA} and $2J_{XA}$ are expected.

The origin of the energy-level manifolds can be illustrated with a vector picture shown in Figure 4.6. $\mathbf{F}_A$ is shown as the sum of $\mathbf{I}_A$ and $\mathbf{S}$. The total angular momentum $\mathbf{F}_A$ is a conserved quantity at zero magnetic field and $\mathbf{I}_A$ and $\mathbf{S}$ oscillate about $\mathbf{F}_A$ at the frequency proportional to the respective energy. For each energy-level manifold the involved angular momenta can be represented by vectors of length $\sqrt{(k(k+1))}$, with k referring to the respective quantum number. Using these vectors, the addition of angular momenta can be represented as vector additions by arranging the vectors in a triangle such that $\mathbf{I}_A+\mathbf{S}=\mathbf{F}_A$. These representations are shown only for those manifolds with maximum f_A. The importance of this picture will become more apparent when introducing additional first-order interactions.

4.5 *J*-coupling spectra of $(XA_n)B_m$ systems

The effect of additional spins coupling into pure XA_n systems on the spectra are additional line splittings of the zero-order spectra. We will analyze typical $(XA_n)B_m$ systems to first order and compare the predictions with experimental results. Typically, it is appropriate to use a first order perturbation approach when the strength of the perturbation is at least ~10 times smaller than the zero order interaction. To zero order, the $(XA_n)B_m$ systems are determined solely by J_{XA} which is a one bond *J*-coupling constant on the order of ~100 Hz or larger. The first order interactions result from additional *J*-couplings through at least two bonds. Here, the additional coupling constants are J_{XB} and J_{AB} which typically are on the order of ~10 Hz. This situation is thus amenable to analysis with a first order approach.

4.5.1 The (XA)B system as simple example

The simplest case of a perturbed XA_n system at zero magnetic field is the (XA)B system. This system will serve as a introduction into the more general case.

Figure 4.7 a) shows a simulated spectrum of the simple (XA)B system using the following coupling constants J_{XA}=150Hz, J_{XB}=-4Hz J_{AB}=8 Hz, which are typical values in organic compounds where X is a ^{13}C nucleus and A and B are ^{1}H nuclei. The peak that, to zero order, is expected at J_{XA} = 150 Hz is now split into a doublet separated by 3/4 (J_{XB}+J_{AB}). Additionally a low frequency peak at 3/4 (J_{XB}+J_{AB}) is observed.

In order to understand the effect of the perturbing spins, let us introduce two additional quantum operators $\mathbf{I}_B$ and $\mathbf{F}$ where $\mathbf{I}_B$ is the angular momentum operator of the B_m group and $\mathbf{F}$ is the total angular momentum operator with quantum numbers f ranging from f_A+i_B to $|f_\mathbf{A}$-$i_B|$. $\mathbf{I}_B$ interacts with the projections of $\mathbf{S}$, and $\mathbf{I}_A$ onto $\mathbf{F}_\mathbf{A}$ ($\mathbf{S}_{\|}$ and $\mathbf{I}_{A\|}$) (see Section 4.6). Figure 4.7 shows a pictorial representation of the sum of $\mathbf{F}_\mathbf{A}$ and $\mathbf{I}_B$, where $\mathbf{I}_B$ and $\mathbf{F}_A$ precess about $\mathbf{F}$. To first order $\mathbf{F}_A$ is simply given as the sum of $\mathbf{S}_{\|}$ and $\mathbf{I}_{A\|}$ This can be intuitively reasoned: The precession frequencies of $\mathbf{I}_A$ and $\mathbf{S}$ about $\mathbf{F}$ is proportional toJ_{XA}, where as the precession frequencies of $\mathbf{I}_B$ and $\mathbf{F}_A$ about $\mathbf{F}$ is proportional to J_{XB}+J_{AB} which are much smaller. Therefore $\mathbf{I}_B$ only interacts with the average values of $\mathbf{S}$ and $\mathbf{I}_A$ given by $\mathbf{S}_{\|}$ and $\mathbf{I}_{A\|}$. More details are provided in the Section 4.6.

Figure 4.7 c) shows the corresponding energy level diagram for the (XA)B system.

Addition of spin B splits the zero order energy level f_A = 1 to f = 3/2 and f =1/2, and the zero order energy level f_A = 0 to to f =1/2. For f_A = 0 the total angular momentum f can only be 1/2 and for f_A=1 the total angular momentum f can have the values 3/2 or 1/2. Whenever f_A = 0, the first order energy shift are zero in general, only energy levels with f_A > 0 will be affected by the additional couplings from the B_m group. In the present case the first order energy shifts, E^1, to the f_A = 1 manifold are given as $E^1_{(F=3/2)}$ = 1/4(J_{XB}+J_{AB}) and $E^1_{(f=1/2)}$ = -1/2(J_{XB}+J_{AB}).

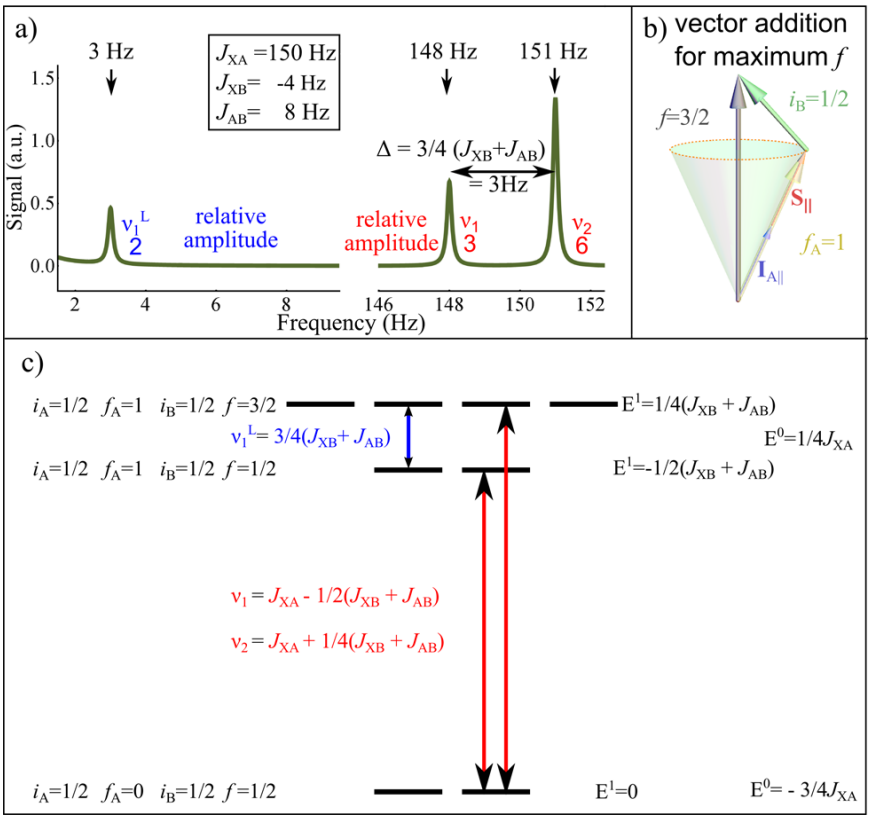

Figure 4.7 a)Simulated zero-field spectrum of a (XA)B system. The high frequency line of the pure J_{XA} spectrum is split into a doublet and a additional low frequency line is observed. b) Geometrical depiction of the addition of angular momentum I_B to the angular momentum F_A of the pure XA system, resulting in the total angular momentum F. In this illustration $S_{||}$ and $I_{||}$ represent the projections of S and I_A onto F_A. c) Energy level diagram for the (XA)B system. The observed transitions at high frequencies are shown with red arrows and the additional low frequency transition is indicated by the blue arrow. For sake of clarity transitions are only shown for one value of m_f.

The selection rules are given as

$$\Delta i_A = 0;\ \Delta i_B = 0;\ \Delta f_A = 0, \pm 1;\ \Delta f = 0, \pm 1;\ \Delta m_f = 0. \quad (4.17)$$

In the case of (XA)B all possible transitions between all angular-momentum manifolds are allowed. We thus observe the zero-order peak for which $\Delta f_A = \pm 1$ split by $3/4(J_{XB}+J_{AB})$. The relative amplitudes of the peaks are 1:2. Additionally, a peak at low frequency appears at the frequency $3/4(J_{XB}+J_{AB})$ due to $\Delta f_A = 0$ transitions between the two split $f_A=1$ manifolds. The observed transitions are depicted by arrows. Red arrows indicate high frequency lines with $\Delta f_A = 1$ and blue arrows indicate low frequency lines with $\Delta f_A = 0$. Note that transitions are always shown for one randomly chosen m_F and the remaining transitions with the same frequency are omitted to avoid overcrowding of the images.

4.5.2 First order energy shifts in $(XA_n)B_m$ systems

Having summarized the main features of the spectrum obtained from the XAB system, we can now move to a more general description of the $(XA_n)B_m$ systems and provide experimental examples that are of increased complexity.

It is possible to derive a general formula for all first order energy shifts based on the discussion above which gives access to the exact positions of all angular-momentum manifolds and hence all frequencies. Here we will attempt to make the formulas somewhat intuitive only hinting at the exact derivation, which will be the subject of a forthcoming publication. As mentioned above the zero-order energies are given by Eq. (4.15). Similarly, the first-order shifts are given by

$$E^1 = (J'_{XB} + J'_{AB})/4\ [f(f+1)-f_A(f_A+1)-(i_B(i_B+1)], \quad (4.18)$$

where J'_{XB} and J'_{AB} are given as

$$J'_{XB} = J_{XB}\,[1+\{s(s+1)-i_A(i_A+1)\}/(f_A(f_A+1))]\ , \quad (4.19)$$

and

$$J'_{AB} = J_{AB}\,[1+\{i_A(i_A+1)-s(s+1)\}/(f_A(f_A+1))]. \quad (4.20)$$

The factors modulating J_{XB} and J_{AB} can be understood as a result of the projection of $\mathbf{I}_A$ and $\mathbf{S}$ onto $\mathbf{F_A}$. This can be understood by noting that, to first order, $\mathbf{I_B}$ only interacts with these projections rather than with $\mathbf{I}_A$ and $\mathbf{S}$ directly. The degeneracy of each energy-level manifold is given by $2f+1$ and the total number of energy levels is $2^{(n+m+1)}$ where, (n+m+1) is the total number of spins in the system. The amplitude of the signal is proportional to $(\gamma_A-\gamma_X)^2$. The relative amplitudes are given by sums over Clebsch-Gordan coefficients and can be calculated as such for the general $(XA_n)B_m$ system (see Section 4.7). The relative amplitudes are given as simple ratios of small integer numbers and they are provided together with the first order simulations next to the respective peaks.

4.5.3 Analysis of selected experimental spectra

The $(XA)B_3$ system: methyl formate-[^{13}C]

Figure 4.8 a) shows the experimental spectrum of methylformate-[^{13}C], which constitutes an $(XA)B_3$ system. Plotted below the experimental spectrum are first and second spectra. In this case both the first and second order spectrum agree well with the experimental spectrum.

The *J*-coupling values used for the simulations are: J_{XA}= 226.5 Hz, J_{XB}=4.0 Hz and J_{AB}=-0.8 Hz. To zero-order one peak at 226.5 Hz is expected. This peak is split into four lines by the additional couplings J_{XB} and J_{AB}. In the present case the strong J_{XA} coupling is 70 times larger than the sum of J_{XB} and J_{AB}, hence it is not surprising that the spectrum is already reproduced excellently to first order. The angular momentum manifolds can be found starting from the facts that s=1/2, i_A=1/2 and i_B=(1/2 or 3/2). To zero-order this gives the energy diagrams of a XA system with $f_{\mathbf{A}}$=0 and $f_{\mathbf{A}}$=1, these are then perturbed by i_B=1/2 or i_B=3/2 respectively. The case of i_B=1/2 has already been fully described for the (XA)B system and, accordingly, we find peaks at all the positions as expected for the (XA)B system. These are ν_1^L at low frequency and ν_2 and ν_3 at high frequency. In addition, we observe two more peaks at high frequency (ν_1 and ν_4) and one additional low frequency peak (ν_2^L).

These additional lines (ν_1, ν_4, ν_2^L) result from the i_B=3/2 configuration which generates additional angular momentum manifolds, two of which have differing first-order energy shifts. These additional shifts are given as

E^1=-5/4(J_{XA}+J_{XB}) for f=1/2 and E^1=3/4(J_{XA}+J_{XB}) for f=5/2. Employing the selection rules as introduced in Eq. (4.17), the additional lines are found to be at frequencies J_{XA}-5/4(J_{XA}+J_{XB}) and J_{XA} + 3/4(J_{XA}+J_{XB}). The additional low-frequency line occurs at 5/4(J_{XA}+J_{XB}). The degeneracy of each manifold is given as 2f+1 but all manifolds with i_B=1/2 occur twice because in a CH_3 group there are two ways to obtain 1/2 in a sum of vectors, where as there is only one way of obtaining 3/2 for i_B when summing over three spin one-half particles.

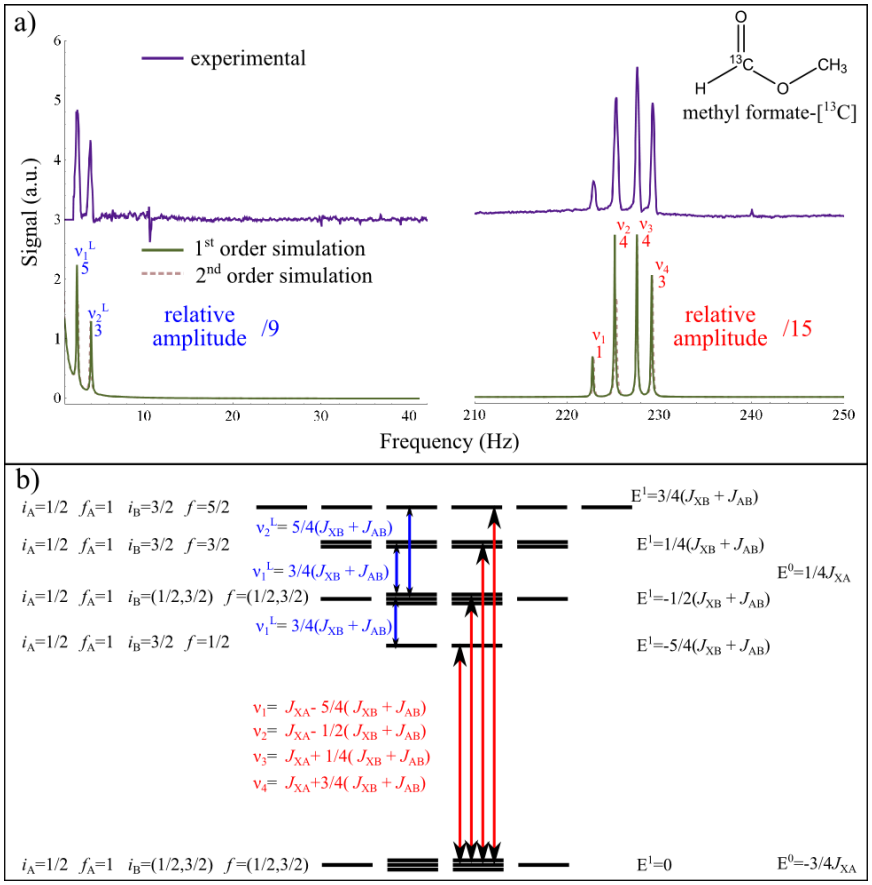

Figure 4.8. Part a) shows the experimental spectrum of a (XA)B_3 system, methyl formate-[^{13}C], together with simulations to first and second order . The high frequency line of the pure XA system occurring at J_{XA} is split into a quartet and two additional lines are observed at low frequency. Part b) provides the energy level diagram for the (XA)B_3 system. The observed transitions at high frequencies are shown with red arrows and the additional low frequency transitions are indicated by blue arrows. For sake of clarity, transitions are only shown for one value of m_F.

The $(XA_2)B$ system: formamide-[^{15}N]

Depicted in Figure 4.9 a) are the spectrum and the simulations for formamide-[^{15}N] which represents a $(XA_2)B$ system. The zero-order peak expected at 3/2 J_{XA} is split into a triplet and three additional low frequency lines are observed. All observed frequencies and amplitudes for the $(XA_2)B$ system are listed. The simulations have been calculated using the following values for the *J*-couplings: J_{XA}=89.3 Hz, J_{XB} = 13.5 Hz and J_{AB} =- 8 Hz. As can be seen from Figure 4.9 a) the second order corrections are larger in this case than in methylformate, which is caused by the smaller ratio between the strong one-bond coupling J_{XA} and the weaker long range couplings J_{XB} and J_{AB}.

The analysis can be performed quickly using the information provided thus far. The zero-order energy levels are given by a XA_2 system which has two f_A=1/2 manifolds and one f_A=3/2 manifolds. Both f_A=1/2 manifolds get split, by the perturbing spin B into two manifolds each. The total angular momentum *f* of those new manifolds are *f*=0 and *f*=1 this is in analogy to the pure XA system where two spin 1/2 particles couple together to form a singlet with *f*=0 and a triplet with *f*=1 illustrating the self-consistency of this approach. The f_A=3/2 manifold of the pure XA_2 system also is split into two manifolds with *f*=1 and *f*=2.

Recalling that the degeneracy is 2*f*+1 for these manifolds we encounter 3 and 5 degenerate levels accordingly. For the central energy levels where f_A=1/2 we do only expect a contribution from J_{XB} and none from J_{AB} because i_A = 0. In analogy to the zero-order energy levels for the XA system here the first order energy shifts are E^1=-3/4J_{XB} for the singlet and 1/4J_{XB} for the triplet. For the lowest energy levels with i_A=1 and f_A=1/2 the contribution to the energy shifts from J_{XB} and J_{AB} is unsymmetrical because $\mathbf{I}_A$ and **S** have differing projections onto $\mathbf{F}_A$. Similarly, for the highest energy levels where i_A=1 and f_A= 3/2 the projections of $\mathbf{I}_A$ and **S** onto $\mathbf{F}_A$ differ, hence the unsymmetrical contribution of J_{XB} and J_{AB} to the first order shifts. Evaluating the general formula Eq. (4.18) results in the frequencies given in Figure 4.9 b next to the depicted energy levels.

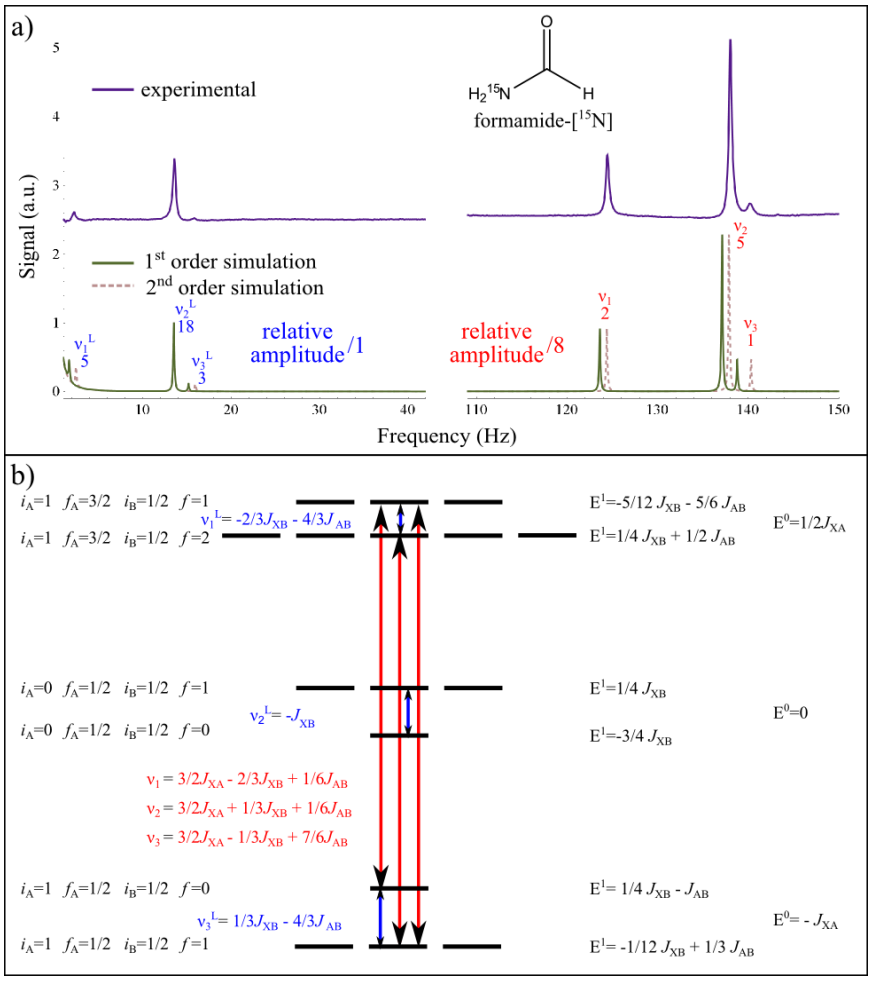

Figure 4.9. Part a) shows the experimental zero-field spectrum of a $(XA_2)B$ system, formamide-[^{15}N], together with simulations to first and second order . The high frequency line of the pure XA_2 system occurring at 3/2 J_{XA} is split into a triplet and three additional at low frequency lines are observed. Part b) provides the energy level diagram for the $(XA_2)B$ system. The observed transitions at high frequencies are shown with red arrows and the additional low frequency transitions are indicated by the blue arrows. For sake of clarity transitions are only shown for one value of m_f.

The $(XA_2)B_3$ system: ethanol-[1-^{13}C]

The spectrum of ethanol-[1-^{13}C], a $(XA_2)B_3$ system, and the respective energy diagram are shown in Figure 4.10. The *J*-couplings used to fit the spectrum are J_{XA}=141Hz, J_{XB}=-4.65 Hz and J_{AB}= 7.1Hz. The observed frequencies together with the respective amplitudes are included. The multiplet (nine lines) at high frequency occurs centered around the zero-order frequency of $3/2J_{XA}$ and seven low frequency lines are observed.

In Figure 4.10 we encounter the same energy levels and transitions as for formamide-[^{15}N] as long as i_B=1/2. The $(XA_2)B_3$ system of course also allows for i_B=3/2 resulting in further angular momentum manifolds and additional splitting. As a result of the B_3 group all manifolds with i_B=1/2 occur twice as discussed for the $(XA)B_3$ system. The energy level diagram in Figure 4.10 b) shows only transitions for i_B = 3/2 for sake of clarity. The transitions for i_B=1/2 are identical to the transitions of the $(XA_2)B$ system discussed above. Interestingly, for the central manifold with i_A=0 and f_A=1/2 the first order energy shifts still are only dependent on J_{XB} and not dependent on J_{AB} simply because i_A = 0, but also the observed pattern of two frequencies at J_{XB} and 2 J_{XB} is analogous to the situation introduced in the beginning for pure XA_3 systems where peaks appear at J_{XA} and 2 J_{XA}.

The first-order energy shifts are calculated using Eq. (4.18). By using the selection rules provided in Eq. (4.17) it becomes apparent that we obtain six lines (ν_1, ν_2, ν_4, ν_6, ν_8, ν_9) in addition to the three lines from the $(XA_2)B$ system (ν_3, ν_5, ν_7) at the high frequencies. At low frequency we obtain four lines (ν_1^L, ν_4^L, ν_5^L, ν_7^L) in addition to the three lines from the $(XA_2)B$ system(ν_2^L, ν_3^L, ν_6^L) . Note, the line at frequency $2/3J_{XB}+4/3J_{AB}$ occurs twice; once from transitions with f_A=1/2 and once from transitions with f_A=3/2. Hence we obtain a total of nine high frequency lines centered on $3/2J_{XA}$ and only seven low frequency lines. Higher order terms may split the overlapping lines.

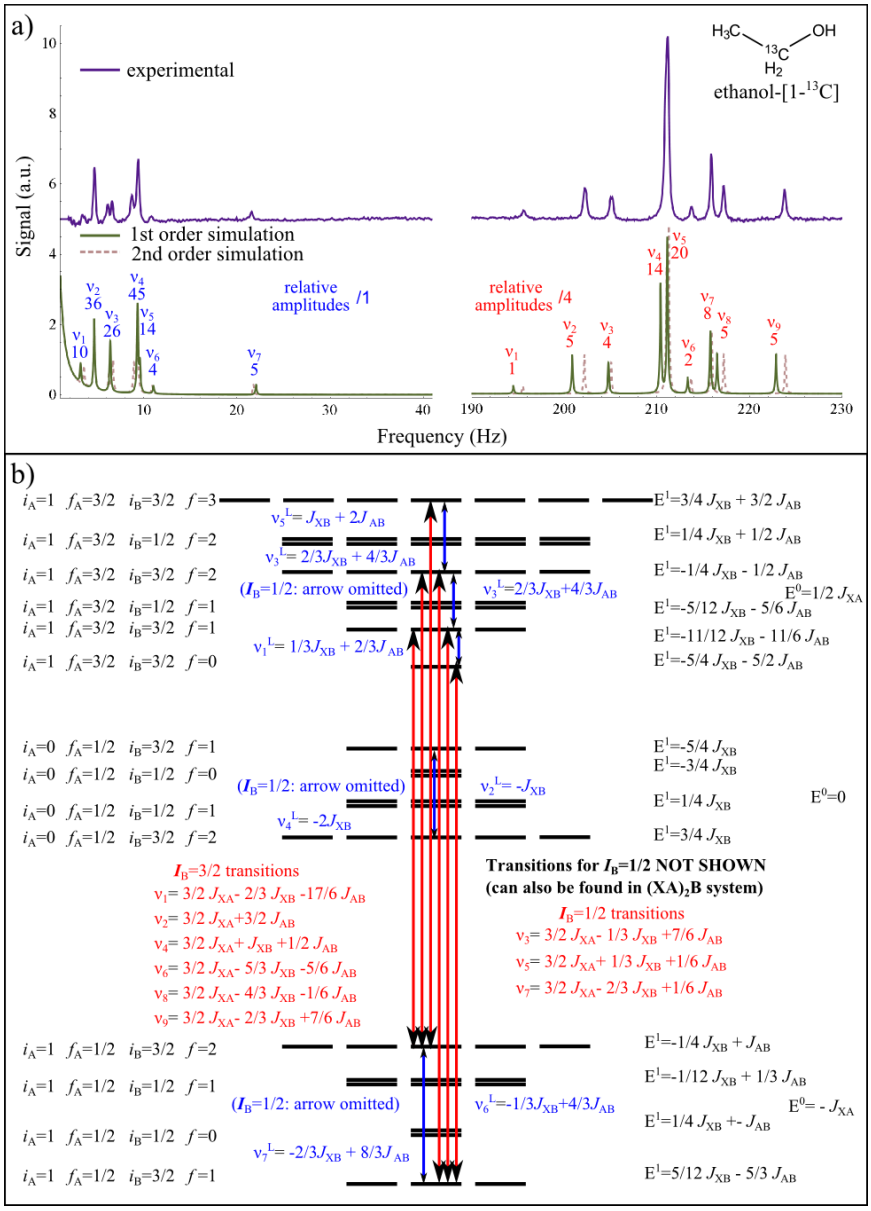

Figure 4.10. Part a) shows the experimental zero-field spectrum of a $(XA_2)B_3$ system, ethanol[1-^{13}C], together with simulations to first and second order. The relative amplitudes are given next to the peaks. The high frequency line of the pure XA_2 system occurring at 3/2 J_{XA} is split into nine lines and seven additional lines at low frequency are observed. Part b) provides the energy level diagram for the $(XA_2)B_3$ system. The observed transitions at high frequencies are shown with red arrows and the additional low frequency transitions are indicated by the blue arrows. For sake of clarity transitions are only shown for one value of m_f and transitions that have been provided for the $(XA_2)B$ system are also not displayed.

The $(XA_3)B_2$ system: ethanol-[2-^{13}C]

The next example, ethanol-[2-^{13}C], contains two high frequency multiplets. Ethanol-[2-^{13}C] constitutes a $(XA_3)B_2$ system. To zero order, two lines at J_{XA} and 2 J_{XA} are expected. These are the frequencies the observed multiplets are centered around. The spectrum and the energy-level diagram are shown in Fig 7. The *J*-couplings used to fit the spectrum are J_{XA}=125.4 Hz, J_{XB}=-2.2 Hz and J_{AB}= 7.0 Hz.

All first order energy-shifts can be calculated using Eq. (4.18) and the transitions are found applying the selection rules given in Eq. (4.17). The degeneracy of each manifold is given $2f+1$ and all manifolds with i_A=1/2 occur twice given the A_3 group. From the energy level-diagram six low frequency lines four high frequency lines around J_{XA} and seven high frequency lines around $2J_{XA}$ are expected. Experimentally we observe only 5 lines at low-frequencies because the low frequency lines (in blue) ν_3 and ν_4 are close together and overlap. The four high frequency lines around J_{XA} are all visible and well separated. This part of the spectrum is interesting also because we can claim that for a $(XA)B_2$ system this is exactly what the spectrum would look like i.e. without the multiplet centered on 2 J_{XA} . In the case of a $(XA_3)B_2$ system a multiplet centered on 2 J_{XA} does appear as shown. In the present case of ethanol-[2-^{13}C] this multiplet appears to only show four lines at first glance. The discrepancy with the theoretically predicted seven lines is due to accidental overlap of the high frequency lines (in red) ν_8 with ν_9 and lines ν_{10} with ν_{11} (see table 6); additionally the line at ν_5 has a weak relative intensity and hence barely shows, even in the simulation.

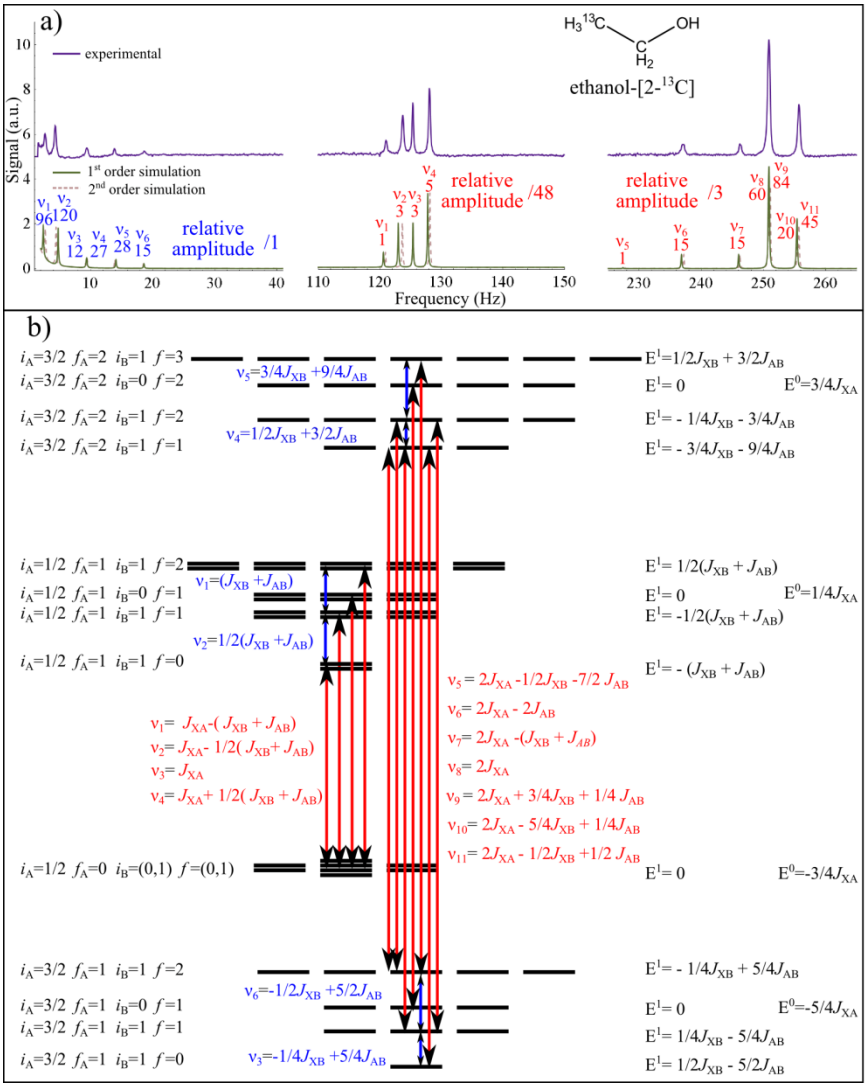

Figure 4.11 Part a) shows the experimental zero-field spectrum of a $(XA_3)B_2$ system, ethanol[2-^{13}C], together with simulations to first and second order. The relative amplitudes are given next to the peaks. The high frequency lines of the pure XA_3 system occurring at J_{XA} and 2 J_{XA} are split into four and seven lines respectively. Additionally, 6 lines at low frequency are observed. Part b) provides the energy level diagram for the $(XA_3)B_2$ system. The observed transitions at high frequencies are shown with red arrows and the additional low frequency transitions are indicated by the blue arrows. For sake of clarity transitions are only shown for one value of m_f.

The $(XA)B_4$ system: glycerol-[2-^{13}C]

Lastly we discuss a case of the spin system in glycerol-[2-^{13}C], that can be represented as a $(XA)B_4$ system despite the fact that the two CH_2 groups in glycerol are not magnetically equivalent. It appears that the coupling between the Figure 4.12 shows the experimental spectrum compared to the simulations and the appropriate energy-level diagram for a $(XA)B_4$ system. The coupling constants used in the simulations are J_{XA}=142.9 Hz, J_{XB}=-3.1 Hz and J_{AB}= 6.3Hz. The high frequency multiplet has six lines and is centered on the zero-order frequency of J_{XA}. At low frequency only three lines appear.

The first-order energy shifts are given by Eq. (4.18). All first order shifts have a symmetric contribution from J_{XB} and J_{AB} because they perturb the XA system in which case the projection of $\mathbf{S}$ and $\mathbf{I}_A$ onto $\mathbf{F}_A$ have identical lengths. The degeneracy of each manifold is $2f$+1, however some manifolds occur multiple times. In the B_4 group, manifolds with i_B = 0 occur twice, manifolds with i_B =1 occur three times and manifolds with i_B=2 occur once. This is the result of the number of possible combinations of four spin-one-half particles to obtain 0, 1 or 2 respectively. The transitions are obtained by employing the selection rules of Eq. (4.17).

Since all the f_A=0 manifolds do not experience any perturbation to first order the positions of the high-frequency peaks are easy to calculate. We obtain a transition from the f_A=0 manifolds to each of the six f_A =1 manifolds giving six lines. Additionally we obtain four low frequency lines, two of which have the same frequency to first order and overlap. These may be split due to higher order effects.

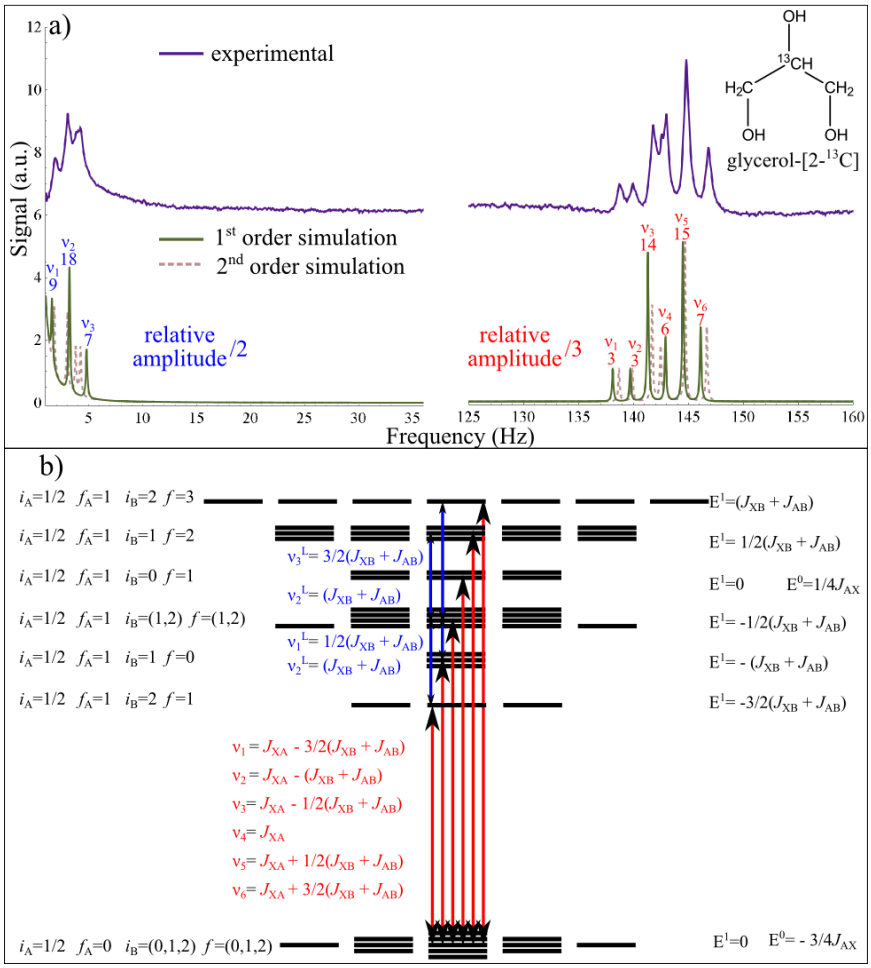

Figure 4.12 Part a) shows the experimental zero-field spectrum of a (XA)B_4 system, glycerol[2-^{13}C], together with simulations to first and second order. The relative amplitudes are given next to the peaks. The high frequency lines of the pure XA system occurring at J_{XA} is split into seven lines. Additionally, three lines at low frequency are observed. Part b) provides the energy level diagram for the (XA)B_4 system. The observed transitions at high frequencies are shown with red arrows and the additional low frequency transitions are indicated by the blue arrows. For sake of clarity transitions are only shown for one value of m_f..

4.6 Energy levels in $(XA_n)B_m$ systems to first order

The full Hamiltonian for the $(XA_n)B_m$ system can be written as

$$H=J_{XA}\,\mathbf{I}_A\cdot\mathbf{S} + J_{XB}\,J\,\mathbf{S}\cdot\mathbf{I}_B + J_{AB}\,\mathbf{I}_A\cdot\mathbf{I}_B. \tag{4.21}$$

To first order the B spins only interact with the projection of $\mathbf{I}_A$ and $\mathbf{S}$ onto $\mathbf{F}_A$, where $\mathbf{F}_A = \mathbf{I}_A+\mathbf{S}$

So we rewrite the Hamiltonian as

$$H=H_0+H_1= J_{XA}\,\mathbf{I}_A\cdot\mathbf{S} + J_{XB}\,J\,\mathbf{S}_{\|}\cdot\mathbf{I}_B + J_{AB}\,\mathbf{I}_{A\|}\cdot\mathbf{I}_B. \tag{4.22}$$

The eigenvalues of H_0 are given by Eq. (2.86) as

$$E_0 = \frac{J_{XA}}{2}[\,f_A(f_A+1) - s(s+1) - i_A(i_A+1)]. \tag{4.23}$$

The projections $\mathbf{S}_{\|}$ and $\mathbf{I}_{A\|}$ are given as

$$\begin{aligned}\mathbf{S}_{\|} &= \frac{\langle \mathbf{S}\cdot\mathbf{F}_A\rangle}{|\,\mathbf{F}_A\,|^2}\mathbf{F}_A \\ \mathbf{I}_{A\|} &= \frac{\langle \mathbf{I}_A\cdot\mathbf{F}_A\rangle}{|\,\mathbf{F}_A\,|^2}\mathbf{F}_A\,.\end{aligned} \tag{4.24}$$

Here we seek to find the eigenvalues of H_1, which are the additional first order shifts:

$$E_1 = \left\langle f, m_f \left| J_{XB}\ \mathbf{S}_{\|}\cdot\mathbf{I}_B + J_{AB}\ \mathbf{I}_{A\|}\cdot\mathbf{I}_B \right| f, m_f \right\rangle. \tag{4.25}$$

If we insert the results from Eq. (4.24) we obtain

$$\left\langle f, m_f \left| J_{XB}\ \frac{\langle \mathbf{S}\cdot\mathbf{F}_A\rangle}{|\,\mathbf{F}_A\,|^2}\mathbf{F}_A\cdot\mathbf{I}_B + J_{AB}\ \frac{\langle \mathbf{I}_A\cdot\mathbf{F}_A\rangle}{|\,\mathbf{F}_A\,|^2}\mathbf{F}_A\cdot\mathbf{I}_B \right| f, m_f \right\rangle. \tag{4.26}$$

In the following we will show, first, how to evaluate $\langle \mathbf{S}\cdot\mathbf{F}_A\rangle$ and $\langle \mathbf{I}_A\cdot\mathbf{F}_A\rangle$, and second, how to evaluate $\langle \mathbf{F}_A\cdot\mathbf{I}_B\rangle$ which then gives the first order shifts. We start from $\mathbf{F}_A=\mathbf{I}_A+\mathbf{S}$, which is rearranged as $\mathbf{I}_A=\mathbf{F}_A-\mathbf{S}$, such that

$$\mathbf{I}_A^2 = \mathbf{F}_A^2+\mathbf{S}^2-2\mathbf{S}\,\mathbf{F}_A\,, \tag{4.27}$$

which is rearranged to give

$$\mathbf{S}\,\mathbf{F}_A = 1/2\,(\mathbf{F}_A^2 + \mathbf{S}^2 - \mathbf{I}_A^2), \tag{4.28}$$

and can be used to evaluate $\langle \mathbf{S}\cdot\mathbf{F}_A \rangle$:

$$\langle \mathbf{S}\cdot\mathbf{F}_A \rangle = \frac{1}{2}(f_A(f_A+1) + s(s+1) - i_A(i_A+1)). \tag{4.29}$$

To evaluate $\langle \mathbf{I}_A\cdot\mathbf{F}_A \rangle$, similarly, we start from $\mathbf{F}_A=\mathbf{I}_A+\mathbf{S}$, which is rearranged as $\mathbf{S}=\mathbf{F}_A-\mathbf{I}_A$, such that

$$\mathbf{S}^2 = \mathbf{F}_A^2 + \mathbf{I}_A^2 - 2\mathbf{I}_A\,\mathbf{F}_A, \tag{4.30}$$

which is rearranged to give

$$\mathbf{I}_A\,\mathbf{F}_A = 1/2\,(\mathbf{F}_A^2 + \mathbf{I}_A^2 - \mathbf{S}^2), \tag{4.31}$$

and allows us to obtain

$$\langle \mathbf{S}\cdot\mathbf{F}_A \rangle = \frac{1}{2}(f_A(f_A+1) + i_A(i_A+1) - s(s+1)). \tag{4.32}$$

Evaluation of $\langle \mathbf{F}_A\cdot\mathbf{I}_B \rangle$ proceeds in analogy to the equations presented in Section 2.2.5

$$\mathbf{F}^2 = (\mathbf{F}_A+\mathbf{I}_B)^2 = \mathbf{F}_A^2 + \mathbf{I}_B^2 + 2\mathbf{F}_A\cdot\mathbf{I}_B, \tag{4.33}$$

we can rearrange to obtain

$$\mathbf{F}_A\cdot\mathbf{I}_B = \frac{1}{2}(\mathbf{F}^2 - \mathbf{F}_A^2 - \mathbf{I}_B^2), \tag{4.34}$$

now we obtain the eigenvalues given in terms of the quantum numbers as

$$\langle \mathbf{F}_A\mathbf{I}_B \rangle = \frac{1}{2}(f(f+1) - f_A(f_A+1) - i_B(i_B+1)). \tag{4.35}$$

Combining the results from Eq. (4.29) (4.32) (4.35) and $|\mathrm{F_A}|^2 = f_A(f_A+1)$ into Eq. (4.26) gives the first order energies in terms of the quantum numbers:

$$E_1 = \frac{1}{2}(f(f+1) - f_A(f_A+1) - i_B(i_B+1)) \times \left[J_{XB} \frac{f_A(f_A+1) + s(s+1) - i_B(i_B+1)}{2 f_A(f_A+1)} + J_{AB} \frac{f_A(f_A+1) + i_B(i_B+1) - s(s+1)}{2 f_A(f_A+1)} \right], \quad (4.36)$$

which is simplified as

$$E_1 = \frac{J'_{XB} + J'_{AB}}{4}(f(f+1) - f_A(f_A+1) - i_A(i_A+1)),$$

where

$$J'_{XB} = J_{XB}\left(1 + \frac{s(s+1) - i_A(i_A+1)}{f_A(f_A+1)}\right) \quad (4.37)$$

$$J'_{AB} = J_{AB}\left(1 + \frac{i_A(i_A+1) - s(s+1)}{f_A(f_A+1)}\right),$$

giving a general formula for the first order shifts as a function of the quantum numbers.

4.7 Amplitudes and selection rules in $(XA_n)B_m$ systems

The amplitude of a specific transition is given as

$$\mathrm{A} = \left\langle s, i_\mathrm{A}, f_\mathrm{A}, i_\mathrm{B}, f, m_f \left| \sum_k \gamma_k \mathrm{I}_{kz} \right| s, i_\mathrm{A}, f_\mathrm{A}', i_\mathrm{B}, f', m_f' \right\rangle^2 . \tag{4.38}$$

This can be expressed in the uncoupled basis using Clebsch-Gordan coefficients as

$$\begin{aligned} \mathrm{A} = \sum_{m_s, m_{i_\mathrm{A}} m_{i_\mathrm{B}} m_s', m_{i_\mathrm{A}}' m_{i_\mathrm{B}}'} & C^{f m_f}_{f_\mathrm{A} m_{f_\mathrm{A}} i_\mathrm{B} m_{i_\mathrm{B}}} C^{f_\mathrm{A} m_{f_\mathrm{A}}}_{s m_s i_\mathrm{A} m_{i_\mathrm{A}}} C^{f' m_f'}_{f_\mathrm{A}' m_{f_\mathrm{A}}' i_\mathrm{B} m_{i_\mathrm{B}}} C^{f_\mathrm{A}' m_{f_\mathrm{A}}'}_{s m_s i_\mathrm{A} m_{i_\mathrm{A}}} \times \\ & \left\langle s m_s, i_\mathrm{A} m_{i_\mathrm{A}}, i_\mathrm{B} m_{i_\mathrm{B}} \left| \sum_k \gamma_k \mathrm{I}_{kz} \right| s m_s', i_\mathrm{A} m_{i_\mathrm{A}}', i_\mathrm{B} m_{i_\mathrm{B}}' \right\rangle^2 , \end{aligned} \tag{4.39}$$

which we can know evaluate using

$$\sum_k \gamma_k \mathrm{I}_{kz} \left| s m_s, i_\mathrm{A} m_{i_\mathrm{A}}, i_\mathrm{B} m_{i_\mathrm{B}} \right\rangle = (\gamma_S m_s + \gamma_I m_{i_\mathrm{A}} + \gamma_I m_{i_\mathrm{B}}) \left| s m_s, i_\mathrm{A} m_{i_\mathrm{A}}, i_\mathrm{B} m_{i_\mathrm{B}} \right\rangle, \tag{4.40}$$

to give

$$\mathrm{A} = \left(\sum_{m_s, m_{i_\mathrm{A}} m_{i_\mathrm{B}}} C^{f m_f}_{f_\mathrm{A} m_s + m_{i_\mathrm{A}} i_\mathrm{B} m_{i_\mathrm{B}}} C^{f_\mathrm{A} m_s + m_{i_\mathrm{A}}}_{s m_s i_\mathrm{A} m_{i_\mathrm{A}}} C^{f' m_f'}_{f_\mathrm{A}' m_s + m_{i_\mathrm{A}} i_B m_{i_\mathrm{B}}} C^{f_\mathrm{A}' m_s + m_{i_\mathrm{A}}}_{s m_s i_\mathrm{A} m_{i_\mathrm{A}}} (\gamma_S m_s + \gamma_I (m_{i_\mathrm{A}} + m_{i_\mathrm{B}})) \right)^2 . \tag{4.41}$$

From this it is apparent that $\Delta s = \Delta i_\mathrm{A} = \Delta i_\mathrm{B} = \Delta \mathrm{m}_s = \Delta \mathrm{m}_{i\mathrm{A}} = \Delta \mathrm{m}_{i\mathrm{B}} = 0$. Additionally, the amplitude A is only non-zero for $\Delta f = f - f' = 0, \pm 1$ and $\Delta m_f = m_f - m_f' = 0$. Which constitute the additional selection rules.

4.8 Ultra narrow lines in zero-field NMR

In this Section we confine our attention on the linewidths that can be observed in zero-field NMR spectroscopy. In typical superconducting high-field NMR spectrometers NMR linewidths of ~0.5 Hz are typical and large amounts of efforts are necessary to improve resolution by using shim coils of multiple orders. In zero-field NMR the magnetic field inside the shields can be easily reduced to the μG level using one simple coil for each of the three spatial directions (x,y and z) The requirements on the coils are low and they can be configured as solenoids, Helmholtz or saddle coils. Once the μG level is reached readjustments are typically not necessary since there are no field drifts as experienced in high-field NMR and measurements are typically not limited by field inhomogeneties. (One μG corresponds to 4.2 mHz proton frequency)

In the following we show multiple examples of zero-field spectra and fit the observed peaks to a complex Lorentzian of the form:

$$\frac{\mathrm{a}}{\mathrm{d}\nu + i\,(\nu\text{-}\nu_0)}\, e^{i\varphi}, \tag{4.42}$$

in order to determine the linewidth and the peak position. The important fitting parameters are the frequency ν_0 and the width dν (The phase, φ, is close to zero in all plots and the amplitude is a non-important trivial fitting parameter that will not be reported in this context)

We begin by analyzing the individual peaks of the spectra presented in Figure 4.5 acquired from ^{13}C formic acid, ^{13}C formaldehyde and ^{13}C methanol. As depicted in Figure 4.13 for formic acid we obtain, for the peak centered at $\nu=J_{XA}$ = 221.181 Hz, a "Half Width at Half Maximum" (HWHM) = dν of 27 mHz corresponding to a decay rate of 5.9 s.

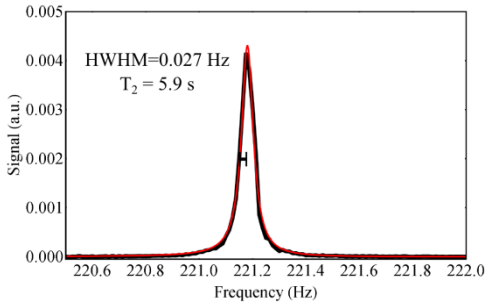

Figure 4.13 Zero-field-NMR spectrum of ^{13}C-formic acid (black trace) and a Lorentzian fit to the observed peak (red trace). The fitting parameters resulted as dν = 27 mHz and ν_0 = 221.181 Hz

Next, in Figure 4.14 the peak produced by ^{13}C-formaldehyde centered at $3/2J_{XA}$= 245.789 Hz is shown fit to a Lorentzian with a HWHM=0.051 Hz corresponding to a decay rate of 3.1s

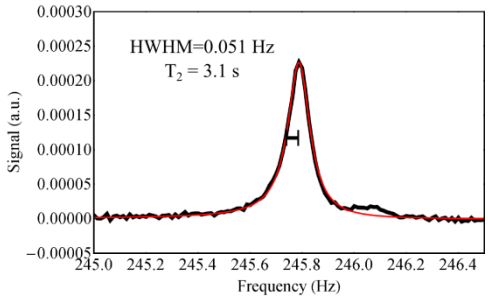

Figure 4.14 Zero-field-NMR spectrum of ^{13}C-formaldehyde (black trace) and a Lorentzian fit to the observed peak (red trace). The fitting parameters resulted as dν = 51 mHz and ν_0 = 245.789 Hz

The ^{13}C Methanol sample produces two peaks centered at J_{XA}= 140.975 and 2 J_{XA}= 281.951 Hz. Note that the frequencies of J_{XA} and $2J_{XA}$ are fit to independent Lorentzians resulting with exactly a 1:2 ratio in frequencies, confirming that the *J*-coupling constants can be determined down to the mHz level using simple 1D zero-field NMR.

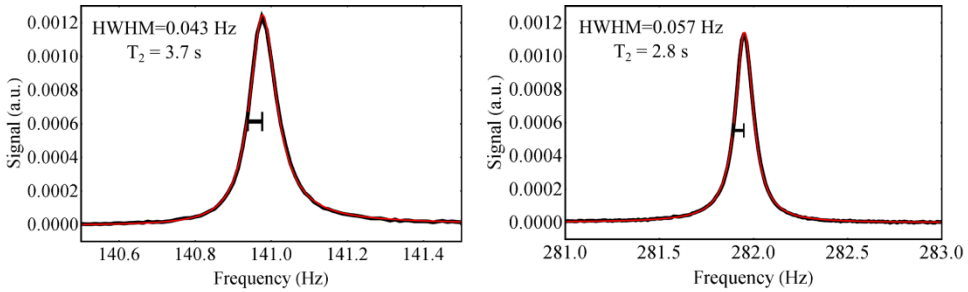

Figure 4.15 Zero-field-NMR spectrum of ^{13}C-methanol (black trace) and a Lorentzian fit to the observed peaks (red trace). The fitting parameters resulted as $d\nu_1$ = 43 mHz, ν_{01} = 140.975 Hz, $d\nu_2$ = 57 mHz and ν_{02} = 281.951 Hz

Similarly to spectra from ^{13}C-methanol, we show in Figure 4.16 spectra from ^{13}C acetic acid yielding two peaks at J_{XA} = 129.502 and 2 J_{XA} =259.004. Again, for the peak at J_{XA} exactly half the frequency of the peak at 2 J_{XA} is obtained, down to the mHz level,

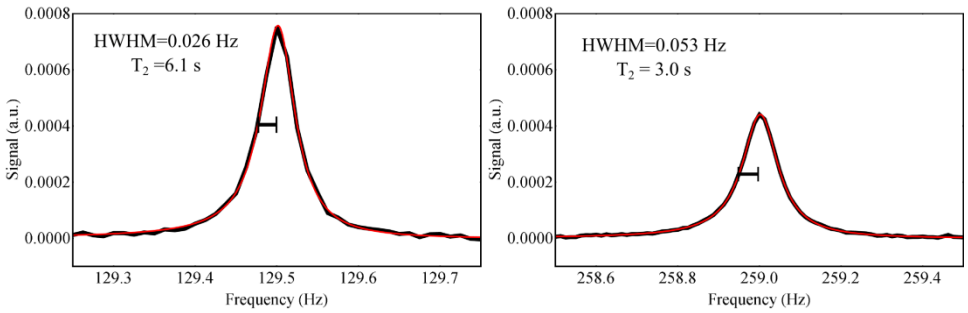

Figure 4.16 Zero-field-NMR spectrum of ^{13}C-2-acetic acid (black trace) and a Lorentzian fit to the observed peaks (red trace). The fitting parameters resulted as $d\nu_1$ = 26 mHz, ν_{01} = 129.502 Hz, $d\nu_2$ = 53 mHz and ν_{02} = 259.004Hz

Interestingly, for both, the ^{13}C-methanol spectrum, as well as, for the ^{13}C-acetic acid spectrum the peaks at J_{XA} are slightly narrower than the peaks at 2 J_{XA}. There are different mechanisms that could be responsible for this broadening. First, the line at J_{XA} results from a coherence between the singlet state (f_A=0) and a triplet state (f_A=1), as depicted in Figure 4.2. The line at 2J_{XA} results from a coherence between a triplet state (f_A=1) and a quintet state (f_A=2), also shown in Figure 4.2. It is known from the literature that singlet

states are protected from some intermolecular relaxation mechanisms, thereby having increased lifetimes.[75–82] In the context of zero-filed-NMR, these effects remain under current investigation.

Second, a non-zero magnetic field can cause individual lines to split as will be described extensively in the following Chapter. For the present discussion it shall suffice to say, that the lines at J_{XA} associated with $f_A=0\leftrightarrow f_A=1$ transitions split into two lines, whereas, the lines at $2J_{XA}$ associated with $f_A=1\leftrightarrow f_A=2$ transitions split into six lines with a larger separation than the lines at J_{XA}, thus a small magnetic field would cause a similar effect, broadening the lines at J_{XA} less than the lines at $2J_{XA}$.

To demonstrate this effect we purposefully applied a magnetic field splitting the NMR lines as demonstrated in Figure 4.16. As can be seen the line of ^{13}C formic acid at J_{XA} is split into two lines of reduced linewidths with HWHM = 0.017Hz and 0.015 Hz. This suggests that some of the broadening observed in Figure 4.16 can be reduced even further by adjustments to the magnetic field. As mentioned, the details of these broadening effects remain under investigation.

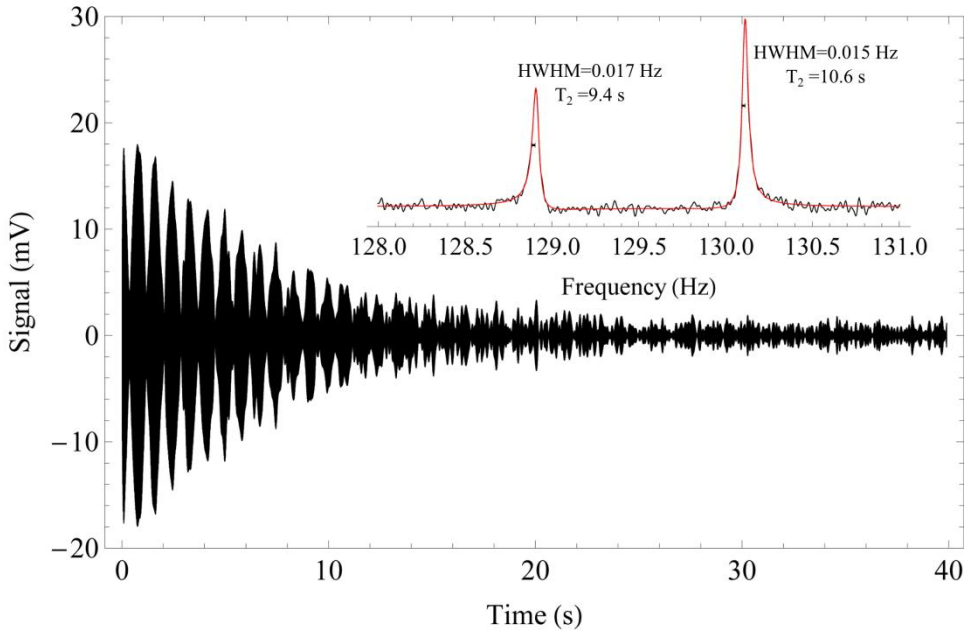

Figure 4.17 Zero-field-NMR FID and its Fourier transform of ^{13}C-2-acetic acid (black trace) and a Lorentzian fit to the observed peaks (red trace). The fitting parameters resulted as $d\nu_1$ = 17 mHz, $d\nu_2$ = 15 mHz for the peaks centered around J_{XA}=129.502 Hz split by a magnetic field.

Lastly, we show, in Figure 4.18, that if the magnetic field is adequately reduced, linewidths close to 10 mHz can be obtained. A zero-field NMR spectrum of singly ^{13}C-labeled benzene is provided. The acquired lines have linewidths of down to 11 mHz corresponding to signal decay times of 14.5 s. Below the experimental spectrum a numerical simulation of the spectrum is shown clearly identifying the compound. In the simulation a decay rate of 15 s was used producing good agreement with the experimental spectrum. More details concerning these measurements and the simulations will be provided in a forthcoming publication by Blanchard et al.

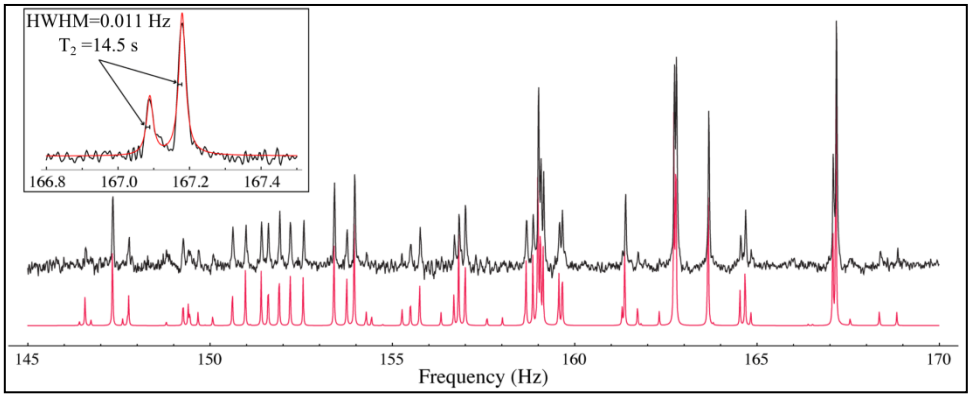

Figure 4.18 Zero-field-NMR spectrum of singly ^{13}C labeled benzene (black trace) and simulation thereof (red trace below). The inset shows two peaks appearing around 167.1 Hz together with a fit to these peaks (red trace). The HWHM resulted as dν = 11 mHz.

4.9 Significance of zero-field NMR for chemical analysis

This contribution provides a tool to analyze zero-field NMR spectra in a methodological and straightforward way without having to resort to non-intuitive full numerical calculations. The presented method of analysis is based on a first-order perturbation approach that results in simple equations for the positions of peaks in given spins systems. The knowledge of the peak positions allows for assignment of peaks to the respective chemicals. For mixtures of chemicals only small amounts of overlap is expected given the excellent resolution, on the order of tens of mHz, in zero-field NMR, plus the large variations in one-bond coupling constants, which spread the observed multiplets widely. Since zero-field NMR is emerging as a cost effective, potentially miniaturizable type of NMR the successful interpretation of the obtained spectra is another key ingredient to make this modality of NMR attractive for applications ranging from bench-top chemical analysis to sample analysis in spaces previously not accessible by traditional NMR.

5. Near-zero-field NMR: the Zeeman field as perturbation

Here, we examine, experimentally and theoretically, the effects of small magnetic fields in near-zero-field NMR. This work has been previously published under the title "Near-Zero-Field Nuclear Magnetic Resonance" by the American Physical Society[28]. In this contribution we show that application of weak magnetic fields results in splitting of the zero-field lines, restoring information about gyromagnetic ratios that is lost in zero-field NMR. In the regime where the Zeeman effect can be treated as a perturbation, we observe high-resolution spectra with easy-to-understand splitting patterns that are in good qualitative and quantitative agreement with first-order perturbation theory. This work forms the basis for a new type of NMR spectroscopy that serves as a complement to high-field NMR, where heteronuclear couplings are almost always treated as a small perturbation to the much larger Zeeman interaction. We also examine the case in which the Zeeman energies are comparable to the *J*-coupling energies, resulting in spectra of maximal complexity. Finally, we note that operating near zero field has two additional consequences. It enables us to take advantage of the spin-exchange relaxation-free (SERF) regime[23], and it facilitates efficient coupling between the nuclear spins and the magnetometer's alkali spins by approximately matching the Larmor resonance frequencies of the two species, without resorting to the use of a solenoid as described in the literature.[8,11,15]

5.1 Pure XA_N systems perturbed by a weak magnetic field

The Hamiltonian in the presence of *J* couplings and a magnetic field is $H = \sum_{j;k>j} J_{jk}\mathbf{I}_j \cdot \mathbf{I}_k - \sum_j \gamma_j \mathbf{I}_j \cdot \mathbf{B}$. Here $\mathbf{I}_j$ represent both like and unlike spins with gyromagnetic ratio γ_j and J_{jk} is the scalar coupling between spins j and k. The effects of dipole-dipole interactions are ignored here, as we work in an isotropic liquid state, although they are responsible for relaxation. In the absence of magnetic fields, the spherical symmetry of the Hamiltonian dictates that eigenstates $|\phi_a\rangle$ are also eigenstates of $\mathbf{F}^2$ and F_z, where **F** is the total angular momentum. $\mathbf{F} = \sum_j \mathbf{I}_j$ with energy E_a, and degeneracy $2f+1$. Application of a magnetic field B_z lifts this degeneracy, splitting the zero-field NMR lines. We first examine the effects of small magnetic fields on a $^{13}CH_N$ system, with N equivalent protons, using perturbation theory. In zero field, the unperturbed energy levels are given as described in Chapter 2 Section 2.2.5

$$E(f, i_A) = J/2[f(f+1) - i_A(i_A+1) - s(s+1)], \tag{5.1}$$

where i_A = 1/2; 1; 3/2,... are the possible spin quantum numbers of the operator $\mathbf{I}_A$ describing the sum of the equivalent proton spins, and s = 1/2 is the spin quantum number associated with the operator **S**, representing the ^{13}C spin. To first order in B_z, eigenstates are those of the unperturbed Hamiltonian, and Zeeman shifts of the eigenvalues can be read from the diagonal matrix elements of the Zeeman perturbation. One finds

$$\begin{aligned}\Delta E(f, i_A, m_f) &= -\left\langle f, m_f \left| B_z(\gamma_H I_{Az} + \gamma_C S_z \right| f, m_f \right\rangle \\ &= -B_z \sum_{m_{fA}, m_s} \left\langle i_A\, s\, m_{i_A}\, m_s \middle| f\, m_f \right\rangle^2 \left(\gamma_H m_{i_A} + \gamma_C m_s\right).\end{aligned} \tag{5.2}$$

Here γ_H and γ_C are the proton and ^{13}C gyromagnetic ratios, and $\left\langle f_A\, s\, m_{i_A}\, m_s \middle| f\, m \right\rangle$ are the Clebsch-Gordan coefficients. The observable in our experiment is the total x magnetization, $M_x(t) \propto \mathrm{Tr}\left(\rho(t)\sum_j I_{jx}\gamma_j\right)$ where ρ(t) is the time dependent density matrix. Writing I_{jx} in terms of the raising and lowering operators, we obtain selection rules for observable coherences: Δf =

0, ±1 and $\Delta m_f = \pm 1$ valid in the limit where $|\gamma_j B| << |J|$. In the case at hand, with N equivalent protons, there is an additional selection rule, $\Delta i_A = 0$, since, in the absence of chemical shifts, the Hamiltonian commutes with $\mathbf{I}_A^2$. Experimentally, we examine the case of N = 1 and N = 3. In the former case, i_A 1/2 , the zero-field levels are a singlet with $f = 0$ and a triplet with $f = 1$. In the presence of a small magnetic field, the singlet level is unperturbed, while the triplet levels split, as shown by the manifolds on the left of Figure 5.1. In the following, $\nu_{f,m_f}^{f',m_f'}$ denotes the frequency of transitions between the states $\left| f, m_f \right\rangle$ and $\left| f', m_f' \right\rangle$. Employing Eq. (5.1) and the selection rules, one finds a single line for transitions with $\Delta f = 0$ between states with $f = 1$, and a doublet for transitions with $\Delta f = \pm 1$ between states with $f = 1$ and $f = 0$:

$$\nu_{1,m_f}^{1,m_f \pm 1} = B_z(\gamma_H + \gamma_C)/2, \tag{5.3}$$

$$\nu_{0,0}^{1,\pm 1} = J \pm B_z(\gamma_H + \gamma_C)/2. \tag{5.4}$$

For the case of N = 3, i_A is either 1/2 or 3/2. The $i_A = 1/2$ transition frequencies are given by Eqs. (5.3) and (5.4) and. The $i_A = 3/2$ manifolds are shown on the right of Figure 5.1, and coherences between $\left| f = 1, m_f \right\rangle$ and $\left| f = 2, m_f \pm 1 \right\rangle$ occur at frequencies given by

$$\nu_{1,m_f}^{2,m_f \pm 1} = 2J + m_f \frac{B_z}{4}(-7\gamma_H + 6\gamma_C) \pm \frac{B_z}{4}(3\gamma_H + \gamma_C). \tag{5.5}$$

There are two additional transitions for states with $f_A = 3/2$ with $\Delta f = 0$ that occur near zero frequency,

$$\nu_{2,m_f}^{2,m_f \pm 1} = \frac{B_z}{4}(3\gamma_H + \gamma_C); i_A = 3/2, \tag{5.6}$$

$$\nu_{1,m_f}^{1,m_f \pm 1} = \frac{B_z}{4}(5\gamma_H - \gamma_C); i_A = 3/2. \tag{5.7}$$

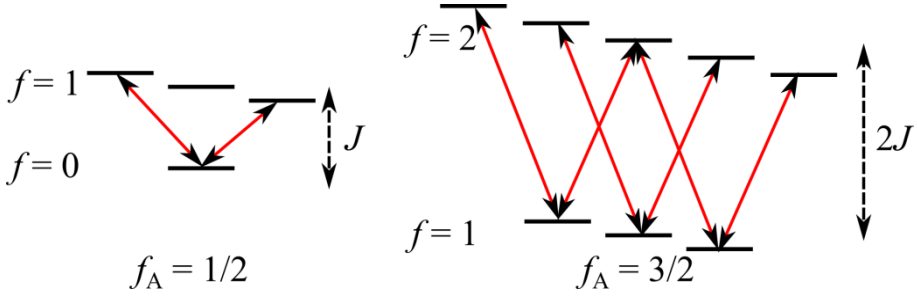

Figure 5.1 Energy levels for a $^{13}CH_3$ group (both left and right). Energy levels for a ^{13}CH group are given by the manifold on the left only.

Equations (5.3) – (5.7) constitute a set of 11 transitions, three appearing near zero frequency, two near J, and six near $2J$, representing the near-zero-field NMR spectrum of a $^{13}CH_3$ group. These calculations are discussed in more depth in the Section 5.4.1, and in Ref. [22].

We now make two observations. (1) Even in more complex molecules with additional nonequivalent spins, the zero-field eigenstates are also those of $\mathbf{F}^2$ and F_z. Therefore, the near-zero-field splitting patterns can be used to identify the angular momenta of the states involved in the zero-field transitions. Transitions between levels with f = 0 and 1 will produce doublets, transitions between levels with f = 1 and 2 will produce a multiplet with six lines, and so on. (2) The selection rules presented here break down as the magnetic field becomes large enough to produce significant mixing of the zero-field eigenstates. Reference [22] shows theoretically that the maximum number of lines for a $^{13}CH_N$ group is $(N+1)^2$, most clearly visible when $|(\gamma_H + \gamma_C)B_z| \approx J$.

5.1.1 Experimental configuration for near-zero-field NMR

Experiments were performed using an apparatus similar to that of Refs. [19,21] and depicted in Figure 5.2. Samples (typically ≈ 200 μL) were contained in a 5 mm NMR tube, and pneumatically shuttled between a 1.8-T prepolarizing magnet and a magnetically shielded enclosure, housing a microfabricated ^{87}Rb vapor cell, the central component of the atomic magnetometer. The cell is optically pumped by z-directed, circularly polarized laser light, tuned to the center of the D1 transition, and probed by y-directed, linearly polarized light, tuned about 100 GHz to the blue of the D1 transition. Optical rotation of the probe light is monitored by a balanced polarimeter. Bias fields and dc pulses of magnetic field, used to excite NMR spin coherences, are applied via a set of coils. At zero field, the magnetometer is primarily sensitive to fields in the x direction with a noise floor of about 40 – 50 fT/√Hz. As the bias field is increased, the magnetometer response moves to higher frequencies, compromising the low- frequency sensitivity by about a factor of 5 for B_z = 3 mG.

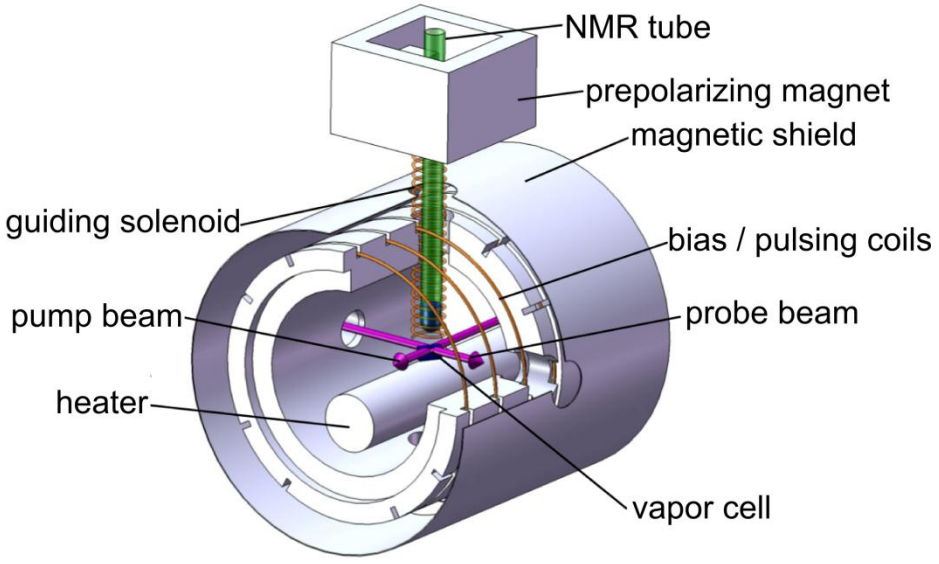

Figure 5.2 Experimental setup for near-zero-field spectroscopy, described in the text.

To maintain a quantization axis during transit of the sample, a solenoid provides a "guiding field". The guiding field is turned off suddenly prior to acquisition of data, and a pulse applied in the z direction, with area such that the proton spins rotate through 4 π and the carbon spins rotate through π (about 480 μs), maximizing the amplitude of zero-field signals. Zero-field and near-zero-field spectra for formic acid ($H^{13}COOH$) are shown in Figure 5.3, each resulting from the average of eight transients. The zero-field spectrum consists of a single line at J = 222 Hz , as well as a dc component, suppressed here for clarity.

The near-zero-field spectrum arising from the 13CH group is as discussed above: a doublet with frequencies $J \pm B_z (\gamma_H + \gamma_C)/2$ and an additional line at $B_z (\gamma_H + \gamma_C) \approx 4{:}7$ Hz. The large peak at 7.5 Hz corresponds to the uncoupled OH group. The asymmetry in the doublet centered about J, reproduced by a full numerical calculation, is due to higher-order corrections to the eigenstates. The peaks are well described by Lorentzians, with half width at half maximum ≈ 0.1 Hz , and the locations of the peaks can be determined with a statistical

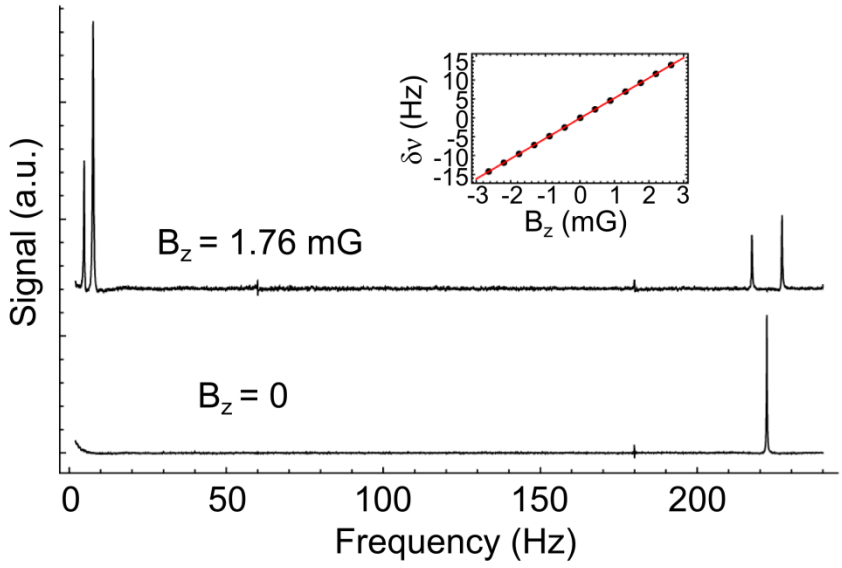

Figure 5.3 ZF and NZF spectra for 13 C labeled formic acid, $H^{13}COOH$. The inset shows the splitting of the two lines centered about J as a function of magnetic field.

uncertainty of about 1 mHz (estimated from the scatter of measurements obtained from the eight single transients in each data set). The splitting of the line at *J* as a function of magnetic field is shown inset, displaying a linear dependence. The slope is in agreement with that predicted by Eq. (5.4), ($\gamma_H + \gamma_C$), at the level of about 0.1%.

To illustrate the case of a $^{13}CH_3$ system, zero-field and near-zero-field spectra for acetonitrile-2 ($^{13}CH_3CN$) are shown in Figure 5.4. For $B_z = 0$, the spectrum consists of a zero-frequency peak, a peak at *J*, and a peak at 2*J*. Application of a magnetic field splits the zero-frequency peak into three lines, whose frequencies are given by Eqs. (5.3), (5.6) and (5.7). The smallest peak at 11.2 Hz corresponds to an uncoupled proton due to an unknown solvent in the sample (likely water). The line at *J* splits into a doublet, whose frequencies are given by Eq. (5.4), and the line at 2*J* splits into six lines, whose frequencies are given by Eq. (5.5). The splitting of the lines at *J* and 2*J* clearly reveals the degeneracy of the zero-field levels. As with the formic acid spectrum, there is some asymmetry present in the multiplets centered about *J* and 2*J*, which is reproduced by

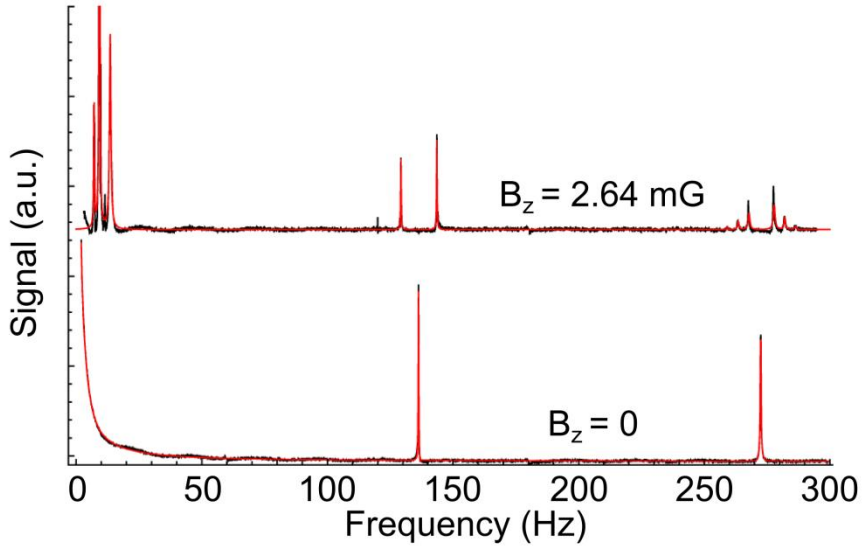

Figure 5.4 Spectra for singly labeled acetonitrile-2, $^{13}CH_3CN$ in zero field and in a field of 2.64 mG. The smooth trace overlaying each data set is a fit described in the text.

numerical simulation. Nevertheless, the relative amplitudes of the lines centered about 2*J* are roughly in the ratio 1:3:6:6:3:1 as expected from first-order perturbation theory (Section 5.4 [27]). Line positions are in excellent agreement with the first-order perturbation treatment. The smooth trace overlaying each data set is a fit to a sum of 11 Lorentzians, whose central frequencies are determined by just two parameters, *J* and B_z, via Eqs. (5.3)-(5.7). The fitted value of B_z for the near zero field case is within 1% of the calibrated value.

5.2 Larger spin systems: fully labeled acetonitrile

To illustrate the utility of near zero field NMR, we examine the case of fully labeled acetonitrile ($^{13}CH_3{}^{13}C^{15}N$). The zero-field spectrum is shown in the bottom trace of Figure 5.5. It is not immediately clear which lines correspond to which zero-field transitions. An expanded view of the zero-field spectrum in the range of 110 to 180 Hz is provided and compared to the spectrum obtained in the indicated finite magnetic fields. We see the appearance of doublets centered at 114, 126, and 151 Hz, indicating that these transitions occur between manifolds with $f = 0$ and $f = 1$. It is interesting to note that these doublets display different splitting

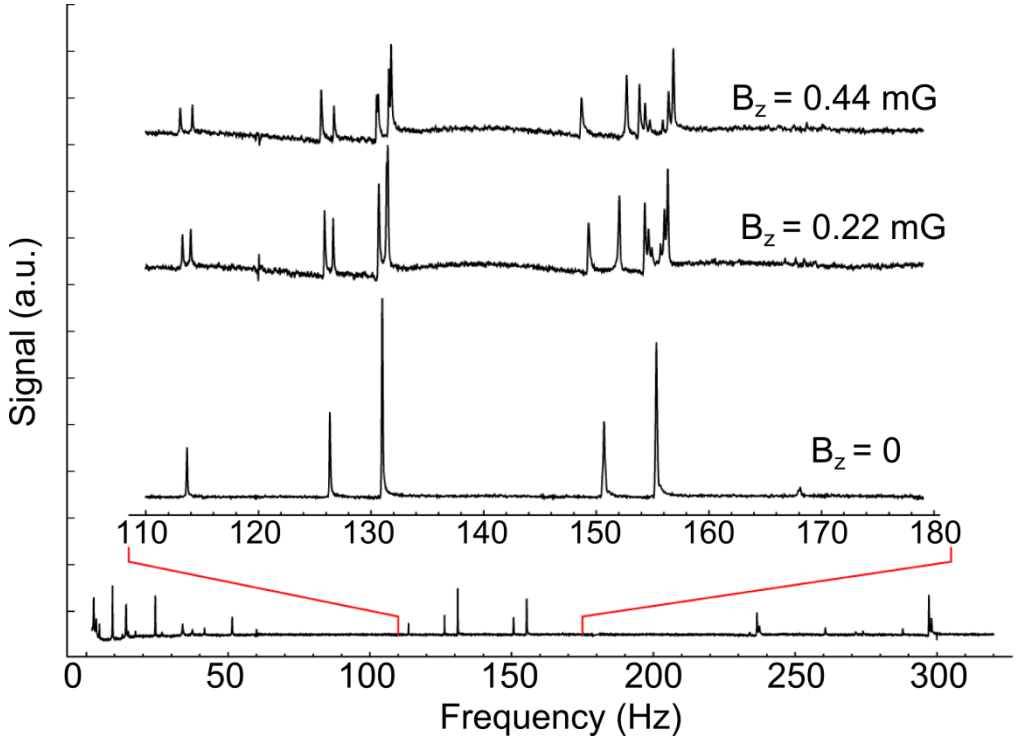

Figure 5.5 Effects of small magnetic fields on fully labeled acetonitrile $^{13}CH_3{}^{13}C^{15}N$. The bottom trace shows the entire zero-field spectrum. The upper traces show the central part of the ZF and NZF spectra in the indicated fields.

due to differences in the Landé g factors for the different manifolds involved in these transitions. The line at 131 Hz splits first into a doublet, which split into a pair of doublets. One can show that such a splitting pattern arises for a $f = 1 \leftrightarrow f = 1$ transition (see Section 5.4 [27]). The small zero-field peak at 168 Hz splits into four lines, barely above the noise, indicating an additional $f = 1 \leftrightarrow f = 1$ transition. Finally, the zero-field peak at 155.5 Hz splits into a sextet indicating the transition is $f = 1 \leftrightarrow f = 2$. The six lines in this multiplet appear ‘‘inside out’’ compared to the six line multiplet observed at 2*J* in 2-acetonitrile due to a reversal in relative magnitude of the Landé g factor. The number of peaks in each multiplet can be understood as follows: starting with a $^{13}CH_3$ group, we confine our attention to the $1 \leftrightarrow 0$ transition with total proton spin = 1/2, yielding transitions in the neighborhood of 1 J_{CH}. Addition of the second ^{13}C splits these levels: $f = 1$ splits to 3/2, 1/2 manifolds, and $f = 0$ manifolds splits to 1/2. Addition of the ^{15}N splits these so we now have $f_a = 2$ or 1, $f_b = 1$ or 0, and $f_c = 1$ or 0. Transitions between $f_a \leftrightarrow f_b$ can be ignored because they occur at low frequency. Employing the $f = 1$ rule we expect three $1 \leftrightarrow 0$ transitions, producing doublets: $f_a = 1 \leftrightarrow f_c = 0$, $f_b = 1 \leftrightarrow f_c = 0$, and $f_b = 0 \leftrightarrow f_c = 1$. Transitions between $f_a = 2 \leftrightarrow f_c = 1$ yields a multiplet with six lines, and transitions with $f = 0$ between $f_a = 1 \leftrightarrow f_c = 1$and between $f_b = 1 \leftrightarrow f_c = 1$ yield multiplets with four lines. More details are presented in Section 5.4.

5.3 Comparable strength of *J*-coupling and Zeeman interaction

In systems with small couplings, such as 1-acetic acid ($CH_3{}^{13}COOH$) which has a two-bond coupling, $2J_{CH}$ = 6.8 Hz , it is possible to explore the regime in which the Zeeman interaction is comparable to the *J*-coupling. Figure 5.6 shows experimental spectra for 1-acetic acid for the indicated magnetic fields. The large peak that does not split is due to the uncoupled OH group, while the rest of the spectrum corresponds to the $CH_3{}^{13}C$ part of the molecule. Initially, the spectrum appears similar to the 2-acetonitrile spectrum, with a doublet at *J*, and an additional doublet at 2*J* composed of several unresolved lines. As the magnetic field is increased, additional lines in the multiplet at 2*J*

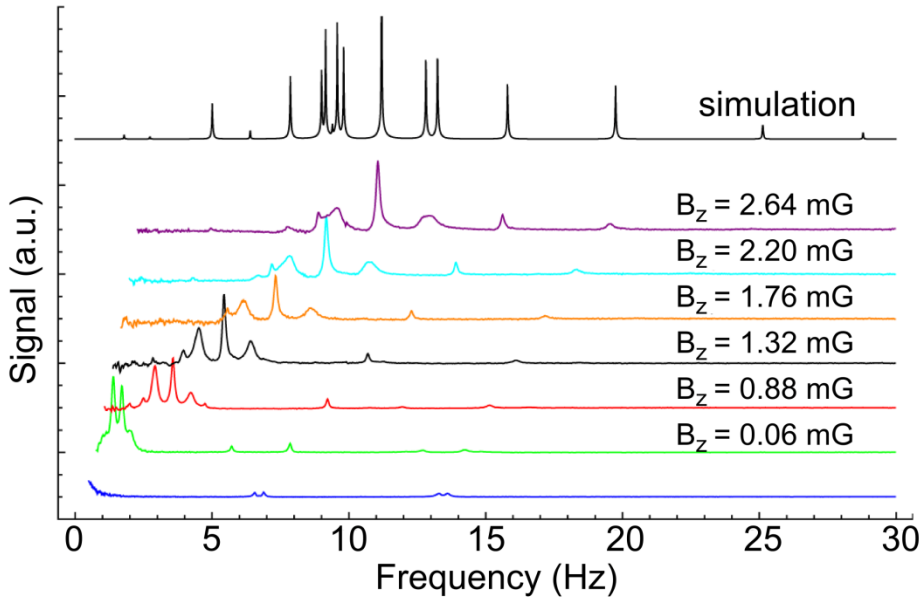

Figure 5.6 Experimental spectra for 1-acetic acid ($CH_3{}^{13}COOH$) in the indicated magnetic fields. The smooth curve at the top of the plot presents the result of a full numerical simulation with high resolution.

become resolved. At the highest magnetic fields, the spectrum displays the highest complexity, and is no longer recognizable from the perturbative treatment presented above. The smooth trace at the top of the plot shows the log of the absorptive component of a high resolution numerical simulation, reproducing all features of the data, to the extent that lines are resolved. Careful examination reveals 17 lines, 1 for the OH group and $(N+1)^2 = 16$ lines, as theoretically predicted [22].

5.4 Calculations of the near zero-field spectra

Here we present detailed calculations of the results presented in the the previous Sections of Chapter 5. To calculate near-zero-field nuclear magnetic resonance spectra, we start from the Hamiltonian containing both scalar and Zeeman couplings:

$$H=H_J+H_Z=\sum_{j;k>j} J_{jk}\mathbf{I}_j\cdot\mathbf{I}_k-\sum_j\gamma_j\mathbf{I}_j\cdot\mathbf{B}\,, \tag{5.8}$$

where H_J and H_Z are the contributions from the scalar couplings and the Zeeman interaction, respectively. Here γ_j is the gyromagnetic ratio of the jth spin and J_{jk} is the scalar coupling between spins j and k. In the absence of magnetic fields, the spherical symmetry of the Hamiltonian dictates that eigenstates $|\varphi_a\rangle$, with energy E_a, are also eigenstates of $\mathbf{F}^2$ and F_z, where $\mathbf{F}=\sum_j \mathbf{I}_j$ is the total angular momentum. Manifolds characterized by the quantum number f have degeneracy $2f+1$. Application of a magnetic field B_z lifts this degeneracy, resulting in a splitting of the zero-field NMR lines. The signal in our experiment is the x component of the magnetization.

$$M_x(t)=n\mathrm{Tr}\left(\rho(t)\sum_j I_{jx}\gamma_j\right), \tag{5.9}$$

where ρ(t) is the time dependent density matrix and n is the molecular density. The initial density matrix ρ_0 can be expressed in terms of the operators $|\varphi_a\rangle\langle\varphi_b|$, each of which evolves as $e^{i\omega_{ab}t}$, where $\omega_{ab} = (E_a - E_b)$. Equation (5.9) can be rewritten

$$M_x(t)=n\sum_{a,b,j}\frac{\gamma_j}{2}\rho_{ab}\langle\varphi_b|(I_{j+}+I_{j-})|\varphi_a\rangle e^{-i\omega_{ab}t}, \tag{5.10}$$

where $\rho_{ab}=\langle\varphi_a|\rho_0|\varphi_b\rangle$ and $I_{j\pm} = I_{jx} \pm iI_{jy}$ are the usual raising and lowering operators. For arbitrary scalar-coupling networks and arbitrary magnetic fields, eigenstates and eigenvalues can be calculated numerically. In the limit where the magnetic field is small, such that $|\gamma_j B_z| << |J_{jk}|$ for all values of j, and k, its effects on the spectra can be calculated analytically using first-order perturbation theory, lending considerable physical insight to the problem.

5.4.1 Calculation from first-order perturbation theory

We first consider the case of a $^{13}CH_N$ system, with N equivalent protons. In zero field, the unperturbed energy levels are given by $E(f, f_A) = J/2[f(f+1) - i_A(i_A+1) - s(s+1)]$, where i_A is the quantum number associated with the operator $\mathbf{I}_A$ representing the sum of the equivalent proton spins, and s is the quantum number associated with the operator $\mathbf{S}$ representing the ^{13}C spin. To first order in B_z , eigenstates are those of the unperturbed Hamiltonian and Zeeman shifts of the eigenvalues can be read from the diagonal matrix elements of the Zeeman perturbation. One finds:

$$\begin{aligned}\Delta E(f, i_A, m_f) &= -\left\langle f, m_f \left| B_z(\gamma_H I_{Az} + \gamma_C S_z \right| f, m_f \right\rangle \\ &= \sum_{m_{fA}, m_s} \left\langle f\, m_f \left| i_A\, s\, m_{i_A}\, m_s \right\rangle \right\langle f_A\, s\, m_{i_A}\, m_s \left| B_z\left(\gamma_H I_A + \gamma_C S_z\right) \right| i_A\, s\, m'_{f_A}\, m'_s \right\rangle \left\langle i_A\, s\, m'_{i_A}\, m'_s \left| f\, m_f \right. \right\rangle \\ &= -B_z \sum_{m_{fA}, m_s} \left\langle i_A\, s\, m_{i_A}\, m_s \left| f\, m_f \right. \right\rangle^2 \left(\gamma_H m_{i_A} + \gamma_C m_s\right).\end{aligned} \tag{5.11}$$

Here γ_H and γ_C are the proton and ^{13}C gyromagnetic ratios, respectively, and $\left\langle i_A\, s\, m_{i_A}\, m_s \left| f\, m_f \right. \right\rangle$ are the Clebsch-Gordan coefficients. Noting that the operators $I_{j\pm}$ in Eq. (5.11) are vector operators with magnetic quantum number ±1, one can employ the Wigner-Eckart theorem to obtain the selection rules for observable coherences: $\Delta f = 0, \pm 1$ and $\Delta m_f = \pm 1$. We note that these selection rules break down in the limit where the Zeeman term is comparable to the *J*-coupling term because of mixing of the zero-field eigenstates with different values of *f*. In the case at hand with N equivalent protons, there is an additional selection rule $\Delta f_A = 0$, since, in the absence of chemical shifts, the Hamiltonian commutes with $\mathbf{F}^2$. The observed frequencies in the spectrum can be obtained using these selection rules and Eq. (5.11). In the following, $\nu_{f,m_f}^{f',m_f'}$ denotes the frequency of transitions between the states $\left| f, m_f \right\rangle$ and $\left| f', m_f' \right\rangle$

In the case of N = 1, we have $f_A = 1/2$, and the zero-field levels consist of a singlet with $f = 0$ and a triplet with $f = 1$. In the presence of a small magnetic field, the singlet level is unperturbed, while the triplet levels split:

$$E(0, 1/2, 0) = -3J/4, \tag{5.12}$$

$$E(1, 1/2, m_f) = J/4 - m_f \, B_z \, (\gamma_H + \gamma_C)/2.$$

With the selection rules presented above, one finds a single line for transitions with $\Delta f = 0$ between states with f = 1, and a doublet for transitions with $\Delta f = \pm 1$ between states with $f = 1$ and $f = 0$:

$$\nu_{1,m_f}^{1,m_f \pm 1} = B_z(\gamma_H + \gamma_C)/2, \tag{5.13}$$

$$\nu_{0,0}^{1,\pm 1} = J \pm B_z(\gamma_H + \gamma_C)/2. \tag{5.14}$$

Energy levels, transitions, and an example of the $f = 1 \leftrightarrow f = 0$ doublet are shown in Figure 5.1. For the case of N = 2, f_A is either 0 or 1 (we did not examine this case experimentally, but include it for the sake of completeness). Adding the ^{13}C spin to the system yields a zero-field manifold with $f = 1/2$ for $i_A = 0$ and unperturbed energy 0. For $i_A = 1$, the zero-field manifolds have $f = 3/2, 1/2$ with energies $J/2$ and $-J$, respectively. A small magnetic field perturbs these levels according to Eq. (5.11)

$$\begin{aligned} E(1/2, 0, m_f) &= -m_f \, B_z \, \gamma_C /2, \\ E(1/2, 1, m_f) &= -J - m_f \, B_z \, (4\,\gamma_H - \gamma_C)/3, \\ E(3/2, 1, m_f) &= J/2 - m_f \, B_z \, (2\,\gamma_H + \gamma_C)/3. \end{aligned} \tag{5.15}$$

Thus, there are three lines corresponding to transitions with $\Delta f = 0$:

$$\nu_{1/2,m_f \pm 1}^{1/2,m_f} = B_z\gamma_C; \; i_A = 0, \tag{5.16}$$

$$\nu_{1/2,m_{f\pm 1}}^{1/2,m_f} = \frac{B_z}{3}(4\gamma_H + \gamma_C); \; i_A = 1, \tag{5.17}$$

$$\nu_{1,m_f \pm 1}^{1,m_f} = \frac{B_z}{3}(2\gamma_H + \gamma_C); \; i_A = 1. \tag{5.18}$$

Transitions with $\Delta f = \pm 1$ and $\Delta m_f = \pm 1$ between states with $f = 1/2$ and $f = 3/2$ for $i_A = 1$ yield four lines, at frequencies given by

$$\nu_{1,m_f \pm 1}^{3/2,m_f} = \frac{3J}{2} + \frac{2B_z}{3} m_f(\gamma_H - \gamma_C) \mp \frac{B_z}{3}(2\gamma_H + \gamma_C). \tag{5.19}$$

For the case of N = 3, iA is either 1/2 or 3/2. The $i_A = 1/2$ energy levels are the same as for the ^{13}CH system, and the transition frequencies are given by Eqs. (6) and (7). For the $i_A = 3/2$ manifolds, evaluating Eq. (5.11), we find

$$\begin{aligned} E(1,\, 3/2,\, m_f) &= -5J/4 - m_f \mathrm{B_z}\,(5\,\gamma_\mathrm{H} - \gamma_\mathrm{C})/2, \\ E(2,\, 3/2,\, m_f) &= 3J/4 - m_f \mathrm{B_z}\,(3\,\gamma_\mathrm{H} + \gamma_\mathrm{C})/4. \end{aligned} \tag{5.20}$$

Transitions between $|f = 1,\, m_f>$ and $|f = 2,\, m_f \pm 1>$ occur at frequencies given by

$$\nu_{1,m_f}^{2,m_f\pm1} = 2J + m_f\,\frac{B_z}{4}(-7\gamma_H + 6\gamma_C) \pm \frac{B_z}{4}(3\gamma_H + \gamma_C). \tag{5.21}$$

There are two additional transitions for states with $i_\mathrm{A} = 3/2$ with $\Delta f = 0$ that occur near zero frequency,

$$\nu_{2,m_f}^{2,m_f\pm1} = \frac{B_z}{4}(3\gamma_H + \gamma_C); i_A = 3/2, \tag{5.22}$$

$$\nu_{1,m_f}^{1,m_f\pm1} = \frac{B_z}{4}(5\gamma_H - \gamma_C); i_A = 3/2. \tag{5.23}$$

Energy levels, transitions, and an example of the $f = 2 \leftrightarrow f = 1$ six-line multiplet are shown in Figure 5.8 (d).

In the presently considered limit of small magnetic fields, the amplitude of a peak corresponding to a transition between states $|\varphi_a>$ and $|\varphi_b>$ can be found from the coefficients in front of $e^{i\omega_{ab}t}$ in Eq. (5.10),

$$a_{ab} = \langle\varphi_a|\rho_0|\varphi_b\rangle\langle\varphi_b|(\mathrm{P_+} + \mathrm{P_-})|\varphi_a\rangle, \tag{5.24}$$

where

$$\mathrm{P_\pm} = \sum_j \gamma_j \mathrm{I}_{j\pm}. \tag{5.25}$$

The polarized part of the initial density matrix corresponding to high-field magnetization with $\mathbf{B}_0$ is

$$\rho \propto \sum_j \gamma_j \mathrm{I}_{jx} = \mathrm{P_+} + \mathrm{P_-}. \tag{5.26}$$

Hence, amplitudes are given by $\langle\varphi_b|(\mathrm{P_+} + \mathrm{P_-})|\varphi_a\rangle^2$. These matrix elements can be found using the Wigner-Eckart theorem for rank 1 vector operators with magnetic quantum number ±1:

$$\langle f, m_f|(\mathrm{P_+} + \mathrm{P_-})|f', m'_f\rangle^2 = \langle f, m_f\|(\mathrm{P_+} + \mathrm{P_-})\|f', m'_f\rangle^2 \langle f, m_f|f', 1, m'_f, \pm1\rangle^2. \tag{5.27}$$

In the case of a $1 \leftrightarrow 0$ transition, the two peaks corresponding to transitions with $\Delta m_f = \pm 1$ have equal intensities. In the case of a $1/2 \leftrightarrow 3/2$ transition, the four peaks have intensities in the ratio of 1:3:3:1. For the $2 \leftrightarrow 1$ transitions, we find that the six peaks are in the ratio of 1:3:6:6:3:1.

5.4.2 Calculation of multiplets for fully labeled acetonitrile

We have analytically calculated the first-order corrections to the energy eigenvalues and the splitting patterns for the case of the $^{13}CH_N$ group. This can be extended to larger spin systems in a straightforward way. We now proceed to analyze the case of fully labeled acetonitrile $^{13}CH_3{}^{13}C^{15}N$. The energy eigenstates $|\varphi_a\rangle$can be approximately constructed by iteratively adding additional spins to the spin pair with the largest spin coupling. This treatment is valid in the limit where the coupling of each additional spin to the previous spin system is small compared to that of all the previous couplings. In the following, $\mathbf{I}_A$ is the sum of the equivalent proton spins, $\mathbf{S}_1$ is the methyl ^{13}C, $\mathbf{S}_2$ is the second ^{13}C, and $\mathbf{N}$ is the ^{15}N spin. In zero magnetic field, the eigenstates of the strong one bond ^{13}CH coupling are those of $\mathbf{F}_1{}^2$ and F_{1z} (here $\mathbf{F}_1 = \mathbf{S} + \mathbf{I}_A$), which can be expressed in terms of the uncoupled states via the Clebsch-Gordan coefficients:

$$\left| f_1, m_1 \right\rangle = \sum_{m_k, m_s} \left\langle f_1 m_1 \middle| i_A s_1 m_{i_A} m_s \right\rangle \left| i_A \; m_{i_A} \; s \; m_s \right\rangle. \tag{5.28}$$

Adding $\mathbf{S}_2$ to $\mathbf{F}_1$ yields the states

$$\left| f_2, m_2 \right\rangle = \sum_{m_1, m_{s_2}} \left\langle f_2 m_2; i_A \middle| f_1 s_2 m_1 m_{s_2} \right\rangle \left| f_1 \; m_1 \; s_2 \; m_{s_2} \right\rangle. \tag{5.29}$$

The quantity $\left\langle f_2 m_2; i_A \middle| f_1 s_2 m_1 m_{s_2} \right\rangle$ is the usual Clebsch-Gordan coefficient for addition of angular momenta $\mathbf{F}_1$ and $\mathbf{S}_2$; the quantum number i_A is included because the same value of f_1 can be obtained with different values of i_A. Finally, adding $\mathbf{N}$ to $\mathbf{F}_2$ yields the states:

$$\left| f, m \right\rangle = \sum_{m_2, m_n} \left\langle f \, m; f_1, i_A \middle| f_2 \, n \, m_2 m_n \right\rangle \left| f_2 \; m_2 \; n \; m_n \right\rangle. \tag{5.30}$$

Now, to find the first-order energy shifts, we calculate the diagonal matrix elements $\langle f\, m|H_z|f\, m\rangle$. Inserting the expressions for the eigenstates, we find

$$\langle f\, m|H_z|f\, m\rangle = -\sum_{\substack{m_n m_2 \\ m_{f_1} m_{s_2} \\ m_{i_A} m_{s_1}}} \langle fm; f_2 f_1 i_A | f_2 n m_2 m_n\rangle^2 \langle f_2 m_2; f_1 i_A | f_1 s_2 m_1 m_{S_2}\rangle^2 \langle f_1 m_1; i_A | i_A s_1 m_k m_{s_1}\rangle^2 \times (\gamma_C m_{s_1} + \gamma_C m_{s_2} + \gamma_N m_n + \gamma_H m_{i_A}) B_z . \quad (5.31)$$

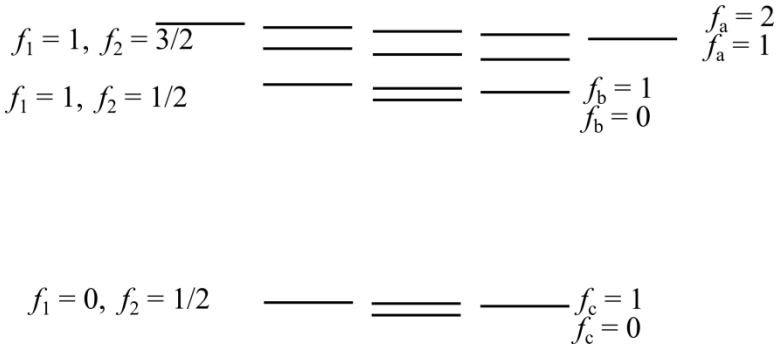

Figure 5.7 Energy levels for fully labeled acetonitrile with protons, in iA = 1/2 manifolds.

We now connect this with the discussion in the main text regarding the fully labeled acetonitrile spectrum. The proton spins can be either $i_A = 1/2$ or $i_A = 3/2$. Confining our attention to the latter, adding the first carbon $\mathbf{S}_1$ to the system yields $f_1 = 0$ and 1, separated by 1 J_{HC}. Adding $\mathbf{S}_2$ to the system produces manifolds with $f_2 = 1/2$ and 3/2 for $f_1 = 1$ and $f_2 = 1/2$ for $f_1 = 0$. Finally, adding the nitrogen spin **N** to the system produces manifolds with $f_a = f = 2, 1$ for $f_2 = 3/2$ and $f_1 = 1$, $f_b = f = 1, 0$ for $f_2 = 1/2$ and $f_1 = 1$, and fc $= f = 1, 0$ for $f_2 = 1/2$ and $f_1 = 0$. These energy levels are shown schematically in Figure 5.7, along with small Zeeman shifts. Lines that occur in the neighborhood of 1 J_{HC} must be due to transitions between states with $\Delta f_1 = 1$. The splitting patterns for a particular multiplet can be determined by applying the selection rules $\Delta f = 0, \pm 1$ and $\Delta m_f = \pm 1$, with amplitudes determined by Eq. (5.27). Traces (a)-(c) in Figure 5.8 show the energy levels and splitting patterns for several of the transitions in fully labeled acetonitrile for protons in the $i_a = 1/2$ state. For contrast, trace (d) shows the splitting pattern for the $f = 1 \leftrightarrow f = 2$

transition for acetonitrile-2 ($^{13}CH_3CN$), displaying an "inside-out" pattern compared to the $f = 1 \leftrightarrow f = 2$ transition shown for fully labeled acetonitrile. This is because of the reversal in relative magnitudes of the Landé g factors for the $f = 1$ and $f = 2$ states.

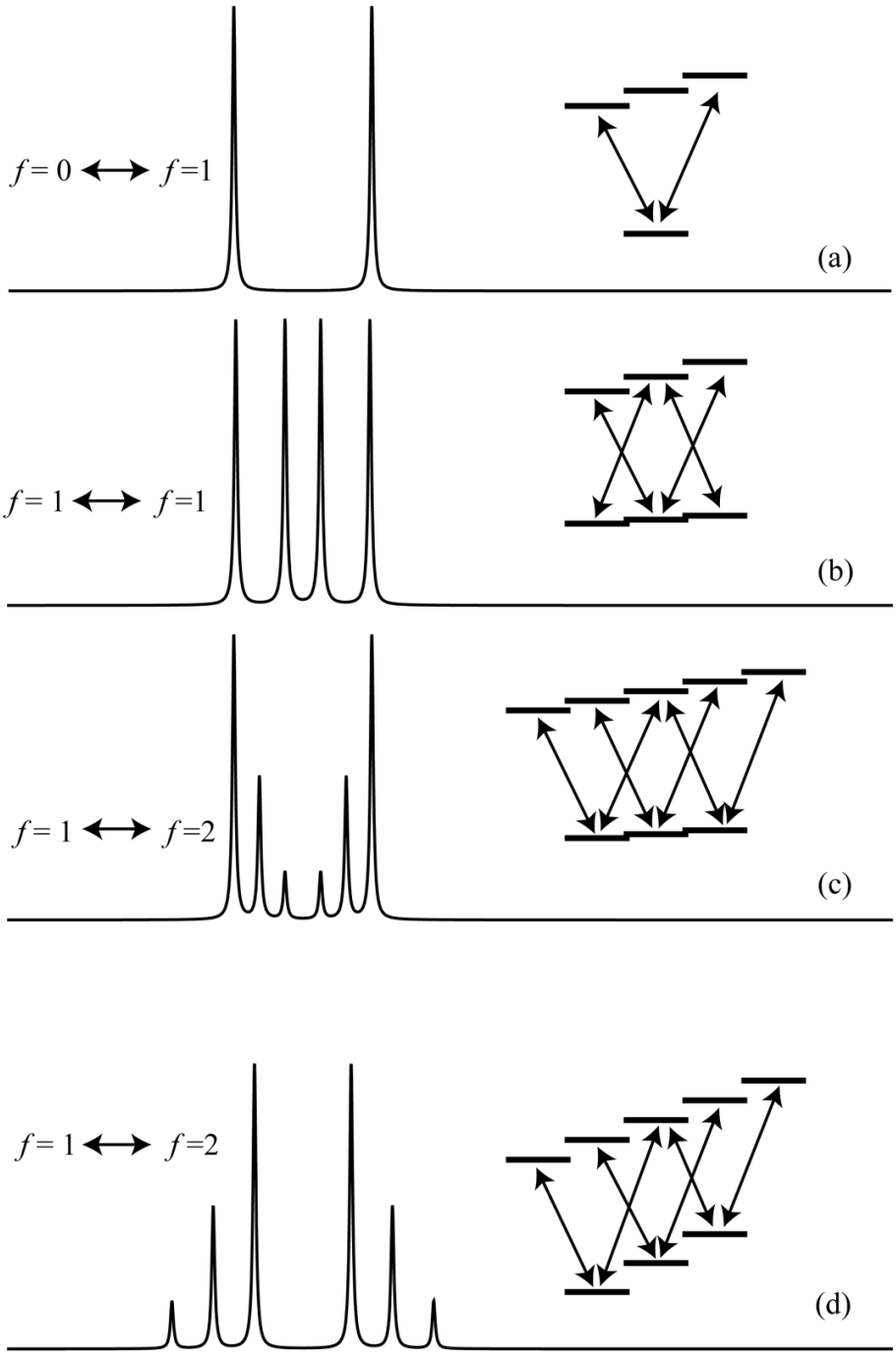

Figure 5.8 Near-zero-field NMR multiplets arising from several different transitions, as indicated. The upper three multiplets correspond approximately to those found in the fully labeled acetonitrile spectra. Trace (d) corresponds to the i_A = 3/2 transitions of labeled acetonitrile-2, displaying an "inside-out" pattern compared to the $f = 1 \leftrightarrow f = 2$ transition of fully labeled acetonitrile.

5.5 Significance of near-zero-field NMR

In conclusion, we have investigated near-zero-field nuclear magnetic resonance, where the effects of magnetic fields can be treated as a perturbation to the scalar *J*-couplings. This work represents a new form of NMR spectroscopy, complementary to high-field NMR, in which heteronuclear scalar couplings are almost always treated as a small perturbation to the dominant Zeeman interaction. We find that the presence of small fields produces splitting of zero-field lines. The splitting patterns have easy-to-understand rules and data are in excellent agreement with the predictions of first-order perturbation theory. It is interesting to note that the phenomenology observed here is similar to that of atomic spectroscopy of multi-electron atoms, and intuition developed in the latter field may be applied to interpretation of NZF NMR spectra. We have also investigated the case where Zeeman and *J*-couplings are comparable, resulting in signals with much higher complexity, potentially useful for NMR quantum computing [22].

6. Parahydrogen enhanced zero-field NMR

In this Chapter, we show that parahydrogen-induced polarization can be used to increase the sensitivity of zero-field NMR measurements by several orders of magnitude. This work has been previously published under the title "Parahydrogen enhanced zero-field nuclear magnetic resonance" by the Nature Publishing Group[21]. Despite the use of atomic magnetometers or SQUIDs, low-field NMR using samples thermally prepolarized in a permanent magnet typically suffers from low signal-to-noise ratio compared to inductively-detected high-field NMR, in part because of the low polarization available from thermalization in a permanent magnet. To avoid this difficulty, in this work we produce large nuclear spin polarization in zero-field NMR by employing the technique of parahydrogen induced polarization (PHIP), whereby order from the singlet state of parahydrogen is transferred to a molecule of interest, either by hydrogenation [30,31,40,83], or through reversible chemical exchange [50,52]. By flowing molecular hydrogen through an iron oxide catalyst at sufficiently low temperature (see Methods), it is possible to realize nearly 100% conversion of orthohydrogen to parahydrogen. This results in significant signal enhancements compared to that obtained using thermal polarization, which is typically in the range of 10^{-5}-10^{-6}. Before proceeding, it is worth noting that light induced drift can also be used for enrichment of nuclear spin isomers in other molecules [84,85], although the demonstrated enrichments are significantly lower, on the order of 2%. When combined with sensitive atomic magnetometers for detection of nuclear spin magnetization, PHIP enables NMR without any magnets. The sensitivity is sufficient to easily observe complex spectra exhibiting ^{1}H-^{13}C *J*-couplings in compounds with ^{13}C in natural abundance in just a few transients, a task that would require considerable signal averaging using thermal prepolarization. While PHIP has been investigated in a variety of magnetic fields, ranging from the earth's field to high field, observation of the resulting NMR signals has always been performed in finite magnetic field. To the best of our knowledge, the work reported here represents the first direct observation of PHIP in a zero-field environment. We show that polarization can be transferred through a number of chemical bonds to remote parts of a molecule, and that zero-field spectroscopy can be used to distinguish between different isotopomers in ethylbenzene, the product of hydrogenation of styrene. The mechanism by which observable magnetization is generated from the parahydrogen derived

singlet order requires only the presence of a heteronucleus, similar to the work of Ref. [86] , in contrast to a more commonly observed mechanism relevant to high field, which requires chemical-shift differences at the sites of the parahydrogen derived protons. Furthermore, our results are of particular interest in the context of recent work demonstrating that the lifetime of singlet polarization in low fields can considerably exceed the relaxation time T_1 of longitudinal magnetization [79,81], These demonstrations of increased singlet lifetime relied on field cycling and high-field inductive detection, and our methodology may provide for more direct observation and exploitation of these effects.

Zero-field NMR spectroscopy of samples magnetized by thermal prepolarization in a permanent magnet was discussed in Chapters 0 and 5. Additional information can also be found in the literature.[19,87]. In an isotropic liquid at zero magnetic field, the only terms in the NMR Hamiltonian are the spin-spin *J*-couplings,

$$H_J = \sum \hbar J_{jk} \mathbf{I}_j \cdot \mathbf{I}_k \ . \tag{6.1}$$

In the important case of XA_N systems, where both X and A are spin-1/2 particles, and each X spin couples to *A* with the same strength *J*, the resulting zero field *J*-spectra are simple and straightforward to interpret, consisting of a single line at *J* for XA, a single line at 3*J*/2 for XA_2, and two lines, one at *J* and one at 2*J* for XA_3. For larger molecules, as employed in the present work, long-range couplings to additional spins lead to splitting of these lines, however, the overall positions of the resulting multiplets remain unchanged. For large spin systems we rely on numerical spin simulations (presented in Section 6.5 below) to understand the splitting pattern, however as shown in Chapter 4 an approach based on perturbation theory yields simple rules for interpretation of the zero field splitting pattern.

Zero-field spectroscopy using parahydrogen induced polarization differs from the case of thermal polarization in both the initial density matrix and in the method of excitation. In the case of homogeneous catalysis, the product molecule starts out with two parahydrogen derived spins in a singlet state. Averaging over random hydrogenation events and subsequent evolution under the *J*-coupling Hamiltonian lead to an equilibrium density matrix described by pairs of heteronuclear and homonuclear scalar spin pairs,

$$\rho_0 = \sum a_{jk} \mathbf{I}_j \cdot \mathbf{I}_k \ , \tag{6.2}$$

which bears no magnetic moment, and is static under the *J*-coupling Hamiltonian. Observable magnetization oscillating along the *z* direction, to which the magnetometer is sensitive, can be produced by applying a pulse of DC magnetic field *B* in the *z* direction. Immediately following such a pulse, the density matrix contains terms of the form $\sin\eta(\mathrm{I}_{jx}\mathrm{I}_{ky}-\mathrm{I}_{jy}\mathrm{I}_{kx})$, where $\eta = Bt_p(\gamma_j-\gamma_k)$, t_p is the pulse duration, and γ_j is the gyromagnetic ratio of spin *j*. Subsequent evolution under the *J*-coupling Hamiltonian results in terms in the density matrix of the form $(\mathrm{I}_{j,z}-\mathrm{I}_{k,z})\sin\eta\sin(J_{jk}t)$, which produces magnetization oscillating in the *z* direction. The dependence on η highlights the role of a heteronucleus in the symmetry breaking of the parahydrogen derived scalar order. Numerical spin simulations of the propagation of the parahydrogen derived scalar order through the molecule and the dependence of the coherence amplitude on pulse area η for a heteronuclear spin pair with scalar order are presented in the Section 6.5. A more detailed analysis of the polarization transfer is presented in Chapter 8.

6.1 Setup and sample preparation for ZF-PHIP experiments

The zero-field spectrometer used in this work is similar to that of Ref. [19] or as described in Chapter 3. The setup is shown in Figure 6.1 (a). The noise spectrum of the magnetometer is shown in (b), and the pulse sequence is shown in (c). We performed zero-field PHIP spectroscopy in hydrogenation reactions of styrene (which forms ethylbenzene) and 3-hexyne (hexene and hexane), 1-phenyl-1propyne (1-phenyl-1propene) and dimethylacetylenedicarboxlyate (dimethylmaleate). In measurements presented in the main text, parahydrogen was bubbled through the solution for ~10 s, the flow was halted, and excitation pulses of DC magnetic field were applied in the *z* direction with $\eta=\pi/2$ for ^{13}C and protons. The resulting *z* magnetization was recorded by the atomic magnetometer. The rate of hydrogenation can be monitored by the signal amplitude as a function of time, as presented in Section 6.4. More details of the experimental setup and procedures can be found in Section 6.1. The zero-field spectrometer is shown schematically in Figure 6.1 (a) An atomic magnetometer, consisting of a Rb vapour cell and two lasers for optical pumping and probing, operates in the spin-exchange relaxation-free [23] regime. The cell is placed inside a set of magnetic shields (not shown), and residual magnetic fields are zeroed to within ≈1 μG. The vapour cell has dimensions 5 mm × 2 mm × 1 mm, contains ^{87}Rb and 1300 torr of N_2 buffer gas, and was microfabricated using lithographic patterning and etching techniques. The cell is heated to 210 ºC via an electric heating element wound around an aluminium-nitride spool. The sensitivity of the magnetometer is about 0.15 nG/Hz$^{1/2}$ above 120 Hz, and the bandwidth is in excess of 400 Hz. A set of coils can be used to apply sharp, ≈1 G DC pulses in arbitrary directions to excite NMR coherences, and a separate set of coils (not shown) controls the ambient magnetic field inside the shields. Mixtures of catalyst, solvent, and substrate could be brought into proximity of the atomic magnetometer via a glass sample tube. The sample was maintained at 80ºC by flowing air through a jacket surrounding the glass tube. In experiments at lower temperature (not presented here), we found that there was some non-uniform broadening of spectra, presumably due to the presence of catalyst in solid form. Parahydrogen was bubbled through the solution via 0.8 mm inner-diameter tube for several seconds at a pressure of about 70 PSI and flow rate of about 120 standard cc/min. The parahydrogen was produced as described in

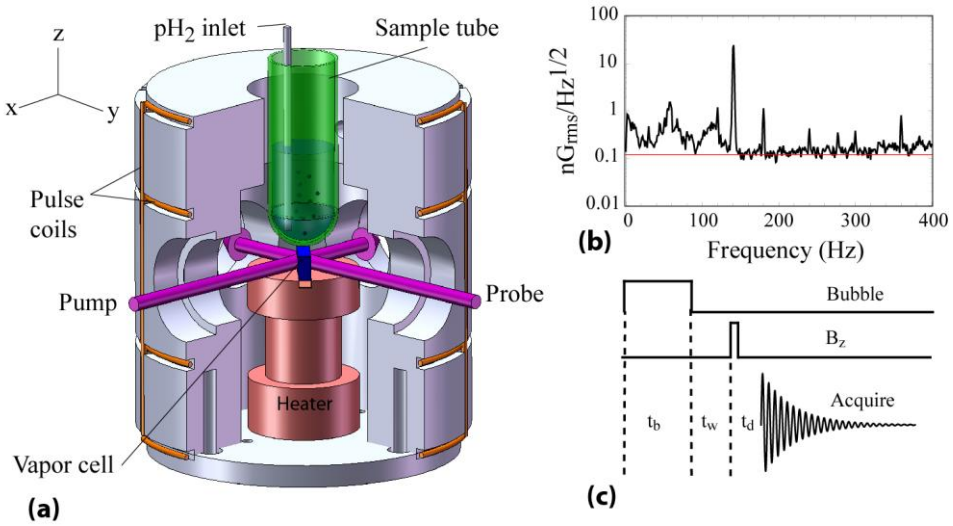

Figure 6.1 Scheme for detecting parahydrogen induced polarization at zero magnetic-field. The experimental setup is shown in (a). A microfabricated alkali vapor cell is mounted inside a set of coils used for applying magnetic field pulses. The alkali vapour is optically pumped with a circularly polarized laser beam, resonant with the D1 transition of ^{87}Rb. A linearly polarized laser beam, tuned about 100 GHz off resonance, is used to probe the alkali spin-precession. The magnetometer is primarily sensitive to magnetic fields in the vertical (*z*) direction. A 7 mm inner-diameter glass tube contains the sample, and a 1/32" inner-diameter teflon tube is used to bubble parahydrogen through the solution. A set of magnetic shields surrounding the magnetometer, not shown, isolates the magnetometer from external magnetic fields. The magnetic field noise spectrum of the magnetometer is shown in (b). Above 100 Hz, the noise floor is about 0.15 nG/Hz$^{1/2}$. The experimental pulse sequence is shown in (c).

Section 3.2.6 Bubbling was halted prior to application of excitation pulses and signal acquisition. Data were acquired with sampling rate of 2000 samples per second. In acquiring the spectrum of styrene with natural-abundance ^{13}C, the phase of the excitation pulses was cycled with respect to that of the 60 Hz line frequency in order to reduce the line noise and its harmonics. Isotopically labeled styrene was obtained from Cambridge Isotope Labs. Natural-abundance styrene and Wilkinson's catalyst[88] were obtained from Sigma-Aldrich. Styrene hydrogenations were performed with 300 μL styrene and 4 mG Wilkinson's catalyst, Tris(triphenylphosphine)rhodium(I) chloride (CAS # 14694-95-2). The 1-phenyl-propyne and dimethyl acetylenedicarboxylate reactions were performed with 100 μL substrate in 300 μl tetrahydrofuran,

catalyzed by 1,4-Bis(diphenylphosphino)butane](1,5-cyclooctadiene) rhodium(I)Tetrafluoroborate, (CAS # 79255-71-3). The hexyne reaction was performed in a solution of 50% tetrahydrofuran with 5 mL total and 30 mG Wilkinson's Catalyst. Most of this volume does not contribute to signal since it is far from the magnetometer.

6.2 ZF-PHIP experiments with ^{13}C labeled styrene

Single shot, zero-field PHIP spectra of ethylbenzene-β^{13}C (labeled $^{13}CH_3$ group), and ethylbenzene-α^{13}C (labeled $^{13}CH_2$ group), synthesized from labeled styrene, are shown in black in Figure 6.2 (a) and (b), respectively. The ethylbenzene molecule is shown in the inset, with the blue carbon indicating the β label, and the green carbon indicating the α label. The spectrum of ethylbenzene-β^{13}C in Figure 6.2 (a) can be understood in terms of the discussion above, with multiplets at $^1J_{HC}$ and $2\times{}^1J_{HC}$, and additional lines at low frequency. Here the superscript indicates the number of bonds separating the interacting pair, and for ethylbenzene-β^{13}C, $^1J_{HC}$=126.2 Hz [89]. Isolated lines in the complex spectrum fit to complex Lorentzians with half-width-at-half-maximum (HWHM) of about 0.1 Hz. It should be noted that this spectrum is similar to the correspondingly labeled ethanol-β^{13}C spectrum reported in Ref [19], although careful inspection reveals small splittings of some lines due to long-range (at least four-bond) homonuclear couplings to protons on the benzene ring. The blue trace shows the result of a numerical simulation accounting for eight spins, including the six spins on the ethyl part of the molecule and the two nearest protons on the benzene ring. The simulation reproduces most of the features of the experimental spectrum quite well, including small splittings of several lines. More details of the numerical simulation can be found in the Section 6.5.

The zero-field PHIP spectrum of ethylbenzene-α^{13}C shown in Figure 6.2 (b) is qualitatively similar to the zero-field spectrum of ethanol-α^{13}C [19], with a multiplet at roughly $3/2\times {}^1J_{HC}$ ($^1J_{HC}$ = 126.2 Hz, measured in house with a 300 MHz spectrometer) and features at low frequency. Many additional lines in the spectrum indicate that long-range couplings to the protons on the benzene ring are important. Since the ethanol-β^{13}C spectrum does not display such complexity, the largest perturbation to the ethyl part of the molecule must be due to three-bond $^3J_{HC}$ couplings.

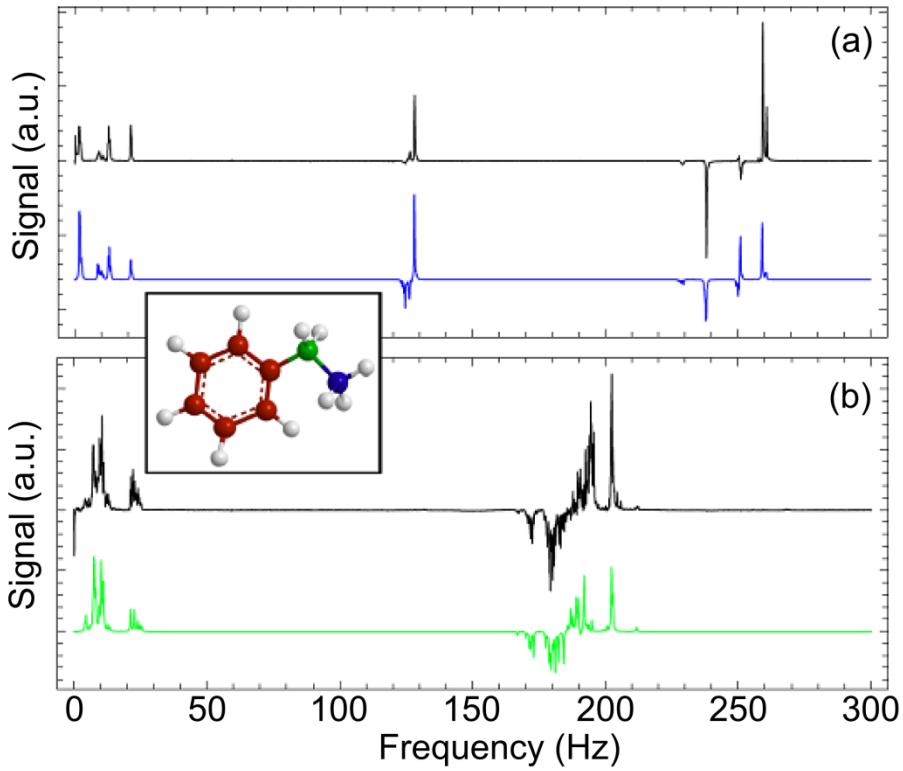

Figure 6.2 Single-shot zero-field PHIP J-spectra (imaginary component) of ethylbenzene-β^{13}C (a) and ethylbenzene-α^{13}C (b), polarized via addition of parahydrogen to labeled styrene. The inset shows the ethylbenzene molecule with the β and α positions indicated by the blue and green carbons, respectively. The blue and green traces in (a) and (b), respectively, are the results of numerical simulations, described in the text.

The green trace shows the result of numerical simulation, consisting of the six spins on the ethyl part of the molecule and the two nearest protons on the benzene ring. Simulation again reproduces most of features of the experimental spectrum, although careful inspection shows a number of additional splittings in the experimental spectrum, indicating that couplings to more remote spins on the benzene ring not included in the simulation, are important. It is worth emphasizing that, despite the similarity of the one-bond heteronuclear *J*-couplings, the spectra associated with different isotopomers display strikingly different features, which appear in different parts of the spectrum, facilitating easy assignment of isotopomers to their respective peaks.

6.3 ZF-PHIP experiments with ^{13}C at natural abundance

The sensitivity of the magnetometer and the degree of parahydrogen induced polarization are sufficient to detect *J*-spectra in compounds with ^{13}C in natural abundance. Figure 6.3 shows the zero-field PHIP spectrum of ethylbenzene with ^{13}C in natural abundance, obtained in just eight transients.

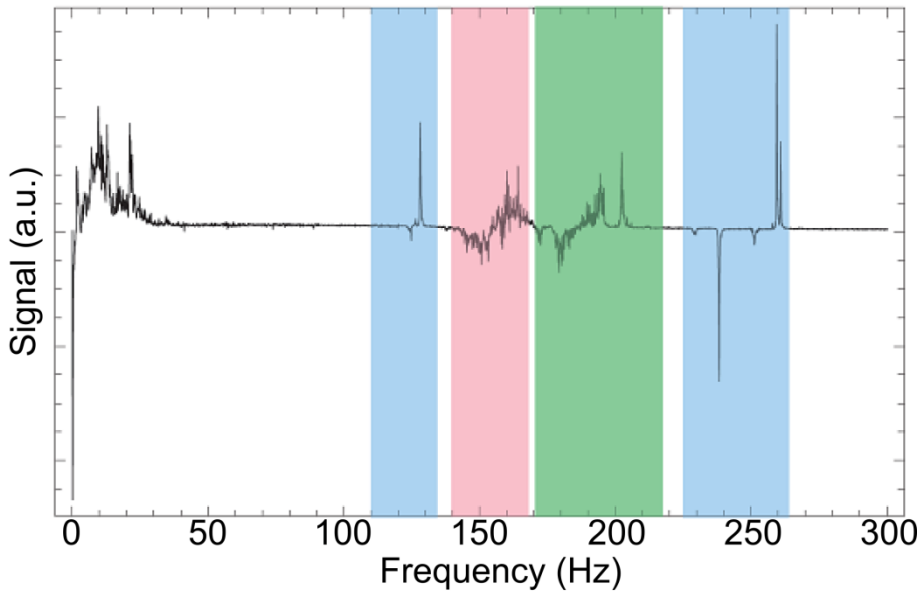

Figure 6.3 Zero-field J-spectrum (imaginary component) of ethylbenzene, produced via parahydrogenation of styrene with ^{13}C in natural abundance. These data result from averaging 8 transients following a pulse of magnetic field in the *z* direction with $\eta \approx \pi/2$. The high frequency components of the signals arising from the α and β isotopomers are easily recognizable from the spectra shown in Figure 6.2, and are highlighted by the green and blue bands, respectively. The signal in the neighbourhood of 156 Hz is due to isotopomers with ^{13}C on the benzene ring, and is highlighted in red.

The spectrum shown here is the sum of spectra associated with the α and β isotopomers shown in Figure 6.2, as well as isotopomers that carry ^{13}C in one of four non-equivalent positions on the benzene ring. The high frequency parts of the spectrum arising from the α and β isotopomers are highlighted in green and blue, respectively. The part of the signal arising from the benzene ring with a single ^{13}C is a multiplet centred about the one-bond coupling frequencies (typically about 156 Hz in aromatic systems), and also a multiplet in the low-frequency range. The high-frequency component is highlighted in red. Interestingly, spectra associated with the α or β isotopomers do not overlap with spectra associated with isotopomers with a ^{13}C on the benzene ring. It is also noteworthy that if the hydrogenation is performed in high field, large chemical shift differences between protons on the benzene ring and the parahydrogen derived protons would inhibit the transfer of polarization to the benzene ring.

To further illustrate the capabilities of zero-field PHIP as a method for chemical fingerprinting, spectra obtained from several different hydrogenation reactions are presented in Figure 6.4: (a) phenyl propyne (forming phenyl propene upon hydrogenation) with a labeled $^{13}CH_3$ group, (b) dimethyl-acetylene-dicarboxylate (dimethyl maleate) with ^{13}C in natural abundance, and (c) 3-hexyne (hexene and hexane) with ^{13}C in natural abundance. isotopomers, and can approximately be understood as follows: For a three-spin system, where one of the parahydrogen derived spins has a strong coupling to a ^{13}C nucleus, one can show that the spectrum consists of two lines centred around the strong coupling frequency, and an additional low frequency peak. The antiphase lines centred about 165 Hz in (b) correspond to the isotopomer where the ^{13}C is directly bonded to one of the parahydrogen derived spins, and is accompanied by a contribution at low frequency. The other three-spin isotopomer, where the strongest coupling to the ^{13}C nucleus is through two bonds, nominally gives rise to three lines at low frequency.

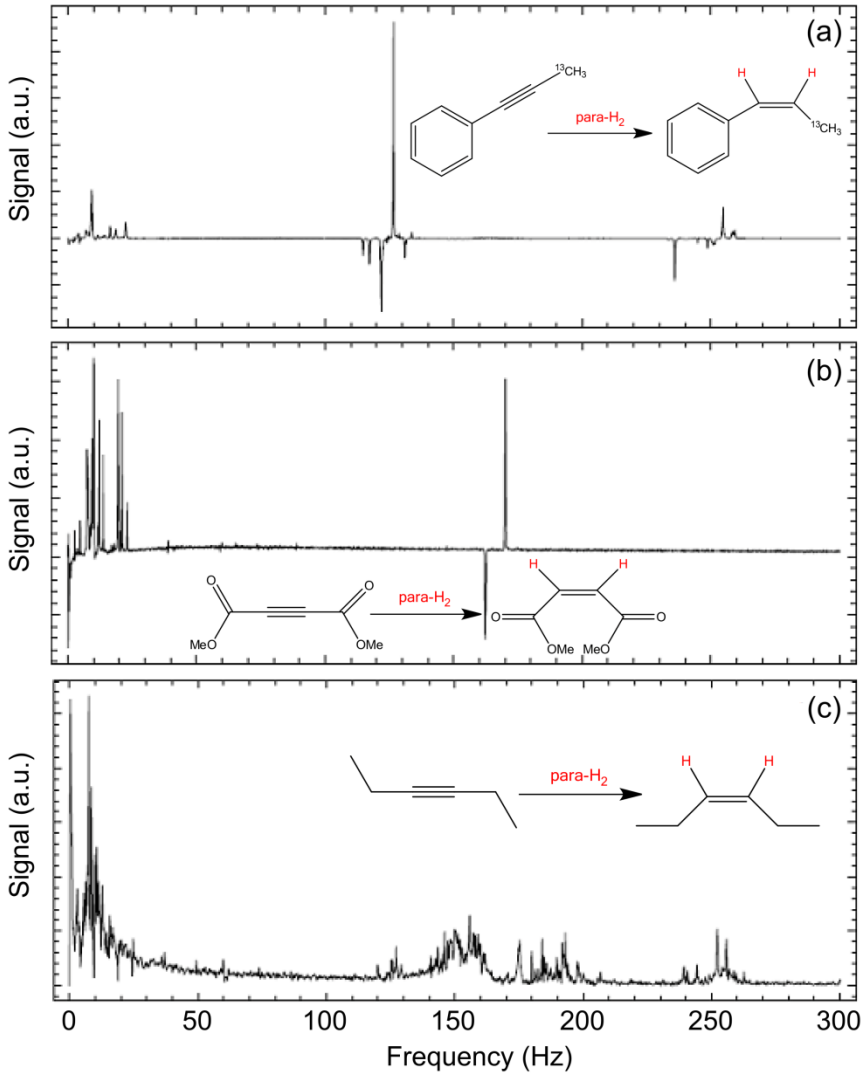

Figure 6.4 Zero-field PHIP spectra for several compounds. In (a) parahydrogen is added to 1-phenyl-1-propyne, labeled with ^{13}C in the CH_3 group. In (b), parahydrogen is added to acetylene dimethylcarboxylate with ^{13}C in natural abundance. In (c) parahydrogen is added to 3-hexyne with ^{13}C in natural abundance (c). In (a) and (b), the imaginary component is presented; in (c), magnitude is presented.

These spectra are the result of averaging 1, 6, and 32 transients respectively. The phenyl propene spectrum displays characteristics similar to the ethylbenzene-β^{13}C spectrum, although the phase and splitting pattern is clearly different since neither of the parahydrogen derived protons are part of the labeled group. The dimethyl maleate spectrum shown in (b) is the superposition of two different ^{13}C There are some residual splittings in the low-frequency part of the spectrum, which will be the subject of future investigation. The spectrum obtained in the hexyne reaction in (c) is the sum of three different ^{13}C isotopomers. For labeled $^{13}CH_3$ groups, signal arises at $^1J_{HC}$ and $2\times{}^1J_{HC}$, where $^1J_{HC} \approx 125$ Hz. For labeled $^{13}CH_2$ groups, the contribution to the signal is centred about $3J/2$, producing signal in the range of 170 to 200 Hz. Long range couplings to other spins yield additional splitting. A more detailed discussion of these spectra and rules for assigning transitions and understanding ZF-PHIP spectra will be presented in a forthcoming publication.

6.4 Observation of Reaction Dynamics with ZF-PHIP

Our technique can be used to monitor the dynamics of a chemical reaction. To illustrate, in Figure 6.5, we plot the area under the magnitude Fourier transform of the ethylbenzene spectra as a function of time for two different conditions.

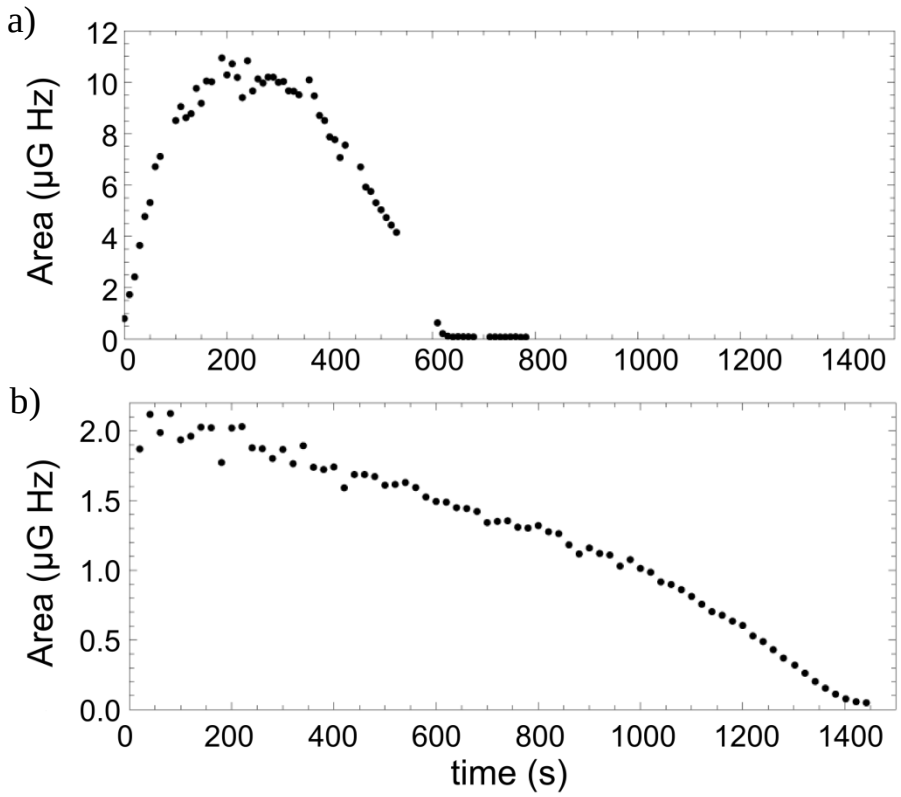

Figure 6.5: Area under the zero-field PHIP spectra of ethylbenzene as a function of time, displaying the dynamics of the reaction, with bubbling (a), and without bubbling (b) in between each transient. In (b), parahydrogen had been bubbled through the mixture for about 100 seconds prior to acquisition of these data.

Data shown in (a) were acquired in the styrene-α ^{13}C reaction, with 1 second of bubbling prior to each excitation pulse. The initial rise in signal amplitude is due to hydrogenation and solvation of Wilkinson's catalyst. While the reaction is limited by the density of dissolved catalyst, the amplitude is roughly flat. When the styrene density drops below a critical value, signal starts to drop. Data in (b) were acquired in the styrene-β ^{13}C reaction without bubbling in between transients (these data were preceded by ≈ 100 total seconds of bubbling). The dissolved parahydrogen forms a reservoir of spin-order, as signal persists for about 20 minutes. In a) the styrene is already consumed after 600 sec because fresh hydrogen is supplied before acquisition of each transient. In b) the reaction is much slower because no fresh hydrogen is supplied and both styrene and hydrogen are consumed. This is also the reason for the smaller maximum amplitude. This may be of considerable use in applications where it is not convenient to bubble through a region of interest, for example, in imaging or spectroscopy in microfluidic devices.

6.5 ZF-PHIP simulations

Calculations for the simulations discussed in the text were performed as follows: The *J*-coupling Hamiltonian is

$$H_J = \sum_{j,k;k>j} J_{jk}\,\mathbf{I}_j \cdot \mathbf{I}_k\,, \tag{6.3}$$

where j and k run over M spins. Given an initial density matrix, ρ_0, the time dependent density matrix is

$$\rho(t) = e^{-i\mathrm{H}_J t}\rho(0)e^{-i\mathrm{H}_J t}\,, \tag{6.4}$$

and the magnetization is determined by

$$M_z(t) = nTr\left[\sum_j \rho(t)\gamma \mathrm{I}_{jz}\right] \tag{6.5}$$

where n is the molecular density and γ_j is the gyromagnetic ratio of the jth spin. Here $\rho(0) = \mathrm{U}_z\,\rho_{\mathrm{ave}}\,\mathrm{U}^{\dagger}{}_z$ is the density matrix following application of a pulse of magnetic field B_z in the z direction, where $U_z = \exp\left[i\sum_j \gamma_j \mathrm{I}_{jz}\mathrm{B}_z\right]$ and ρ_{ave} is the result of averaging the density matrix for product molecules created at random times.

The initial density matrix is determined by averaging over molecules created at t'

$$\rho_{ave} = \frac{1}{t}\int_0^t e^{-iH_j t'}\rho_s e^{-iH_j t'}dt'. \tag{6.6}$$

Here ρ_s is the polarized part of the density matrix immediately following the addition of the parahydrogen derived spins,

$$\rho_s = \mathbf{1}/4 - \mathbf{I}_1 \cdot \mathbf{I}_2\,, \tag{6.7}$$

with all other spins unpolarized. The result of this averaging is a density matrix described by pairs of heteronuclear and homonuclear singlets,

$$\rho_{ave} = \sum_{j,k;k>j} a_{jk}(t)\,\mathbf{I}_j \cdot \mathbf{I}_k\,. \tag{6.8}$$

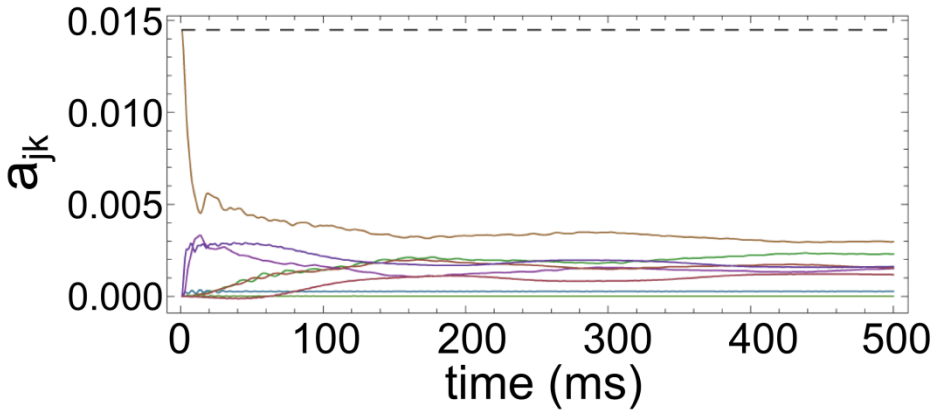

Figure 6.6: Coefficients $a_{jk}(t)$ as a function of time after the beginning of random hydrogenations. The brown trace with the nonzero initial value corresponds to the parahydrogen derived spin pair. The dashed line is the sum of all a_{jk}.

To illustrate the propagation of "singlet order" through the molecule, Figure 6.6 shows the coefficients $a_{jk}(t)$ (solid traces) as a function of time since the start of hydrogenations. For these calculations, the model system consisted of 6 spins, a $CH_2{}^{13}CH_3$ system. The term corresponding to the singlet order between the parahydrogen derived spins is given by the brown line, initially the only nonzero a_{jk}. It is interesting to note that the sum $\sum_{j,k>j} a_{jk}(t)$ is constant, as indicated by the dashed line. More details of the propagation of the singlet order through a molecule will be presented in Chapter 8. The simulations presented in Figure 6.6 of the main text were performed on a truncated molecule consisting of eight spins, the five protons and the ^{13}C on the ethyl part of the molecule, and the two nearest protons on the benzene ring. Including more spins is possible however our numerical code begins to run slowly. The *J*-coupling parameters used in these simulations for ethylbenzene-β ^{13}C can be found in the literature[89,90], $^1J(HC)$ =126.264 Hz, $^2J(HC) = -4.906$, $^4J(HC) = -0.245$ Hz, $^3J(CH_2, CH_3) = 7.596$ Hz, $^4J(H, CH_2) = -0.639$ Hz, and $^5J(H, CH_3) = -0.02$, with errors quoted at the mHz level. We measured the heteronuclear coupling parameters for ethylbenzene-α ^{13}C on a 300 MHz spectrometer finding, $^1J(HC) = 126.3$ Hz, $^2J(HC) = -4.2$ Hz, and $^3J(HC) = 3.8$ Hz. We conservatively estimate uncertainty in our measurements

at the level of 100 mHz. Simulations were not dramatically changed by varying the coupling parameters by 100 mHz.

We now illustrate briefly how magnetization is generated starting from scalar order. Following addition of parahydrogen to a substrate molecule, evolution under the *J*-coupling Hamiltonian leads to terms in the density matrix of the form $a_{jk}\ \mathbf{I}_j\mathbf{I}_k$ (here **I** spins do not necessarily have the same gyromagnetic ratio). Suppose we now apply a pulse in the z direction with magnitude B_z and duration t_p. The density matrix following the pulse is

$$\rho_0 = R_z\,(B_z\,t_p)\,\rho_s\,R^{\dagger}{}_z\,(B_z\,t_p), \tag{6.9}$$

where

$$R_z(B_z t_p) = \exp\left\{ i\sum_j \gamma_j I_{jz} B_z t_p \right\}. \tag{6.10}$$

Focusing our attention on two spins, j and k, one can show as detailed in Chapter 8 that the density matrix following the pulse is

$$\rho_0 = a_{jk}\left(I_{jz}I_{kz} + ZQ_x\cos\eta + ZQ_y\sin\eta\right), \tag{6.11}$$

where

$$\begin{aligned} ZQ_x &= I_{jx}I_{kx} + I_{jy}I_{ky} \\ ZQ_x &= I_{jx}I_{ky} - I_{jy}I_{kx} \\ ZQ_z &= \frac{1}{2}I_{jz} - I_{kz}, \end{aligned} \tag{6.12}$$

and $\eta = B_z\ t_p\ (\gamma_j - \gamma_k)$. These operators are orthonormal under the trace operation, and have the following convenient commutation relations:

$$[ZQ_x\ ,\ ZQ_y] = i\ ZQ_z\ , \tag{6.13}$$

and cyclic permutations thereof,

$$\begin{aligned} [ZQ_x,\ H_J] = 0 \quad ,\quad [I_{jz}I_{kz},\ H_J] = 0, \\ [ZQ_z\ ,\ H_J] = -\ i\ J\ ZQ_y,\quad [ZQ_y,\ H_J] = i\ J\ ZQ_z, \end{aligned} \tag{6.14}$$

and with $H_Z = B_z(\gamma_j\ I_{jz} - \gamma_k\ I_{kz})$

$$[ZQ_x\ ,\ H_Z] = -\ iB_z\ (\gamma_j - \gamma_k)\ ZQ_y\ , \tag{6.15}$$

$$[ZQ_y , H_Z] = iB_z (\gamma_j - \gamma_k) ZQ_x ,$$
$$[ZQ_z , H_Z] = 0 ,$$
$$[I_{jz}I_{kz}, H_Z] = 0 ,$$

for $B_x=B_y = 0$. The time dependence is determined by the Liouville equation:

$$\frac{d\rho}{dt} = i\left[\rho, H_J\right]. \tag{6.16}$$

We expand ρ in terms of the operators ZQ_x , ZQ_y , ZQ_z , insert it into Eq. (6.16), make use of the commutation relations of Eq. (6.13), and solve the resulting set of coupled first-order differential equations for the coefficients in the expansion of ρ. We find

$$\rho(t) = a_{jk}\left(I_{jz}I_{kz} + ZQ_x \cos\eta + ZQ_y \sin\eta\cos Jt - \sin\eta\sin Jt\, ZQ_y\right). \tag{6.17}$$

Employing Eq. (6.5), we find that the magnetization is

$$M_z(t) = \frac{N}{2} a_{jk}\left(\gamma_k - \gamma_j\right)\sin Jt\sin\eta. \tag{6.18}$$

This gives both the phase of the signal following the pulse, and indicates that the optimum pulse amplitude is $\eta = \pi/2$.

It is worth emphasizing the following intuitive interpretation of the above discussion. Prior to application of a pulse of magnetic field in the z direction, the initial scalar spin order is proportional to $I_{jz}I_{kz} + ZQ_x$. The $I_{jz}I_{kz}$ term can be ignored since it commutes with H_Z and H_J. A pulse along the z direction with $\eta = \pi/2$ rotates ZQ_x into ZQ_y, which then precesses about the Hamiltonian, proportional to ZQ_x, resulting in an oscillating ZQ_z term which bears observable magnetization.

6.6 Significance of ZF-PHIP and conclusions

Finally, we make several observations: 1) Here we operate in zero magnetic field. Working in small but finite fields on the order of 1 mG may yield additional information regarding molecular structure, albeit at the expense of additional spectral complexity. [22] 2) A common objection to low- and zero-field NMR is that spectra become complex as the number of spins increase, as exemplified by comparison of the ethanol-α^{13}C spectrum reported in Ref. [19] and the ethylbenzene-α ^{13}C obtained here. The increasing complexity of spectra with spin system size is a feature that is also encountered in standard high-field NMR, and has been successfully addressed by application of multi-pulse sequences and multidimensional spectroscopy. The theory of multiple pulse sequences for zero-field NMR has been worked out some time ago [91], and presumably, many of the techniques developed for high field could be adapted to zero-field. 3) We achieve linewidths of about 0.1 Hz. For ^{13}C-H *J*-coupled systems, the dispersion in signal is about 300 Hz, so roughly 1500 lines can fit in a spectrum without overlapping. This is similar to what may be achieved in a 400 MHz spectrometer if we assume proton chemical shifts ranging over 6 ppm and proton linewidths of about 0.5 Hz. 4) The sensitivity of the magnetometer used in this work was about 0.15 nG/Hz$^{1/2}$ using a vapour cell with a volume of 10 mm^3. Sensitivities about 2 orders of magnitude better have been achieved in larger vapor cells [92], which will enable measurements on larger samples with much lower concentration.

In conclusion, we have demonstrated NMR without the use of any magnets by using parahydrogen induced polarization and a high sensitivity atomic magnetometer with a microfabricated vapour cell. The mechanism by which the symmetry of the singlet states is broken in zero field relies only upon the presence of heteronuclear *J*-coupling and not chemical shifts, in contrast to many experiments performed in high field. Hydrogen-carbon *J*-couplings through at least three bonds, and hydrogen-hydrogen couplings through four bonds are observed. We also observe that polarization is naturally transferred through several bonds to remote parts of the molecule. This can be contrasted with *in-situ* hydrogenation in high field, where chemical shifts larger than *J*-couplings prevent efficient polarization transfer without the use of auxiliary RF pulses. Sensitivity is sufficient to perform *J*-spectroscopy on samples with ^{13}C in natural abundance with little signal averaging. The resulting spectra, while

exhibiting a large number of lines, can easily be divided into different parts, which can directly be assigned to different isotopomers of the molecule at hand. While our technique may appear limited to molecules to which hydrogen can be added, recent advances using iridium complex catalysts enable polarization of molecules without hydrogenation[50,52], significantly expanding the scope of applicability of zero-field PHIP as detailed in the following Chapter.

7. Zero-field NMR using parahydrogen in reversible exchange

This Chapter describes the first NMR experiments in zero field employing non-hydrogenative parahydrogen induced polarization (NH-PHIP) producing signal amplification by reversible exchange (SABRE).[50–52] This work has been previously published under the title "Zero-field NMR using parahydrogen in reversible exchange" by the American Chemical Society[93]. Following the approach used in Refs. [19,21,28] we work at zero magnetic field by eliminating the Earth's magnetic field with μ-metal shields, and we use an all-optical rubidium magnetometer for detection. In addition to cryogen-free and potentially portable nature of our technique, the magnetically shielded environment has high absolute spatial and temporal homogeneity. We demonstrate that this technique enables the detection of small quantities of analyte (down to 6 mM in a sample volume of 250 μL i.e. 100 nL as neat liquid) while retaining all analytically useful spectral information of the zero-field spectrum. The sensitivity of the present experiments is also illustrated by the first observation of zero field NMR signals from nitrogen-15 in natural abundance. In contrast to previous work at high magnetic field[50–52] and at low magnetic field,[49,94] the NH-PHIP process presented here evolves entirely at zero field. The spectra exhibit significant shifts in line positions as a function of the molecular environment, in this case, due to solvent effects. The acquired spectra are in agreement with computer-simulated spectra, showing the dependence on the topology and parameters of the *J*-coupling network and demonstrating the high information content of zero-field spectra. It is important to note that the NH-PHIP method is not limited to a specific substrate but can be used on a growing class of compounds containing nitrogen-heterocycles[50,95] as well as amino acids and peptides.[96]

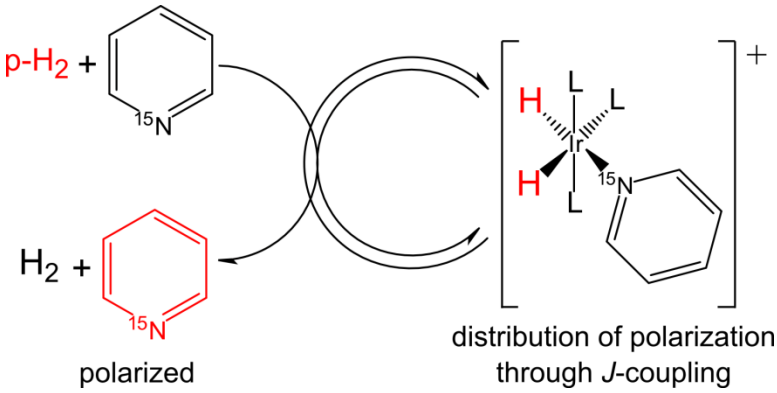

Figure 7.1 NH-PHIP transfer mechanism. Hydrogen and pyridine bind reversibly to the catalytic intermediate. Polarization is transferred from parahydrogen to pyridine through the network of *J*-couplings.

Figure 7.1 illustrates the NH-PHIP transfer process, which occurs when parahydrogen and the analyte are in reversible exchange via an iridium-based catalytic intermediate. During the time period in which an analyte molecule and a parahydrogen molecule are simultaneously bound to the same metal complex, a *J*-coupling network is formed, causing the singlet spin order of parahydrogen to spread throughout the metal complex; in particular, scalar spin order develops among the spins of the analyte, which persists in the analyte after the complex dissociates.[51] This scalar spin order is a form of polarization not bearing magnetization and without directionality, since there is no magnetic field along which alignment of the polarization could occur. Fortunately, spin order involving heteronuclear pairs can be converted to observable magnetization by application of a DC magnetic-field pulse. A coil is used to apply these pulses in the vertical direction. Such a DC pulse breaks the symmetry of the initial state for heteronuclear pairs because it rotates nuclei with differing gyromagnetic ratio by differing angles. Thereby the pulse creates the coherences whose ensuing evolution produce observable oscillations of the vertical component of magnetization. The duration of the pulse is short and the amplitude is strong compared to the *J*-couplings such that evolution under the *J*-couplings can be ignored during the pulse. Scalar spin order transferred to homonuclear ^{1}H pairs is not excitable because it has singlet character and the symmetry is not broken by a pulse acting on nuclei with identical gyromagnetic ratio. Sections 7.1 and 7.2 provide a more detailed description of the experimental setup, as well as a discussion of the polarization process. Additionally, a two-spin model is presented that describes

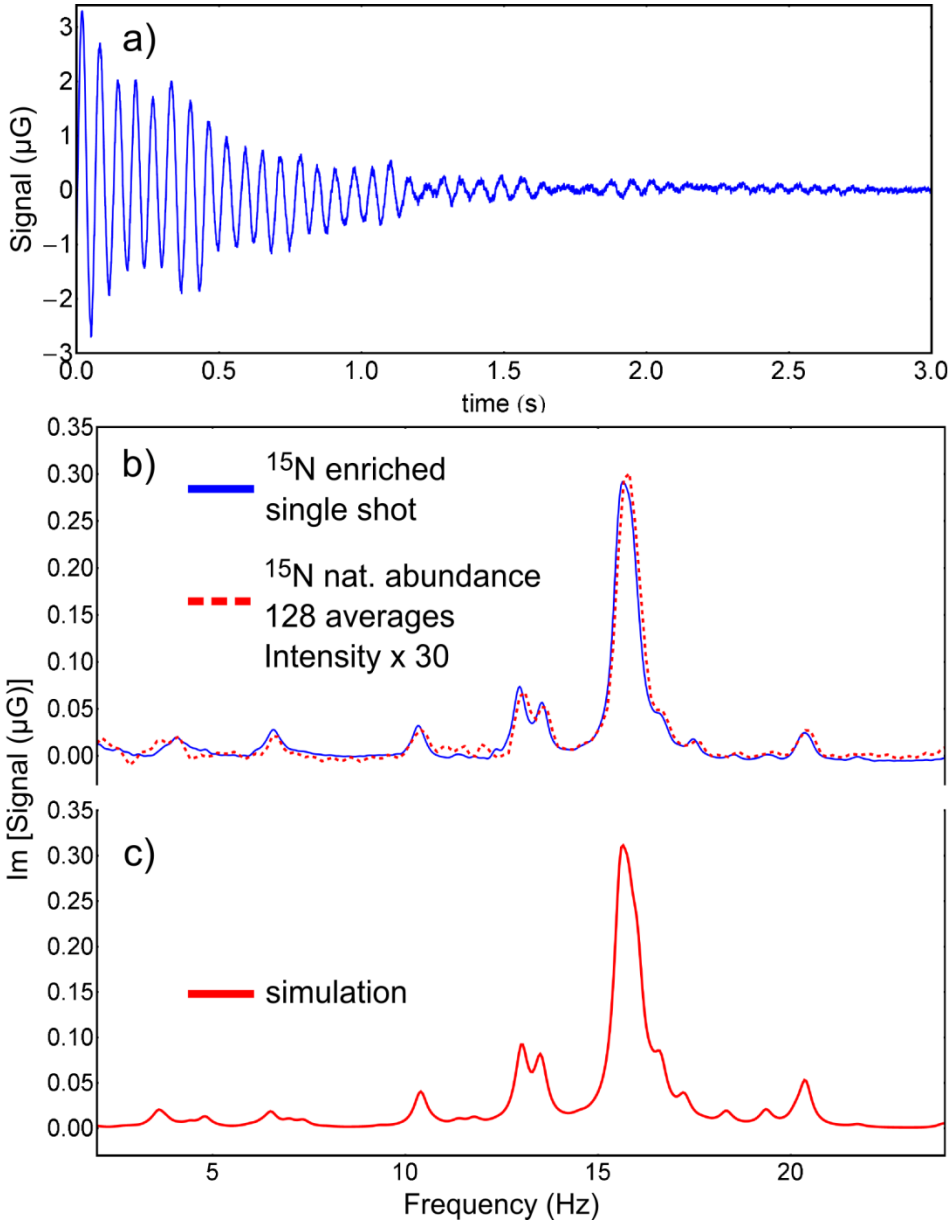

Figure 7.2. a) Single-shot transient and b) the imaginary part of its Fourier transform for NH-PHIP polarized pyridine. The solid blue trace in a) and b) shows data acquired with a 250 μL sample after 10 s of bubbling parahydrogen through a solution containing Crabtree's catalyst (0.6 mM), with methanol as solvent and ^{15}N-labeled pyridine as analyte at a concentration of 40 mM. The red-dashed spectrum in b) is obtained from pyridine at natural abundance of ^{15}N (0.36 %) at a concentration of 3 M, which implies a 10 mM concentration of ^{15}N-containing pyridine. In c) a numerically simulated spectrum is provided for comparison.

the effect of the DC-pulse on a heteronuclear singlet and the ensuing evolution under the *J*-coupling Hamiltonian.

A single-shot transient and the imaginary part of its Fourier transform obtained with ^{15}N-labeled pyridine are shown by the solid blue curves in Figure 7.2 a) and b). The single-shot signal-to-noise of the largest peak is close to 300 at a noise floor of 1 nG. The dashed red curve in Figure 7.2 b) shows that it is possible to acquire identical spectra from pyridine with ^{15}N at its low natural abundance of 0.36%. For the unlabeled sample, the concentration of the analyte was larger by a factor of 75 than for the labeled sample.

Note, however, that the signal does not scale linearly with the concentration of the analyte but is dependent on many parameters such as exchange rates and the concentrations of parahydrogen, catalyst and analyte.

The spectrum can be approximately understood as follows: The largest *J*-coupling in ^{15}N-pyridine is the two-bond coupling, $^2J_{NH}$, between the ^{15}N and the two equivalent nearest protons, approximately forming an AX_2 system. Such a system yields a peak at $3J/2$.[19] Since $^2J_{NH}$ = 10.14 Hz (see Chapter 4), we expect signal at ~15.3 Hz. Long-range couplings to other protons produce a number of additional sidebands and a small shift of the largest peak to ~15.6 Hz. Note that the imaginary component of the Fourier transform is shown (without additional phasing). In these NH-PHIP experiments the imaginary part is absorptive because the evolution starts from a non-magnetized state (see Section 7.2). These features are also reproduced by a simulation shown in the solid red trace in part c) of Figure 7.2. (Details concerning the simulation are provided in Section 7.2) Interestingly, despite the excellent SNR for the ^{15}N containing isotopomers of pyridine it was not possible to detect ^{13}C-pyridine isotopomers at their natural abundance (see Section 7.2.2). We attribute this to the low (1.1%) abundance of ^{13}C and the higher signal complexity in isotopomers with both ^{13}C and ^{15}N, as discussed in the SI.

For comparison with the NH-PHIP experiments, we performed measurements of thermally polarized ^{15}N-labeled pyridine. These experiments were performed with an identical 5 mm NMR tube. A sample of 250 μL neat (14 M) ^{15}N-labeled pyridine was polarized in a 1.6 T permanent magnet and then pneumatically shuttled to the zero-field region for detection.[28] The time for transfer of the sample from the magnet into the detection region was approximately 250 ms. The NMR tube traveled in a solenoid that provided a "guiding field," ensuring that the spins remained magnetized parallel to the guiding field during the shuttling. Upon arrival of the sample in the zero-field

region, the guiding field was turned off suddenly with respect to any spin dynamics that occur under the influence of the *J*-couplings, and the spectrum shown in Figure 7.3 was acquired. Note that for this experiment, evolution starts from a magnetized state and it is the real part of the Fourier transform that is absorptive, as in conventional 1D NMR. (see Section 7.2)

After averaging 128 transients, the SNR of the main feature centered near 17 Hz is ~70. Comparison of this value to the single-shot SNR of ~300 for the NH-PHIP measurements gives an estimate of the achieved sensitivity enhancement: scaling by $\sqrt{128}$ for the number of averages and by 14M / 40mM for the difference in concentration reveals a sensitivity gain of $\sim 1.7 \times 10^4$ with NH-PHIP.

Additionally, a frequency shift of the main peak of (1.2 ± 0.1) Hz is observed. For NH-PHIP measurements in methanol the main peak is centered around 15.6 Hz and shifts to 16.8 Hz in the neat liquid. The frequency shift is presumably due to the change in the microscopic environment associated with the presence of the solvent. This effect has been documented in detail in measurements performed at high field with cryogenically cooled magnets,[97,98] but the experiments presented here demonstrate that similar information can be extracted using zero-field spectroscopy with optical detection.

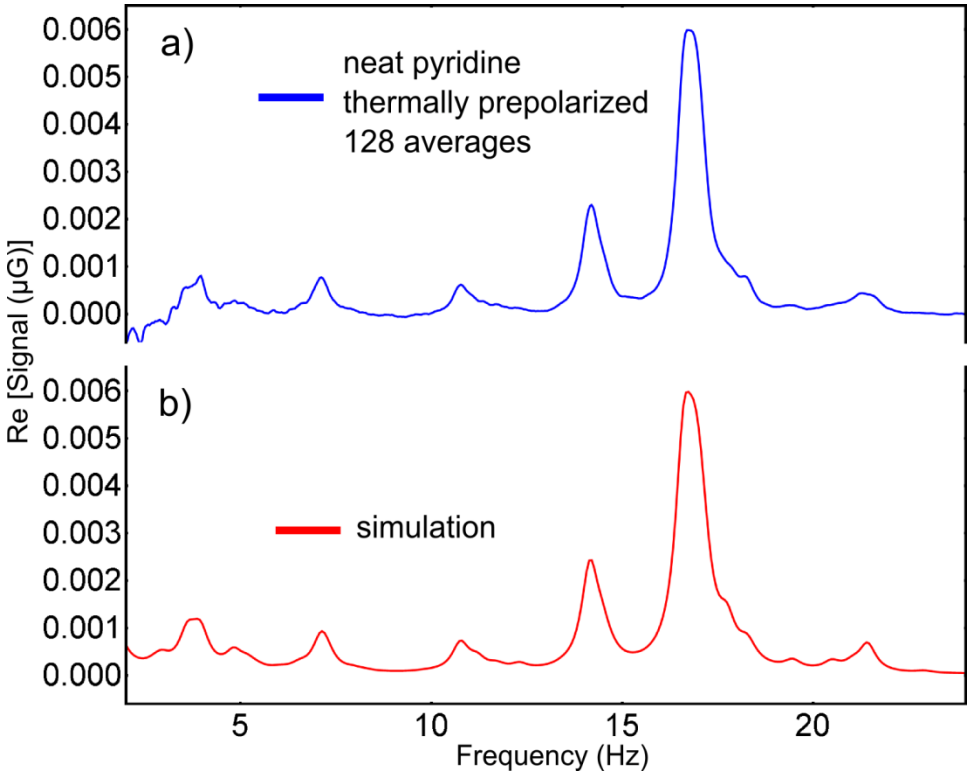

Figure 7.3 Spectrum obtained after averaging 128 transients of neat ^{15}N-labeled pyridine, prepolarized in a 1.6 T permanent magnet and shuttled into the zero-field region for detection. In a) the experimental data is shown and b) shows the simulated spectrum.

Finally, we show that NH-PHIP is particularly promising for analysis of compounds in low concentration. Table 1 provides the signal-to-noise ratio obtained for five different concentrations of ^{15}N-pyridine.

Table 8.1). Signal-to-noise ratio (SNR) of the largest spectral peak at 15.6 Hz as a function of analyte concentration. Above 40 mM pyridine concentration, we observe constant SNR of about 300. All identifying spectral features have SNR >1 for concentrations down to 6 mM. In these experiments, the noise floor was about ~1 nG.

Concentration	6 mM	12 mM	40 mM	80 mM	160 mM
SNR	20 ± 20	160 ± 20	300 ± 20	280 ± 20	290 ± 20

All measurements were performed at a catalyst-to-analyte ratio of 1:6 by weight. For concentrations down to 40 mM the signal appears independent of the amount of analyte, and is presumably dictated by the amount of dissolved parahydrogen. This is in agreement with the findings by Gong et al.[49]. At a concentration of 6 mM, the main peak at ~15.6Hz has an SNR of ~15. At that concentration smaller peaks that are 10-30 times weaker than the main peak have an SNR on the order of one, and spectral information is lost at lower concentrations. At the expense of spectral information, it is possible to go to even lower concentrations, as demonstrated in Ref. [49].

7.1 Setup and sample preparation for ZF-NH-PHIP experiments

The experimental setup employed here was similar to that used in previous work[19,21]. The sample was contained in a standard 5 mm NMR tube placed directly above a zero-field alkali-vapor magnetometer. This detector consists of microfabricated 5 mm × 2 mm × 1 mm rubidium cell, thereby reducing much of the size requirements associated with traditional high-field NMR. The sample, with a total volume of 250 μL, was composed of pyridine (Sigma CAS# 34322-45-7) and Crabtree's catalyst (1,5-Cyclooctadiene)(pyridine) (tricyclohexylphosphine)-iridium(I) hexafluorophosphate (Sigma CAS# 64536-78-3) in anhydrous methanol (Sigma CAS# 67-56-1) as solvent. The sample was held at a temperature of 40 °C. The tube was connected to a gas manifold and parahydrogen was bubbled through the solution at a flow rate of 50 sccm at a pressure of 70 psig (5.8 bar). Bubbling was stopped 0.3 s prior to acquisition. All measurements were performed at a catalyst-to-analyte ratio of 1:6 by weight (following Ref. [49]). The sensitivity of the magnetometer to fields in the vertical direction (i.e. the direction of detection) is about 1 nG/Hz$^{1/2}$ in the frequency range of 0-20 Hz, where signals occur in the present work.

A schematic of the experimental setup is provided in Figure 7.4. Detection is performed with a Rb-vapor atomic magnetometer, operating in the spin-exchange relaxation-free regime[23] and using two lasers for optical pumping and probing[19,21,28]. The vapor cell has dimensions 5 mm × 2 mm × 1 mm, contains ^{87}Rb and 1300 torr of N_2 buffer gas and is operated at 190 °C.

The magnetic field of the pulses was 0.917 G, calibrated by determining the length of a π–pulse on proton spins of water (~128 μs), prepolarized in a 1.6 T permanent magnet. In order to establish zero field, the Earth's magnetic field is shielded with a set of four layers of μ-metal shielding. Any remaining fields are reduced to the μG level with a set of three orthogonal shimming coils. Data were acquired with a sampling rate of 2 kS/s.

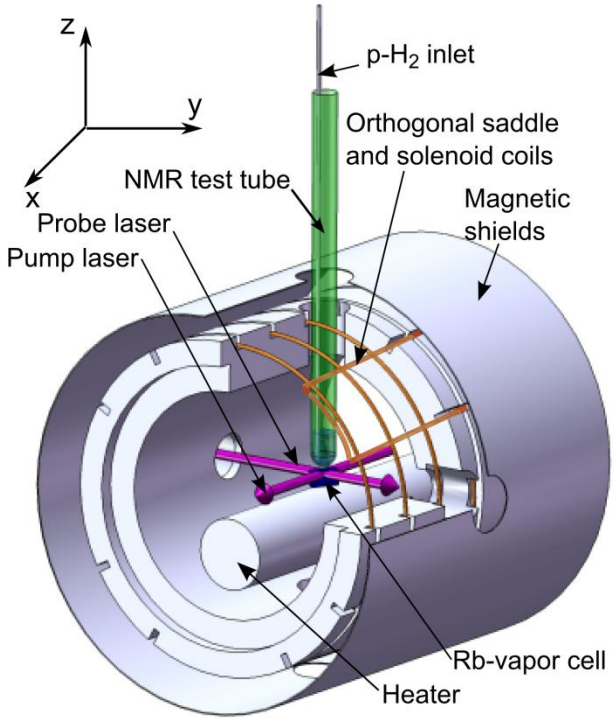

Figure 7.4) Experimental setup: The central part of the magnetometer is the Rb-vapor cell heated to 190 °C. The magnetometer is operated in a pump-probe mode using 795 nm diode lasers. Pulses of DC magnetic field can be applied with a set of coils to the sample held in a 5 mm NMR tube. Saddle and solenoid coils are available to control the magnetic field in all three directions. To achieve zero magnetic field, the entire setup is surrounded by four layers of μ-metal magnetic shields. (Only the innermost layer is shown.) The coils are used to compensate for any remaining magnetic fields down to the μG level.

Parahydrogen was produced at 29 K by flowing hydrogen gas through a bed of hydrated iron(III) oxide (Sigma CAS# 20344-49-4) catalyst in a setup similar to that described in Ref. [99], and the parahydrogen was stored in an aluminum canister at room temperature at an initial pressure of 150 PSI. The population of the parahydrogen state was in excess of 98%, determined by NMR measurements of the orthohydrogen signal in a 300 MHz Bruker Avance NMR spectrometer. The rate of thermalization of the parahydrogen back to a 1:3 para-ortho mixture of hydrogen was on the order of 1% per day.

The timing sequence of the experiment is as follows: parahydrogen is bubbled through the solution for ten seconds, the bubbling is stopped, a pulse

of DC magnetic field is applied, and the resulting transient is acquired. Ten seconds of bubbling time was chosen to allow for the distribution of the scalar order driven by the *J*-coupling. Since the *J*-couplings are weak (on the order of 10 Hz) sufficient time must be allowed for the redistribution of scalar order. For bubbling times longer than 10 s any further signal gain is offset by spin relaxation.

7.2 NH-PHIP at Zero Field: a Two Spin Model

The chemical processes involved in the NH-PHIP polarization mechanism are described in the literature[51]. Here we provide a simplified picture of the polarization transfer mechanism at zero field to enable understanding of the origin of the detected signal. Parahydrogen is bubbled through a solution containing the catalyst and the analyte (^{15}N-pyridine). The hydrogen and the pyridine bind reversibly to the catalytic intermediate, alternating between being bound to the iridium center and remaining unbound in solution. The complex that includes the bound ligands and the iridium center imposes a *J*-coupling network, and singlet spin order initially present in a bound parahydrogen molecule spreads throughout the network driven by the *J*-coupling Hamiltonian. The *J*-coupling Hamiltonian H_J is given as sum over scalar products between all possible spin pairs including homo- and heteronuclear spin pairs:

$$\mathrm{H}_J = \sum_{j,k>j} J_{j,k}\, \mathbf{I}_j \cdot \mathbf{I}_k \ , \tag{7.1}$$

and the initial density matrix ρ_0 has a term proportional to the scalar product between the two parahydrogen derived spins directly bound to the iridium center:

$$\rho_0 = \tfrac{1}{4}\, \hat{1} - \mathbf{I}_1 \cdot \mathbf{I}_2, \tag{7.2}$$

Since both the initial singlet and the *J*-coupling Hamiltonian transform as scalars, spreading of the initial spin order under H_J yields a spin state that also transforms as a scalar. After spreading of the spin order, the ensemble averaged density matrix thus includes contributions from scalar products of the form $\mathbf{I}_j \cdot \mathbf{I}_k$, between arbitrary spins in the complex, i.e. for homo- and heteronuclear pairs, as well as higher-order scalar operators involving multiple spins. Our discussion here uses a 2-spin model to illustrate the way in which a scalar product $\mathbf{I} \cdot \mathbf{S}$ involving a heteronuclear spin pair in the analyte molecule gives rise to observable signal. Similar considerations apply for hydrogenative PHIP and are presented in Ref. [21]. A more detailed discussion of the spreading of spin order from an initial singlet will be provided in Chapter 8.

Upon dissociation of the analyte from the catalyst, only the spin terms involving nuclei on a given pyridine molecule, are retained. This scalar order, obtained using NH-PHIP at zero field, can be transformed into an observable magnetization with a pulse of DC magnetic field. We consider the evolution of a heteronuclear term $\rho_{IS} \propto \mathbf{I}\cdot\mathbf{S}$ during the pulse and the ensuing evolution. (Homonuclear terms are not discussed because they do not change under the applied pulses and do not produce observable signal. Their evolution under the zero-field Hamiltonian only produces scalar order that does not bear magnetization.) The scalar product can be expressed as:[21,31]

$$\mathbf{I}\cdot\mathbf{S} = \mathrm{I_x S_x} + \mathrm{I_y S_y} + \mathrm{I_z S_z} = \mathrm{ZQ_x} + \mathrm{I_z S_z}, \tag{7.3}$$

where ZQ_x is the x-component of a set of zero-quantum operators[1]:

$$\begin{aligned} \mathrm{ZQ_x} &= \mathrm{I_x S_x} + \mathrm{I_y S_y}, \\ \mathrm{ZQ_y} &= \mathrm{I_y S_x} - \mathrm{I_x S_y} \\ \mathrm{ZQ_z} &= \frac{1}{2}(\mathrm{I_z} - \mathrm{S_z}). \end{aligned} \tag{7.4}$$

These operators obey the commutation rules for a set of Cartesian components of angular momentum:

$$[\mathrm{ZQ_i}, \mathrm{ZQ_j}] = \varepsilon_{ijk}\, i\, \mathrm{ZQ_k}, \tag{7.5}$$

where ε_{ijk} is the Levi-Civita symbol. Expressing $\mathbf{I}\cdot\mathbf{S}$ in the form given by Eq. (7.3) is convenient for two reasons. First, the operator I_zS_z commutes with both H_J and the pulse Hamiltonian H_{DC} (as shown below); so, the spin order represented by I_zS_z does not evolve coherently during the experiment nor does it contribute to the signal. The term ρ_{IS} in the initial density matrix may thus be considered proportional to ZQ_x. Furthermore, for an initial density matrix ZQ_x, the evolution under H_{DC} and H_J may be represented as a sequence of rotations that convert the density matrix into a linear combination of ZQ_x, ZQ_y, and ZQ_z. This can be demonstrated by first noting that the Hamiltonian for the DC pulse applied along the *z* axis is

$$\begin{aligned} \mathrm{H_{DC}} &= -\mathrm{B_z}\left(\gamma_\mathrm{I}\mathrm{I_z} + \gamma_\mathrm{S}\mathrm{S_z}\right) = \\ &-\mathrm{B_z}\left[\frac{(\gamma_\mathrm{I}+\gamma_\mathrm{S})}{2}(\mathrm{I_z}+\mathrm{S_z}) + \frac{(\gamma_\mathrm{I}-\gamma_\mathrm{S})}{2}(\mathrm{I_z}-\mathrm{S_z})\right]. \end{aligned} \tag{7.6}$$

The term $I_z + S_z$ produces no evolution, since it commutes with both the initial density matrix and with $I_z - S_z$. We can therefore consider the pulse Hamiltonian to be

$$-B_z \frac{(\gamma_I - \gamma_S)}{2} (I_z - S_z) = -B_z(\gamma_I - \gamma_S)\, ZQ_z. \tag{7.7}$$

Application of the pulse causes the density matrix to rotate in the transverse plane spanned by ZQ_x and ZQ_y, as shown in Figure 7.5. (The weak effects of the *J*-couplings during the pulse can be safely neglected.) During a pulse, the density matrix evolves as

$$\rho(t) = ZQ_x \cos(\omega t) + ZQ_y \sin(\omega t), \tag{7.8}$$

where the frequency ω is given by

$$\omega = -B_z(\gamma_I - \gamma_S). \tag{7.9}$$

At the end of the pulse, which maximizes the signal intensity (e.g. a π/2 pulse in the *ZQ*-subspace), the density matrix is aligned along ZQ_y. The term ZQ_y then evolves under H_J. Since all terms in the *ZQ*-subspace commute with I_zS_z, we may consider that $H_J \propto ZQ_x$. The *J*-coupling thus causes the density matrix to precess in the plane spanned by ZQ_y and ZQ_z. While ZQ_y exhibits no

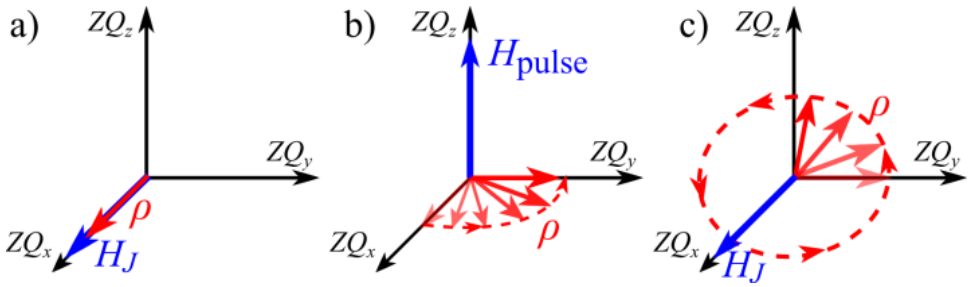

Figure 7.5 Depiction of the evolution of the density matrix in the "zero-quantum space" under the pulse and the zero-field *J*-coupling Hamiltonian. a) Initially, at zero field, the scalar spin order that develops during the NH-PHIP is parallel to the *J*-coupling Hamiltonian (both shown as vectors in this representation). b) Upon application of a π/2 pulse in the z direction, the density matrix is rotated to ZQ_y. c) After the pulse, the density matrix rotates about the zero-field Hamiltonian, creating an oscillating ZQ_z term that bears observable magnetization.

magnetization and is not directly observable, the spin order described by ZQ_z does correspond to sample magnetization; since the gyromagnetic ratios of spins *I* and *S* are different, a net magnetization is present when the two spins are oriented in opposite directions. A Fourier transform of the oscillating sample magnetization associated with the precession of the density matrix in the *ZQ*-subspace yields the zero-field spectrum.

7.2.1 Validation of the Two-Spin Model

We make two distinct observations that validate the two-spin model. The first observation is that all NH-PHIP transients recorded start at zero net magnetization, which implies that the imaginary part of the Fourier transform is absorptive. The pulse itself does not produce magnetization, but rather creates the ZQ_y term that evolves into the observable ZQ_z term after a period of evolution under H_J. The second observation validating the two-spin model is the behavior during the pulse. The ideal pulse for maximizing the signal, when starting from a density matrix ZQ_x, is a $\pi/2$ pulse in the *ZQ*-subspace. The $\pi/2$-pulse length depends on the difference in gyromagnetic ratios of the two spins *I* and *S*, since the density matrix precesses in the transverse plane of the *ZQ*-subspace at frequency $\omega = -B_z(\gamma_I - \gamma_s)$. Figure 7.6 shows the experimentally measured dependence of observed signal intensity at the strongest spectral peak vs. proton tip angle α (a proton π–pulse is 128 μs long). This way of formatting the x-axis highlights the fact that the observed nutation frequency is indeed faster than the pure proton nutation by a factor of $\eta = -(\gamma_H - \gamma^{15}_N)/\gamma_H = -1.10$. Overlaying the data is a fit to a sinusoid $\sin(\eta\alpha)$ with $\eta = (-1.09 \pm 0.02)$ in agreement with the prediction of the two-spin model. The error in η stems mainly from inaccuracies in the calibration of the proton tip angle. In this specific case, η is larger than unity because the gyromagnetic ratios of ^{1}H and ^{15}N have opposite signs, with $\gamma(^1\text{H}) = 4.258$ kHz/G and $\gamma(^{15}\text{N}) = -0.432$ kHz/G.

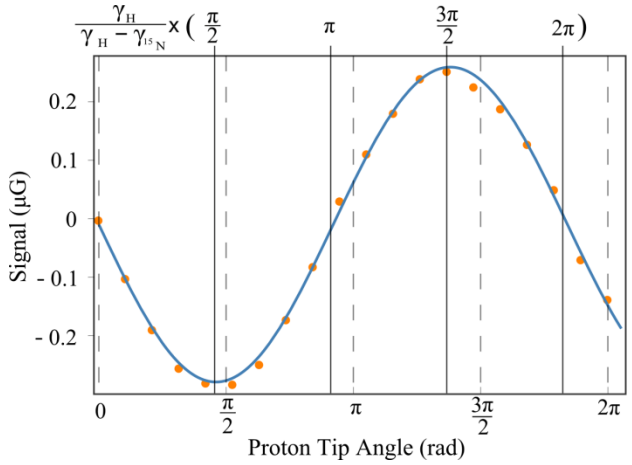

Figure 7.6 Signal intensity as a function of pulse length. The pulse length is given as a proton tip angle, which has been calibrated on water samples beforehand to have a length of 128 μs for a π rotation. The graph shows a fit to a sinusoid $\sin(\eta\alpha)$, with $\eta = -(\gamma_H - \gamma_{15N}) / \gamma_H$.

Given the large SNR in the NH-PHIP measurements it is possible to post-process the data to increase the spectral resolution. Figure 7.7 shows the NH-PHIP spectrum obtained by multiplication of the transient by a shifted Hamming window[100]. Note that this process reveals a splitting of the largest peak. In Figure 7.7 as well as in Figure 7.2, we compare the experimental spectra to simulations performed by numerically diagonalizing the *J*-coupling Hamiltonian, expressing the initial density matrix in terms of its eigenstates and propagating the density matrix under the *J*-coupling Hamiltonian. The *J*-coupling values used in the simulations are given in Table 7.1. In the simulations we postulate an initial density matrix of the form.

$$\rho(0) = c_1 (\mathbf{I}^{(2)} \cdot \mathbf{S} + \mathbf{I}^{(6)} \cdot \mathbf{S}) + c_2 (\mathbf{I}^{(3)} \cdot \mathbf{S} + \mathbf{I}^{(5)} \cdot \mathbf{S}) + c_3 (\mathbf{I}^{(4)} \cdot \mathbf{S}) , \qquad (7.10)$$

where S represents the ^{15}N nucleus and I represents the ^{1}H nuclei, which are numbered according to the position in the molecule shown in the inset Figure 7.7. Subsequently, the evolution under the pulse Hamiltonian H_{DC} and the *J*-coupling Hamiltonian H_J were simulated. A relaxation time constant was chosen that produced linewidths similar to those observed experimentally. Eq. (7.10) is a natural guess of the initial density matrix, for several reasons. First, the zero-field Hamiltonian is spherically symmetric, which implies that the initial scalar order associated with the singlet state of parahydrogen can only evolve into scalar terms. Second, the system is symmetric under exchange of spins 2 and 6 or 3 and 4. Finally, homonuclear scalar pairs are neglected because they do not evolve under the application of a magnetic field pulse, and

their evolution during the detection period only produces scalar order free of magnetization. A more rigorous but much more complex simulation to obtain the correct initial density matrix should include the propagation of the scalar order through the iridium complex and the unbound analyte driven by the different and large (>10 spins) *J*-coupling networks present during the reversible exchange. Choosing $c_1 = 1$, $c_2 = 0.5$ and $c_3 = 0$ produces good agreement with the experimental spectrum. In Figure 7.7 the imaginary part of the experimental spectrum is compared with simulation for this choice of c_1, c_2, and c_3. All features of the experimental spectrum, including the phase, are reproduced by the simulation. It should be noted, however, that the phases and amplitudes of all lines in the spectrum are strongly dependent on the initial density matrix and the coefficients c_i. For instance, relative phase shifts of up to 180° between individual lines can be observed in the simulations when changing the relative sign or size of the coefficients.

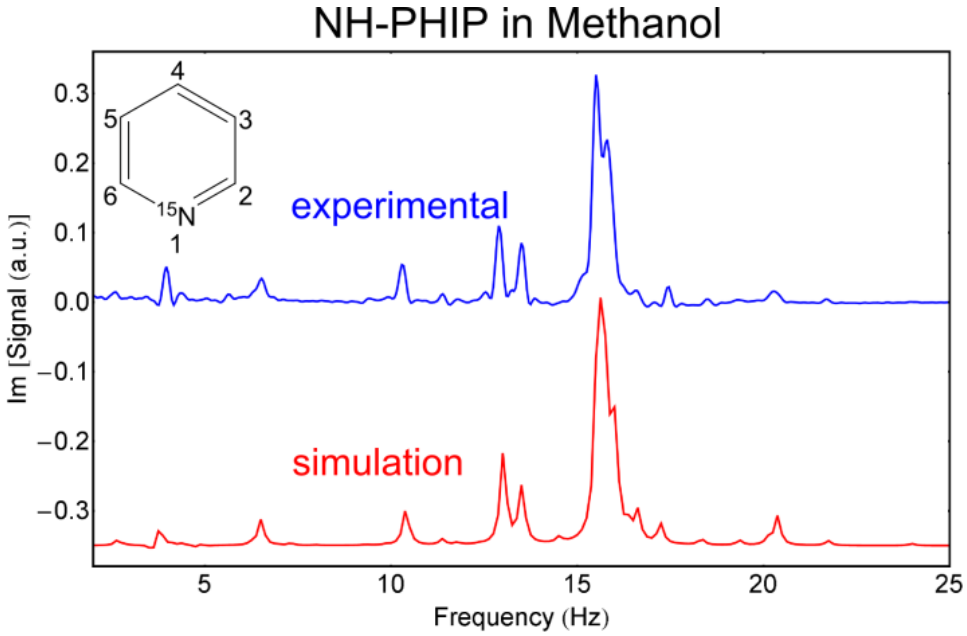

Figure 7.7 NH-PHIP-zero-field spectra after multiplication of the transient by a shifted Hamming window for increased resolution. The upper curve (blue) shows experimentally acquired and processed data and the lower curve (red) shows simulated data. An additional splitting of the main spectral peak due to the smaller long-range couplings can be observed. The *J*-coupling values used in the simulation are given in Table 7.2.

In Figure 7.3 measurements of thermally polarized ^{15}N-labeled pyridine are also compared to simulations. In these measurements the density matrix corresponding to thermal polarization immediately after turning off the guiding field has a term proportional to ($\gamma_I I_z + \gamma_S S_z$). Since $\gamma_I \neq \gamma_S$, this density matrix does not commute with the zero-field Hamiltonian H_J, and evolution occurs without application of any additional pulse. In this case we chose a thermally polarized initial density matrix for the simulation, i.e. $\rho(0) = \gamma_S S_z + \Sigma_k (\gamma_I I_{z,k})$, where the index k labels the five protons of pyridine. As can be seen from the values in Table 7.2, the coupling constants that yield agreement between experiment and simulation vary slightly when the chemical environment of the pyridine is changed.

Table 7.2) *J*-coupling values (in Hz) used to simulate zero-field pyridine spectra from NH-PHIP in methanol and from thermally prepolarized neat pyridine. The values are taken from a) Ref. [97], b) Ref. [98] and c) Ref. [101]. J_{12} is adjusted slightly to improve agreement between experiment and simulation. The original value from the reference is given in parenthesis.

J-coupling constant	NH-PHIP spectrum of pyridine in methanol	thermal spectrum of neat pyridine
J_{12}	-10.14 (-10.06)[a]	-10.93 [b]
J_{13}	-1.56 [a]	-1.47 [b]
J_{14}	0.18 [a]	0.27 [b]
J_{23}	4.87[c]	4.88[a]
J_{24}	1.85 [c]	1.83 [a]
J_{25}	1.01 [c]	0.97 [a]
J_{26}	-0.15 [c]	-0.12 [a]
J_{34}	7.65 [c]	7.62 [a]
J_{35}	1.35 [c]	1.38 [a]

The presence of the catalytic species in the case of NH-PHIP is most likely not responsible for any of the observed shifts given the good agreement between experiment and simulation using the literature values that were obtained from solutions without any metal ions[97,98,101]. Also, the original NH-PHIP literature describes polarization enhancement of free pyridine in solution and does not report large contributions of intermediately bound pyridine to the signal[50].

7.2.2 Current sensitivity limits

Lastly, we discuss the apparent lack of signals from ^{13}C-pyridine isotopomers. In these isotopomers the one-bond *J*-coupling constants between ^{13}C and ^{1}H range from 123 Hz to 150 Hz. For ^{13}C containing pyridine, signals around the one-bond *J*-coupling values are expected.

Figure 7.8 shows a spectrum of ^{15}N labeled pyridine after 108 averages. The SNR of the main peak at 15.6 Hz is close to 3200. Despite this good SNR for the ^{15}N-containing compound there is no detectable signal at higher frequencies that would be produced by isotopomers containing ^{13}C. In this case, where ^{15}N-enriched pyridine was employed, the main reason for the lack of high frequency (100-300Hz) signals is that, in addition to the low natural abundance of ^{13}C (~1%), pyridine isotopomers containing both ^{13}C and ^{15}N produce complex spectra, such that intensity is spread throughout many lines. According to our simulations (not shown) for one particular ^{15}N-^{13}C-isotopomer more than 60 lines are spread across a range of ~35 Hz surrounding the one-bond ^{13}C-^{1}H *J*-coupling constant. A small additional factor is that signals are proportional to the difference in gyromagnetic ratio of the observed nuclei. The signals associated with ^{13}C are additionally reduced be the ratio $(\gamma(^{1}\mathrm{H})-\gamma(^{13}\mathrm{C}))/(\gamma(^{1}\mathrm{H})-\gamma(^{15}\mathrm{N})) = 0.68$ even when the pulse length is optimized for ^{13}C-^{1}H pairs.

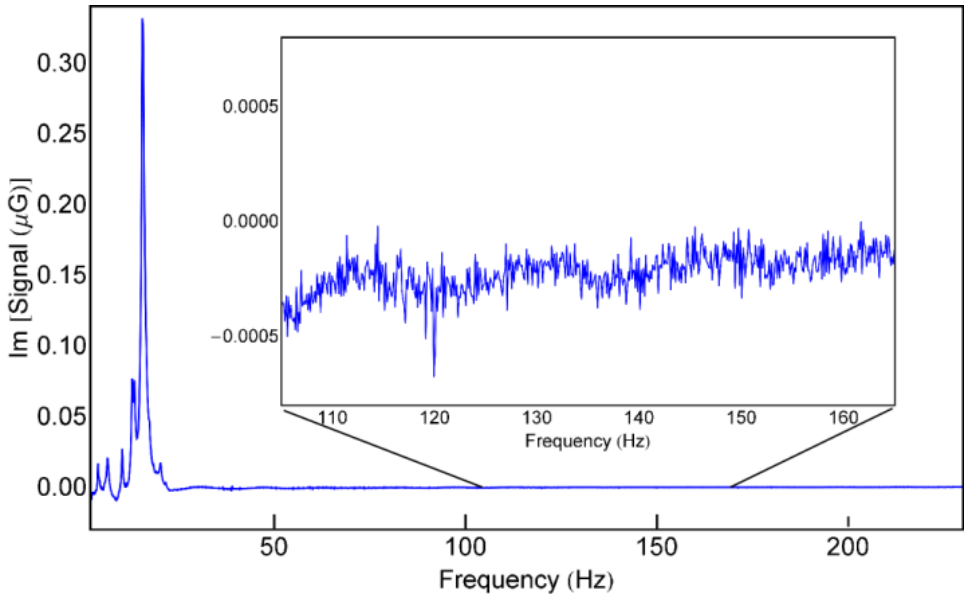

Figure 7.8 NH-PHIP-zero-field spectrum of ^{15}N labeled pyridine after 108 averages. The SNR of the main peak is ~3200. The inset shows the observed noise in the range from 105 to165 Hz. The only apparent peak is at exactly 120 Hz which is a remainder of discrete noise at multiples of 60 Hz. No apparent signals are detected associated with one-bond coupling constants between ^{13}C and ^{1}H expected in that window.

Similarly, in experiments that show signals with ^{15}N-pyridine at its low natural abundance, signatures of ^{13}C-containing isotopomers could not be detected. In these experiments the majority (99.7%) of ^{13}C-pyridine isotopomers contain ^{14}N. Here we attribute the lack of high frequency lines to fast relaxation due to the large quadrupole moment of ^{14}N. This is supported by the observation that in other experiments on thermally polarized ^{14}N-containing compounds we generally observe weak or no zero-field NMR signals. These effects remain under current investigation.

7.3 Significance of ZF-NH-PHIP and concluding remarks

In conclusion, we have demonstrated that NH-PHIP can be used in zero-field NMR spectroscopy. Polarization, in the form of scalar order, can be obtained at zero magnetic field, which can be converted to magnetization solely through the presence of a heteronucleus. The sensitivity is enhanced by four orders of magnitude as compared to measurements using thermally prepolarized samples at 1.6 T. While inductive detection at zero field is generally insensitive, the optical magnetometer enables the acquisition of information-rich *J*-coupling spectra that can be used for chemical identification and fingerprinting, as demonstrated by our results and their agreement with numerical simulation and theory (see Section 7.2). The combination of non-perturbative hyperpolarization and detection by optical methods that we demonstrate here will broaden the applicability of low and zero-field NMR in chemical analysis. NH-PHIP works on a wide and still growing range of analytes.[50,95,96] The presented analysis suggests that all NH-PHIP substrates are polarizable and detectable under identical zero-field conditions. In the future, we expect the combination of sensitive optical magnetometers with general hyperpolarization techniques such as NH-PHIP to enable chemical analysis in locations not accessible by traditional bulky and expensive NMR technology, thereby making NMR more widely used.

8. A three spin model for the zero-field PHIP experiments

In this Section we shall consider the case of hydrogenation of a simple molecule containing a single ^{13}C label, forming a 3-spin system upon hydrogenation. As experimental analogue we chose the hydrogenation of acetylene-dimethyl-carboxylate forming dimethyl-maleate presented in Figure 8.1

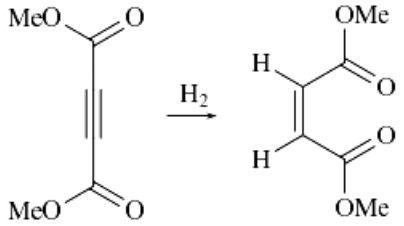

Figure 8.1: Hydrogenation of the acetylene dimethylcarboxylate

The spin system formed by the dimethyl-maleate upon hydrogenation can be one of the three possible ^{13}C isotopomers of the molecule. Here, we will only consider the two cases where the ^{13}C is close to the double bond in the center of the molecule. The isotopomer with ^{13}C in the methyl group is only weakly coupled to the parahydrogen derived hydrogens in the center of the dimethyl-maleate molecule and does not give an observable signal. Both remaining isotopomers can be modeled by a 3-spin system containing two protons and one ^{13}C (on either the carboxy or the vinyl position). In this Section, we demonstrate that the singlet symmetry is broken by the difference in the two proton-carbon scalar coupling, and as a consequence, the initial proton singlet state is spread over the 3-spins meaning that proton-carbon scalar product ($\mathbf{I}_A \cdot \mathbf{S}$) terms are generated. This feature is an important result because, as we have demonstrated in Sections 6.5 and 7.2, it is this heteronuclear singlet order, which is converted into detectable magnetization.

8.1 Evolution of the initial density matrix upon hydrogenation

In this and the following Sections the PHIP zero-field dynamics will be presented from two perspectives. The first involves typical high-field NMR operators and the second involves the usage of angular momentum operators and manifolds as used in Chapter 4. They both are equivalent descriptions linked through basis transforms but appear with different flavor and giving different physical insight.

We begin by defining the proton spins as $\mathbf{I}_A$ and $\mathbf{I}_B$ and the ^{13}C spin as $\mathbf{S}$.

Using these definitions the initial density matrix ρ_0 for a molecule just after hydrogenation is given by:

$$\rho_0 = 1/4\ \mathbf{1} - \mathbf{I}_A \cdot \mathbf{I}_B\ . \tag{8.1}$$

This assertion relies on the fact that spin dynamics at zero field occurs on timescales of a few hundreds of hertz, where the described hydrogenation reactions at a molecular level occur on timescales of picoseconds. We, hence, assert that the spin state of the parahydrogen is suddenly projected onto the hydrogenated molecule. The Hamiltonian of the hydrogenated molecule is determined by the network of scalar coupling in the absence of magnetic field and given by:

$$\mathrm{H}_{ZF} = J_{XA}\ \mathbf{S}\cdot\mathbf{I}_A + J_{AB}\ \mathbf{I}_A\cdot\mathbf{I}_B + J_{XB}\ \mathbf{S}\cdot\mathbf{I}_B\ . \tag{8.2}$$

First we will evaluate the proton singlet spin dynamics at zero field after the hydrogenation. In order to do so, we need to calculate all the terms that will be generated by the evolution of the density matrix ρ(t) under the Hamiltonian H_{ZF}. The dynamics of the system's density matrix is calculated by integrating the Liouville equation:

$$\frac{d\rho}{dt} = -i[\mathrm{H}_{ZF}, \rho]. \tag{8.3}$$

To that end, we need to evaluate the commutators of the different terms in the Hamiltonian with the initial density matrix. We will ignore the identity term in ρ_0 as it commutes with every operator. For the remaining terms in the

Hamiltonian and the initial density matrix the following commutation relations hold:

$$[\, \mathbf{I}_A \cdot \mathbf{I}_B \,,\, \mathbf{I}_B \cdot \mathbf{S} \,] = [\, \mathbf{I}_A \cdot \mathbf{S} \,,\, \mathbf{I}_A \cdot \mathbf{I}_B] = [\, \mathbf{I}_B \cdot \mathbf{S} \,,\, \mathbf{I}_A \cdot \mathbf{S}] \,. \tag{8.4}$$

We introduce the operator Γ so that:

$$[\, \mathbf{I}_A \cdot \mathbf{I}_B \,,\, \mathbf{I}_B \cdot \mathbf{S} \,] = i\boldsymbol{\Gamma}. \tag{8.5}$$

Γ is a 3-spin operator independent of the projection basis and antisymmetric with respect to 2-spin permutation. This inherent symmetry is also apparent when representing Γ in terms of projction operators:

$$\begin{aligned} \boldsymbol{\Gamma} = {} & \mathbf{I}_{Az}\, \mathbf{I}_{By}\, \mathbf{S}_x + \mathbf{I}_{Ay}\, \mathbf{I}_{Bx}\, \mathbf{S}_z + \mathbf{I}_{Ax} \mathbf{I}_{Bz} \mathbf{S}_y \\ & (\, \mathbf{I}_{Ax}\, \mathbf{I}_{By}\, \mathbf{S}_z + \mathbf{I}_{Ay}\, \mathbf{I}_{Bz}\, \mathbf{S}_x + \mathbf{I}_{Az}\, \mathbf{I}_{Bx}\, \mathbf{S}_y \,). \end{aligned} \tag{8.6}$$

In order to obtain the individual terms that are generated the zero field dynamics, we can calculate the commutator of Γ with the respective terms of the zero field Hamiltonian:

$$\begin{aligned} [\, \mathbf{I}_A \cdot \mathbf{I}_B, \Gamma] \; &= i/2 \,(\, \mathbf{I}_A \cdot \mathbf{S} - \mathbf{I}_2 \cdot \mathbf{S}) \;, \\ [\, \mathbf{I}_B \cdot \mathbf{S} \,, \Gamma] \; &= i/2 \,(\, \mathbf{I}_A \cdot \mathbf{I}_B - \mathbf{I}_A \cdot \mathbf{S} \,), \\ [\, \mathbf{I}_A \cdot \mathbf{S} \,, \Gamma] \; &= i/2 \,(\, \mathbf{I}_B \cdot \mathbf{S} - \mathbf{I}_A \cdot \mathbf{I}_B \,). \end{aligned} \tag{8.7}$$

Since no term other than Γ and all the 2-spin scalar product terms appear in Eqs. (4) and (7), we can evaluate the spin dynamics in this particular case. The starting density operator only contains identity and $\mathbf{I}_A \cdot \mathbf{I}_B$ terms. As a result of the shown commutation relationships, the spin evolution is limited to the subspace defined by the 3 different 2-spin scalar products operators and the operator Γ. The density matrix at any time t can thus be written as:

$$\rho(t) = a(t)\, \mathbf{I}_A \cdot \mathbf{I}_B + b(t)\, \mathbf{I}_A \cdot \mathbf{S} + c(t)\, \mathbf{I}_B \cdot \mathbf{S} + d(t) \boldsymbol{\Gamma}. \tag{8.8}$$

We introduce the following short hands:

$$\begin{aligned} \alpha &= J_{XB} - J_{XA} \\ \beta &= J_{AB} - J_{XB} \\ \gamma &= J_{XA} - J_{AB,} \end{aligned} \tag{8.9}$$

such that using Eqs. (3), (4), (5) and (7), we can write more specifically:

$$\frac{d\rho}{dt} = -\left[a(t)\alpha + b(t)\beta + c(t)\gamma\right]\mathbf{\Gamma} + \frac{1}{2}d(t)\left[\alpha\mathbf{I}_A\cdot\mathbf{I}_B + \beta\mathbf{I}_A\cdot\mathbf{S} + \gamma\mathbf{I}_B\cdot\mathbf{S}\right] \quad (8.10)$$

Since the three scalar product operators and the operator $\mathbf{\Gamma}$ are orthogonal under the trace operation, the evolution of a, b, c and d can be separated from Eq. (8.10) and give the differential system:

$$\begin{aligned}
\frac{da}{dt} &= \frac{\alpha}{2}d(t)\\
\frac{db}{dt} &= \frac{\beta}{2}d(t)\\
\frac{dc}{dt} &= \frac{\gamma}{2}d(t)\\
\frac{dd}{dt} &= -\left[\alpha a(t) + \beta b(t) + \gamma c(t)\right].
\end{aligned} \quad (8.11)$$

Upon differentiation of the last line, we obtain:

$$\frac{d^2d}{dt^2} = \frac{\alpha^2+\beta^2+\gamma^2}{2}d(t). \quad (8.12)$$

The exact solution to this equation can be calculated given the initial condition $\rho_0 = 1/4\ \mathbf{1} - \mathbf{I}_A\cdot\mathbf{I}_B$, which means that, for t = 0, we have a(0) = −1 and b(0) = c(0) = d(0) = 0.

Therefore:

$$d(t) = \frac{\alpha}{\omega}\sin(2\pi\nu t), \quad (8.13)$$

where:

$$\nu = \sqrt{\frac{\alpha^2+\beta^2+\gamma^2}{2}}. \quad (8.14)$$

From the expression of d(t), we can deduce the expressions for $a(t)$, $b(t)$ and $c(t)$:

$$a(t) = -1 + \frac{1}{2\nu^2}\alpha^2(1-\cos(2\pi\nu t)),$$
$$b(t) = \frac{1}{2\nu^2}\alpha\beta(1-\cos(2\pi\nu t)), \qquad (8.15)$$
$$c(t) = \frac{1}{2\nu^2}\alpha\gamma(1-\cos(2\pi\nu t)).$$

Another important feature appears as we consider all the scalar product components of the density matrix. It turns out that, according to Eq. (8.11), we can obtain:

$$\frac{d(a+b+c)}{dt} = 0. \qquad (8.16)$$

which also implies that a(t)+b(t)+c(t)=constant. This feature is a restriction on the spin dynamics that makes its description simpler as only two out of the three 2-spin scalar amplitudes are therefore needed to fully describe the system.

An alternative approach for understanding the PHIP effects on a 3-spin system is the usage of angular momentum manifolds, much in analogy to the description used in Chapter 4 to explain thermally produced zero-field spectra. For that purpose we construct our three spin system and the according angular momentum manifolds by first adding the angular momentum of the ^{13}C spin **S** to one of the parahydrogen derived ^{1}H spins $\mathbf{I}_A$. This process yields a total angular momentum $\mathbf{F}_A$, which gives the zero-order energy levels as a singlet with $E_{fA=0}$ = -3/4 J_{XA} and a triplet with $E_{fA=0}$ = +1/4 $J_{XA.}$ The addition of the second more weakly coupled parahydrogen derived spin, $\mathbf{I}_{B,}$ gives the total angular momentum, $\mathbf{F}_A+\mathbf{I}_B=\mathbf{F}$**,** of the system determining the new angular momentum manifolds of the three spin system. In Figure 8.2 the energy level manifolds are depicted. The zero-order singlet with f_A= 0 becomes a doublet with f =1/2 and the f_A=1 triplet is split into a doublet with f=1/2 and a quadruplet with f_A=3/2.

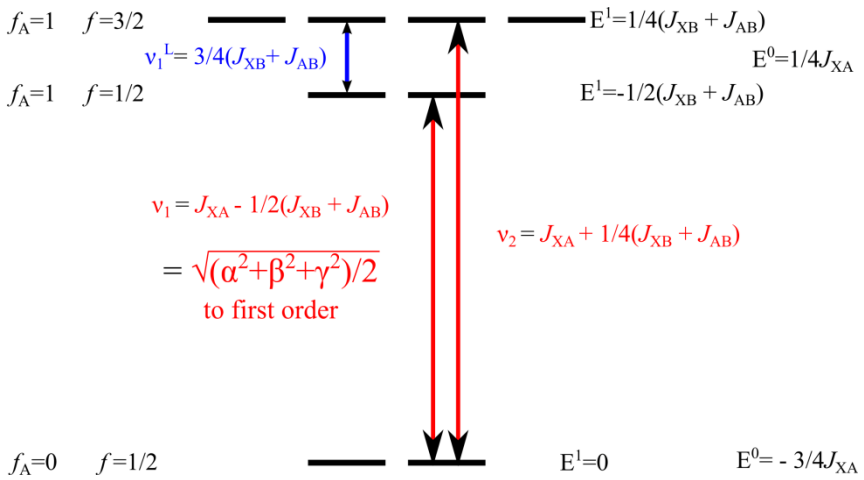

Figure 8.2 Energy level diagram for a general 3-spin system coupled by a scalar coupling Hamiltonian.

We label the basis states in the basis of $\mathbf{F}^2$ in the following order

$$
\begin{aligned}
|n\rangle &= |\, f_A,\ f,\ m_f \,\rangle \\
|n_1\rangle &= |0,\ 1/2,\ -1/2\rangle \\
|n_2\rangle &= |0,\ 1/2,\ +1/2\rangle \\
|n_3\rangle &= |1,\ 1/2,\ -1/2\rangle \\
|n_4\rangle &= |1,\ 1/2,\ +1/2\rangle \\
|n_5\rangle &= |1,\ 3/2,\ -3/2\rangle \\
|n_6\rangle &= |1,\ 3/2,\ -1/2\rangle \\
|n_7\rangle &= |1,\ 3/2,\ +1/2\rangle \\
|n_8\rangle &= |1,\ 3/2,\ +3/2\rangle
\end{aligned}
\qquad (8.17)
$$

Using these basis states we can express the initial density matrix in this basis: $1/4\mathbf{1}\text{-}\mathbf{I}_A\cdot\mathbf{I}_B$,

$$\rho_0 = \begin{pmatrix} \frac{1}{4} & 0 & -\frac{\sqrt{3}}{4} & 0 & 0 & 0 & 0 & 0 \\ 0 & \frac{1}{4} & 0 & -\frac{\sqrt{3}}{4} & 0 & 0 & 0 & 0 \\ -\frac{\sqrt{3}}{4} & 0 & \frac{3}{4} & 0 & 0 & 0 & 0 & 0 \\ 0 & -\frac{\sqrt{3}}{4} & 0 & \frac{3}{4} & 0 & 0 & 0 & 0 \\ 0 & 0 & 0 & 0 & 0 & 0 & 0 & 0 \\ 0 & 0 & 0 & 0 & 0 & 0 & 0 & 0 \\ 0 & 0 & 0 & 0 & 0 & 0 & 0 & 0 \\ 0 & 0 & 0 & 0 & 0 & 0 & 0 & 0 \end{pmatrix} \tag{8.18}$$

and the only off diagonal elements are between states $|n_1\rangle$,$|n_2\rangle$,$|n_3\rangle$ and $|n_4\rangle$ which are the f=1/2 states. Since the Hamiltonian must also be diagonal in that basis all evolution is restricted to the f=1/2 state space after hydrogenation. Not surprising, the frequency of oscillation is given by the energy difference between the involved manifolds.

$$\nu = \sqrt{\frac{\alpha^2 + \beta^2 + \gamma^2}{2}}, \tag{8.19}$$

which to first order just like derived in Section 4.6 is given as

$$\nu = J_{XA} - \frac{1}{2}(J_{XB} + J_{AB}). \tag{8.20}$$

In conclusion of this Section, it is important to note that the symmetry breaking of the parahydrogen singlet under the influence of the zero field Hamiltonian is that it comprises all the possible 2-spin scalar product terms amongst all the nuclei of the hydrogenated molecule. This is crucial in the sense that, upon hydrogenation of a ^{13}C isotopomer, a set of heteronuclear 2-spin scalar product terms will be generated, and that these terms are used for the generation of observable magnetization.

8.2 Incoherent averaging

In the previous Sections, we have demonstrated that the density matrix of a parahydrogenated molecule evolves under the zero-field Hamiltonian and generates scalar terms involving all the spins connected to the initial proton-proton singlet by a *J*-coupling network. During a experimental parahydrogenation experiment many individual molecular parahydrogen reaction occur over the course of an extended time during which parahydrogen is consumed. We shall call this time the "bubbling time", during which parahydrogen is provided and the reaction continues. The density matrix of the ensemble of spins that correspond to the hydrogenated sample is a time average of the previously calculated terms over the bubbling time. Since the bubbling time is much longer than the evolution period of the *J*-coupling, any term in the previous general evolution will be averaged. We can describe the incoherently averaged density matrix ρ_{av} by calculating the averages of the coefficients given in Eq. (8.15):

$$\rho_{av} = -1 + \frac{1}{2\nu^2}\alpha^2 \mathbf{I}_A\mathbf{I}_B + \frac{1}{2\nu^2}\alpha\beta\,\mathbf{I}_A\mathbf{S} + \frac{1}{2\nu^2}\alpha\gamma\,\mathbf{I}_A\mathbf{S}. \tag{8.21}$$

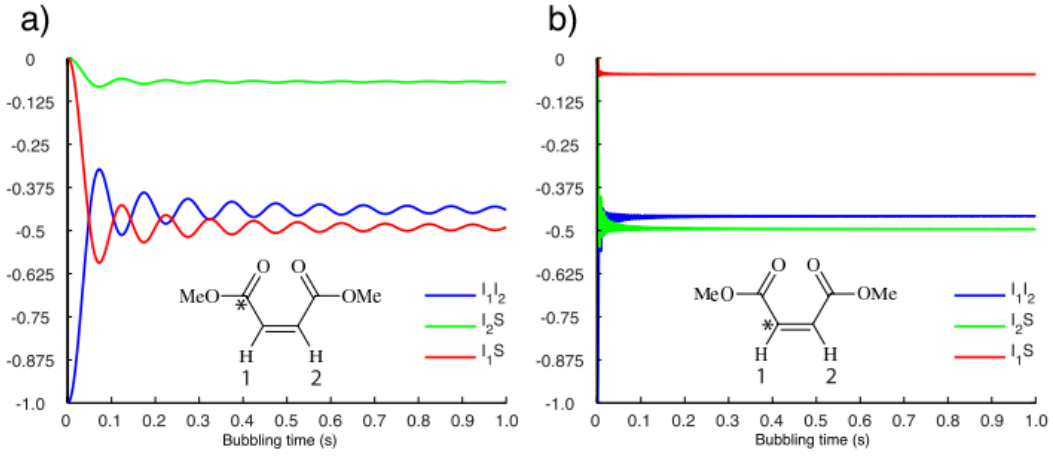

Figure 8.3 Buildup of the different possible terms in a 3-spin system defined by two protons A and B, and a carbon X, with the couplings corresponding to those of different isotopomers of the dimethyl-maleate: a)^{13}C on the carboxylate group: (J_{XA} = 2.7 Hz, J_{XB} = 13.3 Hz, J_{AB} = 12 Hz) b)^{13}C on the vinyl group (J_{XA} = 167.7 Hz, J_{XB} = −2.5 Hz, J_{AB} = 12 Hz[13]).

The incoherently averaged density matrix does not contain terms invovling Γ. This is consistent with the dynamics as, according to Eq. (8.13), the function d(t) that characterizes the amplitude of this term does not have a constant component. This result can be simulated for the vinyl and carboxy ^{13}C isotopomers of the dimethylmaleate, and we can see the rapid buildup of the different 2-spin scalar products as presented on Figure 8.3.

As a function of bubbling time many hydrogenation reactions occur, starting evolution in the individual molecules. The overall density matrix of the sample arrives at its average value on a timescale dictated by the *J*-coupling values in the respective spin-system.

The process of incoherent averaging can also be described by using the angular momentum manifolds formalism. Simply, the off-diagonal elements of the initial density matrix are eliminated. In this case $1/4\mathbf{1}\text{-}\mathbf{I}_A\mathbf{I}_B$ is averaged such that

$$\rho_{\mathrm{av}} = \begin{pmatrix} \frac{1}{4} & 0 & 0 & 0 & 0 & 0 & 0 & 0 \\ 0 & \frac{1}{4} & 0 & 0 & 0 & 0 & 0 & 0 \\ 0 & 0 & \frac{3}{4} & 0 & 0 & 0 & 0 & 0 \\ 0 & 0 & 0 & \frac{3}{4} & 0 & 0 & 0 & 0 \\ 0 & 0 & 0 & 0 & 0 & 0 & 0 & 0 \\ 0 & 0 & 0 & 0 & 0 & 0 & 0 & 0 \\ 0 & 0 & 0 & 0 & 0 & 0 & 0 & 0 \\ 0 & 0 & 0 & 0 & 0 & 0 & 0 & 0 \end{pmatrix}, \tag{8.22}$$

which shows that the hydrogenation procedure in average creates population of 1/4 on $|f_A=0, f=1/2\rangle$ states and 3/4 population on $|f_A=1, f=1/2\rangle$ states.

8.3 Generation of signal

Analysis of the generation of signal can proceed as described in Sections 6.5 or 7.2 using the zero-quantum operator formalism, which gives a nice picture and interpretation of the pulse and ensuing evolution in terms of NMR operator formalism yet fails to predict the exact shape of the spectrum.

Hence, we will proceed, here, with the description based on the angular momentum manifolds. As introduced in Section 6.5 the part of the pulse Hamiltonian that acts on the spin system is given as:

$$H_P = 1/2\ (I_{Az}+I_{Bz}-S_z)\ . \tag{8.23}$$

In the $\mathbf{F}^2$ basis this Hamiltonian is given as:

$$H_P = 1/2 \begin{pmatrix} \frac{1}{2} & 0 & \frac{1}{\sqrt{3}} & 0 & 0 & -\sqrt{\frac{2}{3}} & 0 & 0 \\ 0 & -\frac{1}{2} & 0 & -\frac{1}{\sqrt{3}} & 0 & 0 & -\sqrt{\frac{2}{3}} & 0 \\ \frac{1}{\sqrt{3}} & 0 & -\frac{1}{6} & 0 & 0 & -\frac{\sqrt{2}}{3} & 0 & 0 \\ 0 & -\frac{1}{\sqrt{3}} & 0 & \frac{1}{6} & 0 & 0 & -\frac{\sqrt{2}}{3} & 0 \\ 0 & 0 & 0 & 0 & \frac{1}{2} & 0 & 0 & 0 \\ -\sqrt{\frac{2}{3}} & 0 & -\frac{\sqrt{2}}{3} & 0 & 0 & \frac{1}{6} & 0 & 0 \\ 0 & -\sqrt{\frac{2}{3}} & 0 & -\frac{\sqrt{2}}{3} & 0 & 0 & -\frac{1}{6} & 0 \\ 0 & 0 & 0 & 0 & 0 & 0 & 0 & -\frac{1}{2} \end{pmatrix}. \tag{8.24}$$

It is useful to look at this Hamiltonian in the $\mathbf{F}^2$ basis because it indicates nicely which energy levels, depicted in Figure 8.2, are connected and which coherences are created.

This Hamiltonian can be applied to ρ_{av} such that after a $\pi/2$ pulse we obtain $\rho_1 = \exp(-i\ H_P\ \pi/2)\ \rho_{av}\ (\exp(i\ H_P\ \pi/2)$.

$$\rho_1 = \begin{pmatrix} 0 & 0 & \frac{-1}{4\sqrt{3}}(i+1) & 0 & 0 & \frac{-1}{4\sqrt{6}}(i+1) & 0 & 0 \\ 0 & 0 & 0 & \frac{1}{4\sqrt{3}}(i-1) & 0 & 0 & \frac{-1}{4\sqrt{6}}(i-1) & 0 \\ \frac{1}{4\sqrt{3}}(i-1) & 0 & 0 & 0 & 0 & \frac{1}{12\sqrt{2}} - \frac{i}{4\sqrt{2}} & 0 & 0 \\ 0 & \frac{-1}{4\sqrt{3}}(i+1) & 0 & 0 & 0 & 0 & \frac{-1}{12\sqrt{2}} - \frac{i}{4\sqrt{2}} & 0 \\ 0 & 0 & 0 & 0 & 0 & 0 & 0 & 0 \\ \frac{1}{4\sqrt{6}}(i-1) & 0 & \frac{1}{12\sqrt{2}} + \frac{i}{4\sqrt{2}} & 0 & 0 & 0 & 0 & 0 \\ 0 & \frac{1}{4\sqrt{6}}(i+1) & 0 & \frac{-1}{12\sqrt{2}} + \frac{i}{4\sqrt{2}} & 0 & 0 & 0 & 0 \\ 0 & 0 & 0 & 0 & 0 & 0 & 0 & 0 \end{pmatrix}. \quad (8.25)$$

The primary purpose of displaying this matrix is again, to show between which states coherences are created. Since the Hamiltonian is diagonal in this basis it is straightforward to find the density matrix as a function of time evolving under the zero-field Hamiltonian.

$$\rho(t)=\exp(-i\, H_{zf}\, t)\, \rho_1\, (\exp(i\, H_{zf}\, t), \quad (8.26)$$

and finally we can calculate the signal as a function of time as

$$\begin{aligned} s(t)=Tr(\rho(t)\,(I_{Az}+I_{Bz}-S_z))= \quad & 1/3\, \sin(2\pi\nu_1\, t) \\ & -1/3\, \sin(2\pi\nu_2\, t) \\ & +1/3\, \sin(2\pi\nu_3\, t). \end{aligned} \quad (8.27)$$

In Figure 8.4 the experimental spectra obtained from the hydrogenation of acetylene-dimethyl-dicarbxoylate are shown overlayed by simulations for the two different isotopomers confirming the theoretical predictions. In particular the blue trace corresponding to the ^{13}C vinyl isotopomer clearly follows the predicted pattern with three visible peaks one peak in the low frequency region given by $3/4(J_{XB}+J_{AB})$ and two antiphase peaks at high frequencies given by $J_{XA}-1/2(J_{XB}+J_{AB})$ and $J_{XA}+1/4(J_{XB}+J_{AB})$. The green trace is the result of a numerical simulation including 6 spins. For the carboxyl ^{13}C isotopomer this is necessary because additional couplings to the methoxy group cause additional splitting and because all coupling constants have the same order of magnitude such that a perturbative description of the frequencies would fail to produce the exact peak positions.

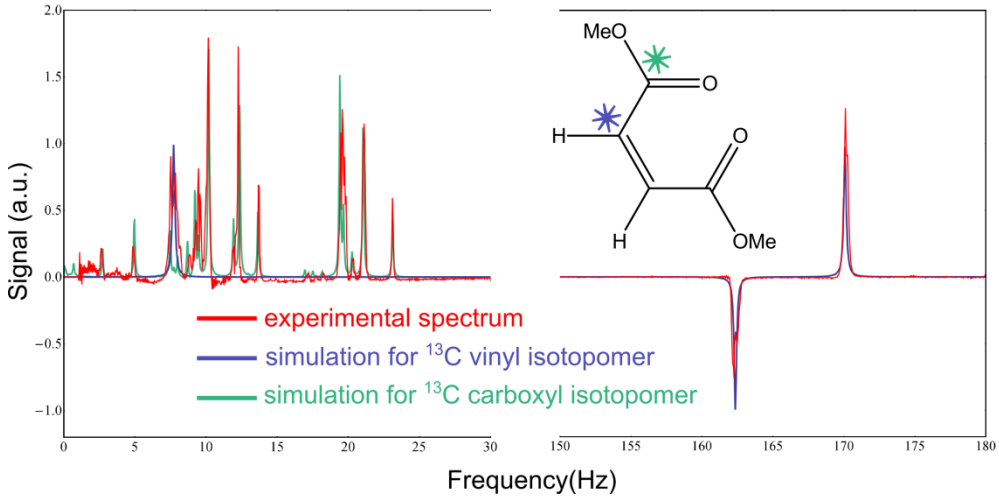

Figure 8.4 Zero-field PHIP spectrum obtained from the hydrogenation of acetylene-dimethyl-dicarboxylate overlayed with simulations for the two isotopomers that produce signal.

9. Conclusions and Outlook

The research described in this thesis further develops zero-field NMR, which holds the promise to enable chemical analysis at greatly reduced cost and in environments not accessible to standard high-field NMR technology. Detection of analytes at low concentrations primarily requires sensitive detectors and sufficient nuclear polarization. The weak thermal polarization of nuclear spins has given NMR, in general, the reputation of being an inherently insensitive method. For example, even in magnetic fields of superconducting magnets the polarization obtained does not exceed 10^{-4}. Combinations of novel detection schemes and of hyperpolarization are thus particularly attractive in unconventional or portable NMR applications. This thesis details the use of mm scale atomic magnetometers with sensitivities of ~20fT/√Hz for the acquisition of zero-field NMR signals generated with thermal prepolarization and hyperpolarization schemes.

The fundamental principles underlying zero-field NMR are outlined from the perspective of the detector and from the perspective of the NMR sample. The detailed analysis of the NMR signal, based on the fundamental properties of quantum mechanical angular momentum, results in the ability of straightforward interpretation and prediction of zero-field NMR spectra. Multiplets observed in zero-field NMR spectra can be quickly assigned to their corresponding spin systems. It is also shown, that the resolution in zero-field NMR can easily be on the order of tens of mHz such that only small amounts of overlap are expected from differing chemicals opening the door for the analysis of complex mixtures. Furthermore, this thesis shows that remaining ambiguities for peak assignment in zero-field NMR spectra can be removed by the application of a small magnetic field, which acts as a perturbation to the dominating *J*-coupling. The Zeeman perturbation causes splittings with simple rules for the resulting multiplets. The multiplets indicate the gyromagnetic ratio of the involved spins as well as the multiplicity of the involved angular momentum manifolds

In addition to the these developments of zero-field NMR with thermally prepolarized samples the thesis introduces parahydrogen induced polarization (PHIP) as a hyperpolarization scheme that can easily be combined with zero-

field NMR. PHIP can be produced directly next to the detector and is shown not to require the presence of a magnetic field. The presented combination of the sensitive atomic magnetometer with the PHIP hyperpolarization scheme allows for the detection of samples with carbon-13 at its low natural abundance of ~1%, which greatly increases the range of analytes that can be analyzed with zero-field NMR. Furthermore, recent advances have enabled the transfer of PHIP to molecules without hydrogenation [50,52] This NH-PHIP technique is introduced as a hyperpolarization technique for zero-field NMR. The detection of samples is demonstrates containing nitrogen-15 at its even lower natural abundance of ~0.36%. Also the NH-PHIP polarization widens the range of analytes that can be hyperpolarized and subsequently analyzed in a zero-field NMR spectrometer. Since PHIP created, excited and measured at pure zero field is a previously unknown phenomenon this thesis also provides theoretical insight by developing a formalism based on angular momenta and the respective operators to predict and understand the observed effects. The formalism is explicitly applied to a three spin system but generalizes to an arbitrary number of spins.

Since the development of zero-field NMR is still at an early stage it is not possible to really and fully gauge its competitiveness with high-field NMR or portable lower resolution versions thereof, but one may leave with the impression that is emerging as a cost effective, potentially miniaturizable type of NMR with great sensitivity that will give access to applications and spaces not accessible conventional high-field NMR.

There is no question that zero-field NMR still has much space to grow into many directions by, either, increasing the sensitivity of the magnetometer, or by implementation of other hyperpolarization techniques, or by the development of multidimensional pulse sequences, or by miniaturization and coupling with microfluidic platforms or any other improvement one may dream of, which could be fun and exciting of their own.

References

1. Bodenhausen, G., Ernst, R.R. & Wokaun, A. *Principles of Nuclear Magnetic Resonance in One and Two Dimensions*. (Oxford University Press: New York, 1987).

2. Slichter, C.P. *Principles of Magnetic Resonance*. (Springer-Verlag: New York, 1990).

3. Greenberg, Y. Application of superconducting quantum interference devices to nuclear magnetic resonance. *Rev. Mod. Phys.* **70**, 175-222 (1998).

4. Budker, D. & Romalis, M. Optical magnetometry. *Nat. Phys.* **3**, 227-234 (2007).

5. Kornack, T.W., Smullin, S.J., Lee, S.-K. & Romalis, M.V. A low-noise ferrite magnetic shield. *Appl. Phys. Lett.* **90**, 223501 (2007).

6. McDermott, R. *et al.* Liquid-state NMR and scalar couplings in microtesla magnetic fields. *Science* **295**, 2247-9 (2002).

7. Trabesinger, A.H. *et al.* SQUID-Detected Liquid State NMR in Microtesla Fields. *J. Phys. Chem. A* **108**, 957-963 (2004).

8. Yashchuk, V. *et al.* Hyperpolarized Xenon Nuclear Spins Detected by Optical Atomic Magnetometry. *Phys. Rev. Lett.* **93**, 1-4 (2004).

9. Zotev, V.S. *et al.* Microtesla MRI with dynamic nuclear polarization. *J. Magn. Reson.* **207**, 78-88 (2010).

10. Appelt, S., Häsing, F., Kühn, H., Perlo, J. & Blümich, B. Mobile High Resolution Xenon Nuclear Magnetic Resonance Spectroscopy in the Earth's Magnetic Field. *Phys. Rev. Lett.* **94**, 1-4 (2005).

11. Savukov, I. & Romalis, M. NMR Detection with an Atomic Magnetometer. *Phys. Rev. Lett.* **94**, 1-4 (2005).

12. Xu, S. *et al.* Magnetic resonance imaging with an optical atomic magnetometer. *Proc. Natl. Acad. Sci. U. S. A.* **103**, 12668-71 (2006).

13. Appelt, S., Kühn, H., Häsing, F.W. & Blümich, B. Chemical analysis by ultrahigh-resolution nuclear magnetic resonance in the Earth's magnetic field. *Nat. Phys.* **2**, 105-109 (2006).

14. Robinson, J.N. *et al.* Two-dimensional NMR spectroscopy in Earth's magnetic field. *J. Magn. Reson.* **182**, 343-7 (2006).

15. Savukov, I.M., Seltzer, S.J. & Romalis, M.V. Detection of NMR signals with a radio-frequency atomic magnetometer. *J. Magn. Reson.* **185**, 214-20 (2007).

16. Appelt, S., Häsing, F., Kühn, H. & Blümich, B. Phenomena in J-coupled nuclear magnetic resonance spectroscopy in low magnetic fields. *Phys. Rev. A* **76**, 1-11 (2007).

17. Ledbetter, M.P. *et al.* Zero-field remote detection of NMR with a microfabricated atomic magnetometer. *Proc. Natl. Acad. Sci. U. S. A.* **105**, 2286-90 (2008).

18. Tsai, L.L., Mair, R.W., Rosen, M.S., Patz, S. & Walsworth, R.L. An open-access, very-low-field MRI system for posture-dependent 3He human lung imaging. *J. Magn. Reson.* **193**, 274-85 (2008).

19. Ledbetter, M.P. *et al.* Optical detection of NMR J-spectra at zero magnetic field. *J. Magn. Reson.* **199**, 25-9 (2009).

20. Appelt, S. *et al.* NMR spectroscopy in the milli-Tesla regime: Measurement of 1H chemical-shift differences below the line width. *Chem. Phys. Lett.* **485**, 217-220 (2010).

21. Theis, T. *et al.* Parahydrogen-enhanced zero-field nuclear magnetic resonance. *Nat. Phys.* **7**, 571-575 (2011).

22. Appelt, S. *et al.* Paths from weak to strong coupling in NMR. *Phys. Rev. A* **81**, 1-11 (2010).

23. Kominis, I.K., Kornack, T.W., Allred, J.C. & Romalis, M.V. A subfemtotesla multichannel atomic magnetometer. *Nature* **422**, 596-9 (2003).

24. Blümich, B., Casanova, F. & Appelt, S. NMR at low magnetic fields. *Chem. Phys. Lett.* **477**, 231-240 (2009).

25. Savukov, I.M. *et al.* MRI with an atomic magnetometer suitable for practical imaging applications. *J. Magn. Reson.* **199**, 188-91 (2009).

26. Kelso, N. *et al.* Distortion-free magnetic resonance imaging in the zero-field limit. *J. Magn. Reson.* **200**, 285-90 (2009).

27. Appelt, S., Häsing, F.W., Kühn, H., Sieling, U. & Blümich, B. Analysis of molecular structures by homo- and hetero-nuclear J-coupled NMR in ultra-low field. *Chem. Phys. Lett.* **440**, 308-312 (2007).

28. Ledbetter, M.P. *et al.* Near-Zero-Field Nuclear Magnetic Resonance. *Phys. Rev. Lett.* **107**, 107601 (2011).

29. Goodson, B.M. Nuclear magnetic resonance of laser-polarized noble gases in molecules, materials, and organisms. *J. Magn. Reson.* **155**, 157-216 (2002).

30. Bowers, C.R. & Weitekamp, D.P. Transformation of Symmetrization Order to Nuclear-Spin Magnetization by Chemical Reaction and Nuclear Magnetic Resonance. *Phys. Rev. Lett.* **57**, (1986).

31. Natterer, J. & Bargon, J. Parahydrogen induced polarization. *Prog. Nucl. Magn. Reson. Spectrosc.* **31**, 293-315 (1997).

32. Abragam, A. & Goldman, M. Principles of dynamic nuclear polarisation. *Rep. Prog. Phys.* **41**, 395-467 (1978).

33. Maly, T. *et al.* Dynamic nuclear polarization at high magnetic fields. *J. Chem. Phys.* **128**, 052211 (2008).

34. Goez, M. Chapter 3 Photo-CIDNP Spectroscopy. *Ann. R. NMR S.* **66**, 77-147 (2009).

35. Walker, T.G. & Happer, W. Spin-exchange optical pumping of noble-gas nuclei. *Rev. Mod. Phys.* **69**, 629-642 (1997).

36. Raftery, D. Xenon NMR Spectroscopy. *Annu. Rep. NMR Spectrosc.* **57**, 205-270 (2006).

37. Navon, G. *et al.* Enhnacement of Solution NMR and MRI with Laser-Polarized Xenon. *Science* **271**, 1848-1851 (1996).

38. Weitekamp, D.P. & Bowers, R.C. Parahydrogen and Synthesis Allow Dramatically Enhanced Nuclear Alignment. *J. Am. Chem. Soc.* **109**, 5541-5542 (1987).

39. Duckett, S.B. & Wood, N.J. Parahydrogen-based NMR methods as a mechanistic probe in inorganic chemistry. *Coord. Chem. Rev.* **252**, 2278-2291 (2008).

40. Bowers, C.R. *Sensitivity Enhancement Utilizing Parahydrogen. Encyclopedia of Nuclear Magnetic Resonance, Online*. *Enc. Magn. Reson.* 1-19 (John Wiley & Sons, Ltd.: Chichester, 2007).doi:10.1002/9780470034590.emrstm0489

41. Duckett, S.B. & Sleigh, C.J. Applications of the parahydrogen phenomenon: A chemical perspective. *Prog. Nucl. Magn. Reson. Spectrosc.* **34**, 71-92 (1999).

42. Korchak, S.E. *et al.* Low-Field, Time-Resolved Dynamic Nuclear Polarization with Field Cycling and High-Resolution NMR Detection. *Appl .Magn. Reson.* **37**, 515-537 (2010).

43. Lingwood, M.D., Ivanov, I. a, Cote, A.R. & Han, S.-I. Heisenberg spin exchange effects of nitroxide radicals on Overhauser dynamic nuclear polarization in the low field limit at 1.5mT. *J. Magn. Reson.* **204**, 56-63 (2010).

44. Halse, M.E. & Callaghan, P.T. A dynamic nuclear polarization strategy for multi-dimensional Earth's field NMR spectroscopy. *J. Magn. Reson.* **195**, 162-8 (2008).

45. Ivanov, K.L. *et al.* Transfer of CIDNP Among Coupled Spins at Low Magnetic. *Appl. Magn. Reson.* **30**, 513-534 (2006).

46. Vermeersch, G., Marko, J., Febvay-Garot, N., Caplain, S. & Lablache-Combier, A. Low-field photochemically induced dynamic nuclear polarization (photo-CIDNP) of diazanaphthalenes. *J. Chem. Soc., Perkin Trans. 2* **2027**, 2027 (1984).

47. Sarvarov, F.S., Salikhov, K.M. & R.Z., S. CIDNP in low magnetic fields. *Chem. Phys.* **16**, 41-47 (1976).

48. Appelt, S., Haesing, F.., Baer-Lang, S., Shah, N.. & Blümich, B. Proton magnetization enhancement of solvents with hyperpolarized xenon in very low-magnetic fields. *Chem. Phys. Lett.* **348**, 263-269 (2001).

49. Gong, Q., Gordji-nejad, A., Blumich, B. & Appelt, S. Letters to Analytical Chemistry Trace Analysis by Low-Field NMR : Breaking the Sensitivity Limit. *Anal .Chem.* **82**, 7078-7082 (2010).

50. Adams, R.W. *et al.* Sensitivity by Polarization Transfer. *Science* **323**, 1708-1711 (2009).

51. Adams, R.W., Duckett, S.B., Green, R. a, Williamson, D.C. & Green, G.G.R. A theoretical basis for spontaneous polarization transfer in non-hydrogenative parahydrogen-induced polarization. *J. Chem. Phys.* **131**, 194505 (2009).

52. Atkinson, K.D. *et al.* Spontaneous transfer of parahydrogen derived spin order to pyridine at low magnetic field. *J. Am. Chem. Soc.* **131**, 13362-8 (2009).

53. Levitt, M.H. *Spin Dynamics, Basics of Nuclear Magnetic Resonance*. (John Wiley & Sons, Ltd.: Chichester, 2008).

54. Cavanagh, J., Fairbrother, W.J., Palmer, A.G. & Skelton, N.J. *Protein NMR Spectroscopy: Principles and Practice*. (Elsevier Academic Press: New York, 2007).

55. Sakurai, J.J. *Modern Quantum Mechanics*. (Addison Wesley: Reading, 1994).

56. Cohen-Tannoudji, C., Diu, B. & Ostrowsky, D. *Quantum Mechanics*. (Wiley: New York, 1977).

57. Shankar *Principles of Quantum Mechanics*. (Plenum Press: New York, 1994).

58. Auzinsh, M., Budker, D. & Rochester, S.M. *Optically Polarized Atoms: Understanding Light-Atom Interactions*. (Oxford University Press: 2010).

59. Savukov, I. & Romalis, M. Effects of spin-exchange collisions in a high-density alkali-metal vapor in low magnetic fields. *Physical Review A* **71**, 2-9 (2005).

60. Allred, J., Lyman, R., Kornack, T. & Romalis, M. High-Sensitivity Atomic Magnetometer Unaffected by Spin-Exchange Relaxation. *Physical Review Letters* **89**, 4-7 (2002).

61. Seltzer, S.J. Developments in Alkali-Metal Atomic Magnetometry. PhD Thesis, Princeton University. (2008).

62. Weinstock, H. *SQUID Sensors: Fuandamentals, Fabrication and Applications*. (Kluwer Academic: Dordrecht, 1996).

63. Drung, D., Bechstein, S., Franke, K., Scheiner, M. & Schurig, T. Improved Direct-Coupled dc SQUID Read-out Electronics with Automatic Bias Voltage Tuning. *IEEE T. Appl. Supercon.* **11**, 880-883 (2001).

64. Oukhanski, N., Stolz, R., Zakosarenko, V. & Meyer, H. Low-drift broadband directly coupled dc SQUID read-out electronics. *Physica C* **368**, 166-170 (2002).

65. Gratta, C.D., Pizzella, V., Tecchio, F. & Romani, G.L. Magnetoencephalography — a noninvasive brain imaging method with 1 ms time resolution. *Rep. Prog. Phys.* **64**, 1759-1814 (2001).

66. Bize, S. *et al.* High-accuracy measurement of the 87 Rb ground-state hyperfine splitting in an atomic fountain. *Europhys. Lett.* **45**, 558 (1999).

67. Barwood, G., Gill, P. & Rowley, W. Frequency Measurements on Optically Narrowed Rb-Stabalised Laser Diaodes at 780 nm and 795 nm. *Appl. Phys. B* **53**, 142-147 (1991).

68. Happer, W. Optical pumping. *Rev. Mod. Phys.* **44**, 169-250 (1972).

69. Rosenberry, M., Reyes, J., Tupa, D. & Gay, T. Radiation trapping in rubidium optical pumping at low buffer-gas pressures. *Physi. Rev. A* **75**, 023401 (2007).

70. Erickson, C.J. Measurements of the magnetic field dependence of the spin relaxation rate in alkali metal vapors. PhD Thesis, Princeton University. (2000).

71. Shah, V., Knappe, S., Schwindt, P.D.D. & Kitching, J. Subpicotesla atomic magnetometry with a microfabricated vapour cell. *Nat. Photonics* **1**, 649-652 (2007).

72. Horowitz, P. & Hill, W. *The Art Of Electronics*. (Cambridge Univeristy Press: Cambridge, 1989).

73. Bernstein, H.J., Pople, J.A. & Schneider, W.G. The analysis of nuclear magnetic resonance spectra. *Can. J. Chem.* **35**, 65-81 (1957).

74. Pople, J.A. & Schaefer, T. The analysis of complex nuclear magnetic resonance spectra. *Mol. Phys.* **3**, 547-556 (1960).

75. Warren, W.S., Jenista, E., Branca, R.T. & Chen, X. Increasing hyperpolarized spin lifetimes through true singlet eigenstates. *Science* **323**, 1711-4 (2009).

76. Carravetta, M. & Levitt, M.H. Theory of long-lived nuclear spin states in solution nuclear magnetic resonance. I. Singlet states in low magnetic field. *J. Chem. Phys.* **122**, 214505 (2005).

77. Pileio, G. & Levitt, M.H. Theory of long-lived nuclear spin states in solution nuclear magnetic resonance. II. Singlet spin locking. *J. Chem. Phys.* **130**, 214501 (2009).

78. Pileio, G., Carravetta, M. & Levitt, M.H. Storage of nuclear magnetization as long-lived singlet order in low magnetic field. *Proc. Natl. Acad. Sci. U. S. A.* **107**, 17135-9 (2010).

79. Pileio, G., Carravetta, M. & Levitt, M. Extremely Low-Frequency Spectroscopy in Low-Field Nuclear Magnetic Resonance. *Phys. Rev. Lett.* **103**, 1-4 (2009).

80. Pileio, G., Carravetta, M., Hughes, E. & Levitt, M.H. The long-lived nuclear singlet state of 15N-nitrous oxide in solution. *J. Am. Chem. Soc.* **130**, 12582-3 (2008).

81. Carravetta, M., Johannessen, O. & Levitt, M. Beyond the T1 Limit: Singlet Nuclear Spin States in Low Magnetic Fields. *Phys. Rev. Lett* **92**, 1-4 (2004).

82. Vinogradov, E. & Grant, A.K. Hyperpolarized long-lived states in solution NMR: three-spin case study in low field. *J. Magn. Reson.* **194**, 46-57 (2008).

83. Canet, D. *et al.* Para-hydrogen enrichment and hyperpolarization. *Concept. Magnetic. Res. A* **28**, 321-330 (2006).

84. Herlemont, F., Khelkhal, M. & Legrand, J. Separation and conversion of nuclear spin isomers of ethylene. *Chem. Phys. Lett.* 424-428 (2000).

85. Sun, Z.-D., Takagi, K. & Matsushima, F. Separation and conversion dynamics of four nuclear spin isomers of ethylene. *Science* **310**, 1938-41 (2005).

86. Aime, S., Gobetto, R., Reineri, F. & Canet, D. Polarization transfer from para-hydrogen to heteronuclei: effect of H/D substitution. The case of AA'X and A2A2'X spin systems. *J. Magn. Reson.* **178**, 184-92 (2006).

87. Zax, D.B., Bielecki, A., Zilm, K.W. & Pines, A. Heteronuclear zero-field NMR. *Chem. Phys. Lett.* **106**, 550-553 (1984).

88. Osborn, B.J.A., Jardine, F.H., Young, J.F. & Wilkinson, G. The Preparation and Properties of Tris(triphenylphosphine)halogenorhodium(I) and Some Reactions

Thereof Including Catalytic Homogeneous Hydrogenation of Olefins and Acetylenes and Their Derivatives. *J. Chem. Soc. A* (1966).

89. Schaefer, T.E.D., Chan, W.K., Sebastian, R. & Hruska, E. Concerning the internal rotational barrier and the experimental and theoretical nJ(13C,13C) and nJ (1H,13C) in ethylbenzene-B-13C. *Can. J. Chem.* **74**, 1626-1637 (1994).

90. Schaefer, T., Penner, G.H. & Sebastian, R. 1H nuclear magnetic resonance and molecular orbital studies of the structure and internal rotations in ethylbenzene. *Can. J. Chem.* **65**, 873-877 (1987).

91. Lee, C.J., Suter, D. & Pines, A. Theory of Multiple-Pulse NMR at Low and Zero Fields. *J. Magn. Reson.* **75**, 110-124 (1987).

92. Dang, H.B., Maloof, a. C. & Romalis, M.V. Ultrahigh sensitivity magnetic field and magnetization measurements with an atomic magnetometer. *Applied Physics Letters* **97**, 151110 (2010).

93. Theis, T. *et al.* Zero-Field NMR Enhanced by Parahydrogen in Reversible Exchange. *J. Am. Chem. Soc.* (2012).doi:10.1021/ja2112405

94. Glöggler, S. *et al.* Selective drug trace detection with low-field NMR. *The Analyst* **136**, 1566-8 (2011).

95. Cowley, M.J. *et al.* Iridium N-heterocyclic carbene complexes as efficient catalysts for magnetization transfer from para-hydrogen. *J. Am. Chem. Soc.* **133**, 6134-7 (2011).

96. Glöggler, S. *et al.* Para-hydrogen induced polarization of amino acids, peptides and deuterium-hydrogen gas. *Phys. Chem. Chem. Phys.* **13**, 13759-64 (2011).

97. Lichter, R.L. & Roberts, J.D. 15N Nuclear Magnetic Resonance Spectroscopy XIII. Pyridine-15N. *J. Am. Chem. Soc.* **93**, 5218-5224 (1971).

98. Jakobsen, H.J., Yang, P.-I. & Brey, W.S. Natural abundance proton-coupled15N NMR spectra of pyridines observed from proton

polarization transfer experiments. *Org. Magn. Reson.* **17**, 290-295 (1981).

99. Koptyug, I.V. *et al.* para-Hydrogen-Induced Polarization in Heterogeneous Hydrogenation Reactions. *J. Magn. Reson.* 5580-5586 (2007).

100. Bigler, P. *NMR Spectroscopy: Processing Strategies*. *Journal of Chemical Education* **75**, (Wiley-VCH:Weinheim: 2000).

101. Hansen, M. & Jakobsen, H. High-resolution 13C NMR spectra and long-range 13C1H spin coupling constants in pyridine and 2-bromopyridine. *J. Magn. Reson.* **10**, 74-84 (1973).